ALMA MATER STUDIORUM
UNIVERSITÀ DI BOLOGNA

DOTTORATO DI RICERCA IN

SCIENZE DELLA TERRA, DELLA VITA E DELL'AMBIENTE

Ciclo 37

Settore Concorsuale: 04/A2 - GEOLOGIA STRUTTURALE, GEOLOGIA STRATIGRAFICA, SEDIMENTOLOGIA E PALEONTOLOGIA

Settore Scientifico Disciplinare: GEO/03 - GEOLOGIA STRUTTURALE

CHARACTERISING FRACTURED CRYSTALLINE BASEMENT EVOLUTION THROUGH TIME, SMØLA ISLAND, MID-NORWAY: AN INTEGRATED APPROACH COMBINING DETERMINISTIC DATASETS FOR STOCHASTIC APPLICATIONS

Presentata da: Matthew Sotheron Hodge

Coordinatore Dottorato

Barbara Cavalazzi

Supervisore

Giulio Viola

Co-supervisore

Jochen Manfred Knies

Esame finale anno 2025

Characterising fractured crystalline basement evolution through time, Smøla island, Mid-Norway

An integrated approach combining deterministic datasets for stochastic applications

Matthew Sotheron Hodge

A thesis submitted in fulfilment of the requirements of
Alma Mater Studiorum Università di Bologna,
for the award of Doctor of Philosophy

February 2025

Supervisor: Professor Giulio Viola

Co-supervisor: Dr Jochen Kneis

Declaration

I hereby declare that the work presented in this thesis has not been submitted for any other degree or professional qualification, and that it is the result of my own independent work.

11 FEBUARY 2025

Matthew Sotheron Hodge (Candidate) ***Date***

Abstract

Geologically old crystalline basement rock volumes, such as Smøla island in the mid-Norwegian passive margin, are generally saturated by intricate natural fracture and fault patterns. Formed through a complex polyphase deformation history, these fracture arrays are commonly difficult to unravel into discrete fracture formation events. As temporal-controls are commonly lacking in these efforts, it is near impossible to discern the evolution of these fracture networks in absolute time. Also typically missing temporal constraints, fracture petrophysical studies have limited abilities to estimate fracture-related petrophysical properties during the development of these networks. Addressing these challenges, this thesis outlines a two-part temporally constrained study. The first part comprises a deterministic characterisation of Smøla, with the second part focussing on stochastic modelling and reconstruction.

By utilising geophysical and remote sensing lineament analysis, field mapping, high resolution drill hole logging, 3D modelling, petrographic and microstructural studies, and fault gouge K-Ar geochronology, five deformation episodes (D_1 to D_5) with associated synkinematic mineralisation, geometric, and kinematic trends were defined. These deformation episodes cover the following geological evolution: Beginning with the post-Caledonian evolution of the regional-scale Møre Trøndelag Fault Complex (MTFC), D_1 (after ~395 Ma) involved epidote-prehnite veining in the framework of brittle sinistral transtension along the MTFC. This was followed by two deformation phases during D_2 (~300 Ma and ~200 Ma) both associated with sericite-chlorite-calcite mineralised faults and shear fractures due to strike-slip faulting. Subsequently, D_3 (~128-100 Ma) chlorite-hematite fractures formed associated with pervasive dip-slip, and possible transpressional faulting along the MTFC. In the later episodes, the D_4 (after ~75 Ma) hematite-zeolite-calcite mineralised veins, and the youngest D_5 (assumed Cretaceous-Paleogene age) quartz-calcite veins both formed due to regional crustal extension and dip-slip (and possible strike-slip) faulting preceding the final stages of the Greenland-Norway break-up.

Incorporating multiscalar geological observations from the first stage, and statistical descriptions of observed fractures on Smøla, the second part of the study used a stochastic 'grown' discrete fracture network (DFN) modelling approach. This modelling incorporated absolute ages to reconstruct the D_1 to D_{4+5} fracture networks in four 500 m^3 DFN models representing different geological times. Using progressive fracture 'back-stripping' for each deformation episode, combinations of newly forming and reactivated fracture sets were simulated, starting from the current fractured rock volume on Smøla (< 70-60 Ma), moving backwards in time to the earliest fracture network in the Devonian (after 395 Ma). From these back-stripped DFNs, three-dimensional (3D) principal permeability tensors and two-dimensional (2D) fracture connectivity maps could be generated for each time-constrained DFN. Assessing the evolution of the fracture networks and the associated petrophysical properties showed how the maximum bulk permeability (K_1) increased through time from 9.47e-14 m^2 to 4.44e-13 m^2 (~3 orders of magnitude) along with the maximum horizontal permeability orientation (K_{Hmax}) shifting from NE-SW to NW-SE. Similarly, fracture connectivity C_B increased (1.01 to 1.79) with rock volume fracture saturation, peaking in the mid-Cretaceous and associated with the D_3 deformation episode. These results match the timing of hydrocarbon generation and secondary migration activity offshore Norway. Further refining the implemented DFN approach with the use of smaller 50 m^3 modelling volumes to mitigate computational efficiency issues combined with fracture conditioning, the DFNs could accurately replicate fracture intensity, orientation trends, and spatial patterns of the sub-seismic scale fracture networks on Smøla.

This study involves a completely new conceptual deterministic-stochastic integrated approach. The methodology demonstrated here can be applied to offshore fractured crystalline basement structural highs to resolve hydrocarbon migration and reservoir charging histories, and to other low matrix permeability basement volumes where constraining the evolution of fracture and fault networks is crucial to understanding geofluid flow pathways through geological time.

Acknowledgements

Although the PhD journey is essentially an individual experience, no PhD is achieved by individual effort alone. Completing this work has depended on a team of people, colleagues, friends, and family - all of whom have contributed in their own way. I am therefore deeply grateful to those who have stood by me with extraordinary patience and unwavering support over the past three years.

Firstly, I extend my heartfelt appreciation to my family back 'home', whose constant support has kept me grounded "*Dant lucem crescentibus orti*". Also, I must profoundly thank my adopted Italian 'family'. Laura Amato, especially, has been an incredible source of care and support throughout this journey. Ezio Amato and others also provided invaluable help in navigating the Italian bureaucracy, enabling this PhD to actually happen. *Grazie mille!* My friends in Bologna and elsewhere are also acknowledged for keeping my spirits high, and for making the time in Bologna very special.

I would like to thank my BASE 3 project colleagues: Guri Venvik, Jochen Kneis, Jasmin Schoenenberger, Øystein Nordgulen, Alejandro Piraquive, and Roelant van der Lelij, for their assistance with drill logging, fieldwork, lab analyses, and for the many productive discussions and constructive insights they have offered. Special thanks are also due to the WSP UK Edinburgh office, where Simon Libby, Fiona McLean, and Mark Cottrell provided essential guidance and support during this study. A particular note of gratitude goes to Alberto Ceccato, whose expertise greatly helped with the processing of the 3D permeability tensor data.

I also acknowledge the generous financial support from the Research Council of Norway (Norges Forskningsråd), under the grant no. 319849, within the ongoing BASE 3 project ("BASE – Basement fracturing and weathering on- and offshore Norway") a joint research project between the Geological Survey of Norway, the University of Bologna, and other industry partners.

My thanks extend to the colleagues from the University of Bologna, especially the Deformation, Fluids and Tectonics (DFT) research team, for their continual support and encouragement. And finally, I wish to express my sincere gratitude to my PhD supervisor, Giulio Viola, whose support, knowledge, patience, and guidance have been invaluable to this work.

Table of contents

Chapter 1: Introduction

1.1 Background and rationale

Geologically old crystalline basement rocks that have experienced prolonged polyphase brittle deformation commonly contain highly complex natural fracture and fault networks (Viola et al., 2009). These networks stem from numerous overprinting deformation and reactivation events over time (Peacock, 2001). The composition and internal anisotropy of the crystalline rocks, and the prevailing stress state, will typically determine where and how these fractures form or reactivate (Crider, 2015). Conceptually, at upper crustal levels, fractures and faults form progressively in a rock volume as a response to multiple deformation episodes, with the population of deformation progressively increasing over time until the rock volume becomes fault and fracture saturated (Viola et al., 2012). When the rock volume is indeed saturated with fractures and faults, further deformation episodes will lead to jostling, or the preferential reactivation of optimally oriented or conditioned structures rather than the formation of newly formed cross-cutting fractures or faults (Viola et al., 2012).

Consequently, unravelling these seemingly chaotic and intricate fracture networks into different genetic, kinematic, and geometric fracture sets is a particularly daunting task (Scheiber and Viola, 2018), which is further complicated by the fact that brittle deformation features are inherently multiscalar, occurring as regional (>kilometre)-scale lineaments down to the micron-scale with intragranular microcracks (Engelder, 1987; Seeburger and Zoback, 1982). Identifying and characterising fracture networks, therefore, requires an approach which incorporates sufficient genetic and geometric information across as many scales as possible.

Fracture networks or systems can include one or potentially more distinct fault or fracture sets (each with a unique range of orientations, mineral infill, and deformation style), with each fracture set generally assumed to have formed during a unique deformation episode (Peacock et al., 2018). Fractures and faults, however, may also be reopened or reactivated after formation during subsequent deformation events (Peacock et al., 2018). The deformation episodes or phases themselves reflect a characteristic regional stress field orientation and magnitude depending on the tectonic regime involved (Fossen et al., 2019). Moreover, these episodes may have distinct deformation styles, and mineral precipitation within the newly forming (or reactivating) fractures depending on the presence and composition of any fluids percolating through the rock volume at that time (Drake et al., 2009).

Viola et al. (2016) and others (e.g. Mattila and Viola, 2014; Viola et al., 2009, 2012) have convincingly shown that it is quite possible to decipher and recognise distinct deformation episodes, and reconstruct complex and extended tectonic histories through the careful structural analysis of deformation features, and by K-Ar geochronology (e.g. Davids et al., 2013; Hestnes et al., 2022; Ksienzyk et al., 2016; Scheiber et al., 2019; Tartaglia et al., 2023; Torgersen et al., 2015; Viola et al., 2018). Incorporating the structural and temporal heterogeneity of the internal structure of fault zones with K-Ar geochronology has further improved the ability to reconstruct complex and long-lasting tectonic histories (Tartaglia et al., 2020). These advances along with other structural geochronology approaches, such as U-Pb dating of calcite veins (e.g. Hestnes et al., 2023), provide an overall sound methodological approach to compiling a tectonic history for a given region, although limitations do exist on dating geologically recent tectonic events. These constraints are due to the disequilibrium of intermediate daughter isotopes in young U-Pb systems or limited growth of new authigenic minerals after recent faulting in K-Ar systems (Hueck et al., 2022; Rasbury and Cole, 2009).

As we can constrain tectonic histories even in these multi-deformed terranes, it is therefore possible to sort discrete structures (or discrete combinations of structures) by either relative or absolute times of formation. Along with separating out faults or fracture sets attributed to distinct deformation episodes, it is of great interest to also study the fracture-related or secondary petrophysical properties associated with each of these deformation episodes. This approach is sound, as the addition of each new fracture set to a pre-existing fracture network modifies, for example, how geofluids flow through a host rock (Cox, 2005). Thus, a fracture network deforming a given rock volume today must be considered as the sum of all inherited past fracture, petrophysical, and fluid flow conduits that progressively formed through geological time. Consequently, we could, for example, attempt to reconstruct petrophysical characteristics, such as secondary permeability or fracture connectivity, for a particular fracture network, forming in the Jurassic, as a response to a specific regional tectonic event occurring at that time.

Such a task, however, remains difficult. Indeed, structural-related (or ‘secondary’) permeability is both short-lived, transient and dynamic, as it is continuously created by fracturing and quickly destroyed by the precipitation of vein-infilling minerals over short geological periods (Cox, 2005, 2010; Sibson, 1994). Consequently, evidence of paleo-permeability in fractured rocks is generally only preserved as sealed fractures (Hosono et al., 2022). Determining fracture connectivity at a specific point in the past is also challenging, as typical field studies cannot fully capture the complexity of fracture networks (Maillot et al., 2016), particularly when they are present in polyphase deformed crystalline basement rocks.

Generally, crystalline basement rocks are characterised by very low matrix permeabilities and porosities, and only the faults and fractures, created through brittle deformation processes within these rock volumes through geological time, will mostly contribute to the (secondary) structural permeability (Gillespie et al., 2020; Holdsworth et al., 2019) and serve as the primary pathways for fluid flow (Caine et al., 1996; Stober and Bucher, 2007). Rock volumes such as these will typically form what is known as 'fracture reservoirs', with geofluids migrating via the permeable interconnected fractures (Holdsworth et al., 2019). Therefore, sealed fractures and veins can be assumed to represent the 'fossil frozen' secondary permeability of crystalline basement volumes and mostly define the record of fluid migration through these rock volumes (Oliver and Bons, 2001).

To effectively describe the complexities of fractured, repeatedly deformed crystalline basement rocks, a specific three-dimensional (3D) modelling approach is required to represent the detailed geometric configurations of these fracture networks. A statistical and stochastic modelling approach is therefore an advantageous method, as it can accommodate and account for the heterogeneity of rock and fracture properties, multiscalar nature, and spatial and geometric variability of natural fracture networks through statistical distributions (Haldorsen and Damsleth, 1990). Thus, in this context, a statistical approach would entail the statistical description of observed fracture data to define deterministic trends and parameters, with a subsequent stochastic approach utilising these deterministic inputs combined with probabilistic algorithms to generate meaningful ('explicit') representations of the observed data (Davy et al., 2018; Welch et al., 2020). These stochastic representations would not be exact replications of the natural fracture systems but instead would possess the same general statistical distributions as the observed data (Welch et al., 2020).

Although this approach can incorporate the natural variability of a fractured rock volume, a limitation of statistical or stochastic modelling is that it can only replicate a geological system at the resolution that is allowed by the quality of the modelling deterministic inputs (Welch et al., 2020). Consequently, sufficiently representative observational data from detailed structural studies, utilising a varied 'toolbox' of study techniques and at a variety of scales, is needed for a stochastic approach to fully capture fracture networks and related petrophysical properties. Additionally, stochastic approaches typically lack an absolute temporal component and so far, only relative timing of fracture or fault formation has been included in stochastic modelling (e.g. Libby et al., 2019, 2024; Maillot et al., 2016).

Consequently, a more comprehensive approach is needed, one that integrates a wide range of multiscalar observational and deterministic data, with absolute time constraints, with a stochastic modelling approach which can adequately generate and capture the complexity of fracture networks at a required resolution. An integrated approach such as this could then allow for the reconstruction of past fracture networks, representing the plumbing systems of 'fossil' fluid flow pathways, and therefore the estimation of specific petrophysical characteristics related to these systems back through time. Establishing a temporal framework is therefore essential for evaluating the evolution of these petrophysical properties through geological time.

To provide such absolute time constraints and detailed multiscalar input datasets to any selected stochastic approach, this project undertook a comprehensive characterisation of fault, fracture, and vein arrays, with selectively K-Ar dating fault gouges on Smøla island, located in the Mid-Norwegian passive margin (Figure 1.1). The fracture networks on the island have formed during a prolonged and polyphase brittle tectonic evolution, making this study area an ideal location for this kind of project.

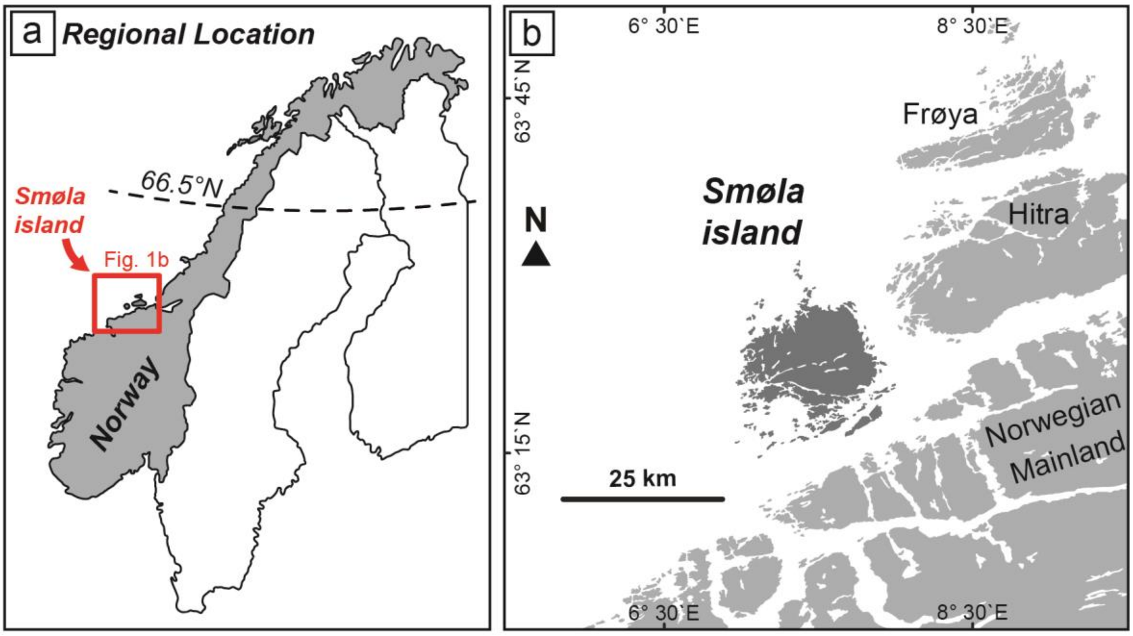

Figure 1.1. Location map of the study area, with (a) the regional setting of the study area within the mid-Norwegian passive margin; and (b) the local position of Smøla island relative to the Norwegian mainland, and the neighbouring islands of Frøya and Hitra.

Smøla island, comprised by crystalline basement rocks (gabbro, diorite, gneiss, and granite) of Caledonian age (Gautneb and Roberts, 1989; Slagstad et al., 2011), is considered an onshore analogue of offshore basement structural highs in the Norwegian sea, due to similar lithological and structural characteristics (Rønning and Elvebakk, 2005; Slagstad et al., 2011). These basement highs when comprising fractured and weathered crystalline rocks, may form unconventional hydrocarbon plays or reservoirs with possible geofluid migration and storage within them (Belaidi et al., 2018; Hartz et al., 2013; Holdsworth et al., 2019; Riber et al., 2015; Trice, 2014). Currently, however, these features are still poorly investigated and minimally understood (Trice, 2014), with any description of their internal structure reliant on coarse low-resolution datasets, such as seismic surveys and sparse drill hole data (Holdsworth et al., 2019; Tanner et al., 2020).

Commonly employed in many studies, relatively coarse-resolution geophysical surveys of basement structural highs (Muñoz-Barrera et al., 2020; Skilbrei et al., 2002) generally are not able to resolve basement volumes sufficiently to define fractured reservoirs. This problem relates to how fluid-flow in these rock volumes may be affected by sub-seismic scale (<30 m feature length) intrabasement structures (Walsh et al., 1998), which cannot be imaged by low-resolution data (Tanner et al., 2020). Therefore, for this study, any stochastic reconstruction of the Smøla fracture networks has a prerequisite of being able to replicate complex fracture systems at or below the sub-seismic resolution. Consequently, as this project will be utilising a wide range of multiscalar datasets from Smøla, as an onshore analogous rock volume, any geological insights from Smøla could then potentially be applied to basement highs offshore or elsewhere with similar geological terranes.

Utilising a detailed observational or deterministic characterisation of fractured crystalline basement rocks, supported by an integrated absolute time component provided by fault gouge K-Ar geochronology, and a subsequent time-constrained stochastic modelling approach has significant impacts on the characterisation of various types of fractured reservoirs. This is highly relevant to, for example, unconventional petroleum reservoirs (in this case comprised by naturally fractured reservoirs), as this novel approach allows for the first time, the estimation of the permeability and connectivity during known reservoir charging events back in geological time. To thoroughly characterise a basement reservoir for greenhouse gas injection and storage, it is essential to achieve an understanding of permeability anisotropy over time and characterise the petrophysical properties of each distinct fracture sets within the reservoir. Furthermore, basement-hosted nuclear waste repositories or containment facilities require nuclear waste to be isolated away from any percolating fluid potentially migrating through local fractures (Mattila and Viola, 2014). This condition requires a detailed understanding of how the petrophysical properties of the immediate fracture network may have varied over time and accurate forecasting of future changes in these properties.

1.2 Study aims

To demonstrate our integrated and time-constrained approach toward the structural characterisation of Smøla island, aiming at providing a range of deterministic inputs for the subsequent stochastic modelling of the local fractured basement blocks, this thesis focuses on the following key research tasks:

1) I will examine and characterise an onshore crystalline basement block by incorporating and integrating numerous multiscalar two-dimensional (2D) and three-dimensional (3D) geological, geophysical, and petrographic datasets. By following an integrated multiscalar approach, I will document a range of different deformation features within the study area, such as natural fractures, faults, and vein networks. The deformation features will be assessed based on their geometry and kinematic characters, relative chronology and cross-cutting relationships, and described in terms of the mineralisation and deformation styles. Then, to incorporate an absolute time dimension into the structural characterisation, this study will undertake K-Ar geochronology analyses of fault gouges. Finally, I will interpret the structural characterisations incorporating the dating results, and unravel a tectonic history and framework for Smøla, and the surrounding passive margin. This approach will ultimately provide a series of observational real-world deterministic characteristics and parameters of the deformation features on Smøla, which can be applied to onshore and offshore crystalline basement volumes.
2) Utilising the multi-scalar deterministic inputs and parameters which are representative of real-world fracture network data, I will combine them with the absolute time dimension, to stochastically reconstruct past fracture networks for a generalised crystalline basement volume set within the study area. I intend to Identify and adapt a stochastic modelling approach to replicate different time-constrained fracture sets and define certain petrophysical properties of the fracture networks and the bulk rock volume. I will model a progressive series of fracture networks with associated petrophysical properties to subsequently determine the evolution of these properties through geological time.
3) I will validate and assess the applied stochastic approach by comparing the obtained modelling outputs against the observed deterministic data. Through this assessment, where possible, the stochastic approach will be refined to be able to more closely replicate the observed fracture networks of interest at the sub-seismic or outcrop-scale. And as a key outcome of the study, I will provide a final workflow and a suite of parameters which can be used to undertake similar stochastic reconstructions of fracture networks elsewhere in crystalline basement volumes, such as the basement structural highs in the offshore domain off Norway.

1.3 Thesis structure

This thesis is structured into ten separate chapters, which, after summarising the theoretical and geological setting of the project, progress on to systematically focus on two main themes: first the deterministic characterisation (which produced a published journal article), and then the stochastic modelling (which produced a journal manuscript currently under revision at the time of the thesis writing), and finally a validation of the modelling work, by comparing the stochastic model output against the actual geology on Smøla island. In more detail, the ten chapters involve the following content:

Chapter 2: “Theoretical background” provides a number of summaries covering the main theoretical concepts and literature knowledge which are relevant to this project.

Chapter 3: “Geological setting” involves outlining the regional and local geology of the study area, with details provided on the published understanding of the tectonic evolution of the passive margin, from the Caledonian Orogeny to the rifting and break-up of Norway and Greenland.

Chapter 4: “Methodology” provides details on the different study methodologies and techniques utilised in the study, including information on the data collection methods, K-Ar geochronology sampling and analysis, and the stochastic (discrete fracture network modelling) approaches used.

Chapter 5: “Multiscalar 3D temporal structural characterisation of Smøla island, mid-Norwegian passive margin: an analogue for unravelling the tectonic history of offshore basement highs” is the complete verbatim inclusion of the published journal article (published in Solid Earth), in which we detail the initial study using geophysical and remote sensing data, field mapping, 3D modelling, petrography, and K-Ar geochronology. This work identified five deformation episodes (D_1 to D_5) from the Carboniferous to Late Cretaceous, revealing insights into the region’s structural evolution.

Chapter 6: “Interlude: transitioning from deterministic descriptions to stochastic simulations” is a brief linking chapter between the deterministic study in Chapter 5, and the stochastic modelling undertaken in Chapter 7. This chapter describes how the observational data (fracture database) was adapted for stochastic modelling in Chapter 7. It also discusses the format of Chapter 7, explaining the publication requirements that the related submitted manuscript has had to comply with.

Chapter 7: “Discrete fracture network modelling reconstructs fracture array and petrophysical property evolution through geological time” involves a current journal manuscript accepted and in press with the Nature Portfolio journal Communications

Earth and Environment. This chapter involves the stochastic modelling results incorporate temporal constraints and 'fracture back-stripping'. The work generated four discrete fracture network (DFN) models to simulate past fracture networks during four deformation episodes (D_{4+5} to D_1). These DFNs allowed bulk permeability and 3D permeability anisotropy (tensors), as well as fracture connectivity estimates through geological time. This work was contrasted and compared to known reservoir charging during offshore hydrocarbon activity in the Norwegian and North seas.

Chapter 8: "Validation and refinement of discrete fracture network (DFN) models by comparative analysis and fracture conditioning" extends the DFN modelling from Chapter 7 to characterise Smøla's sub-seismic fracture networks at the drill core scale, validating and refining both DFN modelling that was done at 500 m^3 and subsequently at 50 m^3 models, to better replicate natural fracture, vein, and fault arrays by deformation episode (D_{4+5} to D_1). This chapter also provides a set of generalised model outputs which can be used in future research to characterise fracture networks structurally similar to Smøla's.

Chapter 9: "Synthesis and discussion" combines the two main themes of the thesis together and offers insights into the results, outlining the assumptions, limitations, and advantages of the stochastic modelling.

Chapter 10: "Conclusion" provides the final combined conclusions of the study, and provides a critical review, with insights and recommendations also offered.

Chapter 2: Theoretical background

2.1 Introduction

This chapter aims to provide the theoretical framework and background for the research undertaken in this thesis. I will begin with the fundamental knowledge that forms the foundation of the study, before shifting into more detailed and specialised information. Currently, integrating an absolute time dimension into structural characterisations of fracture networks and fracture modelling remains challenging. Previous studies have tried to resolve this issue by using stress-related fracture nucleation and propagation, stress-field trajectories of known ages, temperature and burial histories, and quartz mineralisation accumulation rates (Becker et al., 2010; Engelder and Geiser, 1980; Laubach and Kira, 2009; Lavoine et al., 2020; Olson et al., 2007); however, these approaches all lack direct dating of the fracture networks. Integrating an absolute time component is crucial, as it permits tectonic histories to be unravelled, and provides insights into the evolution of fracture networks and their associated petrophysical characteristics. Consequently, I will cover the theoretical information required to complete such a study, highlighting these knowledge gaps, and present a roadmap outlining how this work intends to contribute to the overall knowledge in this field.

2.2 Tectonic reconstructions

Geological descriptions based on directly observed geological features (from for example, geophysical images, remote sensing, drill core, and field outcrops) together with structural measurements (altogether forming what I generally refer to as "deterministic inputs") form the key inputs to enable reconstructions of rock deformation processes, and ultimately provide the structural framework required to unravel complex tectonic histories through geological time (Peacock and Sanderson, 2018). Consequently, I will now summarise the foundational theory used to interpret geological structures aiming to make tectonic reconstructions.

2.2.1 Structural terminology

A full review of the terminology used to describe geological structures is obviously beyond the scope of this thesis, as adequate textbooks and reviews already exist (see Peacock et al., 2016; Schultz and Fossen, 2008). However, for this project, I have selected specific terms to refer to various deformation features, which are outlined below and require a standardised utilisation of terminology.

For the purposes of this thesis, a structural discontinuity is a plane of weakness or planar mechanical flaw which has formed because of brittle deformation (adapted from Schultz

(2019)). In this thesis, I generally refer to any structural discontinuity within a rock mass as a 'fracture'. Fractures are defined as discontinuities characterised by two planar surfaces enclosing a mechanically weak zone that, if open, facilitates fluid flow (Schultz, 2019; Schultz and Fossen, 2008). Geometrically, fractures are typically planar discontinuous features with discrete lengths exceeding their widths (Schultz, 2019). In the literature (e.g. Dershowitz and Einstein, 1988), the term 'joint' commonly describes unmineralised fractures with no shear component (purely dilational features) (Schultz and Fossen, 2008). I refrained from using this specific term to refer, instead, to these features as tensile or dilational fractures.

Where necessary, I used the term 'vein' to describe features involving zones of mineral growth originally precipitated from a fluid within sites of dilation (Bons et al., 2012). Fractures infilled with secondary minerals are therefore referred to as veins. Considering that veins can be either tensile or shear-related (or a combination), I used the modifiers 'shear' or 'tensile' as additional descriptors for these features. Further relevant to tensile deformation features documented in this thesis, I used 'hydraulic breccia' to describe breccias (in other words a fault rock containing more than 30% visible rock clasts) interpreted to have formed through hydraulic fracturing due to fluid overpressure and later cemented by distinct mineral phases (Peacock et al., 2016).

In referring to a subset of fractures, I refer to 'faults' as structural discontinuities exhibiting significant shear-related displacement between two blocks juxtaposed along the fault plane (Schultz, 2019). Specifically, in this thesis, faults which are less than 1 cm in width are termed 'shear fractures', while those up to ~10 cm are referred to as 'shear bands', which may represent compact shear zones. Faults exceeding 10 cm in width are generally called 'faults' in the text. These faults are further described by referring to the terms 'fault core', which is used to describes a localised highly deformed zone, generally composed of gouge or cataclasite, representing or associated with the principal slip surface of the fault; and the term 'damage zone' to describe the surrounding area characterised by a high abundance of interconnected fractures in the wall rocks adjacent to the fault core (Schultz and Fossen, 2008).

Fault breccias are typical fault rocks (used here instead of the term 'hydraulic breccia' when mechanical grinding and fragmentation is suspected), which are characterised by more than 30 % visible clasts (or fragments) to the overall rock volume (Sibson, 1977). 'Gouge' is used to describe specific fault rocks, wherein visible clasts make up less than 30 % of the total rock volume (Sibson, 1977). These gouge intervals, and often breccias, are typically unconsolidated and friable in hand specimens. This contrasts with more consolidated fault rock features, which in this thesis only involve the term 'cataclasite'. I thus use the terms ‘protocataclasite’, ‘cataclasite’, and ‘ultracataclasite’ to describe varying matrix-to-clast ratios, with protocataclasites containing 10–50 % matrix, cataclasites 50–90 %, and ultracataclasites more than 90 % matrix (Sibson, 1977). These features form through processes of brittle fragmentation and mechanical comminution (Peacock et al., 2016).

Finally, the term ‘lineament’ is used to describe regional to kilometre-scale linear features or traces affecting topography, which may represent crustal faults or structures (Peacock et al., 2016). Lineaments can also be related to stratigraphic layering, contacts or igneous banding as well as man-made artifacts, and, as such, thus unrelated to (brittle) deformation.

2.2.2 Characterising brittle rock failure

Before using deformation features to reconstruct a tectonic history, understanding how these different features form is crucial to interpreting the conditions that were present when they formed. Within the brittle regime, homogeneous and intact rocks exposed to deviatoric stress may undergo tensile, hybrid, or shear failure (Engelder, 1999; Price and Cosgrove, 1990; Sibson, 1998). These failure types can be described by both the Griffith and Coulomb criteria and are graphically illustrated in Figure 2.1a with the aid of the Mohr circle: The Griffith criterion, $\tau^2=4\sigma'_n T+4T^2$, defines tensile fracture nucleation and growth, relating shear stress (τ) to tensile strength (T) and effective normal stress (σ'_n) and within the host rock in tensile conditions; the Coulomb criterion, on the other hand, describes shear failure, and is expressed as $\tau=C+\mu_i(\sigma_n-P_f)$, where C is the cohesive strength, μ_i is the coefficient of internal friction, and σ_n-P_f is the effective normal stress (Brace, 1960; Jaeger et al., 2007).

Rock failure (including fracture formation) occurs when the rock strength (including tensile or shear strengths) is exceeded by the applied stresses, influenced by fluid pressure (Figure 2.2) (Jaeger et al., 2007). Within a fluid-saturated crust, the applied effective compressional stress (compression being denoted as positive) involves three principal stress components, namely the maximum (σ'_1), intermediate (σ'_2), and least (σ'_3) compressive stresses, where $\sigma'_n=\sigma_n-P_f$ describes the effective normal stress (Sibson, 1998). Tensile failure, and development of tensile fractures, will therefore occur when the least effective compressive stress (σ'_3) equals or exceeds the tensile (or tensional) strength of the rock (T), when there is no shear component and σ'_n is tensile (<0) (Jaeger et al., 2007) (green Mohr circle on Figure 2.1a). Hybrid failure, and development of mixed tensile-shear fractures, occurs when the tensile least effective compressive stress ($\sigma'_3<0$) equals the tensile strength of the rock, creating tensile incipient fractures, which, in response to the applied shear stress ($\tau>0$), start to interact and connect causing fracture propagation (Jaeger et al., 2007; Ramsey and Chester, 2004) (orange Mohr circle on Figure 2.1a). Shear failure, on the other hand, occurs when the resolved shear stresses (τ) exceed the rock's shear strength (defined by the cohesive strength (*C*) and internal friction coefficient (μ_i), where friction depends on normal stress (σ_n) and the internal angle of friction(ϕ)), when the effective normal stress is compressional ($\sigma'_n>0$) (Jaeger et al., 2007), creating shear fractures and faults (red Mohr circle on Figure 2.1a).

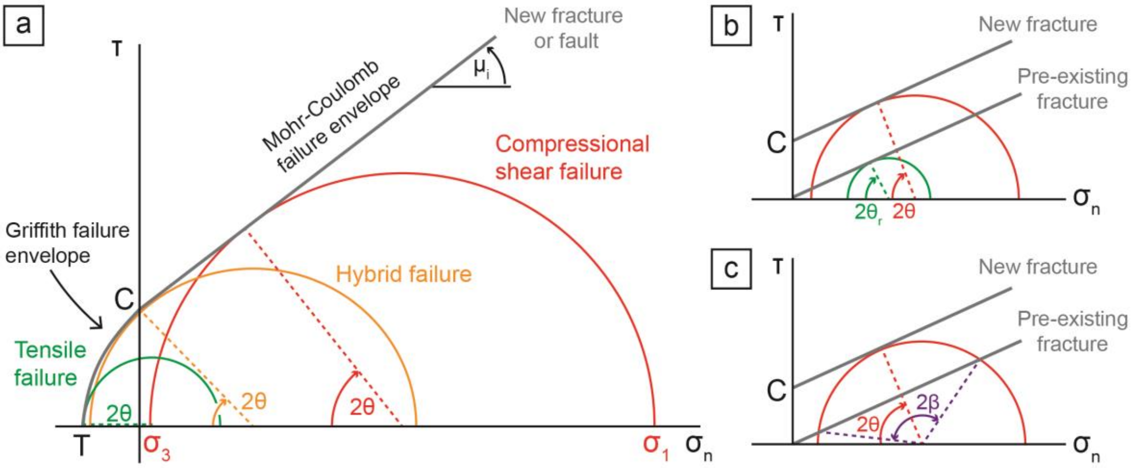

Figure 2.1. Mohr diagrams showing conditions of brittle failure and reshear, with τ being the shear stress, σ_n the normal stress, C the cohesive strength, and T, the tensile strength; (a) The three main types of brittle failure being tensile (green Mohr circle), hybrid (tensile-shear; orange Mohr circle), and compressional shear failure (red Mohr circle) relative to the Griffith and Mohr-Coulomb failure envelope ($\tau=C+\mu_i(\sigma_n-P_f)$), which has a slope of μ_i. The differential stress (σ_1-σ_3) is shown for the shear failure only. The angle between the maximum principal stress (σ_1) is given by θ. (b) Mohr diagram showing the conditions of either formation of new shear fractures or reactivation of a pre-existing non-optimal fracture. (c) Mohr diagram showing the required differential stress difference between forming a new shear fracture and reactivating an inherited fracture. Modified from (Ramsey and Chester, 2004; Sibson, 1985, 1998).

Relevant to this thesis, rock volumes with low primary permeability and porosity, like crystalline basement rocks (e.g., granites) at mid to upper-crustal levels, generally have negligible grain-boundary pore fluid pressures (Yardley and Bodnar, 2014). Brittle failure and fracture formation in these rocks can therefore involve hydrofracturing (tensile to hybrid fractures) due to high local fluid pressure (overpressure) compared to the surrounding pore fluid pressures (Bons et al., 2022). High fluid pressure conditions associated with fault-rupture, specifically, may occur episodically in what is known as 'fault-valve behaviour' (Sibson, 1992), as illustrated in Figure 2.2a. Although dependent on various factors (for example, the fault mode and regime, cohesive strength, and stress accumulation), tectonic loading during interseismic intervals increases shear stress and pore fluid pressure (along with a reduction of the effective normal stress on the fault, as discussed above). This weakening process continues until coseismic rupture occurs, during which permeability is transiently created, and facilitating localised fluid migration with a drop in pore fluid pressure (Figure 2.2b) (Cox, 2005; Sibson, 1992). This process can occur numerous times, potentially reopening existing fractures or reactivating faults (Sibson, 1992).

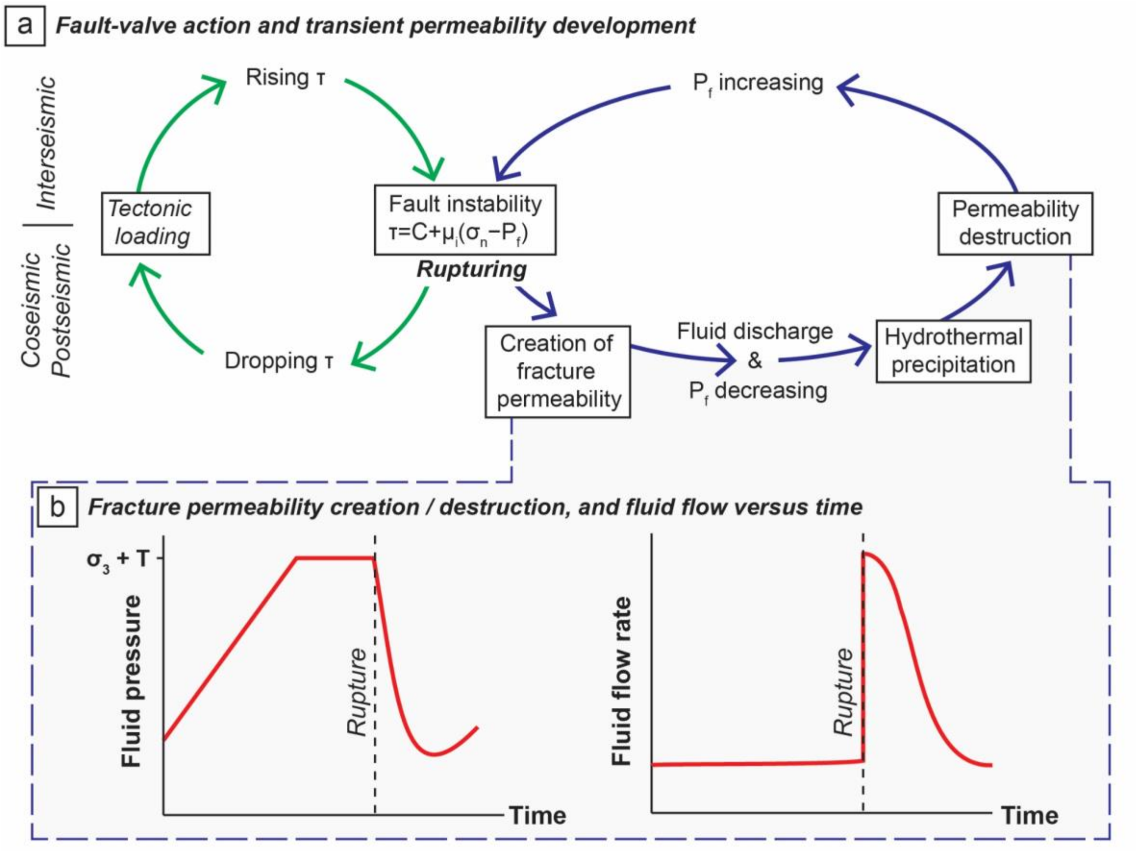

Figure 2.2. (a) Episodic fault rupture-related transient creation and destruction of permeability, described by cyclic 'fault-valve behaviour'. (b) Temporal fluid pressure and fluid-flow conditions relative to the time of fault rupture. Modified from Cox (2005) and Sibson, 1992a).

Additionally, hydrofracture formation is enhanced when pore fluid pressure increases with depth, as described by the pore-fluid factor $\lambda_v = P_f/(\rho_r gz)$, where ρ_r is the density of the overlying rock, g the gravitational acceleration, and z is depth (Rubey and Hubbert, 1959). This factor is, therefore, the ratio between pore fluid pressure and the overlying rock overburden-derived pressure (lithostatic pressure). Generally, depending on depth, pore fluid pressure can vary from hydrostatic pressure conditions ($\lambda_v \approx 0.4$; related to pressure of water column at depth) to lithostatic conditions ($\lambda_v = 1$) (Sibson, 1992). In some cases, including being at depth or within a reservoir below an impermeable unit, the pore fluid pressure may become suprahydrostatic or overpressured ($\lambda_v > 0.4$), and approach lithostatic values (Cox, 2010; Sibson, 1992). Fluid overpressure can also derive from other causes, such as fluid influx or porosity collapse or destruction owing to mineral precipitation (Bons et al., 2022; Cox, 2005). Overall, hydrofractures (potentially arrays of fractures) will form when pore fluid pressures (P_f) conditions are greater than σ_3, and match or exceed lithostatic pressure (σ_v) (Sibson, 1992, 1996).

Consequently, the applied stress state of a rock volume, and the pore-fluid pressure conditions strongly influence brittle rock failure within the crust. Documenting the deformation style, and type of deformation feature, can provide clues on fracture mechanisms, as well as the magnitudes and orientations of the prevailing stress field, and, therefore, the tectonic regime.

2.2.3 Orientations of fractures and faults to the stress field

Fractures forming within an intact and isotropic rock mass, will typically develop at specific angles to the applied principal compressional stresses ($\sigma_1>\sigma_2>\sigma_3$) (Jaeger et al., 2007). For example, as shown in Figure 2.3, shear fractures may form conjugate pairs, with the acute bisector angle (2θ) between the fractures enclosing the maximum compressional stress (σ_1), the intersection of the fractures being parallel to the intermediate compressional stress (σ_2), and the obtuse bisector between the fracture planes enclosing the least compressional stress (σ_3) (Scholz, 2019; Sibson, 1998). If we visualise the different brittle failure types in a Mohr-Coulomb-Griffith space (Figure 2.1a), the acute bisector angle, 2θ, is formed from each Mohr circle centre to the intersection point with the Coulomb failure envelope.

The angle, θ, therefore represents the angle from the fracture to the maximum compressive stress σ_1 and is expressed as $\theta=45-((\tan^{-1}\mu_i)/2)$, where $\tan^{-1}\mu_i$ represents the angle of internal fiction (ϕ), influencing the slope of the Coulomb failure envelope (Jaeger et al., 2007; Scholz, 2019). As shown in Figure 2.1a, for each failure type, 2θ changes depending on the size and location of the Mohr circle (in turn dependent on the magnitude of differential stress (σ_1-σ_3), and whether the least compressive stress (σ_3) is tensile (<0)) relative to the failure envelope, and ϕ. This angle θ, for newly forming shear fractures (assuming high C and μ_i), is commonly ~30° (related to ϕ, and corresponding to an optimal arrangement when the failure plane has sufficiently high shear stress and low normal stress acting on it, which is controlled by, amongst other factors, P_f and confining pressure (Fossen, 2010b)), while for tensile fractures (with 2θ not clearly visible on Figure 2.1a), will be ~0° (Ramsey and Chester, 2004). Hybrid fractures, being a transitional fracture type between tensile and shear failure types, has 2θ<60° and therefore θ<30°, and have been considered to have a maximum 2θ angle of 45°, suggesting a θ of ≤22.5° (Hancock, 1991).

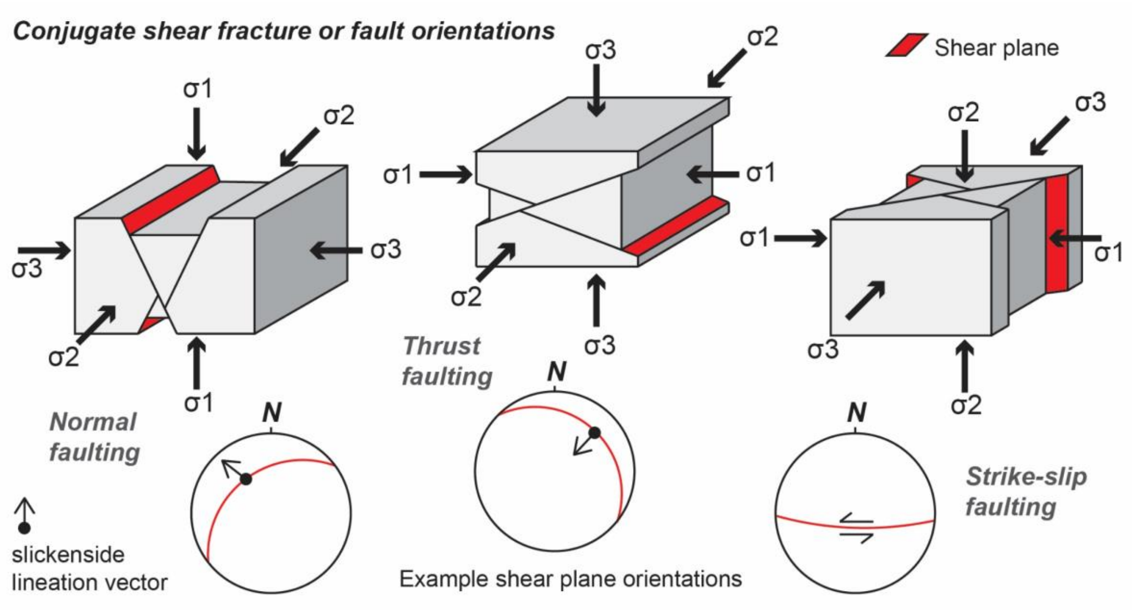

Figure 2.3. Faulted 3D block models illustrating the possible orientation of faults or shear fractures (and their conjugates) relative to applied principal stress axes, following the Andersonian theory of faulting (Anderson, 1951). Examples of faulted surfaces (stereonet plots) are provided alongside the various modes of faulting, with slickenside orientations which provide kinematic indicators. Modified from Fossen (2010b).

Provided our host rock is isotropic and homogenous and these angular relationships between the different fracture types and the applied principal compressive stresses, we can interpret the orientation of the prevailing stress field at the times of fracture formation, and therefore the tectonic regime. Faults or fractures that conform to the Andersonian theory (Anderson, 1951) and the Coulomb criterion, develop with one of the principal stress axes vertical ($\sigma_{v}=\sigma_1$, or σ_2, or σ_3) (associated with a 'free' topographical surface), with the other stress axes horizontal. Additionally, within this stress state three main types of faults can form, being normal, thrust, or wrench (strike-slip) types (Anderson, 1905). Therefore, if $\sigma_{v}= \sigma_1$, we can expect a normal fault (or shear fracture) to develop with a dip of ~60° with respect to the topographic surface, with a thrust fault developing with a dip of ~30° if the $\sigma_{v}= \sigma_3$. If, however, $\sigma_{v}= \sigma_2$, a strike slip (wrench) fault will form with a vertical dip, inclined 30°, to the horizontal σ_1 direction.

2.2.4 Reactivation versus new structures

After a fracture or fault forms in the upper crust, it either becomes a mechanically weaker or stronger zone owing to either strain weakening (due to grain size reduction and frictional strength decrease) or strain hardening (owing to mineral precipitation or cementation increasing cohesion) respectively (Ferrill et al., 2020; Holdsworth, 2004). To illustrate this situation, faults or fractures will typically reactivate following the Coulomb failure criterion, using the frictional reactivation criterion, $\tau=C+\mu_s \sigma'_n$, where the shear stress (τ) is dependent on the cohesive strength of a fault or fracture (*C*), and the static coefficient of rock friction (μ_s) (Sibson, 1985, 1998). Cohesion (*C*) or cementation of a fault or fracture involves the intergranular forces that exist within a rock volume and reflects the shear stress needed for shear failure without applied normal stress (σ_n=0) (Fossen, 2010b). The other important component, the static co-efficient of friction (μ_s), which involves the force required to initiate frictional sliding, was demonstrated experimentally by Byerlee (1978) to involve values ranging from 0.6 (with a well-developed gouge zone) and 0.85 (no gouge zone), while typically a new fracture will have a coefficient of internal friction (μ_i) of 0.75 (Sibson, 1985, 1998). To both illustrate how reactivation of a cohesionless (*C*=0) may differ from shear failure of a new fracture with cohesion (*C*>0), and assuming both fractures possess the same friction coefficients (μ_s=μ_i=0.75) we have plotted them up on Figure 2.1b & c.

On Figure 2.1b, representing the failure envelope of a pre-existing fracture, we can see that owing to the lack of cohesion, which would result in a lower shear strength than intact rock, reshear on these features would require a lower differential stress (green Mohr circle) than for a new fracture (red Mohr circle) (Etheridge, 1986; Sibson, 1985). The reactivation angle θ_r, also shown on Figure 2.1b, is the angle at which reshear may occur relative to the maximum compressive stress, and it is defined as θ_r=45-((tan$^{-1}\mu_s$)/2), with θ_r between 25° - 30° with an ideal angle of ~30° if $\mu_s \approx 0.75$ (Sibson, 1985, 1998).

If however, the fault or fracture has an orientation with a $\theta_r > 30°$ to the maximum compressive stress, the fracture is likely to only reactivate if the P_f is very high, σ_3 is tensile (σ_3<0), and if μ_s is low (<0.5) such as the case in a very well-developed gouge zone; otherwise, the fault or fracture is too misoriented to reshear (Sibson, 1985).

The orientation of any pre-existing fracture or fault to a prevailing stress field is therefore a crucial factor in determining whether a fault or set of fractures will reactivate. As shown on Figure 2.1c, any pre-existing fracture will preferentially reactivate if the θ_r orientation is within the 2β range (between purple lines in the Mohr circle), with fracture orientation outside of this range too severely misoriented for reshear (a new fracture or fault will preferentially form instead) (Etheridge, 1986; Nortje et al., 2011). Consequently, fractures which are favourably oriented to a prevailing stress field, can be predisposed to reshear. This tendency is further enhanced by high fluid pressure conditions or perturbations to the applied shear stress (such as from tectonic loading due to crustal extension) occur, which can encourage either dilatant or shear reactivation. This is particularly evident in fracture saturated crustal volumes, where any change of the applied stress field, will rather induce 'jostling', whereby a portion of available pre-existing optimally oriented fractures will reactivate rather than any new fractures forming (Viola et al., 2012).

2.3 K-Ar geochronology

The primary geochronological or dating tool utilised in this thesis is Potassium-Argon (K-Ar) dating of selected, structurally constrained fault gouges. This section will outline the main theoretical background related to how K-Ar works and is applied in tectonic reconstruction studies.

2.3.1 The Potassium-Argon (K-Ar) system

Using the $^{40}K/^{40}Ar$ (K–Ar) geochronology tool requires understanding of the underlying process whereby naturally occurring ^{40}K decays to the stable isotope ^{40}Ar (Figure 2.4). Radiogenic ^{40}K decays to two daughter elements, either in the most common case (89 % of the time) to Calcium (^{40}Ca), or more rarely (11 % of the time) to Argon (^{40}Ar) (Bowen, 1994; Kelley, 2002). In the case of ^{40}Ar, this decay proceeds predominantly by electron capture (the nucleus captures one of its own electrons) whereby either the resultant ^{40}Ar atom is in an 'excited state' requiring the ejection of a gamma ray, or in a 'ground state' where the ^{40}Ar is stable without requiring further energy release (Bowen, 1994). Additionally, positron decay (very rarely occurring) may result in the resultant ^{40}Ar atom releasing two gamma rays (combine energy of 1.02 MeV) before being stable (Bowen, 1994). This decay process (involving both ^{40}Ca and ^{40}Ar) has a half-life ($T_{1/2}$) of approximately 1.25 billion years, allowing us to date samples with ages on the tens of thousands to billion-year time-scales (Bowen, 1994; Kelley, 2002; Murphy et al., 1979).

Assuming the geological system (typically a mineral grain) experiencing ^{40}K decay to the stable isotope ^{40}Ar, has since remained closed, with no fractionation, newly forming radiogenic ^{40}Ar remains trapped within the host crystal matrix (Clauer, 2013; Kelley, 2002). Consequently, assuming that these conditions have been constant, the age since the ^{40}K became trapped is given by $t = (1/\lambda)\ln[(^{40}Ar^{*}/^{40}K(\lambda/\lambda_e))+1]$, where λ is the decay of ^{40}K to ^{40}Ca, λ_e is the ^{40}K to ^{40}Ar, $^{40}Ar^{*}$ is the quantity of radiogenic ^{40}Ar, ^{40}K quantity of ^{40}K, with the dating assuming decay constants λ_e and λ of 0.581×10^{-10} a^{-1} and 4.962×10^{-10} a^{-1} respectively, and no inherited ^{40}Ar present in the sample initially (Bowen, 1994). This age therefore captures either when the sample medium (crystal grain for example) cooled and therefore 'locked in' the ^{40}K abundance, or metamorphism reset the ^{40}Ar content, assuming gas loss.

However, as ^{40}Ar is typically in the gaseous phase (>62.3 °C), and unbonded to surrounding atoms, variations in temperature (thermal equilibrium), recrystallisation, diffusion, weathering, and deformation may all affect the 'storage' of ^{40}Ar within a given crystal lattice (Bowen, 1994). The type of mineral initially hosting ^{40}K and consequently the structure of the crustal lattice will also impact the retention of ^{40}Ar over geological time (Kelley, 2002).

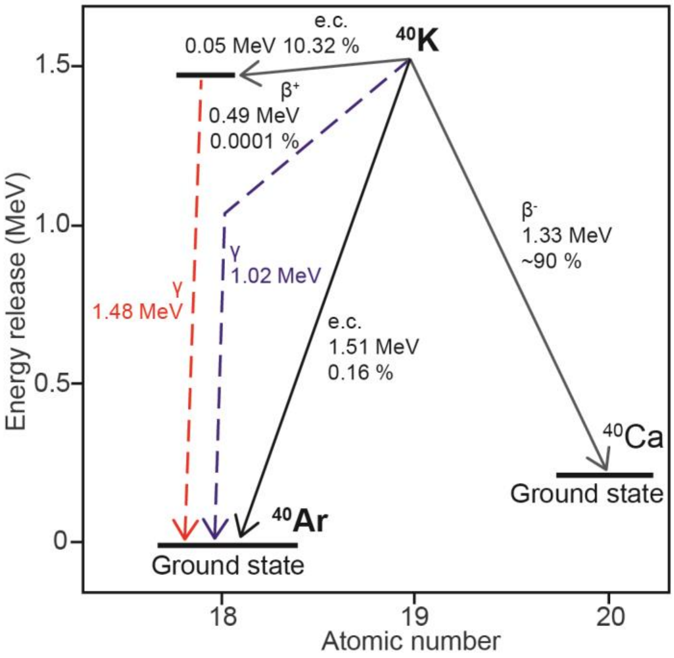

Figure 2.4. The radiogenic decay process of naturally occurring ^{40}K to stable ^{40}Ca and ^{40}Ar. The annotation "e.c." stands for electron capture. Modified from Kelley (2002).

Along with the lattice diffusion, temperature has a major role in ^{40}Ar retention and depending on the type of mineral and size of the mineral grains, this closure temperature for most common minerals used in K-Ar dating mostly ranges from 150 °C (for K-feldspar) up to 600 °C (for hornblende) (Tagami, 2012). If the system experiences temperatures exceeding the closure temperatures, ^{40}Ar is lost out of the system, through the mineral lattice, and subsequently out along grain boundaries. The loss of ^{40}Ar impacts the age determination and provide lower ages. Therefore, utilising the K-Ar dating techniques requires careful characterisation of the samples, in terms of mineralogy, fluid interaction, or deformation to determine whether potential ^{40}Ar may have occurred.

2.3.2 Dating authigenic minerals

In this thesis, I primarily use K-Ar dating of Potassium-bearing clays such as illite, and white micas (muscovite and sericite). I will therefore discuss the different characteristics of these minerals relevant to K-Ar dating.

Illite, a phyllosilicate clay mineral ($K_{0.75-0.88}(Al,Fe,Mg)_2(Al,Si)_4O_{10}(OH)_2$), will typically form in fault-related gouge pockets with fractures and faults from retrograde hydration reactions (Hueck et al., 2022; Zwingmann and Mancktelow, 2004). Low temperature illite crystallisation and growth within such deformation features occur during hydrothermal flow of fluids with ~150 °C temperatures (typically at ~5 km depths, assuming ~30 °C /km geothermal gradients) and fluid-rock interaction (illitisation) enhanced during deformation events (Tagami, 2012). The illite mineral involves three different layer stacking polytypes related to temperature, namely 1M, $1M_d$, and $2M_1$ (Hueck et al., 2022). The 1M and $1M_d$ are the low temperature polytypes which will typically crystallise under diagenetic conditions (80 to 150 °C) (Hueck et al., 2022). The $2M_1$ polytype, on the other hand, crystallises under higher temperature conditions (150 to 300 °C) (Hueck et al., 2022). The closure temperature of illite, when ^{40}Ar loss is experienced, is 250-350 °C (Hueck et al., 2022). For most K-Ar studies, the lower temperature polytypes $1M/1M_d$ provides the most likely neocrystallised polytypes, associated with faulting, while the $2M_1$ is generally associated with an inherited protolithic or detrital component (the same structure as muscovite) (van der Pluijm et al., 2001; Viola et al., 2016; Zwingmann et al., 2010).

However, it is important to note that authigenic illite can also form through the weathering of K-feldspar (for example) or within sedimentary rocks within saprolitic horizons (e.g. Fredin et al., 2017), with care required when interpreting any K-Ar dating results. These weathering-related illite minerals commonly form illite-smectite crystals with the smectite content increasing with lower temperatures (Hueck et al., 2022). Any K-Ar dating results of these illite-smectite minerals therefore reveal the age of saprolite formation rather than synkinematic illite growth.

In addition to potassium-bearing clay minerals, authigenic white mica, including muscovite or fine-grained sericite ($KAl_2(AlSi_3O_{10})(OH)_2$) provide an additional target mineral for K-Ar dating. Hydrothermal fluid flow-related sericitisation and greenschist metamorphic conditions mineral growth (for example retrograde replacement of plagioclase feldspar) generally are the processes responsible for crystallisation (Hueck et al., 2022; Wibberley, 1999). White micas typically crystallise at higher temperature conditions (>300 °C) than illite, with closure temperatures for different grain sizes between ~275–425 °C (Hueck et al., 2020). However, muscovite can reset during lower temperatures during syn-kinematic recrystallisation (Hueck et al., 2020). Synkinematic illite dating is considered the best way to understand brittle regime fault activity at lower temperature conditions (Hueck et al., 2022; Viola et al., 2016). However, as white micas have a closure temperature which includes the brittle-ductile transition for quartzo-feldsparthic crust (~300-400 °C) (Fossen, 2010b), dating of these mica minerals can capture fault activity at >10 km depth conditions (assuming a similar ~30 °C /km geothermal gradient).

Other minerals that can be dated using K-Ar geochronology include potassium feldspar (K-feldspar), biotite, zeolite, and amphibole, all of which contain varying weight percentages (wt%) of Potassium within their crystal structures (Hestnes et al., 2022). Of these, Potassium feldspar and amphibole are particularly noteworthy, as they are the most likely sources of inherited detrital or protolithic material derived from the host rocks examined in this thesis. Contamination of host rock material (typically as host rock fragments or clasts with the sampled fault rock material), generally results in mixed dating results with inherited ages of cooling, older fluid flow, or crystallisation affecting the overall determination wt% or abundance of K and Ar (Hueck et al., 2022; Torgersen et al., 2015; Viola et al., 2016). It is important to note, however, that illite and white mica can also provide inherited ages (detrital, igneous, or metamorphic-related).

2.3.3 The 'Age attractor' model

The 'Age Attractor' model proposed by Torgersen et al. (2015) and Viola et al. (2016), provides a framework on which to interpret K-Ar dating results, and is graphically illustrated in Figure 2.5.

Sorted into several grain size fractions (typically from <0.1 μm to 10 μm), the dating results are arranged from the finest grain size fraction, commonly yielding the youngest and assumed authigenic age (therefore considered to be the most geologically meaningful and reliable), to the largest grain size fraction, which commonly returns the older (assumed protolithic or inherited) age (Torgersen et al., 2015; Viola et al., 2016). In Figure 2.5, these two size fractions are also indicated with small yellow and purple hexagonal shapes (representing two different illite mineral grain populations) for the smallest and largest grains size fractions respectively.

Between the two end-members of grain size fractions and K-Ar ages, the intermediate grain size fractions (in this thesis involving 0.1-0.4, 0.4-2, and 2-6 μm fractions) exhibit mixed ages which derive from the combination of younger authigenic illite (assumed) growth on older protolithic mineral cores (Torgersen et al., 2015; Viola et al., 2016). On Figure 2.5, these are represented by medium-sized two-colour hexagonal shapes, with the inner purple cores associated with the older inherited grains, and the outer yellow rims related to younger growth.

Tracing a mixing line through the ages from the coarsest grain size fraction to the smallest grain size fraction (shown for each sample on Figure 2.5 as green, orange, and red lines), forms an inclined age spectrum (Hueck et al., 2022). These inclined age spectra mixing lines result in the youngest (or final) age acting as an 'age attractor' where the mixing line for each sample converges (Torgersen et al., 2015; Viola et al., 2016).

Clustering of ages, or distinct plateaus in the age spectra lines provide evidence for possible authigenic episodes, which must be interpreted carefully considering all sources of potassium (as mentioned above), and the host rock and fault history (possible multiple reactivations) (Hestnes et al., 2022).

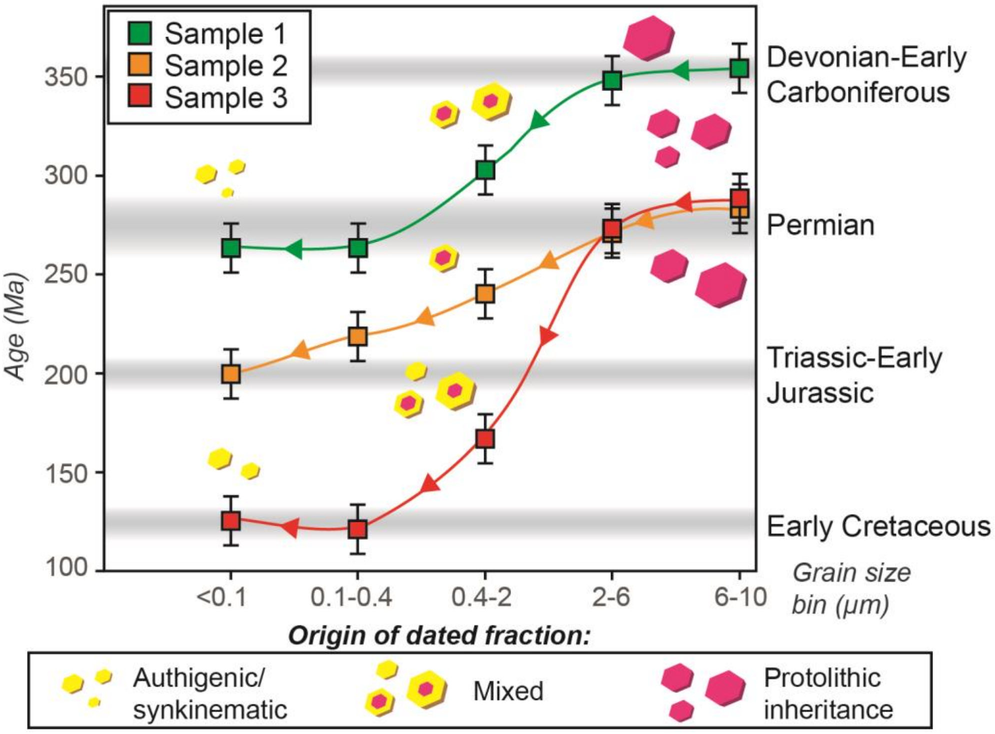

Figure 2.5. A generalised 'cartoon' of a typical K-Ar age versus grain size fraction spectra plot, depicting the 'Age Attractor Model', whereby mixing lines (green, orange, and red) evolve from the oldest age related to the coarsest grain size fraction, to the youngest age associated with the finest grain size fraction. Modified from Viola et al. (2016).

A final note on the K-Ar dating utilised and discussed within this thesis is warranted here. Although typically the term 'date' is used for results of isotropic dating analysis without a time interpretation, I have used the term interchangeably with "age", which typically does have a time interpretation.

2.4 Fracture network characteristics

I now outline the key characteristics of fracture networks (or system) at both the individual fracture and network-wide (macro) levels. Fracture networks consist of multiple fracture sets, each defined by distinct orientation and size trends, which can form complex arrays. The following sections will briefly discuss how fracture networks are characterised, focusing on dimension, abundance, and petrophysical properties such as permeability and connectivity. Fracture network topology, which involves the characterisation of the spatial arrangement and intersection/termination of fractures will also be outlined.

2.4.1 The 'P-system'

Originally conceived by Dershowitz and Herda (1992), the 'P-system' (or 'P_{xy} system') incorporates multiple spatial dimensions into describing fracture networks. The 'P-system' can characterise fracture networks from data derived from one-dimensional drill hole traces or scan lines (1D), two-dimensional maps or orthophotographs (2D), and from three-dimensional tomography scans or rock volumes (3D) (Sanderson and Nixon, 2015). These characterisations involve the abundance of fractures within a selected unit dimension, with the name given to the type of abundance determined by the dimension of the feature: for counts of features the abundance is called 'frequency', while for lengths of features and areas of features, 'intensity' is instead used (Sanderson and Nixon, 2015).

Therefore, combining the dimensions of features with the dimension of the spatial unit as shown on Figure 2.6, the abundance of fractures per spatial unit is classified with P_{xy}, where 'P' represents "persistence", with the subscripts 'x' representing the dimension of the sampling region, and 'y' the dimension of the fracture (Dershowitz and Einstein, 1988; Dershowitz and Herda, 1992; Sanderson and Nixon, 2015). Of particular use in this thesis, the following type of fracture intensities (and frequency) is important (coloured blocks on Figure 2.6):

1) P_{10} provides the 1D linear fracture intensity for fractures (along a line trace or drill hole) which is provided by the formula $P_{10} = NL/L$, where NL represents the number of fractures and L is the unit length and has the unit of measure 1 m^{-1} (Dershowitz, 1984).
2) P_{21} denotes the 2D areal intensity for fractures (within a trace plane or surface), and is calculated using $P_{21} = \Sigma L/A$, where ΣL is the sum of the fracture lengths, and A is the surface unit area, where P_{21} uses the units of measure $m.m^{-2}$ (Dershowitz, 1984; Sanderson and Nixon, 2015).
3) P_{32} represents the 3D volumetric intensity (within a volume or rock mass) and is provided by the formula $P_{32} = \Sigma A_i/V$, where ΣA_i is the sum of the fracture surface areas, and V is the unit rock volume, with P_{32} using the unit of measure $m^2.m^{-3}$ (Dershowitz, 1984; Sanderson and Nixon, 2015). When using fracture shapes which approximate circular disks, as is the case in this thesis, the sum of fracture surface areas (ΣA_i) is approximated by $\Sigma(\pi/4)l^2$ (Maillot et al., 2016).

The importance of these various intensity parameters relates to their application within a study such as this. The P_{10} parameter is the most accessible intensity measure that can be determined from outcrop scan lines or measured along the length of a drill hole (Dershowitz and Herda, 1992; Golder Associates (UK) Ltd., 2001). Utilising multiple drill holes with variable orientations, or outcrop studies over diversely oriented rock exposures, affords well-resolved P_{10} estimates and mitigates potential orientation bias of the scan lines (e.g. Terzaghi, 1965). Importantly, the P_{10} value can be converted to a P_{32} estimate using the Wang et al. (2005) method, which accounts for the geometry and intensity of the fractures. Direct measurement of the P_{32} intensity measure is difficult to do, typically requiring 3D tomography scans of rock volumes (Li and Elmo, 2024). Consequently, converted P_{10} values are an ideal alternative. P_{32} is a crucial parameter for 3D volumetric fracture modelling (Davy et al., 2018), and is thus utilised extensively within this thesis as a modelling input variable. The remaining parameter, the areal intensity value, P_{21}, is easily calculated from remote sensing trace maps or outcrop mapping (e.g. Ceccato et al., 2022). In this thesis, using 2D trace maps extracted from 3D fracture models (generated using P_{32} measures), the calculated P_{21} values are employed as a comparison between observed and simulated areal intensities.

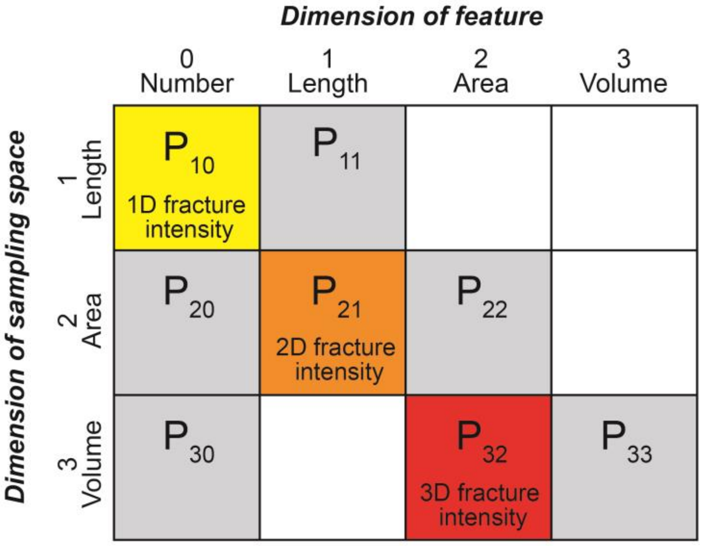

Figure 2.6. The P_{xy} system after Dershowitz and Herda (1992), shown in tabular form, with the P_{xy} classification provided by the dimension of the sampling region (x) and dimension of the fracture (y). Modified from Sanderson and Nixon (2015).

In this thesis, I specifically use the P-system to therefore describe the natural fracture patterns in drill core, maps, and in outcrops that have been used to provide deterministic inputs for the stochastic fracture modelling, as well as modelling outputs (discussed below).

2.4.2 Fracture attribute scaling behaviour

The length or radius sizes and spacing patterns of natural fracture network populations are typically best described by Exponential (Random or Poisson), Log-normal, and Power-law distributions (Bonnet et al., 2001; Dichiarante et al., 2020). These three distribution types are shown on Figure 2.7, by cumulative number of fractures against the fracture lengths for this example.

Fracture networks following an exponential, random, or Poisson distribution (Figure 2.7a) are characterised by at least one variable (nucleation location, length, or orientation) exhibiting randomness in its distribution (Dichiarante et al., 2020; Gillespie et al., 1993). The randomness in fracture propagation for exponential distribution fracture networks implies a uniform stress distribution in the rock volume (Dershowitz and Einstein, 1988), with minimal clustering or trends in fracture location or orientation observable in outcrop (typically difficult to discern clear fracture sets).

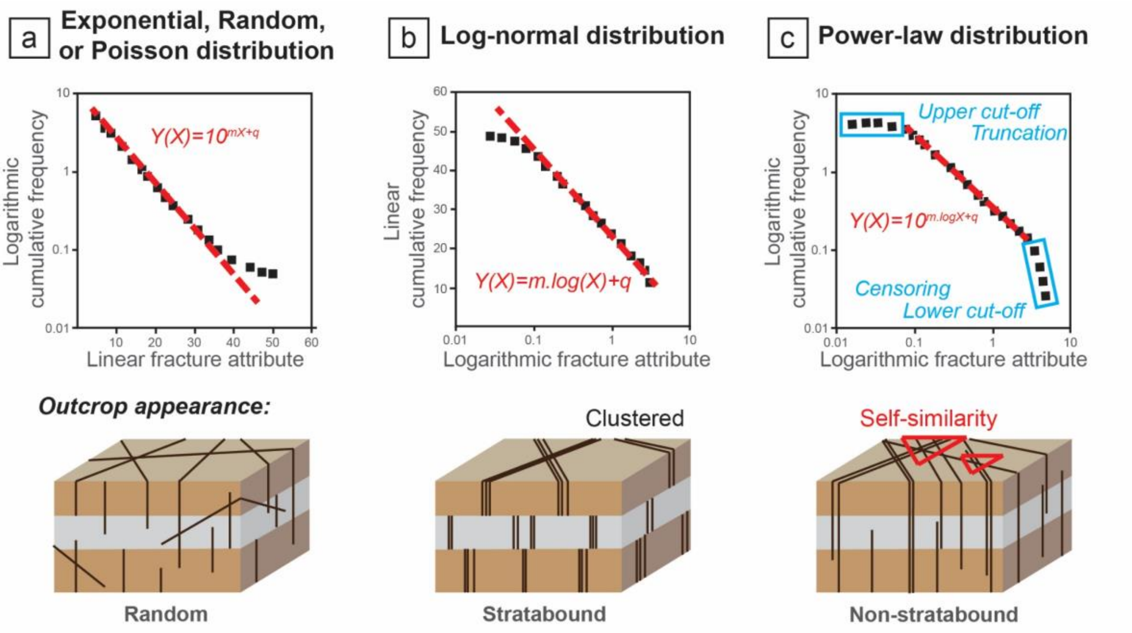

Figure 2.7. Idealised fracture size vs cumulative number frequency plots. (a) is the Exponential, Random, or Poisson type distribution, (b) the Log-Normal distribution, and (c) the Power-law distribution characterised by scale-invariant fracture scaling behaviours. Along with the plots, cartoons of typical outcrop exposures give an example of the fracture network appearance for each distribution type. Modified from Dichiarante et al. (2020).

Log-normal type fracture networks (Figure 2.7b) have a distribution strongly affected by rock or mechanical layering, which have a strong influence on at least one of the variables (for example fracture length, which is truncated by the boundaries of the rock layering) (Dichiarante et al., 2020). Additionally, fracture networks following a log-normal distribution typically also exhibit spatial clustering in terms of fracture nucleation (Gillespie et al., 1993). Overall, log-normally distributed fractures will typically have many small versus fewer larger fracture sizes, and the number of smaller fractures impacted by resolution effects (some small fractures are not detectable (Dichiarante et al., 2020) (Figure 2.7b).

Fracture networks that fit a power-law distribution (Figure 2.7c) typically exhibit a scale-invariant behaviour in terms geometric properties and spacing (Dichiarante et al., 2020). Particularly, this scale invariance leads to fractal fracture patterns with a constant ratio of the abundance of small fractures to large fractures (Barton, 1995; Dichiarante et al., 2020). Consequently, there is no dominant or typical fracture length size (or spacing) that characterises a power-law distributed fracture networks within the limits of the scale range (involving at least several orders of magnitude) (Bonnet et al., 2001). As a result, fracture networks that are assumed to have a power-law distribution are useful for characterising fracture networks at a variety of scales (they possess 'self-similarity'). Importantly however, power-law distributions do suffer from sampling bias, in which censoring (large fractures are incompletely documented owing to sample boundary limitations – shown in Figure 2.8a) and truncations (small fractures are not documented owing to resolution effects) of the fracture traces (Figure 2.7c), which leads to uncertainty in ascribing a fracture network to a specific distribution type (Dichiarante et al., 2020).

2.4.3 Fracture network topology and measuring connectivity

Fracture and fault arrays can be characterised using network topology (Figure 2.8a), which describes the relationships between different geometric components, such as intersecting fractures (Peacock and Sanderson, 2018; Sanderson and Nixon, 2015). In a 2D space (such as an outcrop exposure surface), a 3D fracture network is simplified into lines, called 'branches', which represent where the fractures intersect with the 2D surface (Sanderson and Nixon, 2015). The ends of these branches, along with their intersections, are represented as points called 'nodes' (Sanderson and Nixon, 2015). The branch types include II (isolated), C-I (semi-isolated), and C-C (connected)-types; and the nodes are sub-divided into I (isolated), Y (terminating or abutting), and X (cross-cutting) types (Manzocchi, 2002; Sanderson and Nixon, 2015).

Natural fracture systems possess connectivity through the intersection (cross-cutting and termination) of different fractures, with these intersections represented by the X and Y-nodes (Dershowitz and Einstein, 1988). Consequently, counting the number of X and Y-nodes and the total number of branches, the proportions of each can be used to analyse the 'interconnectedness' of selected fracture network (Nyberg et al., 2018). To undertake this analysis, the number of connections per branch (C_B) is used as a measure of network fracture connectivity (Sanderson and Nixon, 2015). The C_B parameter is therefore defined as $C_B = (3N_Y + 4N_X) / N_B$, where N_y is the number of Y-nodes, N_x is the number of X-nodes, and N_B is the total number of branches, with the parameter expressed as a dimensionless value $0.0<C_B<2.0$ (Sanderson and Nixon, 2015). This value and the proportions of both nodes and branches can be plotted on ternary diagrams such as those shown in Figure 2.8b.

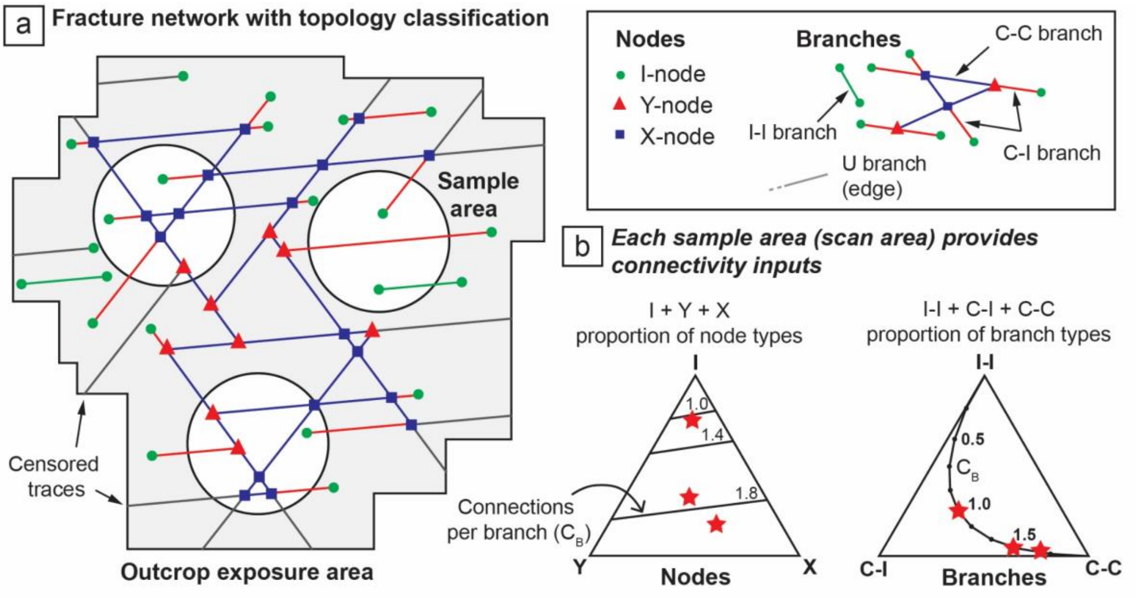

Figure 2.8. Network topology classification of a 3D natural fracture network on a 2D surface. (a) A simplified example of an outcrop surface crosscut by a fracture network sub-divided into different branch types, with the branch intersections and branch tips allocated to different node types (types are indicated in the adjacent legend). Node and branch type abbreviations are described in the text. (b) Ternary plots classifying the three different sample areas in the outcrop exposure areas by proportions of node and branch types. This is used to determine the overall connectivity (C_B) of the fracture network. Modified from Sanderson and Nixon (2015) and Nyberg et al. (2018).

As the C_B formula uses the total number of branches (N_B) as the denominator, the connected nodes (Y and X-types) counts (the numerator of the formula) are normalised against all the branches, even the isolated branches, which do not impact fluid flow-related connectivity. The C_B metric is therefore limited, in that it cannot differentiate between total connectivity, referring to the entire fracture network, whether necessarily participating in fluid flow or not, and the actual connectivity. This actual connectivity, on the other hand, only considers the connected fractures which do facilitate fluid flow, otherwise known as the backbone pathway by Cox (2005). To address this issue, two other parameters, namely branch clusters and enclosed ‘blocks’, can be used as proxies to estimate how much of a fracture network is constituted by connected fractures (and thus background connectivity), and the overall rock deformation state (Nyberg et al., 2018; Petrik et al., 2023).

Applying cluster and block analysis of 2D fracture traces yields two key parameter types: The first parameter types are the abundance and total trace length of connected branch clusters, representing the combined lengths of all interconnected fractures within a cluster. These clusters involve distinct sub-networks of interconnected fractures within larger fracture networks, and if characterised, can indicate the degree of connectivity of a fracture network (Nyberg et al., 2018). Generally, a few large clusters imply well-connected fracture networks, while many small clusters indicate a prevalence of isolated fractures or minor local networks of connected fractures.

The second parameter type is the abundance of enclosed regions or 'blocks' bound by connected fractures (being C-I, and C-C-type branches), which provides the dimensionless block intensity (R_{22}) metric, reflecting the degree of deformation of a fractured rock (Petrik et al., 2023; Sanderson et al., 2019). To calculate dimensionless block intensity, the formula $R_{22} = 1/(R+1)$ is used, with R representing the number of enclosed regions within the area of interest, with the metric expressed as a value $0.0<R_{22}<1.0$ (0.0 represents a completely disaggregated rock, and 1.0 an intact rock) (Petrik et al., 2023; Sanderson et al., 2019).

Overall, connectivity is a crucial parameter to define fracture networks, as when a fracture network becomes interconnected at a large-scale (across a reservoir), the so-called 'percolation threshold' is reached (Manzocchi, 2002). This threshold is defines the point at which enough fractures intersect (becoming interconnected) to form a network which extends from a fluid reservoir transecting through an entire rock volume (forming a flow backbone), thus enabling fluid flow across the fracture system (Cox, 2005). Cluster analysis, as outlined above, can therefore demonstrate and quantify these interconnected fractures as potentially 'percolating' clusters. If these clusters indeed involve enough connected fractures to span across a medium (thus satisfying the percolation threshold), they will allow fluid flow to occur (Adler and Thovert, 1999). The factors that can control the percolation threshold include the fracture intensity (higher intensity may result in fewer isolated fractures), and the size and orientation of the fractures (Cox, 2005; Gillespie et al., 2020). The percolation threshold itself will not be dealt with directly in this thesis and is included here only as additional context.

2.4.4 Permeability

2.4.4.1 Factors and characteristics controlling permeability

Permeability (K) is the measure of how easily a fluid can flow through a through a medium (Nolen-Hoeksema, 2014). Applying Darcy's Law (Darcy, 1856), the intrinsic permeability of a porous material, of known dimensions, can be determined using the formula $K=(Q\eta L)/(A\Delta P)$, which depicts horizontal laminar flow in a medium during steady-state conditions (Filomena et al., 2014). Q is the flow rate, η the viscosity of the fluid, L the length of sample, *A* the cross-section area of the sample, and ΔP the pressure difference between the inflow and outflow of the fluid (Filomena et al., 2014).

However, when a medium is also cross-cut by fractures or other planar discontinuities, permeability can be sub-divided into either primary (matrix) or secondary (structural or fracture-related) permeability (Selvadurai et al., 2005; Sibson, 1996), with each requiring a specific method for estimation. The permeability which therefore encompasses the combined permeability of the entire rock mass is termed 'bulk permeability' in this thesis ($K_{bulk} = K_{matrix} + K_{fractures}$).

As this study addresses rock volumes that are crystalline and have low matrix permeabilities (outlined further in this Chapter), the structural permeability will control most of the rock mass's bulk permeability. It therefore follows that the bulk permeability of a fractured crystalline rock mass is better described by a cubic law (assuming laminar flow between two parallel smooth plates) that incorporates the presence of fractures (Ioannou and Spooner, 2007). A simplified method to estimate permeability therefore makes use of either $K=(nd^3)/(12)$ (Ioannou and Spooner, 2007) or $K=(d^3)/(12S)$ (Brace, 1980), where n is the abundance of fractures, d the fracture aperture, and *S* the fracture spacing. Thus, in an impermeable rock volume, the primary control on secondary permeability is the aperture of the individual fractures (Gale, 1982). This is because in fractured rock volumes, and as highlighted by the equations above, fluid flow through fractures is proportional to the cube of the fracture aperture, directly affecting bulk permeability (Gale, 1982). As a result, the fracture (or fault) infill-type possessed by each fracture (Figure 2.9), which is potentially variable over a fracture network, will affect the aperture of the fractures and therefore the bulk permeability in this case.

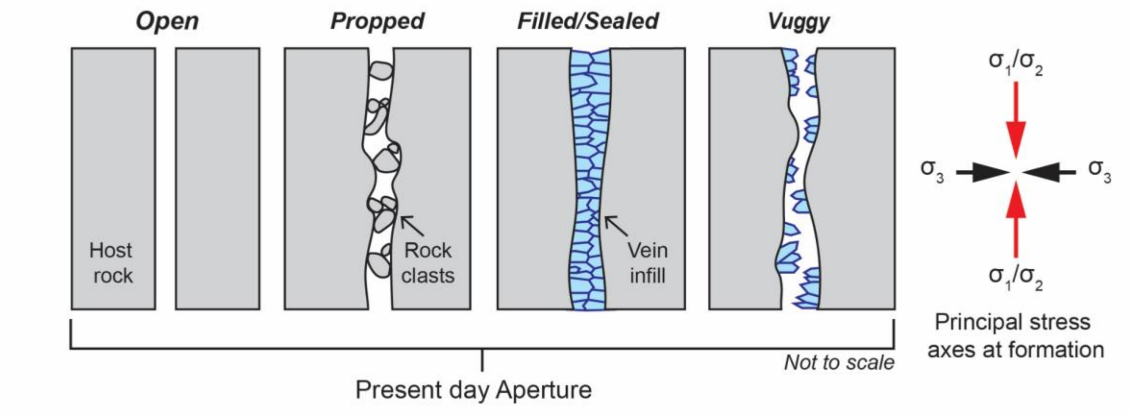

Figure 2.9. Four examples of fracture apertures observed in outcrop, with infill types reflective of present-day fractures in outcrop (assuming extended geological time as elapsed since formation). The fractures illustrated relative to the applied stress field at time of formation, particularly if they

are tensile fractures, they will open orthogonal to the least compressive stress σ_3. Modified from Dichiarante et al. (2020).

Generally, as fluids in the upper crust flow preferentially through fractures rather than intact rock volumes (especially if the host rock lacks significant porosity/primary permeability) (Cox, 2010). Fractures oriented to enhance connectivity, particularly through more fracture intersections, improve fluid flow (opposed to isolated fractures) (Oliver and Bons, 2001). Therefore, secondary permeability (and bulk permeability) is highly influenced by fracture network connectivity (as discussed above) (Gillespie et al., 2020). Worth briefly mentioning here, a separate but related concept, fluid flux is the fluid flow rate through a matrix's pore spaces or interconnected fractures (channelised flow), which corresponds to hydraulic conductivity or transmissivity (Nolen-Hoeksema, 2014).

Fault-valve rupture-related fracture formation and opening (open fracture in Figure 2.9) significantly increases flux and discharge (Figure 2.2b) (Cox, 2005; Sibson, 1992). This process directly affects fracture aperture over time and structural permeability. Notably, the stress-related opening and closure of fractures can also control structural permeability creation and destruction. During tectonic loading, increasing shear stress may result in rock dilation and fracture opening (Sibson, 1994, 1996). Subsequent brittle failure can also cause fracture formation and opening, with the aperture oriented according to the prevailing stress field, resulting in directional permeability (Figure 2.9) (Sibson, 1994, 1996). On the contrary, fracture closure and related permeability destruction may occur during the post-seismic decreases in shear stress (along with increasing mean stress), or over time when fractures are oriented orthogonally to the direction of maximum lithostatic pressure (σ_v), generally the case with horizontal fractures, resulting in fracture and pore collapse (Cox, 2005; Sibson, 1994). In this thesis, however, even though stress-related permeability creation and destruction is an important process, it will not be explored further.

As previously mentioned earlier in the Chapter, secondary permeability created is transient and will eventually be destroyed by vein infill mineralisation (Caine et al., 1996; Sibson, 1992, 1996), such as illustrated by the filled/sealed and vuggy fractures in Figure 2.9. The migrating fluids themselves therefore affect the fractures through metasomatism and precipitation, causing the fractures and fault zones to become eventually sealed (Scholz, 2019). Accordingly, faults or fractures can, through time, potentially act as either conduits or barriers to fluid flow (Caine et al., 1996; Peacock, 2001). This temporal variability in secondary permeability is evident when comparing fractures of different ages, whereby older fractures which formed prior to fault ruptures may be sealed, and therefore act as low permeability barriers, while younger cross-cutting open fractures formed during a later fault rupture will significantly enhance secondary permeability (Peacock, 2001).

Spatial variability in secondary permeability is also evident and is particularly demonstrable between fault cores (during interseismic periods or fault activity quiescent), damage zones, and the surrounding host rock volumes. Caine et al. (1996) showed how the permeability estimates for fractured damage zones are two to three orders of magnitudes higher than the surrounding host rock volume, and four to six magnitudes higher than the fault cores with pore-spaces infilled with precipitated minerals. The bulk permeability structure of a fractured and faulted rock volume is therefore highly complex with significant permeability contrasts in relatively short distances (Caine et al., 1996; Scibek, 2020).

A further notable factor influencing secondary permeability is the presence of 'propped' fractures (Figure 2.9). Fragments of host rock or clastic sediments trapped within faults during deformation or deposition of overlying sediments, can keep fractures permanently open, enhancing permeability and facilitating geofluid migration (Holdsworth et al., 2019).

2.4.4.2 Permeability tensor

As already outlined above, fractures and other types of discontinuities (for example brittle faults) significantly influence permeability in relatively impermeable rocks. When these features possess trends or variability in orientation or another geometry characteristic (such as aperture), they will typically cause a 3D permeability anisotropy within a rock volume (Ioannou and Spooner, 2007). To estimate this 3D permeability anisotropy, a permeability tensor can be derived for a selected rock volume (Oda, 1985; Snow, 1969). This is because a second-order tensor can describe the fluid outflow of one or more parallel-plate openings, representing idealised fractures, in a medium volume (Ioannou and Spooner, 2007; Snow, 1969). The permeability of both fractured and continuous rock masses, experiencing identical hydraulic gradients and laminar flow conditions (following Darcy's Law), can be expressed using a permeability tensor (Ioannou and Spooner, 2007). Both rock conditions can be treated the same because sufficiently connected fractured rock masses, such as the case in this thesis, exhibit similar behaviours to porous mediums (Oda, 1985; Oda et al., 2002).

While a comprehensive description of the permeability tensor theory is beyond the scope of this thesis, a detailed explanation is available in Oda (1985). Here, I will however briefly outline the derivation of the permeability tensor using the methods of Golder Associates (UK) Ltd. (2001), Oda (1984), Oda (1985), Oda et al. (2002). As a note, I have used a different format to document the relevant mathematical equations in this section compared to the rest of the thesis. I have also included along with the equations, a system of equation numbering to aid the cross-referencing between the descriptions.

To begin the derivation, it is important to consider fractures located within an impermeable rock mass, as numerous disk shapes, each of which possessing a measured orientation, and a normal vector (n) extending orthogonally from the upper and lower disk surfaces (the normal vector, n, represents both the +n and -n vector extending from each surface of the fractures) (Oda, 1984, 1985). To then statistically represent the orientation distribution of these fracture normal vectors, Oda (1984) proposed an approach using the mass moment of inertia of all the fracture unit normals (N) within a unit sphere:

$$\mathrm{N} = \int_{\Omega/2} n_i n_j E(\mathrm{n})\, d\Omega \qquad \text{Eq. 1}$$

with N representing the number of fractures within the unit sphere (Ω), n_i, n_j are the components of the unit normals to the fractures, E(n) the density function describing the fracture unit normal vectors, n, distributed around a solid angle Ω/2, and Ω is the solid angle related to the surface of a unit sphere (Golder Associates (UK) Ltd., 2001; Oda, 1984).

Subsequently, by applying N from Equation 1, the geometrical distributions of the 'k$^{\text{th}}$' fracture among N number of fractures (within a unit sphere Ω), the fracture tensor, F_{ij}, (or 'crack tensor') as derived by Oda (1985) can be calculated. The additive form of the fracture tensor is shown below (Golder Associates (UK) Ltd., 2001) in Equation 2:

$$F_{ij} = \frac{1}{\mathrm{V}} \sum_{\mathrm{k}=1}^{\mathrm{N}} A_k T_k n_{ik} n_{jk} \qquad \text{Eq. 2}$$

where F_{ij} is the fracture tensor, V is the volume of the grid cells, N is the abundance of fractures within the grid cells, A_k is the area of the k$^{\text{th}}$ fracture, T_k is the assumed transmissivity value of the k$^{\text{th}}$ fracture, n_{ik}, n_{ij} are the geometric components of the unit normal vector of the k$^{\text{th}}$ fracture (Golder Associates (UK) Ltd., 2001). In this thesis, I have utilised assumed transmissivity values based on idealised hydraulic conductivity and reservoir approximates (incorporating fracture length and aperture values).

Having defined the fracture tensor (Equation 2), the equivalent permeability tensor (K_{ij}) can next be defined and is provided below in Equation 3:

$$K_{ij} = \frac{1}{12}(F_{kk}\delta_{ij} - F_{ij}) \qquad \text{Eq. 3}$$

where the K_{ij} is the permeability tensor, δ_{ij} is the Kroenecker's delta, F_{ij} is the fracture tensor provided by Equation 2, and $F_{kk} = F_{11} + F_{22} + F_{33}$ (refer to Equation 4 below) (Golder Associates (UK) Ltd., 2001). The permeability tensor as used here, does assume that the utilised fractures have sufficient connectivity and adequate fracture radius sizes (Ioannou and Spooner, 2007; Oda, 1985), which is considered to be acceptable as I am applying the method to highly fractured crystalline basement rocks.

Both the 'crack' tensor and the permeability tensor are symmetrical, as shown below in 3 x 3 matrix form, and can be diagonalised into the respective principal components (Oda, 1985):

$$[F_{ij}] = \begin{bmatrix} F_{11} & F_{12} & F_{13} \\ & F_{22} & F_{23} \\ \text{Symm.} & & F_{33} \end{bmatrix} = \begin{bmatrix} F_1 & 0 & 0 \\ & F_2 & 0 \\ \text{Symm.} & & F_3 \end{bmatrix} \qquad \text{Eq. 4}$$

$$[K_{ij}] = \begin{bmatrix} K_{11} & K_{12} & K_{13} \\ & K_{22} & K_{23} \\ \text{Symm.} & & K_{33} \end{bmatrix} = \begin{bmatrix} K_1 & 0 & 0 \\ & K_2 & 0 \\ \text{Symm.} & & K_3 \end{bmatrix} \qquad \text{Eq. 5}$$

with F_1, F_2, and F_3 being the maximum, intermediate, and minor axes of the fracture tensor, F_{ij}; and K_1, K_2, and K_3 are the maximum, intermediate, and minor components of the permeability tensor, K_{ij}, (Oda, 1985). As K_{ij} is related to P_{ij}, the principal component axes are coaxial of each other, but with the maximum permeability axes K_1 coinciding with the minimum fracture axis F_3 (Oda, 1985). Consequently, a permeability tensor can describe a permeability anisotropy, with the lowest permeability direction orthogonal to the most permeable features, while the highest permeability direction parallel to the most permeable features or along the intersection of fractures (e.g. Ceccato et al., 2021a).

In summary, the presence of well-connected, open fractures (such as located in damage zones) or propped-open fractures, contrasted with low permeability host rocks, and impermeable fault cores (and older sealed and vuggy fractures or veins) imparts a 3D permeability anisotropy, which can be described using the geometric components of the fractures, a calculated fracture tensor, and finally a derived permeability tensor.

2.5 Geofluids

Geofluids, or crustal fluids, which potentially migrate because of fracture-related permeability, can be sub-divided into several types based on their origin. These include mantle-derived or magmatic-related fluids, devolatilisation or metamorphic reaction-related fluids, sedimentary basin rock pore-fluid-related, or surface-related (meteoric or seawater) (Cox, 2005). While a full discussion on the fluid origin, chemical composition, and types of fluid-rock metasomatism is beyond the scope of this thesis, an excellent review of these topics is provided by Yardley and Bodnar (2014). This section will instead focus on the types of crustal geofluids most relevant to this thesis.

In general, geofluids consist of aqueous fluids with three main components: water (H_2O), salts (typically chlorides), and gases (CO_2, SO_2, and N_2 from deeper fluid sources; and CH_4, and H_2S from shallow fluid sources)(Yardley and Bodnar, 2014). The specific composition of a geofluid, particularly between the H_2O, salts, and gas components, depends on its origin within the crust and influence of different geofluid interaction.

For example, fluids sourced from or associated with magmatic activity (such as pluton emplacements), commonly contain a higher concentration of dissolved ionic species and metallic elements, because of scavenging of source rocks by hydrothermal circulation driven by geothermal or magmatic-related thermal gradients (in places resulting in ore deposit formation) (Cox, 2005). The specific type of magmatic rocks has a strong influence of chemical constituents, for example, fluids exsolving from silicic magma, are commonly enrich in Na, K, and Fe cations (Yardley and Bodnar, 2014), while fluids associated with more mafic magmas are commonly more enriched in Ca cations (Yardley and Bodnar, 2014). Overall, the migration of magmatic-related fluids (and including metamorphic fluids) is also strongly affected by the density contrast between geofluids and host rocks, at certain depths (Yardley and Bodnar, 2014), in addition to thermal gradients, and hydraulic gradients created by tectonic activity (Putnis and Austrheim, 2010; Sibson, 1994).

Sedimentary basins, another important source of geofluids, produce mostly basinal brines characterised by high salinity fluids (dominated by Na and Ca cations) (Yardley and Bodnar, 2014), as well as hydrocarbons if sufficient organic matter is present and favourable conditions for the kerogen thermal maturation occur (Palumbo et al., 1999). Expulsion of these fluids commonly occurs as a consequence of basin overpressuring, and extension-related seismicity laterally draws these fluids out along intersecting major normal faults (Holdsworth et al., 2019; Sibson, 1994).

Surface-related fluids such as meteoric water or seawater on the other hand, typically dominated by Na and Mg cations (Yardley and Bodnar, 2014), can migrate into the crust through gravitational seepage along fault or fracture networks (including Topographically induced flow) (Cox, 2005). For example, evidence for this process is shown by the calcite veins studied by Hestnes et al. (2023), using $\delta^{18}O$ and $\delta^{13}C$ stable isotope analysis, indicate that calcite mineralisation was sourced from groundwater in crystalline basement rocks, potentially influenced by oxidised surface organic material or seawater.

Evidence of past fluid migration is recorded by veins and the alteration zones, or selvages, surrounding them (Oliver and Bons, 2001). These features provide a record of metasomatic processes, including fluid-rock interactions and chemical mass transport (Oliver and Bons, 2001). The types of minerals that may precipitate from a specific fluid are influenced by factors such as fluid composition (such as dissolved cation content), temperature, redox conditions, pH, origin, and age (Drake et al., 2009). By constraining the temporal relationships between different mineral phases, it is possible to reconstruct the sequence of fluid-related events and infer the types of geofluids involved. For example, we can use observed regional-scale albitisation of granitic rocks, with clear field-evidence of albite replacement of plagioclase, along with hematite staining/veins (derived from albite-plagioclase replacement, and reworking from chlorite-biotite retrograde reactions), to provide a record of distinct fluid migration episodes (e.g. Indrevær et al., 2014; Putnis and Austrheim, 2010).

2.6 Fractured reservoirs

Fractured reservoirs are characterised by geofluid storage and migration primarily occurring along and through interconnected natural fractures (providing ‘secondary’ or structural permeability) (Holdsworth et al., 2019). The host rocks generally exhibit very low intrinsic matrix permeability and porosity (commonly being thus referred to as ‘tight’ formations), with significant permeability almost entirely attributed to the fracture network (Gillespie et al., 2020; Holdsworth et al., 2019). This contrast in petrophysical properties between the rock matrix and fractures is highlighted by permeability values: crystalline rock matrix permeabilities typically range from 1.0e-24 to 1.0e-18 m² (Selvadurai et al., 2005), while fault zones, inferred to have similar values to fractures when not acting as fluid barriers (see Permeability section above), range from 8.0e-16 to 6.0e-11 m² (Scibek, 2020). Although fractures may only contribute around 1 % of the total rock volume in terms of porosity, fault and fracture networks may significantly enhance the overall reservoir bulk permeability (Gillespie et al., 2020).

Fractured reservoirs are classified into four types, as defined by Nelson (2001), which are shown in Table 2.1. Crystalline basement reservoirs are commonly classified as Type I fractured reservoirs (Gillespie et al., 2020). Crystalline basement fractured reservoirs are distinct from, for example, carbonate Type I reservoirs, in that they typically have complex geological histories (Trice, 2014). These histories result in heterogeneous inner volumes, commonly comprised by multiple rock types such as granite, granodiorite, gneiss, dolerite, and basalt (Biddle and Wielchowsky, 1994; Trice, 2014). This heterogeneity, and that certain faults or fractures may act as either fluid conduits or as fluid barriers (as previously discussed), suggests that basement reservoirs can be compartmentalised, with different compartments exhibiting varying bulk permeabilities (Biddle and Wielchowsky, 1994; Gillespie et al., 2020).

When crystalline basement reservoirs form geofluid traps, they typically occur as 'buried hill' type structures or faulted (or fault-tilted) basement blocks (Biddle and Wielchowsky, 1994; Trice, 2014) (Figure 2.10). These blocks are often uplifted during extensional tectonics, particularly in the footwall of normal faults, or may represent paleo-topographic features (Gillespie et al., 2020; Holdsworth et al., 2019). If forming a petroleum trap, source rocks (commonly younger sedimentary units) for migrating oil and gas will typically be proximal to the fractured basement volume, with reservoir charging involving laterally migrating hydrocarbons into the basement rocks (Holdsworth et al., 2019; Trice, 2014). A low-permeability, clay-rich unit will commonly cap the trap, separated by an unconformity from the basement, acting as a seal to prevent further fluid migration or escape (Holdsworth et al., 2019; McCaffrey et al., 2020).

Table 2.1. Types of fractured reservoirs based on the contributions that either the matrix or the fractures and faults make towards geofluid storage and flow (modified from Trice et al. (2022))

Type	Matrix	Fault/Fracture network	Comment
I	Very low porosity Very low permeability	Flow and storage	Storage and flow via fractures
II	Low porosity Low permeability	Flow and (storage)	Fractures are flow pathways, some minor contribution from the matrix
III	High porosity Low permeability	Flow	Fractures are flow pathways; matrix contributes significantly
IV	High porosity High permeability	Enhanced flow	Matrix provides the storage and flow, some permeability enhanced by fractures

At the unconformity, the upper surface of the basement may be weathered or represent a paleo-erosional surface, with higher porosity from weathering or sediment infilling fractures, further enhancing the bulk permeability (Biddle and Wielchowsky, 1994; Holdsworth et al., 2019). Geofluids within the crystalline basement typically migrate upward through well-connected fractures (Figure 2.10) driven by buoyancy or tectonically induced seismicity (as previously outlined) (Holdsworth et al., 2019; Yardley and Bodnar, 2014). These geofluids, if hydrothermal, may result in the open natural fracture system being sealed through mineralisation, or in rare cases being popped-open by growing hydrothermal minerals (Gillespie et al., 2020). Overall, however, when characterising a fractured crystalline basement reservoir, the focus is usually on defining the fracture network rather than the host rocks in detail (Bonter and Trice, 2019).

Although porosity is a key petrophysical property in fractured reservoir characterisation, this thesis focuses more on connectivity and permeability characteristics. Porosity will therefore only be discussed when essential.

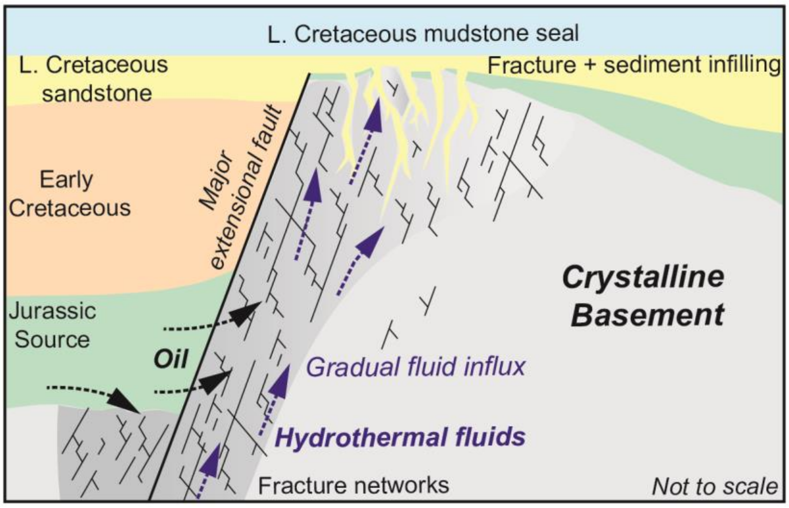

Figure 2.10. Generalised representation of a fractured reservoir, specifically the 'Buried Hill'-type associated to basement structural highs. Both oil and hydrothermal fluids are indicated percolating through a network of interconnected fractures from either an overpressured sedimentary basin, or from deeper hydrothermal fluid sources. Modified from Holdsworth et al. (2019).

2.7 Discrete fracture network (DFN) modelling

Natural fracture networks are difficult to image in 3D due to sampling biases (as mentioned above), with 2D eroded outcrops or 1D drill hole data providing limited representations, and seismic data, owing to their coarse resolution, are unable to resolve individual fractures (Welch et al., 2020). Therefore, we must use methods that generate representative fracture network characterisations replicating observed networks without the need for full 3D imaging (Bonneau et al., 2013). Stochastically recreating natural fracture networks on Smøla island is a key component of this thesis. Accordingly, I now outline the most relevant theoretical background of the approach and toolset.

2.7.1 Theory

The discrete fracture network (DFN) modelling method has been extensively used since the 1980's and is now a well-established and routine approach for simulating fractured rock volumes (Dershowitz and Einstein, 1988; Jing and Stephansson, 2007; Long et al., 1985; Welch et al., 2020). For the DFN modelling method used in this study, individual fractures are simulated using quantitative definitions of observed fracture geometric characteristics, with overall fracture networks modelled using statistical descriptions of examined natural fracture interactions (topological terminations or cross-cutting relationships) and intensity (Libby et al., 2024). Applying these observed quantitative and statistically described fracture parameters, stochastic representations of the fractures (and networks) are generated as 3D objects within a homogeneous matrix (adopted in this thesis to simplify rock mass properties) assumed to be mechanically stiffer and impermeable compared to the fractures (Davy et al., 2018; Jing and Stephansson, 2007).

In more detail, fractures are typically generated at random locations within the matrix volume using a Poisson point process, making the method stochastic (Davy et al., 2018; Libby et al., 2024). The stochastic fracture properties are based on statistical distributions (statistical density functions) of geometric characteristics such as orientation, size, shape, and aperture with fracture intensity (P_{21} or P_{32}) determining their abundance (Davy et al., 2018; Libby et al., 2024). Importantly, therefore DFN models possess statistical variability in the output results compared against the deterministic input geology (Davy et al., 2018).

As shown on Figure 2.11, field observations and measurements of individual fractures and fracture sets from outcrop mapping and drill hole fracture logs allow a natural fracture network to be characterised. The observed qualities of this natural network (deterministic properties) are then used to define the geometric and statistical properties of stochastic fractures (Davy et al., 2018; Jing and Stephansson, 2007; Welch et al., 2020). These deterministic inputs form the ‘DFN recipe’, providing the necessary components for stochastic modelling within a given volume. Importantly, the quality of the DFN recipe and its deterministic inputs directly influence whether the stochastic DFN model can effectively replicate the observed fracture network.

Relevant to this thesis, there are three types of DFN modelling approaches for characterising fracture networks: 1) The simplest, a probabilistic fracture modelling geometric approach using a Poisson point process (Dershowitz and Einstein, 1988; Libby et al., 2019). 2) A geomechanical modelling approach that incorporates fracture propagation, termination, and nucleation processes, accounting for fracture generation and stress field evolution (Bonneau et al., 2013; Davy et al., 2013; Dershowitz et al., 2019; Libby et al., 2019; Maillot et al., 2016); and 3) A kinetic or ‘grown’ DFN approach that uses mechanistic rules to model sequential, polyphase fracture generations, which grow and interact dynamically over time (Libby et al., 2019, 2024; Maillot et al., 2016).

While these approaches can generate ‘static’ DFN models, which describe the geometry of fractured rock (the focus of this thesis), they do not necessarily create ‘dynamic’ (calibrated fracture) models for hydraulic fluid flow testing (outside the scope of this project) (Golder Associates (UK) Ltd., 2001). ‘Static’ DFN models can, however, provide 3D estimations of bulk petrophysical properties, such as volumetric permeability tensors and fracture connectivity (Welch et al., 2020).

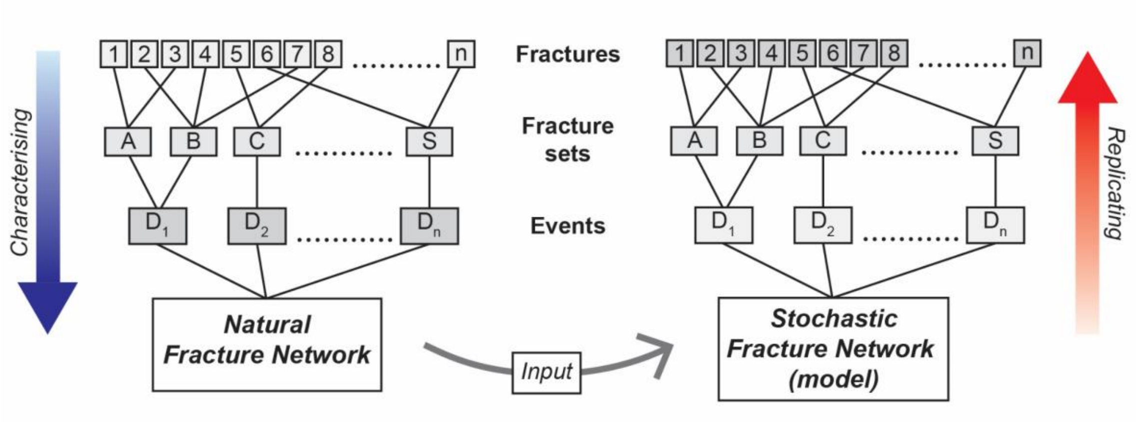

Figure 2.11. Schematic representation of how discrete fracture network (DFN) models use characterised natural fracture networks to recreate and generate stochastic fracture networks. The deformation episodes (or events) are especially key to understanding the chronological order of fracture formation when generating ‘grown’ DFNs. It is important to note, however, that it is commonly difficult to exactly recreate a natural fracture system stochastically, as models generally need to be simplified to generate fractures at a specific scale. Modified from Peacock et al. (2018).

2.7.2 Modelling procedure and fracture reconstruction

The different DFN modelling approaches each offer different advantages and limitations. However, the ‘grown’ DFN technique primarily incorporates a temporal component into the modelling and provides a more computationally efficient method to model fractures in 3D within modelling volumes of hundreds of metre-scales, when compared to other geomechanical approaches (including Thomas et al. (2020) or Paluszny et al. (2020)) which typically also incorporate stress evolution into the modelling process (Libby et al., 2019, 2024). These other geomechanical DFN approaches typically have limitations in how many individual fractures can be simulated (typically in the magnitude of hundreds of fractures) or require smaller modelling volumes, while the ‘grown’ DFN can generate more than a million individual fractures within larger volumes (Libby et al., 2024). Even so, DFN modelling does involve complex algorithms and is still computationally demanding on most hardware platforms. Aside from computational efficiency, the ‘grown’ DFN method has also demonstrated satisfactory replication of the termination or arresting relationships (Y-nodes) between fractures of different relative ages (Libby et al., 2019, 2024), which is a significant challenge in generating realistic DFN models.

The mechanistic rules of the ‘grown’ DFN modelling approach involve the following framework: 1) Generated fractures are ‘seeded’ (nucleated) from random locations within the model volume and propagate outwards with radiating rays (forming approximately planar disks) growing in predetermined number of timesteps (to simulate fast or slow fracture propagation) (Libby et al., 2019). 2) Fracture sets of different generations (shown on Figure 2.11 as the D’s) can be modelled sequentially, with interactions (cross-cutting or abutting) between fractures controlled by termination probabilities, based on observed field termination relationships (Libby et al., 2019). These termination interactions can be set between simultaneously growing fractures (the same age), and between younger and older fractures (the older fractures grow first and form pre-existing features, which the younger fractures may or may not terminate against). 3) Fractures grow until a certain number of rays terminate or their target equivalent radius size is reached (Libby et al., 2019, 2024). The size distribution (ratio of small versus large fractures) of each fracture generations is scaled according to the deterministic inputs defined from natural fracture size distribution data (for example a power-law distribution). 4) Fracture growth and further fracture ‘seeding’ continues until the target fracture intensity is achieved (Libby et al., 2019).

Once a ‘grown’ DFN model has finished growing all the fractures for each deformation phase, the model is ‘realised’ and can subsequently be compared to the observed fracture networks, and if necessary, it can be adjusted to better match the deterministic data (Bym et al., 2022). Overall, however, the use of multiple deformation phases to sequentially grow the fractures, more closely replicates the polyphase deformation-related saturation of rock volumes (e.g. Viola et al., 2012). The final ‘static’ DFN model can then be used for bulk petrophysical property estimation, via, for example, grid-based calculations of the 3D permeability tensor (e.g. Oda, 1985).

Chapter 3: Geological setting

3.1 Introduction

Smøla island, the study area of this project, is located within the mid-Norwegian passive margin (Figure 3.1), a region that has experienced a prolonged and complex geological history spanning >300 Myrs (Corfu et al., 2014; Peron-Pinvidic and Osmundsen, 2018). To frame this study within the broader geological context, I will therefore briefly summarise the key elements of the region's geological history, initially focusing on the margin's relevant geological features at the regional-scale and then describing Smøla island's geology at the more local scale.

3.2 Regional Geology

Smøla island is comprised by oceanic nappe rocks (magmatic arc and oceanic crustal rocks), originally emplaced and accreted above the subducting Iapetus lithosphere and Baltica continental margin, outboard of Baltica within the Iapetus Ocean (Corfu et al., 2014; Jakob et al., 2022). The plutonic rocks on Smøla, dated by U-Pb to 445.7 ± 3.8 Ma (Slagstad et al., 2011; Tucker et al., 2004), were emplaced preceding the onset of continental collision between Laurentia and Baltica at ~430 Ma, during the Scandian Phase of the Caledonian Orogeny (e.g. Gee et al., 2008; Slagstad and Kirkland, 2018; Tucker et al., 2004).

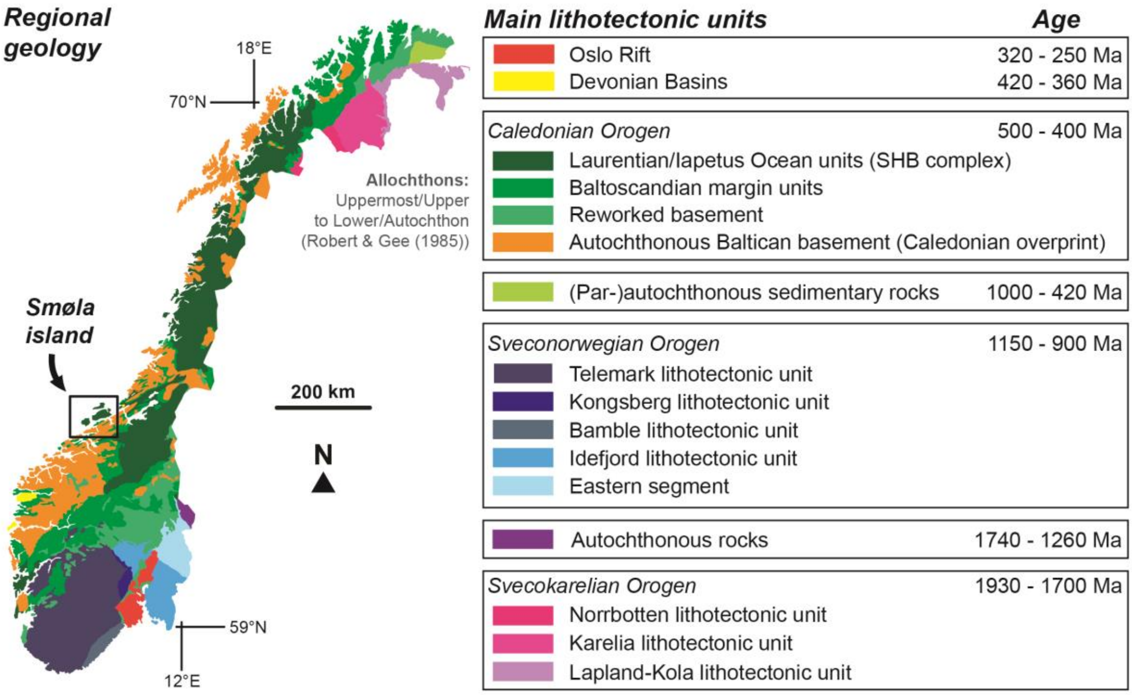

Figure 3.1. Simplified geological map of Norway with major lithotectonic units shown. Modified from the Bedrock map of Norway, Geological Survey of Norway (2021).

These oceanic nappe rocks on Smøla form part of the plutonic Smøla-Hitra Batholith (SHB) complex (Gautneb and Roberts, 1989), and were historically allocated to the Caledonian Upper Allochthon (Roberts and Gee, 1985).

3.2.1 Caledonian orogeny

The closure of the Iapetus Ocean and the subsequent Scandian Phase of the Caledonian Orogeny (Figure 3.2), lead to nappe formation and transposition of the Smøla SHB rocks (included within the 'Støren Nappe') towards the SE on average and above the allochthonous continental Neoproterozoic Baltoscandian nappes (Lower to Middle Allochthon after Roberts and Gee (1985)), and additionally over the underlying autochthonous to parautochthonous Palaeo to Mesoproterozoic Baltican crystalline basement of the Western Gneiss Region (WGR) (Corfu et al., 2014; Tucker et al., 2004). Accommodating the orogenic-related crustal shortening, major low-angle basal detachments formed separating the underlying Baltican basement and the overlying allochthonous nappes (Fossen, 1992) (Figure 5.1c). Likewise, in places within the overlying allochthonous thrust nappe wedge, NE-SW trending east-verging folds (locally recumbent to upright) developed, with cross-cutting shallowly to moderately-dipping thrusts and imbrications (commonly dipping W to NW towards the Caledonian orogenic hinterland) (Robinson et al., 2014; Tucker et al., 2004).

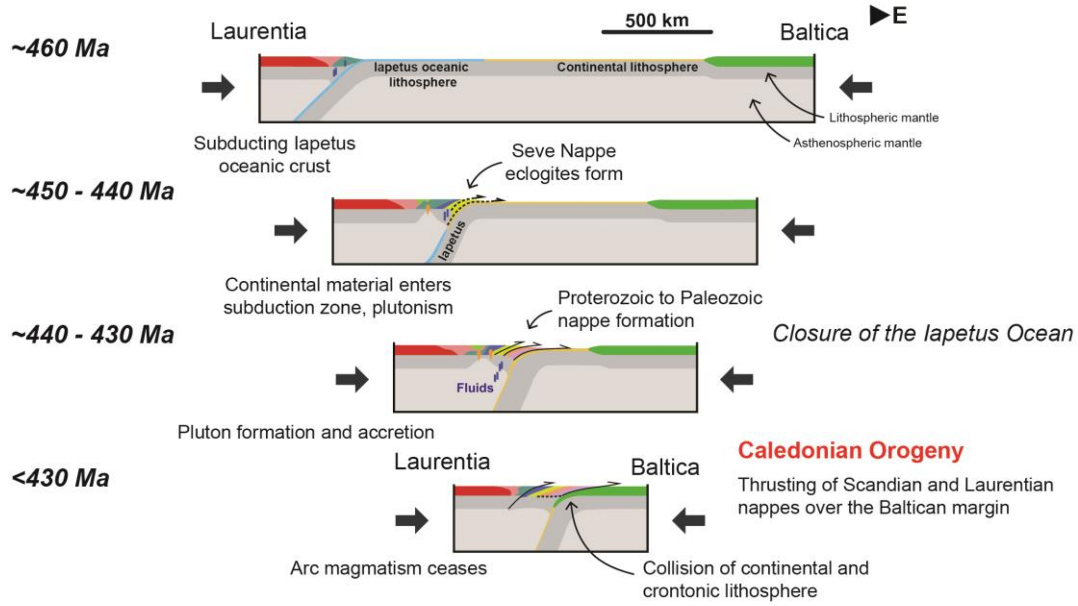

Figure 3.2. Conceptual ~E-W continent-scale cross-sections offering a summary of the main Caledonian orogenic phases during the collison of Baltica and Laurentia, and the eventual closure of the intervening Iapetus Ocean. Throughout these stages, the Iapetus oceanic crust was progressively subducted below Laurentia, with nappes forming and thrusting over the Baltican margin. Modified from Jakob et al. (2022).

3.2.2 Break-up and rifting and passive margin evolution

During the late stages of the Caledonian Orogeny (post peak-Scandian Phase; ~425 Ma) the Central Norwegian Caledonides experienced orogenic collapse and tectonic inversion (Fossen et al., 2017) (Figure 3.3), leading to very significant crustal extension during the Devonian (405 – 390 Ma) and pervasive reactivation of earlier, favourably oriented thrusts and structures (Fossen, 2010a; Fossen et al., 2017). Moreover, new crustal-scale brittle extensional shear zones developed such as the NE-SW striking, steeply NW dipping Møre-Trøndelag Fault Complex (MTFC on Figure 3.5), and the more shallowly-dipping Høybakken Detachement (HD) to the NE of Smøla (Olsen et al., 2007; Osmundsen et al., 2006; Watts et al., 2023). The late-Caledonian extensional phase resulted in the SHB rocks of Smøla being translated approximately westward, with both strike-slip and down-faulting across the MTFC (Redfield et al., 2004; Watts et al., 2023). During the later parts of this episode, extensional (possible pull-apart) basins formed associated with the brittle extensional shear zones, such as the Edøyfjorden Basin proximal to Smøla (Figure 3.5; associated with the MTFC) and the Bjugn–Ørlandet Basin (associated with the HD) to the NE of Smøla (Bøe et al., 1989; Bøe and Bjerkli, 1989; Fossen et al., 2017; Osmundsen et al., 2006).

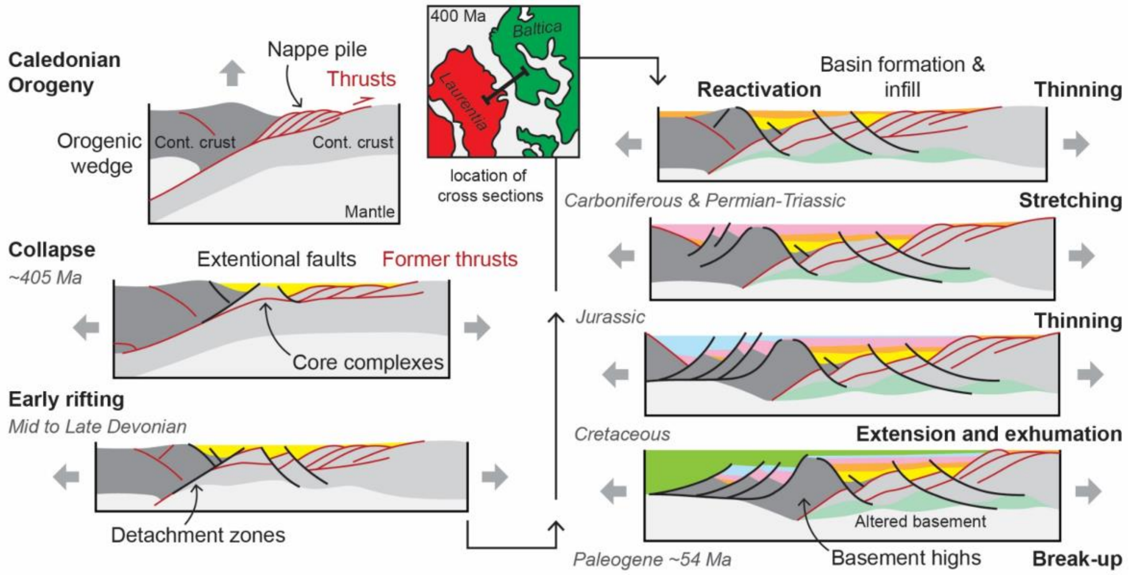

Figure 3.3. Representative cross-sections illustrating the key stages in the post-Caledonian rifting and eventual break-up of Norway and Greenland. Approximate location of the cross-section is indicated on the insert of the Laurentia and Baltica configuration at ~400 Ma. Older thrust faults are indicated with red lines, with later extensional faults illustrated with black lines. Modified from Peron-Pinvidic and Osmundsen (2020).

The continuation of post-Caledonian crustal extension and rifting from the Late Devonian to the Late Cretaceous/Early Paleogene (Figure 3.3) eventually led to the break-up of the Greenland and Eurasia plates at ~54 Ma, and the subsequent formation of the North Atlantic (Bunkholt et al., 2022; Peron-Pinvidic and Osmundsen, 2018). Throughout this time, multiple phases of stretching and rifting episodes occurred, most notably during the Permian-Early Triassic, Mid Jurassic-Early Cretaceous, Late Cretaceous-Palaeocene, and early seafloor spreading (Ægir Ridge) during the Palaeocene-Eocene (Faleide et al., 2008; Mosar et al., 2002; Peron-Pinvidic and Osmundsen, 2018). These events produced discrete generations of basins (such as the Froan, Vøring, and Møre Basins) along the newly-forming Norwegian shelf, which progressively infilled with synrift sediments reflecting the time of rifting/basin growth (Figure 3.3) (Faleide et al., 2008; Zastrozhnov et al., 2020). In places, structural highs of Caledonian-aged and underlying Baltica crystalline basement, such as the Frøya High (located to the NW of Smøla), formed between these basins through rift-related exhumation (Muñoz-Barrera et al., 2020). Bounding the structural highs and the different basins, are crustal-scale extensional faults, with smaller-scale extensional faults also present within the basins (Figure 3.3) (Mosar et al., 2002; Skilbrei et al., 2002). Overall, the protracted rifting and hyper-extension of the Norwegian continental margin resulted in a highly attenuated and structurally complex terrane offshore, reactivating and overprinting the existing inherited Caledonian deformation features (Mosar et al., 2002; Zastrozhnov et al., 2020).

3.2.3 Møre-Trondelag Fault complex

To the S and SE of Smøla (and bounding the Devonian Bjugn–Ørlandet Basin), the NE-SW striking MTFC is the most prominent large-scale structural feature proximal to the island (Figure 3.5). The structure, with a width of 10 to 50 km, extends lineally for >600 km from Central Trøndelag into the northern part of the North Sea, exerting a significant geometric control on both the Norwegian coastline and the Møre Basin offshore (Watts et al., 2023). The MTFC branches into two sub-parallel strands, the Hitra–Snåsa Fault (HSF) to the NW (the most proximal to Smøla), and the Verran Fault (VF) to the SE (Olsen et al., 2007; Watts, 2001; Watts et al., 2023). From both seismic surveys in the Edøyfjorden Basin (to the S of Smøla; Figure 3.5) and onshore exposures on the Fosen Peninsula to the ENE of Smøla, the MTFC dips steeply at approximately 60° to 71° towards the NW (Bøe and Bjerkli, 1989; Watts et al., 2023). Both brittle and ductile fault rocks characterise the HSF fault with early well-developed mylonites, crosscut by cataclasites, pseudotachylites, breccias, gouges, and wide damage zones defined by fracture and vein arrays (Watts, 2001; Watts et al., 2023). Both the cataclasites and veins have composite and cross-cutting infill minerals, including epidote, quartz, zeolite, prehnite, and calcite, indicating significant fluid migration through the MTFC during multiple tectonic episodes (Osmundsen et al., 2006; Watts, 2001; Watts et al., 2023).

The kinematic evolution of the MTFC is polyphasic and complex, with numerous previous studies providing different kinematic and tectonic solutions over time (e.g., Grønlie and Roberts, 1989; Seranne, 1992; Watts, 2001; Redfield et al., 2004; Tartaglia et al., 2022; Watts et al., 2023). Overall, the MTFC is believed to have experienced at least five major tectonic episodes, of which any/all of these events may have potentially affected Smøla: I) initial ductile sinistral strike-slip movement during the Devonian, II) brittle sinistral transtension during the Carboniferous-Permian, III) brittle normal fault movement on the VF during the Permian-Triassic, IV) possible dextral strike-slip on the VF during the Jurassic-Cretaceous, and V) possible dip-slip displacement on the VF during the Cenozoic (Bøe and Bjerkli, 1989; Sherlock et al., 2004; Watts et al., 2023). These episodes suggest that, from Permian times, most of the fault activity shifted onto the VF further away from Smøla (Watts et al., 2023), even though different apatite fission track-based cooling histories into the Jurassic-Cretaceous from Smøla, over both the HSF and VF fault strands and into the WGR, suggest a more intricate history (Redfield et al., 2004).

3.2.4 Regional (paleo-) stress field evolution

The regional tectonic (paleo-) stress field history for the mid-Norwegian passive margin, encompassing Smøla island (herein called mid-Norway), has been documented by Tartaglia et al. (2023). In SW Norway, at Bømlo island, Scheiber and Viola (2018) also provided constraints on the regional stress field history applicable to that area, which we will include as a comparison. Both studies used a multiscalar approach, integrating lineament mapping, outcrop mapping, structural and kinematic analyses, and K-Ar geochronology to constrain stress fields (Scheiber and Viola, 2018; Tartaglia et al., 2023). Additionally, as the majority of these paleostress field estimates typically possess at least one approximately subvertical compressive stress axis, I assume near-Andersonian stress conditions (Anderson, 1951) and simplify their principal compressive stresses ($\sigma_1>\sigma_2>\sigma_3$) into SH_{max} (σ_1 or σ_2) and SH_{min} (σ_3 or σ_2) for ease of comparison in the summary below:

I. During the Scandian phase of the Caledonian Orogeny (~435 Ma) SH_{max} was oriented NW-SE to WNW-ESE, with compressional and transpressional faulting regimes both affecting mid-Norway and SW Norway (Scheiber and Viola, 2018; Tartaglia et al., 2023).

II. In the Devonian, the SH_{max} orientation for SW Norway, was NE-SW, with NW-SE oriented transtension (SH_{min}) (Scheiber and Viola, 2018). For mid-Norway, no Late Devonian-Early Carboniferous stress field is available, but the SH_{max} orientation may have shifted ~N-S, with a contractional to transpressional tectonic regime (possibly related to Early Devonian transtensional faulting on the MTFC) (Tartaglia et al., 2023).

III. In the Permian-Triassic, the tectonic regime became extensional, with SH_{min} oriented ENE-WSW (Scheiber and Viola, 2018). As with the Devonian, no stress field solution exists for mid-Norway, but there is some indication that rifting may have initiated in this region during this time (Tartaglia et al., 2023).

IV. From the Triassic to Jurassic, SH_{min} in Mid-Norway was oriented E-W with crustal stretching (Tartaglia et al., 2023). In SW-Norway Jurassic fault reactivation indicated SH_{min} orientations WNW-ESE to NW-SE (Scheiber and Viola, 2018).

V. In the Cretaceous, extension in mid-Norway indicates SH_{min} orientations from NW-SE to WNW-ESE (Tartaglia et al., 2023), with this SH_{min} orientation matching that in SW Norway (Scheiber and Viola, 2018). The extensional stress field, however, contrasts with the contemporary stress field orientation for mid-Norway, which had inverted to a compressional WNW-ESE to NW-SE oriented SH_{max} (Roberts and Myrvang, 2004).

3.2.5 Characterisation of basement plays offshore Norway

While basement structural highs (horst-like features formed during crustal extension) have generally been understudied in the past, a number of such intrabasinal features offshore Norway have undergone some exploration and characterisation (Trice et al., 2022). Here, I will briefly discuss two of such basement structural highs (Figure 3.4), the Frøya and Utsira highs, in terms of their structural geology, lithological composition, and exploration history with relevant results.

The Frøya High (Figure 3.4a) is located in the mid-Norwegian passive margin, within the Norwegian Shelf (Trøndelag Platform), and is bound to the west by the Rås Basin (Møre Basin) and the Halten Terrace (both Late Jurassic to Early Cretaceous rifting related), and to the east by the Froan Basin (Permian to Early Triassic rifting related) (Faleide et al., 2015). To the NW, the basement high is flanked by a major NE-SW trending and NW-dipping extensional fault structure, known as the Klakk Fault Complex (Bunkholt et al., 2022; Muñoz-Barrera et al., 2020). This fault complex exhibits, in places, fault slip displacements of up to 20 to 35 km, with the Frøya High forming the footwall of this fault zone (Bunkholt et al., 2022; Muñoz-Barrera et al., 2020). The high itself is comprised by basement granite, diorite (dated by U-Pb to 447 ± 4 Ma), and metamorphic units (Slagstad et al., 2011; Trice et al., 2022).

Geophysical survey results (airborne magnetics and seismic reflection surveys) and mud loss during drilling into the high indicate that the Frøya High may be highly fractured at its top (Trice et al., 2022). However, the extent of weathering of the feature remains uncertain (Trice et al., 2022). Considering that the region experienced significant weathering (and saprolitisation) during the Triassic (Fredin et al., 2017), it is likely that the upper carapace of the basement high is indeed weathered.

Geological characterisation work on Frøya High has included geophysical investigations (2D and 3D seismic reflection surveys) and drill testing (Bunkholt et al., 2022; Muñoz-Barrera et al., 2020; Skilbrei et al., 2002; Trice et al., 2022). Most of this work has been for hydrocarbon exploration purposes, with oil identified (a 'oil show') in a drill hole from the "Skalman prospect" (Trice et al., 2022). As the Frøya High is considered a Type I or Type II fractured reservoir, the source of the oil is likely migrating hydrocarbons from the Jurassic Kimmeridge Clay in the North Sea, or Cretaceous sedimentary units from the Møre Basin (Rås Basin) from the west (Trice et al., 2022) via interconnected fractures.

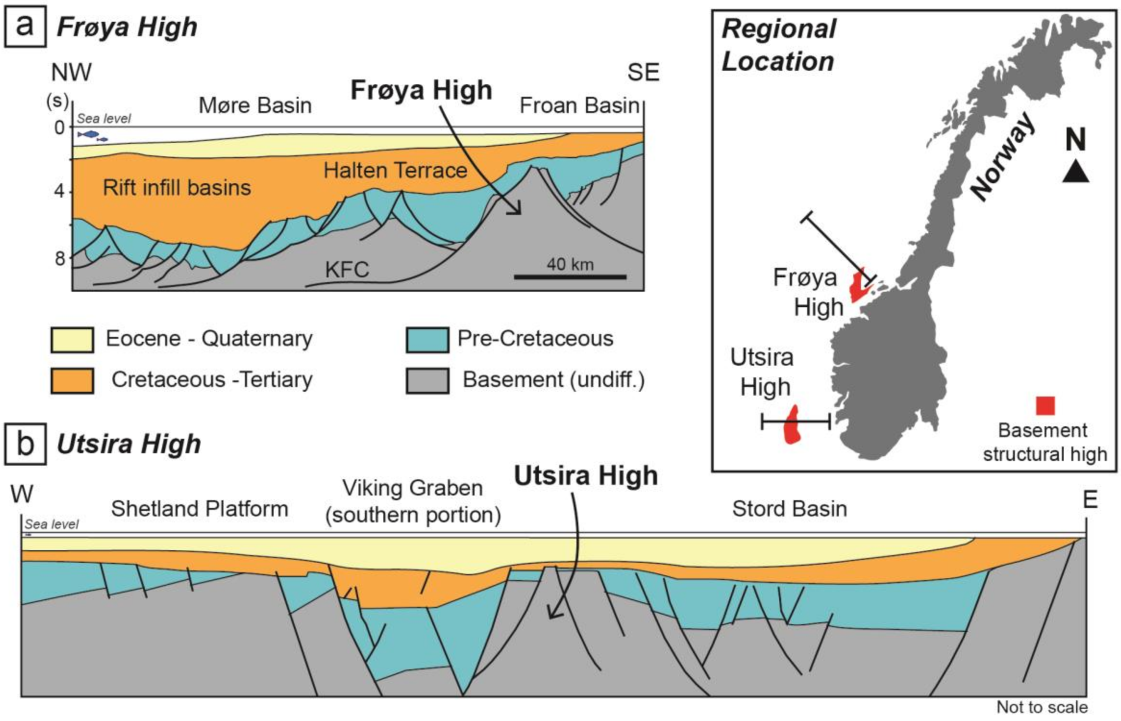

Figure 3.4. Representative cross-sections through two basement structural highs, the Froya and Utsira High offshore Norway. "KFC" stands for Klakk Fault Complex. Modified from Trice et al. (2022), Zastrozhnov et al. (2020), and Riber et al. (2015).

The Utsira High (Figure 3.4b), on the other hand, is located offshore SW Norway in the Norwegian North Sea. The basement high is bound to the west by the Gudrun Terrace and the Permo-Triassic to Jurassic-aged N-S trending Viking Graben (southern portion), to the east by the Stord Basin (formed from the Devonian to Jurassic), and to the south by the Ling depression (Riber et al., 2015).

From several drill holes, the basement rocks on the Utsira High have been identified as consisting of leucogabbro, volcanics, and granite, which have crystallisation ages between 421 ± 3 Ma and 463 ± 6 Ma (Slagstad et al., 2011). These basement rocks are typically highly fractured and extensively weathered (Riber et al., 2016). The weathering dates back to when the basement rocks of the Utsira High were subaerially exposed during the Late Triassic, with considerable saprolite subsequently developing (Fredin et al., 2017; Riber et al., 2015, 2016; Trice et al., 2022). The high was later covered by a combination of Jurassic to Cretaceous sandstone, shale, and chalk deposits, which form a regional seal (Riber et al., 2016; Trice et al., 2022).

Compared to the Frøya High, prospecting work on and around the Utsira High (ongoing since the 1960's) has identified numerous oil and gas shows, and discovered considerable petroleum finds (Riber et al., 2015). This includes the significant 7000 barrel of oil per day (bopd) yield from the Rolvsnes well (horizontal appraisal well) (Trice et al., 2022). Like the Frøya High, the Utsira High is considered a Type I or Type II fractured reservoir, with migration of hydrocarbons likely from the Late Jurassic Kimmeridge Clay source rocks in the Viking Graben (Trice et al., 2022) also through fracture systems and potentially weathered basement volumes.

3.3 Local Geology

On a local scale, Smøla island is comprised of several Caledonian-aged bedrock types (Figure 3.5) including gabbro (norite-hyperite; predominately located on the western-portion of Smøla), granodiorite, diorite (the most common lithology), tonalite, quartz-feldspar and amphibolite-biotite gneiss, alkali granite, quartz monzonite to monzo-granite, Ordovician limestone and volcanics (andesitic to rhyolitic; located in a faulted block on the SE-portion of Smøla), and late cross-cutting dykes of felsic to mafic compositions (Bruton and Bockelie, 1979; Fediuk and Siedlecki, 1977; Gautneb, 1988; Gautneb and Roberts, 1989; Roberts, 1980).

Although the different bedrock types crop out in relatively homogenous blocks over the island, between and within these bedrock types, there exists complex intrusive and cross-cutting relationships in places, including varying intrusive to faulted contacts, internal igneous layering, and lithological inclusions and enclaves (Gautneb and Roberts, 1989), consequently, the relative genetic formation of these different units is poorly resolved. However, in addition to the 445.7 ± 3.8 Ma (U-Pb) age of a dated granodiorite on Smøla (Slagstad et al., 2011), a granitic dyke (granophyre) from another part of island, was dated to 428 ± 10 Ma (Rb/Sr) (Gautneb, 1988), providing at least an Ordovician-Silurian age envelope for the plutonic rocks on Smøla. To the S and SE of Smøla (Edøyfjorden Basin) on smaller islands (including Edøya and Kuli), the Caledonian-aged bedrock is unconformably overlain by Devonian-aged sedimentary units (late Silurian - Middle Devonian) of the Smøla Group (Bøe et al., 1989; Fediuk and Siedlecki, 1977).

These rocks include siliciclastic deposits of red-oxidised polymictic conglomerate, siltstone, and sandstone (Bøe et al., 1989), and are associated with Devonian extensional basins along the MTFC (Bøe and Bjerkli, 1989).

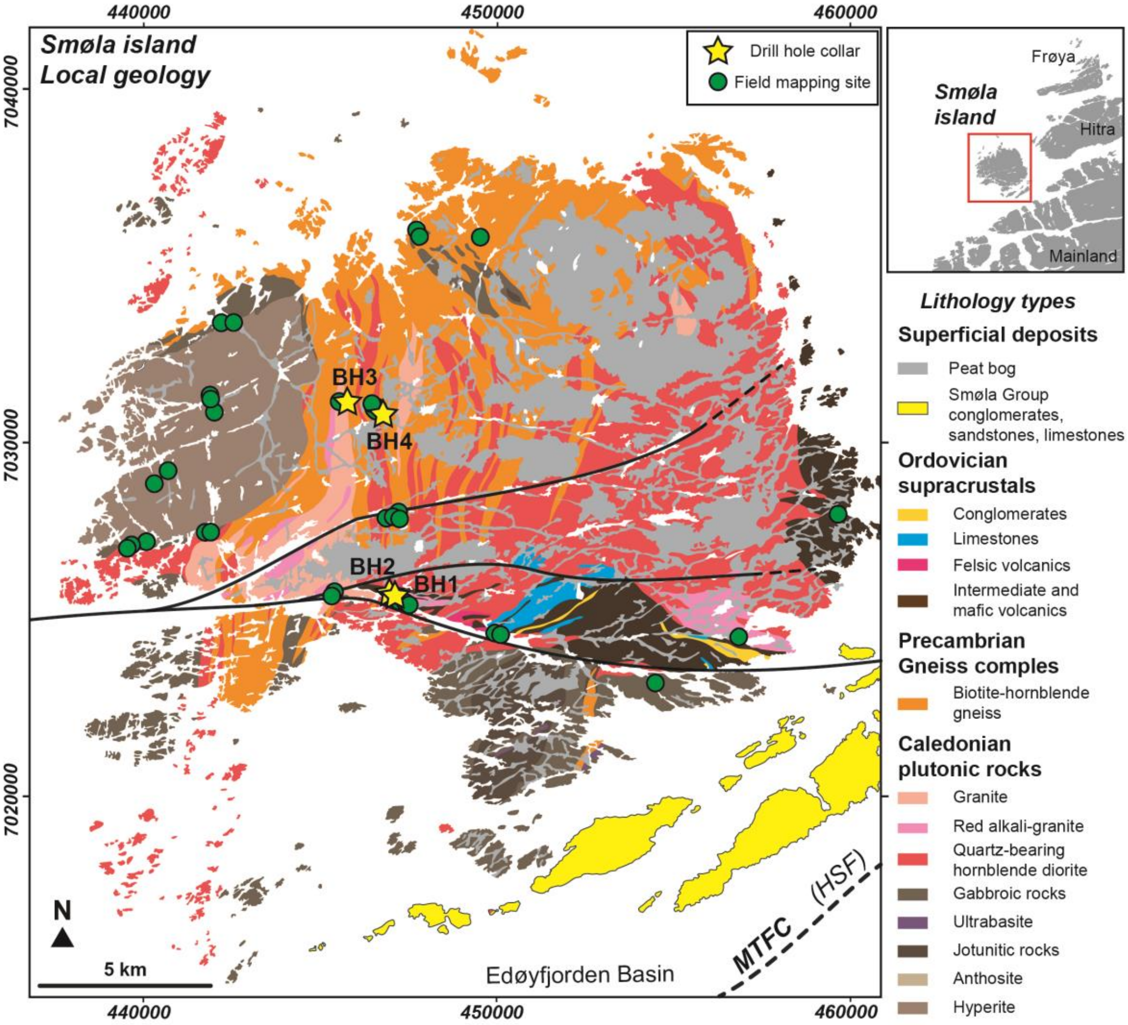

Figure 3.5. Local geology map of Smøla island with field mapping sites and drill hole locations. Modified from Fediuk and Siedlecki, (1977). "MTFC" stands for Møre-Trøndelag Fault Complex and "HSF" stands for Hitra–Snåsa Fault. Interpretive fault traces also shown as solid black lines.

Overall, the different bedrock units (and Devonian sedimentary rocks) on Smøla exhibit limited Caledonian regional metamorphism (on average sub-greenschist facies conditions), and preserve evidence of only weak ductile deformation (Tucker et al., 2004). Deformation features are few tight N-S trending folds in specific gneissic units, and open to tight E-W, NE-SW, and rare N-S trending folds in other plutonic rocks (Fediuk and Siedlecki, 1977). The weak ductile deformation and metamorphism of Smøla's plutonic rocks implies relatively low strain transport and transposition onto a high nappe level during Caledonian nappe emplacement, followed by a relatively low temperature translation and down-faulting over the MTFC, during late to post-Caledonian extension (Tucker et al., 2004). The ductile deformation features that are, however, preserved in the Devonian sedimentary units, including NE-SW trending asymmetrical to upright folds, axial-planner cleavage and associated phengite growth, do indicate that some possible shortening occurred during the Late-Caledonian orogenic collapse-related extension (Bøe et al., 1989; Fossen, 2010a). After this episode, the post-Caledonian structural evolution of Smøla is poorly understood, however apatite fission track (AFT) samples collected over Smøla show Late Triassic exhumation/cooling ages of ~200 Ma (Redfield et al., 2004), which suggests large-scale tectonic processes were active over Smøla after the Devonian.

Chapter 4: Methodology

4.1 Introduction

This study has utilised a diverse range of multiscalar data types and associated techniques and methodologies. These data types and methods include airborne geophysical survey analysis, field mapping, drill hole logging, petrographic and microstructural analyses, K-Ar geochronology, network topology analysis, and discrete fracture network modelling. Given the multiscalar nature of the data, this chapter presents the methodologies in order of resolution scale, starting with the coarsest resolution-related methods moving to the finest resolution-related activities, before outlining the dating and modelling methodologies.

Of particular note for the reader, portions of the methodology details included here relating to Chapters 5 and 7 were originally presented as Supplementary material in a published journal article and a manuscript currently under review, with the current locations:

- https://doi.org/10.5194/se-15-589-2024-supplement (Hodge et al., 2024b)
- https://assets-eu.researchsquare.com/files/rs-4844693/v1/2b2a1135a9e03D$_2$936863c31.pdf (Hodge et al., 2024a, subject to change depending on the outcome of the review and publishing process).

These Supplementary materials have been adapted and integrated into this chapter, with Chapter 5 methodologies outlined first, followed by those for Chapter 7.

4.2 Lineament mapping

The geophysical data used in this study were supplied by the Norwegian Geological Survey (NGU) and stems from three different airborne magnetic surveys (in 2011, 2012, and 2013) flown with line spacings between 250 m and 1000 m (60 m-200 m flight altitude), with the flight lines being oriented NW-SE (315°/135°) or N-S (0°/180°) depending on the survey flown. The data from the different surveys were subsequently merged and levelled to produce single geophysical grids over the Smøla region. Prior to the lineament mapping and structural interpretation, the merged geophysical data were processed into different transformations and filter products (Nasuti et al., 2015). The geophysical products used in this study include the total magnetic intensity (TMI) product, the reduce to pole (RTP) transformation, and derivative filter products, which include first vertical derivative (1VD), analytical signal (AS), total horizontal derivative (THD), and the tilt derivative (TDR). All the products are sun-shaded from the NE (045°). A full description of the geophysical data processing and merging methodology is available in Nasuti et al. (2015). The orthophoto imagery and DTMs used were also provided by the NGU and the DTMs are greyscale sun-shaded imagery generated from high-resolution LiDAR surveys (1 m/pixel) previously flown over the mid-Norwegian region. The DTMs are sun-shaded from the NW (315°).

The lineament mapping following techniques from White (2014), Scheiber et al. (2015), and Scheiber & Viola (2018) within a geographic information systems (GIS) software platform. The magnetic filters and transformations used in the mapping were based on scale. At the coarser resolutions, the TMI and RTP products were used, and at finer-resolutions the 1VD, THD, and TDR products were preferred. This preference is due to how long wavelength magnetic signal variability is shown in the TMI and RTP products while short-wavelength magnetic signal variability is enhanced and shown in the 1VD and other filter products. The lineament mapping was undertaken manually at variable scales, identifying magnetic fabric truncations, offsets, linear features, and magnetic domain contacts that exhibit lateral continuity. Possible intrusive contacts and metamorphic foliation traces were ignored for the lineament mapping where no visible structural offset could be interpreted. Zones of evident negative magnetic signal (possible remnant magnetism), suggesting depletion of magnetic minerals owing to major fluid-flow (e.g., Grant, 1985), were also used to identify higher order lineaments (which may correspond to major fault structures). As a continual process during the lineament mapping, topographical features on the DTM (if over onshore areas of Smøla) were used to identify surface traces of the magnetic lineaments, and thus the exact placement and extent of the lineament polyline.

4.3 Field studies and mapping

The field mapping and outcrop studies were undertaken in the Norwegian summer of 2022, and involved work at 65 outcrop locations across Smøla island (Figure 3.5), with systematic structural data collection, outcrop sketching, and petrographic and geochronological sampling completed. Before the fieldwork commenced, desktop planning was undertaken using Google Earth^{TM} imagery, digital terrain model (DTM), radiometric, and airborne geophysical data. A selection of 67 potential sites were identified proximal to obvious structural features or major geophysical/DTM lineaments (fieldwork only made use of some of these sites, with many new sites identified while in the field). Initially, the surrounding areas proximal to the drill sites were focussed on (BH1, BH2, and BH3, BH4), with other key sites visited and studied along roads and coastlines (outcrop exposures through most flat-lying areas of Smøla is poor owing to glacial erosion, weathering, and glacial till cover).

Orientation data of representative deformation features were collected using a Breithaupt 3031 GEKOM N Pro Basic Stratum Compass using standard geological fieldwork methods. In addition to using a typical geological field book, a rugged tablet with ArcGIS Field Maps© software was used for data capture and storage. Deformation features studied included tensile to shear fracture, veins, slickenside surfaces, foliated mélange, ductile shear zones, brittle fault gouge, cataclasites, and breccias. A similar approach to identifying different structural 'sets' of deformation features was taken as for the drill core logging. These structural 'sets' were based on different mineral coating/infill, orientation trends, and cross-cutting relationships. Descriptions of fault rock and shear zones were completed to identify fault gouge zones for K-Ar sampling, and to produce a structural framework for understanding the dating results later. Fault gouge zones were fully described in the field, with quantitative information recorded regarding the matrix to fragment %, size of fragments, and dominant mineral phases present within the gouge.

4.4 Drill hole logging

Two phases of drill logging were completed at the NGU headquarters in Trondheim, Norway between the 11th of January to the 4th of February 2022, and from the 2nd of May to the 21st of May 2022. The drill logging work was completed on four diamond drill holes, which were previously drilled by GEO DRILLING AS on Smøla island (Figure 3.5), between the 4th of October 2019 and the 10th of December 2019. The drill holes' coordinates and orientation parameters are shown in Table 4.1:

Table 4.1. Drill parameters for the Smøla drill holes (collar coordinates in WGS 1984 UTM 32N)

Drillhole ID	X (UTM)	Y (UTM)	Z (m)	Azimuth (°)	Inclination (°)	Hole depth (m)
BH1	447080	7025814	6.37	334	57	99.35
BH2	447008	7025835	7.22	304	60	111.1
BH3	445820	7031251	27.15	030	59	71
BH4	446841	7030851	26.88	284	59	108
					Total	**389.45**

Overall, the four drill holes possess approximately 75% of the total drill hole lengths as oriented drill core, with the drill cores having an 'ori-line' (commonly a black or red coloured line drawn by the drillers along the drill core) indicating the bottom of the recovered drill core pieces. Additionally, the four drill holes were orientated by down-hole surveys (collected using a DeviCore BBT continuous orientation tool) which provided 5 cm down-hole intervals of drill direction (azimuth) and inclination of the hole from the drill collar to the end of hole (EOH). Along with the orientation surveys, acoustic and optical downhole televiewer surveys are also collected for the drill hole lengths.

The oriented drill cores permitted structural orientation measurements of various intersected deformation features within the 'fresh' rock volume below the weathered carapace. These features included shear veins/fractures, tensile veins/fractures, hybrid veins, shear bands, lithological contacts, slickensides, foliation, breccias, gouges, and cataclasites. Typically, only representative deformation features were measured for wider intervals (not every feature was measured, with on average of only one to two features measured per metre), to record the average orientation/characteristic trend of deformation features only. The orientation data were collected using the α, β, γ angle method as described by Holcombe (2013) to orient both planar and lineated features in drill core relative to the 'ori-line'/bottom of the core pieces. To measure these different angles, two different instruments were used: for the α and β angles (describing a plane cutting through the drill core, e.g., a vein) a kenometer was used, whilst for the γ angle (describing a line within a plane cutting through the drill core, for example, a slickenline on a shear surface) a rotating protractor was used. The α, β, and γ angle data were then later converted to dip, dip direction (for planar features) and plunge, trend direction (for linear features) using two different software products, ioGAS (Imdex Limited, 2022) and GeoCalculator (Holcombe, 2014).

Other quantitative data collected included aperture and void widths of the deformation features (mm width), average sizes of included fragments and % estimations of matrix to fragments within fault rocks (e.g., fault breccias). Other qualitative data collected related to the type of feature measured included deformation style, level of strain, fracture infill/coating mineralogy, fracture morphology, genetic relationships/relative timing (as well as interpretive deformation 'set' allocation), slickenside characteristics, fault rock descriptions, and whether the different features are either open or closed/'sealed'. Alteration and lithology logging data were also collected through the drill holes. All data were compiled throughout the logging process within Excel spreadsheet format, with the down-hole depths (mid-point depths of discrete features, and from-to depths for intervals) recorded for each deformation feature, fault rock intersection, and lithology and alteration intervals.

4.5 Optical petrographic and microstructural analyses

A total of 74 polished petrographic thin sections were produced from drill cores (BH1, BH2, BH3, and BH4) during the core logging period at the NGU in Trondheim, and from outcrop samples collected on Smøla. Of these, 42 sections were assessed to be of sufficient quality, and included for further analysis. The remaining 32 were discarded due to several reasons, which included that, for example, many fault gouge samples, although previously impregnated with resin, did not return viable thin sections for optical petrographic study.

The petrographic and microstructural work was subsequently undertaken at the University of Bologna's Deformation, Fluids, and Tectonics (DFT) petrographic laboratory, using a Nikon Eclipse C*i* POL petrographic microscope using transmitted light. The analyses initially focussed on confirming the mineralogy assemblages of the host rock, followed by confirming the types of infill minerals of different deformation features, including vein infill and secondary mineralisation in gouge and breccia. The crystallisation textures, morphology, and genetic information (documenting cross-cutting or coeval mineralisation) were recorded for each sample. Finally, I undertook a detailed microstructural assessment of the deformation features present in the thin sections. The microstructural studies recorded the type and style of deformation, associated mineralisation, degree of deformation, and any relative age (genetic) information (including structural reworking and whether any deformation features cross-cut each other).

4.6 K-Ar geochronology

To add the temporal dimension to this study, K-Ar geochronology was undertaken in partnership with the NGU laboratory in Trondheim. This section will therefore summarise and outline the main activities and methods used during this phase of the study.

4.6.1 Sampling

Representative fault rock material, including gouge and breccia material, were collected from outcrop faults exposures, and fault intersections in drill core (Figure 4.1). The sample material was only collected from structures with orientation information (at least dip and dip direction), with sampling aiming to test as many different structures of different geometries as possible. Additionally, care was taken to sample as many varieties as possible of different mineral infill (vein infill, or secondary mineralisation in the gouge matrix). At least 200 – 300 g of friable material were collected using a scoop or gardening spade, which was cleaned between each sampling occasion to avoid any sample contamination. Seven samples were collected in total, with the list of K-Ar geochronology samples summarised in Table 5.2 and fully described in Appendix A.

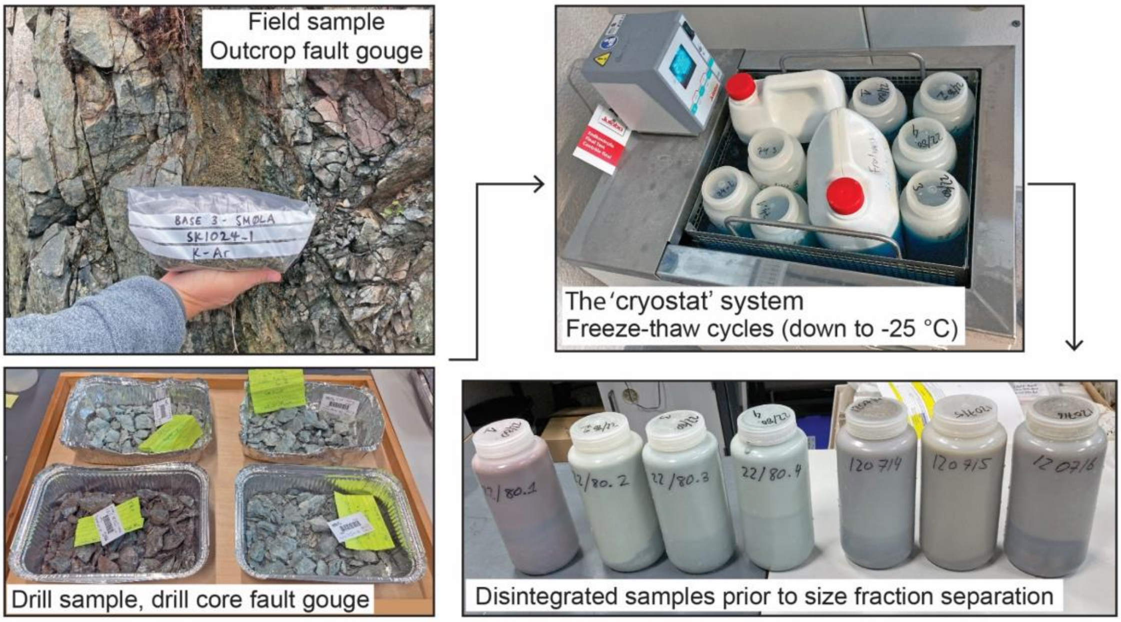

Figure 4.1. Sample collection of field and drill hole fault gouge samples for K-Ar geochronology. All collected samples, underwent repeated freeze-thaw cycles in a 'cryostat' system to gradually disintegrate them prior to further grain size seperation via centrifugation and Stoke's law settling.

4.6.2 Analysis

The seven collected gouge and breccia samples were processed at the dedicated K-Ar geochronology NGU laboratory in Trondheim. Initially, all the samples were gradually disintegrated through repeated freeze-thaw cycles in a 'cryostat' system (Figure 4.1). This process avoids any mechanical grinding or comminution of the particle sizes and therefore prevents possible contamination of the finer size fractions by coarser fragmented potassic-bearing mineral phases. Following this, the samples underwent separation into <0.1 µm, 0.1-0.4 µm, 0.4-2 µm size fractions using high-speed centrifugation and 2-6 µm, 6-10 µm size fraction separation in distilled water using Stoke's law. Each of these size fractions then underwent quantitative analysis for both potassium (K) and argon (Ar) using total digest ICP-OES for K, and a Isotopx NGX multi collector noble gas mass spectrometer system for Ar. A full description of the K-Ar analysis methodology is available in Viola et al. (2018).

Additionally, each size fraction underwent X-ray diffraction (XRD) analysis for mineral composition characterisation using a Bruker D8 Advance (Da Vinci System). Randomly oriented samples were prepared by side-loading and analysed with a Bruker D8 Advance X-ray diffractometer operating with a Cu X-ray tube (40 kV/40 mA) and Lynxeye XE detector. The XRD scan was performed from 3 to 75° 2q with a step size of 0.02° 2q, a measurement time of 0.5 seconds per step, and rotation speed of 30 per minute. Fixed divergence had an opening of 0.6 mm and primary and secondary soller slits were 2.5°.

A knife edge was used to reduce scatter radiation. Mineral identification was carried out with the automatic and/or manual peak search-match function of Bruker's Diffrac.EVA V6.1 software using both Crystallographic Open Database (COD) as well as the PDF 4 Minerals database from the International Centre for Diffraction Data (ICDD). For further clay minerals study, oriented mounts of fractions 2-6 μm were prepared by letting 1 ml of sample suspension dry out on a glass slide. These slides were measured from 2 to 40° 2q at room temperature, after treatment with ethylene glycol for 24 hours, and after heating at 550°C for 1 hour.

Mineral quantification was performed on randomly prepared specimens using Rietveld modelling with TOPAS 5 software. Refined parameters included crystallite size, unit cell dimensions, sample displacement, preferred orientation as well as background coefficients. The lower detection limits are mineral-dependent and estimated to be 1-2 wt% with an approximate uncertainty for the Rietveld modelling (i.e., quantification) of at least 2-3 wt%.

4.7 FracMan modelling procedure

An important component of this Thesis involved discrete fracture network (DFN) modelling. The DFN modelling was undertaken in FracMan 8 (WSP UK Limited, 2024), using an academic licence supplied by WSP UK for Bologna University. This section will therefore outline the generation of the various input types, parameters, and data utilised in the DFN modelling. I will then also summarise and describe the different DFN modelling procedures and methodologies.

4.7.1 Trace maps and frequency vs fracture length distribution

To define deterministic 2D inputs to DFN modelling, surface lineament traces were picked at 1:500, 1:7 500, 1:25 000, and 1:100 000 scales over various regions of Smøla (Figure 4.2). This was done in addition to the lineament picking work previously detailed in this Chapter, using orthophoto imagery, digital terrain models (DTM) from Lidar surveys (1 m/px resolution), and aeromagnetic survey data provided by the Geological Survey of Norway (NGU). The picking process followed typical lineament mapping methodologies (Scheiber et al., 2015; White, 2014) within a geographic information system (GIS) software platform.

For the 1:100 000 scale geophysical imagery, lineament mapping was performed manually to identify magnetic fabric truncations, offsets, linear features, and magnetic domain contacts with lateral continuity. For the 1:7 500 and 1:25 000 trace mapping on the DTM imagery, linear topographical features and disruptions were used to place the traces. The 1:500 scale trace mapping on the orthophoto and DTM imagery involved manual tracing of visible fractures (based on true colour variations) on exposed rock surfaces, and topographical features. In total, 9554 interpreted fracture traces were mapped over the different scale maps. The fractures were then measured for length and azimuth within a GIS software platform. Subsequently, all these fractures were plotted using a rose diagram plotting application (Munro and Blenkinsop, 2012). Major azimuth trends (four sets) were then separated out of the total lineament traces and exported to determine the lineament trace length distributions for each azimuth trend.

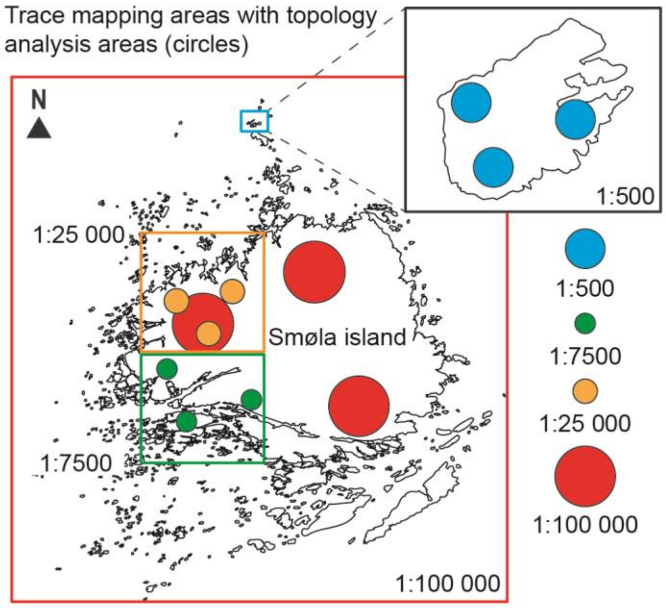

Figure 4.2. Location map of boundary areas used in the lineament trace mapping over Smøla, with representative circular scan areas used in topological analyses of deterministic lineament maps, coloured by mapping scale (1:500 to 1:100 000).

Importing these traces into FracMan (WSP UK Limited, 2024) and using the Plot Power Law Function, I could confirm whether the lineament trace length distributions fit power-law distributions (after removing possibly censored trance lengths below the cut-off length, with no upper cut-off length selected) (shown in Table B1, in Appendix B).

The size distributions are represented as cumulative distribution functions (CDF) $N_{\geq L} = (L/L_n)^{-\alpha}$, with N being the cumulative number of fractures of size ≥L, L the fracture length, Ln is largest fracture length, and α is the scaling exponent describing the fracture length distribution (Cladouhos and Marrett, 1996). This relationship is shown on the log-log plots of $N_{\geq L}$ versus L by linear regression lines, with negative slopes corresponding to -α, through the different cumulative distribution functions. All the mapped lineament trace size distributions are assumed to fit power-law distributions and therefore exhibit scale-independent fractal behaviour in terms of fracture patterns (e.g. Dichiarante et al., 2020). The entire set of lineament traces plotted by map scale yielded fracture lengths ranging from 0.03 m to 13641.66 m (Table B1), providing data coverage from the <metre-scale to the kilometre-scale.

This data coverage, the regression lines-derived α slope exponent, and the linear intensity (P_{10}) values (outlined below) from the drill hole televiewer data (captured at the centimetre-scale) allow us to extrapolate the size distribution down to below the seismic resolution scale (<10-30 m).

4.7.2 Time-constrained field and drill hole deterministic inputs

Field work, downhole televiewer data, and high-resolution logging of the four oriented diamond drill holes from Smøla led to the identification of five systematic fracture sets, outlined here in more detail. The downhole televiewer data provided by the NGU offered in-situ geometric information for drill-intersected structures. These data were sorted using the FracMan 'set identification' tool (WSP UK Limited, 2024), by pole to planes clusters. Mean fracture pole vector orientations were then assigned to each identified fracture set, incorporating Terzaghi corrected Kamb contouring (2σ intervals) for each drill hole (Table 4.2).

Table 4.2. Terzaghi correction parameters used for each drill hole (BH1 to BH4).

Drill ID	Azimuth	Inclination	Max. Corr. Factor
BH1	330	60	7
BH2	300	60	7
BH3	30	58	7
BH4	280	59	7

As each drill hole exhibited at least three distinct fracture set orientations, an overall twelve initial fracture sets were identified. Of these, five fracture sets were selected for the DFN modelling based on the visual similarity of their fracture orientations to the fractures observed in outcrops on Smøla. The four drill holes were also used to produce downhole linear fracture intensities (P_{10}) for each fracture set, defined as $P_{10} = N_L/L$, where N_L is the number of fractures and L is the unit length (Dershowitz, 1984). The P_{10} values were then converted to volumetric fracture intensity based on the Wang et al. (2005) C13 conversion method in FracMan ($P_{32}=C_{13}*P_{21}$), where P_{32} is defined as $P_{32} = \Sigma A_i/V$, where ΣA_i is the sum of the fracture surface areas, and V is the unit rock volume (Dershowitz, 1984; Sanderson and Nixon, 2015). The drill hole televiewer data are included online at https://data.mendeley.com/datasets/ctpphnptc5/2, in the table labelled "Drillholes_- Televiewer_Data".

To confirm the P_{32} values derived from the drill holes, the areal intensity (P_{21}) values for each trace set (NE-SW, E-W, N-S, and NW-SE) mapped on the 1:500 trace map was also converted to P_{32} values for comparison (Table B2, in Appendix B), using the $P_{32}=C_{23}*P_{21}$ relationship. P_{21} is defined as $P_{21} = \Sigma L/A$, where ΣL is the sum of the fracture lengths, and A is the surface unit area (Dershowitz, 1984; Sanderson and Nixon, 2015). The 'shallow' fracture set attributed to D_2 were also included (assumed to have the same P_{21} value as the E-W fracture set). Initially, an isotropic fracture orientation was assumed with a C_{23} conversion factor of 1.23 ($4/\pi$) using the method of Dershowitz (1984). Then, using the orientations derived from the drill holes and Fisher distribution concentration (κ) parameters, I converted the P_{21} values to P_{32} using the $1/C_{23}$ factor table (Wang et al., 2005).

The P_{32} values derived from the drill holes were then used to infer the target volumetric intensities for the DFN modelling. For each generation of DFN model, the target P_{32} value of the newly forming fracture set, dated to the relevant deformation episode, was adjusted down to between 0.4 and 0.6 (typically between 30 to 80 % of the associated deterministic P_{32} value). This adjustment, primarily for computational efficiency reasons, was necessary due to the modelling volume size (ensuring reasonable model processing runtimes). Interpretive assumptions based on fracture set exposure in outcrops and drill core guided the amount of P_{32} adjustment. These adjusted P_{32} values fall within the 1:500 trace map derived P_{32} values (converted from P_{21}), and the drill hole derived values (converted from P_{10}; Table B2). Inherited fracture sets (representing older fracture events) present in the DFN models had their P_{32} values additionally adjusted to lower values (typically by 50 % of the initial target P_{32} value used for that specific fracture set) to further improve computational efficiency and, more importantly, simulate selective reactivation of the inherited fractures (assuming not all inherited fractures were open or active during later deformation episodes). The target P_{32} values used for each model are provided in the Table B3 in Appendix B.

4.7.2.1 Aperture input

Fracture apertures were defined for the various fracture sets based on hundreds of direct 'paleo-aperture' (feature true thickness) field measurements from the drill holes (mean mineralised vein and fault true thickness values for each fracture set are outlined in detail in Appendix B, and illustrated in Figure B1). The 'paleo-aperture' values varied by fracture set, with D_1 possessing the smallest average value and D_5 the largest average value. These 'paleo-aperture' values are assumed to represent the void thickness of the fractures prior to their mineral infill (Leckenby et al., 2005), but as fractures may open repeatedly (Ramsay, 1980), I use them here for scaling purposes only. Accordingly, beginning with the assumed largest aperture of 0.1 mm for the final fracture set (corresponding to the largest 'paleo-aperture' value), the fracture set apertures were scaled relative to the 'paleo-aperture' values, with a progressive decrease in aperture towards the oldest fracture set (corresponding to the smallest 'paleo-aperture' value). If supposing a cubic flow law-type fluid flow behaviour, the later fractures will therefore have significantly more influence on permeability than the earlier fractures with smaller aperture values (Gale, 1982; Leckenby et al., 2005).

For the 'paleo-apertures', true thickness measurements of 665 fractures and veins from the four drill holes were sorted into the D_1 to D_5 deformation episodes by mineral infill types. The resulting mean averages for each deformation episode are plotted and indicated on Figure B1 in Appendix B. By using these paleo-aperture values, relative and scaled to the largest assumed actual aperture of 0.1 mm, the scaled apertures are 0.03 mm for D_1, 0.04 for D_2, 0.09 for D_3, and 0.1 for D_{4+5}. A scale factor of 0.009 (e.g. 11 mm (paleo-aperture value for D_{4+5}) × 0.009 = 0.1 mm) has therefore been used. For this modelling, the scaled aperture value for each fracture set was set as constant, with no variation with fracture length size (equivalent radius). This scaling follows the overall trend of increasing paleo-aperture through time (and actual aperture at the time of fracture formation), with particularly large paleo-aperture values for the quartz-carbonate (+/- zeolite) (D_{4+5}) associated veins. As a final point, the final aperture values have not been adjusted or corrected for roughness factor and for modelling simplicity reasons, are also assumed to be planar features. The dataset of 665 fracture and vein (true) thickness measurements are available online at https://data.mendeley.com/datasets/ctpphnptc5/2, in the Excel spreadsheet labelled "Fracture_Vein_Paleoaperture _Measurements".

4.7.2.2 Permeability input

Permeability values, used in the DFN modelling for the individual fracture sets, are based on granitic fault zone permeabilities (K) compiled by Scibek (2020). K values vary from 8.0e-16 to 6.0e-11 m^2, with an average of 5.1e-12 m^2, which I have selected as the input for our DFN models. For the modelling, the permeability value for each fracture set was set as constant, with no variation between the individual fractures (by length or aperture) and different fracture sets. Moreover, the K values were also compared to handheld air–minipermeameter (TinyPerm–3) readings from the Smøla drill cores (including matrix material) and on cataclasite/gouge zones in outcrops from similar settings on Bømlo island, Norway (Ceccato et al., 2021b). The comparison showed a similar range, with Smøla K values of 9.87e-18 to 8.42e-11 m^2 and Bømlo of 1.5e-15 to 3.7e-12 m^2, supporting our permeability value choice.

4.7.2.3 Fracture termination relationships

To stochastically replicate the natural cross-cutting and terminating relationships between the different fracture sets, I defined a matrix of termination probabilities for the four fracture sets that geometrically correspond to the 2D lineament traces (Table 7.3). Namely, the NE-SW lineament traces are associated with the D_1 deformation episode (epidote-prehnite fractures), the E-W lineament traces with D_2 (sericite-chlorite-carbonate fractures), the N-S traces with D_3 (chlorite-hematite fractures), and the NW-SE traces with D_{4+5} (quartz-calcite-zeolite fractures). The shallowly dipping fracture set, also attributed to D_2, did not however have a distinguishable 2D map-view set on which to define termination probabilities, so it is not included. I selected, through visual inspection, three representative areas for each of the four trace map scales (Figure 4.2 & Figure B2). Within these representative areas, each mapped lineament trace, sorted by set, was assessed for different termination types, with each instance manually counted. These relationships were either within the same fracture set, or against other fracture sets. The result of this analysis is provided in Chapter 7.

For the DFN modelling, I reduced the relative termination probabilities for certain fracture sets to improve computer efficiency, as the original probabilities led to very high processing times. As this study presents a conceptual approach rather than a full replication of the Smøla rock fracture pattern (like any other modelling study), I have simplified the modelling process. The most significant adjustment to the termination probabilities involved reducing the probability percentage of the N-S traces against E-W traces by 55% to decrease fracture interactions (which was significantly increasing model processing runtimes). Other reductions ranged between 3% and 26% in specific cases. However, most termination probabilities remain similar to the original deterministic values. These changes impacted the abundance of node types in some model outputs, which for example potentially increased the fracture connectivity value (C_B) for the D_3 model.

4.7.3 DFN Modelling methodology

4.7.3.1 'Grown' DFN modelling methodology

Using FracMan (WSP UK Limited, 2024), I generated four 'grown' DFN models (single realisations) within 500 m^3 volumes (Figure 4.3), as per the modelling approach described by Libby et al. (2019, 2024). Integrating the temporal component, these models represent a stochastic representation of each deformation episode, each possessing a selected number of time-defined fractures sets. In the software, the model representing the most recent geological time had five fracture sets (labelled Set A, B, C, D, E in the software, with Set A being the oldest and Set E the youngest). Each successive model progressively featured fewer generated fracture sets, following the concept of fracture back-stripping (Youngest featuring Sets A to E, then Sets A to D, followed by Sets A to C, and the oldest only Set A).

For each model, and each fracture set, using the “Grown Fracture Network” definitions dialog box in FracMan (WSP UK Limited, 2024), I input the various parameters (previously outlined in this Chapter) including the target P_{32}, geometric (size and orientation values), growth parameters, as well as the shadow size factor (fracture spacing), termination probabilities (“chance to terminate” in the software), and growth time (both the total generation timesteps, and the fracture growth time steps, which controls the speed of fracture growth). Finally, I input the fracture-related petrophysical properties (permeability and aperture values, as outlined above). The models were then run successively, with the various fracture sets generated stochastically from the oldest to the youngest, with each younger fracture set interacting with the older fracture sets. Importantly, some fracture sets are present in more than one model, for example Set A (representing the oldest fractures), but between the different models the stochastic fractures belonging to the same fracture set (e.g. Set A) will differ owing to the ‘seeding’ of each fracture in a random location and the size and orientation distributions). No two models are therefore the same even if the input parameters are identical.

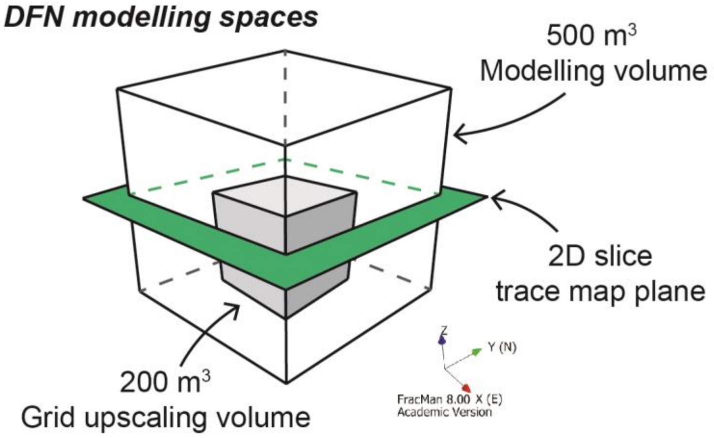

Figure 4.3. The two different 3D volumes used for the DFN modelling in Chapter 5. A larger modelling volume of 500 m^3 (outer block) and a smaller grid volume of 200 m^3 (grey block) is nested within the 500 m^3 volume. Slicing through these volumes, is the 2D trace map plane used for the network topology analysis for each model (green surface).

4.7.3.2 Grid upscaling and permeability estimation

Following the stochastic fracture generation step, I nested a smaller 200 m^3 grid upscaling volume with 1000 grid cells inside each of the four 500 m^3 modelling volumes (Figure 4.3) to avoid edge-effects. These edge-effects are due to the grown fractures in

FracMan (WSP UK Limited, 2024) potentially expanding outside the 500 m^3 modelling volume. This means that in the volume inside and along the modelling volume boundary, can have lower the fracture intensities. The size of each of the grid cells within the 200 m^3 grids are set at 20 m^3, representing the 'representative elemental volume' (REV). The grid cell size has been selected based on the recommendation by Oda (1988) that the REV dimensions need to be at least three times larger than the average fracture trace lengths for the modelled fractures to delimit a representative volume. In this thesis, average fracture trace lengths range from 3.29 m to 5.80 m for all the fracture sets (17.4 m^3 is therefore the minimum recommended size for the REV).

The stochastic fractures (one or more fracture sets, depending on the selected model) that are located within each of the 200 m^3 grids were then used with the FracMan Grid Upscaling Tool (WSP UK Limited, 2024). For each 200 m^3 grid, I utilised the "Compute Oda Permeability" tool in the software. This tool then generated a 3 x 3 matrix of directional permeability values for every simulated fracture (based on the geometry) within each grid cell, using the Oda (1985) method (as outlined in Chapter 2). Subsequently, the directional permeability values related to all the fractures within every grid cell, were summed together to provide 'Oda Permeability' principal direction values in m^2. These principal values correspond to the principal permeability axes (K_i) classified as maximum (K_1), intermediate (K_2), and minimum (K_3) elements. Additionally, for each grid cell, FracMan generated x, y, z components for each eigenvector classified as 'Oda' V_1, V_2, and V_3; with the resultant eigenvector for V_1 corresponding to K_1, V_2 to K_2, and V_3 to K_3. Lastly, volumetric fracture intensity P_{32} values were generated for each of the 1000 grid cells. All the different outputs for each DFN were then exported from FracMan into Microsoft Excel spreadsheet format and are available online at https://data.mendeley.com/datasets/ctpphnptc5/2 within the Excel file "DFN_Output_K_PPT".

To estimate mean orientations for the principal permeability axes (K_1, K_2, K_3) related to each of the 1000 grid cells (done systematically for each 200 m^3 grid), the eigenvector components ('Oda' V_1 (x, y, z), V_2 (x, y, z), and V_3 (x, y, z)) were converted into related principal direction vectors (corresponding to the principal permeability axes) with trend and plunge orientations (x, y components for the trend, and the z component for the plunge). Thus altogether, for each 200 m^3 grid, 1000 K_1 axes, 1000 K_2 axes, and 1000 K_3 axes were oriented and generated. A full description of how the DFN output 'Oda' eigenvector components were converted into oriented axes, please refer to Appendix B. Subsequently, I plotted each 200 m^3 grid's 3000 principal permeability axes (K_1, K_2, K_3), onto a specific stereonet. The principal permeability axes plot as linear data representing three mutually perpendicular axes for each grid cell. Finally, I undertook eigenvector analysis of the plotted data using stereographic software, following the method by

Watson (1966), to estimate the mean orientations of the K_1, K_2, K_3 axes, based on the cluster distributions of the 1000 trend and plunge orientation data for each axis.

To briefly outline the eigenvector analysis I point out that for each principal permeability axis (for example the K_1 vector data), the 1000 data points plotted on the stereonet are initially considered to each represent a single unit of mass (Watson, 1966). Using a spherical projection, a rotational axis can be defined through the centre of the stereonet to the location of the lowest moment of inertia; which is as close as possible to all unit masses and lies within the highest concentration of the 1000 data points (Watson, 1966; Whitaker and Engelder, 2005). This rotation axis is coaxial with the major (e_1) eigenvector, corresponding to the mean statistical orientation of the plotted data (Watson, 1966). Perpendicular to e_1, the minor (e_3) eigenvector corresponds to the maximum moment of inertia, with the intermediate (e_2) eigenvector plotting orthogonally to both e_1 and e_3 (Watson, 1966). Representing the mean orientation of each principal permeability axis, the e_1 eigenvector was then used to represent the mean K_1, K_2, and K_3 for each 200 m^3 grid, and therefore illustrating the permeability tensor anisotropy for each time-specific DFN model.

4.7.3.3 Fracture conditioning

In FracMan (WSP UK Limited, 2024), the downhole fracture datasets (televiewer data) were sorted by geometric constraints into possible observed fracture sets corresponding to distinct deformation episodes. New DFN models were generated using a smaller 50 m^3 modelling volume (within the previous 200 m^3 grid volume) with fracture input parameters which more closely match the deterministic characteristics of the observed fracture datasets in the drill holes. Subsequently, selected stochastic fracture sets (corresponding to a selected 50 m^3 DFN model, and a specific deformation episode) were matched to the observed televiewer data using the fracture conditioning tool ("Fracture Conditioning" definition in the software) in FracMan (WSP UK Limited, 2024). The fracture conditioning algorithm initially identified stochastically generated fractures which 'best fit' observed fractures either by spatial location, or fracture orientation (Golder Associates (UK) Ltd., 2001). The process then adjusts or regenerates the stochastic fractures to match the observed local drill hole data and then regenerates the fractures (less stochastically and more deterministically), while maintaining the overall model parameters such as fracture intensity (P_{10} or P_{32}) (Golder Associates (UK) Ltd., 2001). An output of 'conditioned' fractures is then generated in the model objects and visualisation window which could then be selected and interrogated.

The process allowed me to semi-quantitatively assess whether the originally generated stochastic model (unconditioned), which has used deterministic inputs derived from real geological data, is significantly different from the observed geological data being replicated. This comparison relied on the difference in fracture count (which, in turn, relates to fracture intensity), spatial pattern or distribution of fractures along the length of a selected drill hole, and the difference in orientation between the modelled and observed. Practically, the semi-quantitatively assessment of these conditioned fractures against the original stochastic fractures and the observed fractures (televiewer data) used both cumulative fracture intensity (CFI) plots and stereonet plots within FracMan. The three datasets were visually compared to determine similarity in the spatial pattern, fracture intensity, and the orientation (dip and dip direction). The modelling input parameters for the modelling procedure are included in Table C1 in Appendix C.

4.8 Topology and fracture connectivity analysis

Prior to the topology analysis, in FracMan (WSP UK Limited, 2024) each DFN model (by deformation episode) was sliced in the X-Y plane to create 2D trace maps through the modelling volume and grid volume (Figure 4.3). The 3D stochastic fractures were captured as 2D lines on the trace maps (representing the intersection lineation of each fracture on the 2D plane).

All 2D deterministic and modelled trace maps were imported in a geographic information system (GIS) software platform, where I used the NetworkGT tool (Nyberg et al., 2018) to analyse and characterise node and branch proportions and network connectivity (“Node and Branch Identification tool”). Initially, the 2D deterministic trace maps underwent polyline repair to ensure that relevant polylines terminated correctly against each other (i.e., 'snapped').

The Network GT tool generates nodes based on polyline intersections (similar to Figure 2.8): 1) polylines with a free endpoint (tip) produce an I-type node, while 2) polylines which terminate up against or splay off another polyline produce a Y-type node, and 3) a crosscutting polyline intersection produces a X-node (involving four branches). Based on the node type, the branch type and number can be determined: I) When a polyline has two I-type nodes, a single isolated branch is produced (I-I-type); II) Where a polyline has one isolated node and a connected (Y or X-type) node, a semi-connected type of branch is produced (C-I-type); and III) when a polyline has both ends involving connected nodes (Y or X-nodes), a fully connected branch (C-C-type) branch is produced.

To fully represent the branch and node networks, I placed three representative circular scan areas over the networks, scaled to the map scale (Figure 4.2). These circular scan areas have diameters of 4 km for the 1:100 000 map, 1.5 km for the 1:25 000 scale map, 1.2 km for the 1:7500 scale map, and 40 m for the 1:500 scale map. Where the circular areas intersect with the polylines of our networks, an edge node (E-node) is produced. An example of these trace maps with the branches and nodes are included in Figure B2 in Appendix B.

The trace maps underwent manual node and branch counting, with only the branch and node types fully within the circular scan areas counted (no edge-nodes or truncated branches). The proportions of node and branch types were then plotted on ternary diagrams (node- or branch-related) using the NetworkGT Topology Parameters tool (Nyberg et al., 2018). Overall, 2685 branches and 2154 nodes were counted for all the different scales. As a demonstrable example, fracture connectivity was then assessed using the average connections per branch (C_B) value, combined for each scale's representative scan areas. The C_B parameter is defined as $C_B = (3N_Y + 4N_X) / N_B$, where N_y is the number of Y-nodes, N_x is the number of X-nodes, and N_B is the total number of branches expressed as $0.0<C_B<2.0$ (Sanderson and Nixon, 2015), and indicates the level of network interconnectedness.

The modelled trace maps underwent the mostly the same identification and counting process for branches and nodes, and estimation of the connectivity values. The only difference from the deterministic trace maps topology analysis process, was the circular scan areas for each modelled trace map had the same diameter (as these maps were the same scale), opposed to the changing scan area diameter associated with each map scale (from 1:500 to 1:100 000). The modelled and deterministic trace maps used for the topology analysis are available online at https://data.mendeley.com/datasets/ctpphnptc5/2 as a zip file labelled "Deterministic_&- _Modelled_Traces", and the C_B calculations are included in Appendix B (Tables B4 and B5).

As a final analysis, the modelled trace maps with the demarcated three representative scan areas (same as above) also underwent cluster and block analyses by deformation episode, using the NetworkGT Topology tools "Define Clusters" and "Identify Blocks" (Nyberg et al., 2018). These analyses were undertaken to supplement and compare against the C_B connectivity measure described above. The tools generated new polyline datasets that merged connected trace lines into distinct clusters, assigning a cluster identifier to each trace line within the clusters (Nyberg et al., 2018). Additionally, they produced a polygon layer defining and extracting 2D areas, known as 'enclosed regions' or 'blocks', which are bound by connected branch types (C-I and C-C branches) (Nyberg et al., 2018).

Each trace line in the cluster dataset has a length measurement (in metres) and a cluster identifier, allowing for the calculation of the total length for each cluster (clusters by scan area are shown in Figure B3, Appendix B). For each scan area, the number of clusters was plotted to show variation by deformation episode (Appendix B, Figure B4a). The combined trace line length in the largest clusters for each scan area was also plotted by deformation episode for comparison (Appendix B, Figure B4a).

Each of the output 2D enclosed regions or blocks (shown in Figure B3, Appendix B) possesses an area size measurement (m^2), which can be compared across different scan areas and deformation episodes. Along with average size, the count of enclosed blocks provided the R_{22} measure, calculated using $R_{22} = 1/(R+1)$ (R representing the number of enclosed regions within the area of interest, with the metric expressed as $0.0<R_{22}<1.0$). Both the average size of the enclosed regions and the R_{22} measure were plotted for each scan area and deformation episode (Appendix B, Figure B4b). Additionally, the relative spatial coverage of the enclosed regions compared to relevant total scan areas were also plotted as proportional circle charts (Appendix B, Figure B4c). The overall results are summarised in Table B6, Appendix B.

Chapter 5: Multiscalar 3D temporal structural characterisation of Smøla island, mid-Norwegian passive margin: an analogue for unravelling the tectonic history of offshore basement highs

---

Matthew S. Hodge[1]*, Guri Venvik[2], Jochen Knies[2], Roelant van der Lelij[2], Jasmin Schönenberger[2], Øystein Nordgulen[2], Marco Brönner[2], Aziz Nasuti[2], & Giulio Viola[1]

1: Department of Biological, Geological and Environmental Sciences, University of Bologna, Italy
2: Geological Survey of Norway (NGU), Trondheim, Norway

This chapter is published in Solid Earth, 13 May 2024, with the following reference: Hodge, M. S., Venvik, G., Knies, J., van der Lelij, R., Schönenberger, J., Nordgulen, Ø., Brönner, M., Nasuti, A., and Viola, G.: Multiscalar 3D temporal structural characterisation of Smøla island, mid-Norwegian passive margin: an analogue for unravelling the tectonic history of offshore basement highs, Solid Earth, 15, 589–615, https://doi.org/10.5194/se-15-589-2024, 2024.

5.1 Abstract.

Smøla Island, situated within the Mid-Norwegian passive margin, contains crystalline basement-hosted intricate fracture and fault arrays formed during a polyphase brittle tectonic evolution. Its detailed study may strengthen correlation attempts between the well-exposed onshore domain and the inaccessible offshore domain, further the understanding of the passive margin evolution, and provide useful constraints on petrophysical properties of fractured basement blocks. A combination of geophysical and remote sensing lineament analysis, field mapping, high resolution drill hole logging, 3D modelling, petrographic and microstructural studies, and fault gouge K-Ar geochronology, made it possible to define five deformation episodes (D_1 to D_5). These episodes occurred between the post-Caledonian evolution of the regional-scale Møre Trøndelag Fault Complex (MTFC) and the Late Cretaceous and younger crustal extension preceding the final stages of Greenland-Norway break-up. Each reconstructed deformation stage is associated with different structural features, fault and fracture geometries, and kinematic patterns. Synkinematic mineralisations evolved progressively from epidote-prehnite, sericite-chlorite-calcite, chlorite-hematite, hematite-zeolite-calcite, to quartz-calcite. K-Ar geochronology constrains brittle deformation to discrete

localisation events spanning from the Carboniferous to the Late Cretaceous. Multiscalar geometrical modelling at scales of 100 m, 10 m, and 1 m helps constrain the extent and size of the deformation zones of each deformation episode, with D_2 structures exhibiting the greatest strike continuity and D_1 features the most localised. Overall, the approach highlighted here is of great utility for unravelling complex brittle tectonic histories within basement volumes. It is also a prerequisite to constrain the dynamic evolution of the petrophysical properties of basement blocks.

5.2 Introduction

Offshore crystalline basement highs are important structural elements of rifted passive margins (Peron-Pinvidic et al., 2013; Zastrozhnov et al., 2020). However, accessing and studying these features is challenging due to their locations beneath deep oceanic waters and younger sedimentary cover. Constraining their structural characteristics and tectonic evolution typically relies on relatively low-resolution datasets, such as seismic surveys and scattered drill hole data (Holdsworth et al., 2019; Tanner et al., 2020), which limits detailed reconstructions. Most of the geological knowledge on offshore basement highs derives from hydrocarbon exploration work, which, until recently mostly focussed on and around their faulted outermost edges, with limited interest in the basement volumes themselves (Riber et al., 2015). On the other hand, following indications that fractured and weathered basement may represent productive unconventional hydrocarbon reservoirs or act as pathways for oil and gas migration, they have recently begun to receive considerable attention (e.g. Belaidi et al., 2018; Hartz et al., 2013; Holdsworth et al., 2019; Riber et al., 2015; Trice, 2014).

A conceptual gap remains regarding the effective role of connected natural fractures and faults hosted within basement volumes (intrabasement structures) in an offshore context (Holdsworth et al., 2019). These structures are difficult to investigate offshore because their size is commonly below seismic resolution (Tanner et al., 2020). Consequently, characterising sub-seismic to regional-scale structures, and their potentially long-lived tectonic evolution, requires more than just low-resolution datasets. To mitigate these challenges, analogue onshore basement exposures can be of great assistance as they provide more extensive and ready site access, and data availability from regional to micro-scale resolutions (e.g. regional geophysical data, field mapping, and thin sections).

The island of Smøla, within the Mid-Norwegian passive margin, forms a subaerial exposure of crystalline basement rocks (Figure 5.1a). The island is an ideal analogue for basement highs offshore Central Norway, owing to both its proximity to the offshore Frøya High, and the similarity of basement geology at both locations (Rønning and

Elvebakk, 2005; Slagstad et al., 2011). Smøla has abundant local and regional structures, which document the tectonic evolution of the margin through time. As such, any geological insights from Smøla could then potentially be applied to basement highs offshore, furthering the understanding of their internal structure, and aiding in the reconstruction of their tectonic evolution.

The brittle tectonic evolution of onshore basement exposures along the Norwegian passive margin has been extensively studied (Redfield et al., 2004; Davids et al., 2013; Ksienzyk et al., 2016; Scheiber et al., 2016, 2019; Scheiber and Viola, 2018; Tartaglia et al., 2020; Fossen et al., 2021; Hestnes et al., 2022), with Tartaglia et al. (2023) providing the latest insights for the Mid-Norwegian portion. Applying the tight constraints from these studies, and a new three-dimensional (3D) perspective from four diamond drill holes on Smøla island, we present a case study that describes and tests a comprehensive workflow for characterising onshore basement blocks. Our multiscalar approach integrates surface geological tools (outcrop mapping and sampling), petrography, regional datasets (airborne magnetic surveys and digital terrain models (DTMs)), along with K-Ar geochronology to constrain the absolute time dimension of the reconstructed tectonic phases. As fault and fracture arrays in crystalline rocks control local secondary permeability (Gillespie et al., 2020), our work has significant implications on resolving reservoir characteristics associated with offshore basement highs, and basement deformation more generally. This study, therefore, offers a method to generate crucial deterministic inputs for modelling basement fractures and petrophysical behaviour over time.

5.3 Geological framework

5.3.1 Regional perspective

Smøla island, located in Central Norway, is set along the Mid-Norwegian passive margin (Figure 5.1a), a region shaped by a prolonged and complex geological history (Peron-Pinvidic and Osmundsen, 2020). The island (Figure 5.1b) is comprised by 445.7 ± 3.8 Ma plutonic magmatic-arc rocks (Slagstad et al., 2011; Tucker et al., 2004) and oceanic crustal units, all of which were emplaced and accreted just prior to the Silurian-Devonian (~430 to 400 Ma) Scandian Phase of the Caledonian Orogeny (Corfu et al., 2014; Gee et al., 2008; Slagstad and Kirkland, 2018; Tucker et al., 2004). Caledonian shortening led to nappe and thrust fault development, with transposition of the Smøla rocks along major detachments over both the allochthonous continental Neoproterozoic Baltoscandian nappes and the underlying autochthonous Palaeo- to Mesoproterozoic

Baltican crystalline basement of the Western Gneiss Region (WGR) (Corfu et al., 2014; Fossen, 1992; Tucker et al., 2004)(Figure 5.1c).

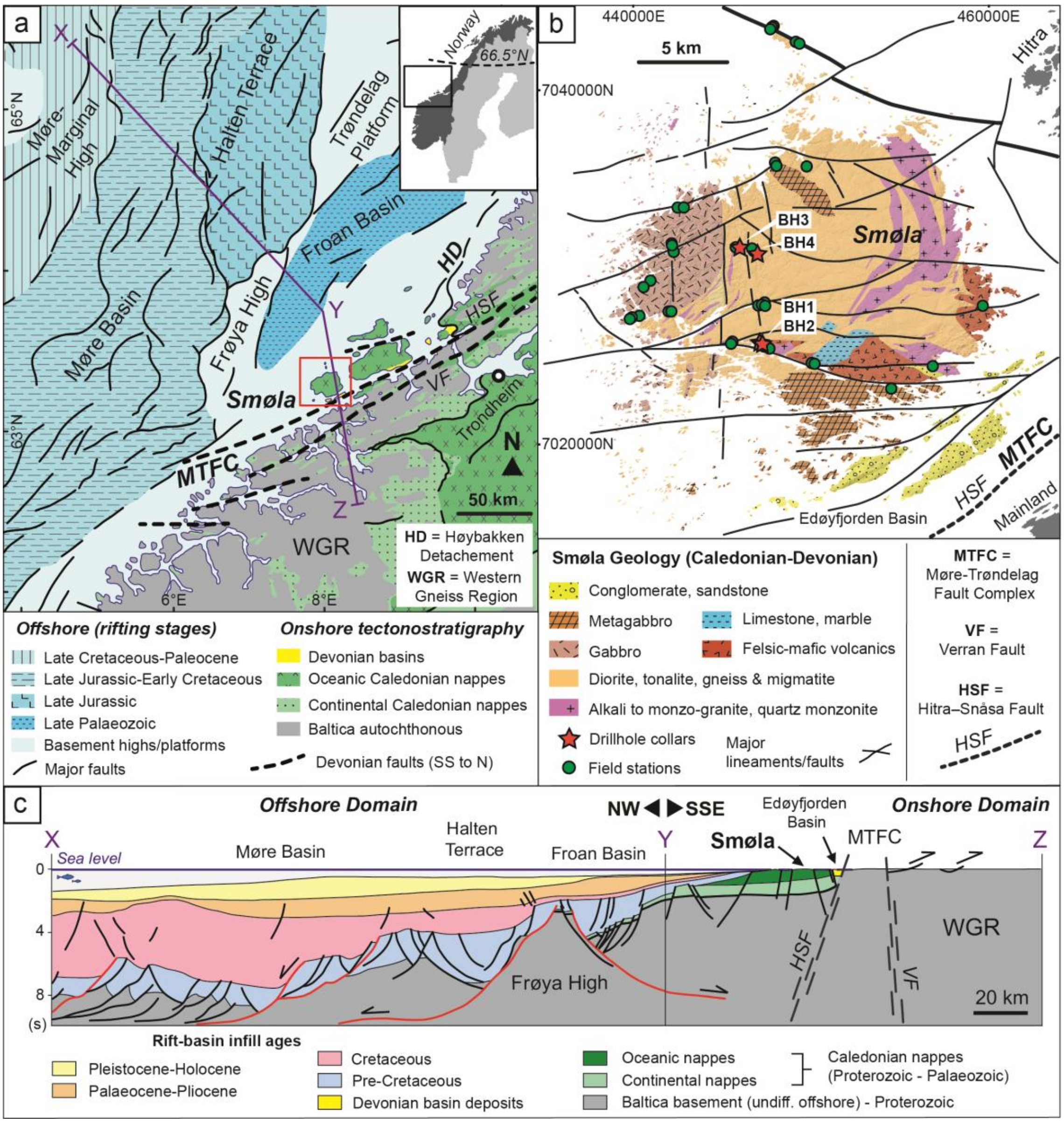

Figure 5.1. The geological context of Smøla island, Central Norway. (a) Regional setting of Smøla on the Mid-Norwegian passive margin. Smøla is separated from the Western Gneiss Region (WGR) by the Møre-Trøndelag Fault Complex (MTFC), with two fault strands, the Hitra–Snåsa Fault (HSF) and the Verran Fault (VF). The Høybakken Detachment (HD) is shown to the NE of Smøla. Major basins are present are to the NW of Smøla, in the offshore domain (e.g. Møre Basin), bound by normal faults and structural highs (e.g. Frøya High) (modified from Faleide et al., 2008; Bedrock map of Norway, Geological Survey of Norway, 2021). (b) The local geology of Smøla, showing the Caledonian and Devonian geology. Significant lineaments and faults (interpreted from airborne geophysics, DTM, and field studies) crosscut the island, with the MTFC (HSF strand) trace indicated. The drill holes (red stars) and outcrop mapping locations (green circles) are shown (modified from Fediuk and Siedlecki, 1977). (c) Onshore-offshore interpretive

geological cross section (X-Y-Z) as shown in Panel A, showing major regional structures and crustal anatomy relative to Smøla. Including the two strands of the MTFC (HSF and VF) and the Frøya High offshore (modified from Zastrozhnov et al., 2020).

During the Early Devonian collapse of the by then overthickened orogen resulted in significant crustal extension by both reactivation of favourably oriented contractional structures (Fossen, 2010a; Fossen et al., 2017) and development of new crustal-scale extensional shear zones, and regional exhumation (Figure 5.1) (Osmundsen et al., 2006). Devonian extension also caused the Smøla rocks to be translated, in response to both strike-slip and down-faulting across the Møre-Trøndelag Fault Complex (MTFC), a regional fault system with complex kinematics that was repeatedly reactivated through time (Grønlie et al., 1994; Grønlie and Roberts, 1989; Redfield et al., 2004; Watts et al., 2023). Smøla experienced limited metamorphic overprint (on average sub-greenschist facies conditions) and only localised ductile deformation (Tucker et al., 2004). Associated with the Devonian tectonic inversion, extensional (possible pull-apart) basins formed in response to brittle extensional faulting, such as the MTFC-related Edøyfjorden Basin proximal to Smøla (Figure 5.1b) (Bøe et al., 1989; Bøe and Bjerkli, 1989; Fossen et al., 2017; Osmundsen et al., 2006).

Post-Caledonian extension and rifting continued to the Late Cretaceous/Early Palaeocene, eventually leading to the Greenland-Eurasia plate break-up at ~54 Ma and opening of the North Atlantic, forming the Norwegian passive margin (Bunkholt et al., 2022; Peron-Pinvidic and Osmundsen, 2018). This prolonged process involved multiple tectonic phases: rift initiation during the Carboniferous, Permo-Triassic crustal stretching and rifting, Late-Triassic to Jurassic crustal thinning, renewed Mid-Jurassic to Early Cretaceous rifting, with extension of the margin during the Late-Cretaceous to Paleocene, and early seafloor formation and spreading during the Paleocene-Eocene (Faleide et al., 2008; Gernigon et al., 2020; Mosar et al., 2002; Peron-Pinvidic and Osmundsen, 2018).

These events produced discrete generations of basins (such as the Froan and Møre Basins) along the newly-forming Norwegian shelf, which progressively infilled with synrift sediments (Figure 5.1a & c) (Faleide et al., 2008; Zastrozhnov et al., 2020). In places, structural highs of Caledonian-aged and underlying Baltica crystalline basement, such as the Frøya High to the NW of Smøla formed through rift-related exhumation between these basins, leading to a remarkable host and graben series (Muñoz-Barrera et al., 2020). Bounding the structural highs and the different basins, are crustal-scale extensional faults (Figure 5.1a & c) (Mosar et al., 2002; Skilbrei et al., 2002). Overall, this protracted rifting and extension history resulted in a highly attenuated offshore domain, reactivating, and overprinting the existing Caledonian deformation features (Figure 5.1a & c) (Mosar et al., 2002; Zastrozhnov et al., 2020).

5.3.2 The geology of Smøla

Smøla is composed of several Caledonian-aged bedrock types traditionally attributed to the Caledonian Upper Allochthon (Roberts and Gee, 1985) (Figure 5.1b), including diorite (the most common lithology), gabbro, tonalite, alkali granite, quartz monzonite to monzo-granite, quartz-feldspar and amphibolite-biotite gneiss, limestone and volcanic rocks (andesitic to rhyolitic in composition in a faulted block on the SE-portion of Smøla). Late, felsic to mafic dykes crosscut all other rock types (Bruton and Bockelie, 1979; Fediuk and Siedlecki, 1977; Gautneb, 1988; Gautneb and Roberts, 1989; Roberts, 1980). In addition to the 445.7 ± 3.8 Ma (1σ) U/Pb intrusive age of a dated granodiorite (Tucker et al., 2004), a granitic dyke was dated to 428 ± 10 Ma (2σ) (Rb/Sr) (Gautneb, 1988), providing an Ordovician-Silurian age envelope for the plutonic rocks on the island. To the S and SE of Smøla the Caledonian bedrock is unconformably overlain by the late Silurian-mid Devonian sedimentary cover of the Smøla Group, and later Jurassic-Cretaceous sedimentary successions (Bøe et al., 1989; Bøe and Bjerkli, 1989; Fediuk and Siedlecki, 1977). These include siliciclastic deposits of red-oxidised polymictic conglomerate, siltstone, and sandstone (Bøe et al., 1989), which fill in Devonian extensional basins (e.g. Edøyfjorden Basin, Figure 3.5 & Figure 5.1b) along the MTFC (Bøe and Bjerkli, 1989).

Further to the S and SE of Smøla (and bounding the Devonian basins), the ~NE-SW striking MTFC is the most proximal and dominant regional-scale structure to the island. This wide (10 to 50 km) structure extends for >600 km from Central Trøndelag into the northern-part of the North Sea, and branches into two sub-parallel strands, the Hitra–Snåsa Fault (HSF) to the NW (the most proximal to Smøla), and the Verran Fault (VF) to the SE (Figure 5.1a,b, & c) (Olsen et al., 2007; Watts, 2001; Watts et al., 2023). The structural evolution of the MTFC is complex, with a polyphase deformation history from the Devonian until the Cenozoic (e.g. Grønlie and Roberts, 1989; Seranne, 1992; Watts, 2001; Redfield et al., 2004; Tartaglia et al., 2023; Watts et al., 2023).

5.4 Materials and methods

This study's multi-technique approach involves a variety of 2D and 3D datasets, ranging from the regional-scale through to the micro-scale. Integrated into these datasets is the absolute time dimension, provided through K-Ar geochronology of structurally well-characterised fault rocks, which give chronological constraints on all other datasets. We briefly outline the methods below, with a more detailed description in Appendix A.

5.4.1 Geophysical and remote sensing data and lineament mapping

The geophysical and DTM data used in this study were acquired by the Geological Survey of Norway (NGU) (Nasuti et al., 2015), with details on survey parameters and data processing available in Chapter 4. Our lineament picking and mapping followed White (2014) and Scheiber and Viola (2018), making use of both the magnetic geophysical and DTM imagery within a geographic information systems (GIS) software platform. The description of the methodology used to identify and place the lineaments is outlined in Chapter 4.

5.4.2 Field work and drill hole logging

The field-based structural data acquisition involved standard geological field methods, including the systematic mapping of representative outcrops and ground-truthing of possible exposed deformation zones identified in the lineament mapping. In total, sixty-six outcrop sites were studied, with data collected recording deformation feature types, fracture/vein mineral infill, fault slip information, host rock lithology, and cross-cutting/genetic relationships between the various features. The four diamond drill holes used in this study (stored in Trondheim) were drilled in 2019 and were designed to target major structures, and sample weathered basement rocks. Geological features in the drill cores were systematically logged downhole (for a total investigated length of 364.9 m of diamond drill core), recording lithology and rock alteration, deformation types, fracture/fault characteristics, mineral infill, and cross-cutting relationships. These data were also used for the 3D modelling of intersected deformation zones in drill holes BH1 and BH2. The methodology used to measure structural data in drill core followed both the methods of Holcombe (2013) and Blenkinsop et al. (2015). A more detailed description of the methodology is available in Chapter 4.

5.4.3 X-ray diffraction and K-Ar dating

Seven structurally controlled fault gouge and breccia samples were collected from fault and deformation zones in both drill core and outcrop, and subsequently processed at the NGU laboratory in Trondheim. Initially, all samples were disintegrated and separated into <0.1 µm, 0.1-0.4 µm, 0.4-2 µm, 2-6 µm, 6-10 µm size fractions. Each of these size fractions then underwent quantitative analysis for both potassium (K) and argon (Ar) using total digest ICP-OES, and a Isotopx NGX multi collector noble gas mass spectrometer system respectively. X-ray diffraction (XRD) analysis was performed on each fraction to determine and quantify the mineralogical composition. A full description of both the XRD and K-Ar analysis methodology is available in Chapter 4 and in Viola et al. (2018).

5.5 Results

5.5.1 Lineament mapping from geophysics and DTM data

The analysis of regional-scale features such as geophysical lineaments and topographic features (Figure 5.2) formed the initial stage of the study. These features occur on the kilometre-scale, and using both geophysical and DTM imagery, can be traced over both off- and onshore areas. The >2000 mapped lineaments (available within the online supplementary data repository) are linear and curvilinear to irregular features which either crosscut or terminate against one another (Figure 5.2a & b). The lineaments are classified based on length and hierarchy of formation: first-order lineaments are potentially major regional structures; second-order lineaments, commonly >10 km in length, are typically major splays or secondary features off the first-order lineaments; while third-order lineaments, typically <10 km in length, constitute the remaining lineaments.

The first, second, and third-order lineaments are sub-divided into four main orientation trends, based on azimuth frequency maxima, which are labelled: L1) N-S, L2) E-W, L3) NE-SW, and L4) NW-SE (Figure 5.2b) (hereinafter as L1 to L4). Determining precise cross-cutting relationships between these lineament trends is often challenging due to imagery resolution and the difficulty of defining lineament end points. However, where possible, interpretive cross-cutting relationships provide a relative timing of lineament formation. The age, cross-cutting, and termination relationships of the specific lineament trends are summarised in Table 5.1, and selectively illustrated in Figure 5.2b.

L1 is most common in the western part of Smøla and offshore in areas A and B on Figure 5.2a. Its lineaments are typically second- to third-order and are crosscut by all other lineaments (Figure 2b.I). Local mutual cross-cutting relationships between L1 and L4 suggest they are likely coeval/conjugates. L1, L2, and L3 lineaments have complex cross-cutting relationships, with L1 being potentially horizontally offset (dextrally and sinistrally) with multiple possible reactivations in places (Figure 5.2b.I & b.II).

The L2 lineaments are most common in central Smøla, particularly in areas B, D, and E, clustering on the NW side of the MTFC (Figure 5.2a), occurring as second-order lineaments and possible splays off the first-order MTFC (HSF) lineament (Figure 5.2a). L2 is crosscut by L1 and L4 (Figure 5.2b.II), and also exhibits mutual cross-cutting (potentially coeval) relationships with the L3 lineaments (which, in turn, typically splay off the E-W structures) (Figure 5.2b.I). Frequently, L1, L2, and L4 (third-order lineaments only) are similarly crosscut by the same lineament trends, indicating that theses lineaments may have formed coevally (Figure 5.2b.II). The longer L2 second-order lineaments do however crosscut most other lineaments (Figure 5.2b.I), suggesting either a later formation or a longer period of activity/reactivation.

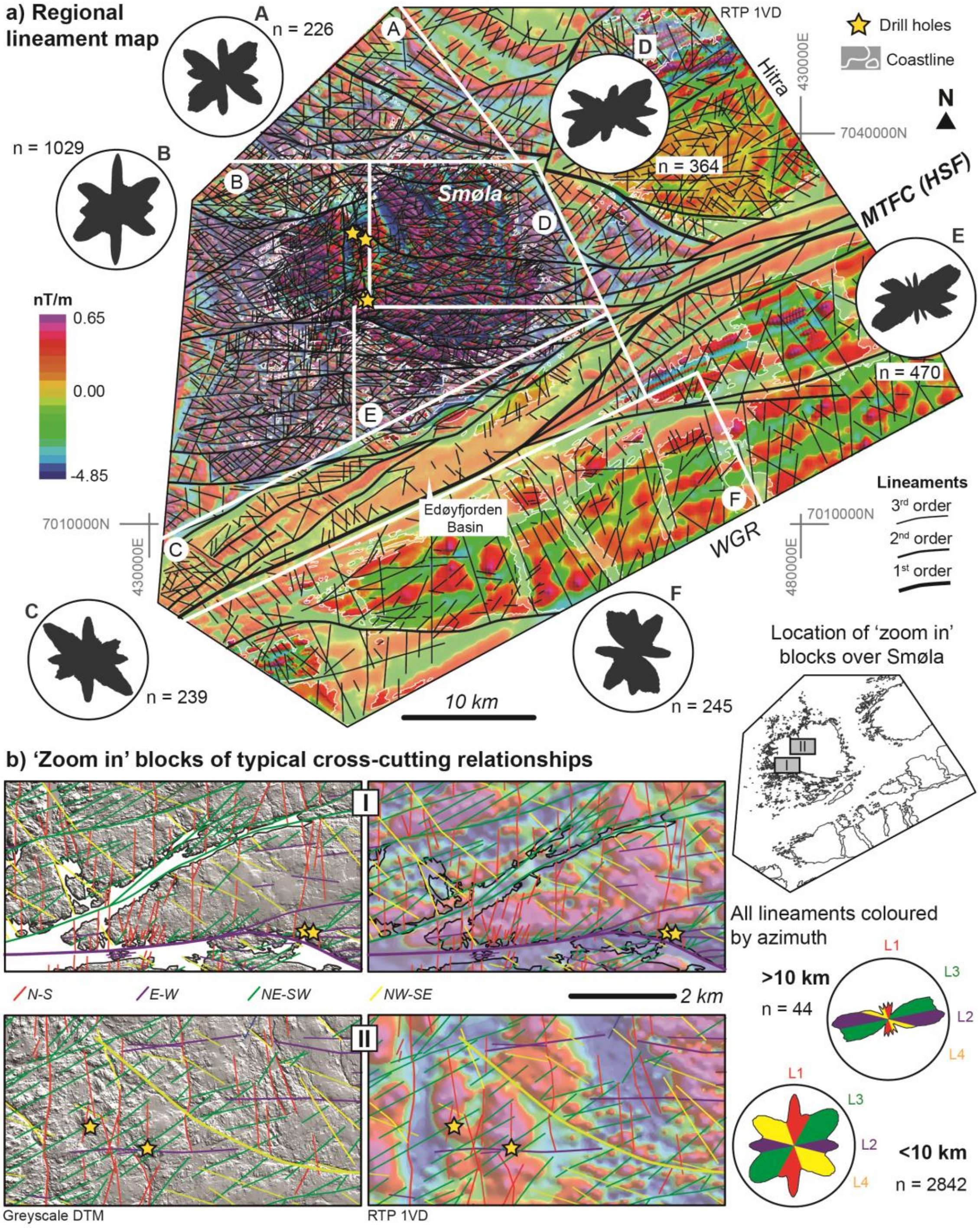

Figure 5.2. (a) Airborne magnetic survey imagery (reduced to pole-first vertical derivative (RTP-1VD)) over Smøla island and surrounding areas (coastline shown in white). Displayed over the magnetic imagery are first, second, and third-order lineaments mapped from both the magnetic data and DTM data. Airborne magnetic survey imagery from Nasuti et al. (2015). The area over Smøla onto the WGR region is sub-divided into A (north of Smøla), B (western and SW of Smøla), C (area over the MTFC), D (NE Smøla), E (SE Smøla), and F (WGR area). Rose plots of strike

trends of mapped lineaments are shown by area. (b) 'Zoom in' blocks showing representative examples of cross-cutting relationships between the different lineament trends (coloured by trend) on both DTM and geophysical imagery (DTM data from the NGU). Locations of the 'zoom in' blocks are displayed on the adjacent schematic map of Smøla (coastline map courtesy of the NGU) along with rose diagrams showing orientation trends of lineaments with >10 km and <10 km lengths. Rose plots use the same colours as the lineaments on the 'zoom in' blocks and are labelled to show the L1 to L4 lineament trends.

The L3 lineaments are pervasive across Smøla within areas A, D, E, B, and F (Figure 5.2a). These lineaments are typically third-order lineaments and sub-parallel to the MTFC (HSF) trend. In the eastern part of Smøla (areas E and D), they cluster on and terminate against the N/NE sides of L2 (Figure 5.2b.I), possibly representing third-order Riedel shears or splays off the second-order L2. In the western part of Smøla they form prominent elongate topographical valleys in the DTM and terminate less commonly against L2. These lineaments crosscut and dextrally offset both the L1 and L4 (less distinctly) and terminate against L2 (infrequently also L4) (Figure 5.2b.II). L3 lineaments are, however, in turn either locally crosscut by, or are terminated up against by L1 and rarely L4 (mutual terminating relationship) (Figure 5.2b.II).

Table 5.1. Interpretive age relationship matrix between the main lineament trends. The lineament trends are ordered as they are discussed in the text. Relationship types include X = cross-cutting, T = terminating, ? = uncertain.

			Younger			
Lineament trends			N-S	E-W	NE-SW	NW-SE
Older	L1	N-S	-	X, T	X	X
	L2	E-W	T, X	-	T	X
	L3	NE-SW	T, X?	X	-	T, X
	L4	NW-SE	X, T	X	X, T	-

L4 is common to the north of the MTFC, over most parts of Smøla and offshore (areas A, B, D, and E on Figure 5.2a). L4 is similarly crosscut by many of the other lineament sets (Figure 5.2b), although locally L4 crosscuts L2 and the L3 lineaments, as well as the magnetic grain (Figure 5.2b), but this may be due to later reactivations. The L4 and L1 lineaments have rare mutual cross-cutting relationships, although in general L1 tends to terminate up against L4.

Representing a later subset of L4, the WNW-ESE striking portion of L4 is also present throughout the study area, although mostly NW of the MTFC, and are either second or third-order lineaments. This late L4 crosscuts all other lineaments, with only rare examples of L1 crosscutting it (Figure 5.2b.II). Similarly, L1 has a younger, possibly reactivated component. These younger L1 lineaments are most abundant in the areas D and B (more NNE-SSW striking), and areas F and E (more NNW-SSE striking) over Smøla and the WGR. Overall, these lineaments terminate against and crosscut all the other lineaments (Figure 5.2b.I & b.II), suggesting an early formation and a possible late reactivation.

5.5.2 Field, drill hole, and petrographic results

Field observations (Figure 5.1b & Figure 5.3) and four diamond drill holes (Figure 5.1b & Figure 5.4) offer a novel 3D perspective on Smøla's geology. Various minerals decorating fracture surfaces, fault rocks, and veins are systematically documented, showing coeval or crosscutting relationships, and orientation trends. (Figure 5.3, Figure 5.5 & Figure 5.6). As such, assemblages of coeval infill minerals have been used to group the deformation features based on the relative timing (labelled D_1 to D_5). The coeval mineral assemblages, with corresponding consistent deformation styles and orientation trends, may represent distinct mineralisation events associated with discrete deformation episodes (e.g. Drake et al., 2009; Viola et al., 2009).

We now systematically describe the progressive deformation and mineralisation types starting from the apparent earliest to the latest features. As a part of the structural characterisation, we have included both the field and drill hole structural data (Figure 5.3). However, the drill hole data were localised in specific parts of the island and biased towards including shallowly dipping features (e.g. Terzaghi, 1965). Therefore, field data primarily inform the structural descriptions, as they illustrate typical geometries and kinematics across Smøla.

5.5.2.1 D_1: epidote-prehnite-stable faulting and veining

The earliest recognised brittle deformation features on Smøla are epidote and prehnite veins, hydraulic breccias, and cataclasites involving at least three different generations of epidote (Ep 1, 2, & 3 on Figure 5.5a & b). Field data reveal two clusters of the shear fractures and veins: one striking ENE-WSW with steep SSE dips, and the other NW-SE with steep NE dips. Major structures associated with fault rocks (red great circles on the 'All planes' plots on Figure 5.3), primarily strike ENE-WSW with steep SSE dips. Slip lineations show varied orientations but have moderate to shallow plunges, trending E or W. Kinematically, most structures with slip-trend information exhibit strike- to oblique-slip motion, predominantly oriented E-W. Overall, the data suggest a sinistral strike-slip regime with NNE-SSW contraction and WNW-ESE extension. Drill data also exhibit similar strike orientations, with an additional trend NW-SE dipping shallowly NE. Kinematically, shear features are mostly normal, dipping moderately to shallowly NE, indicating a mean NE-SW extension direction.

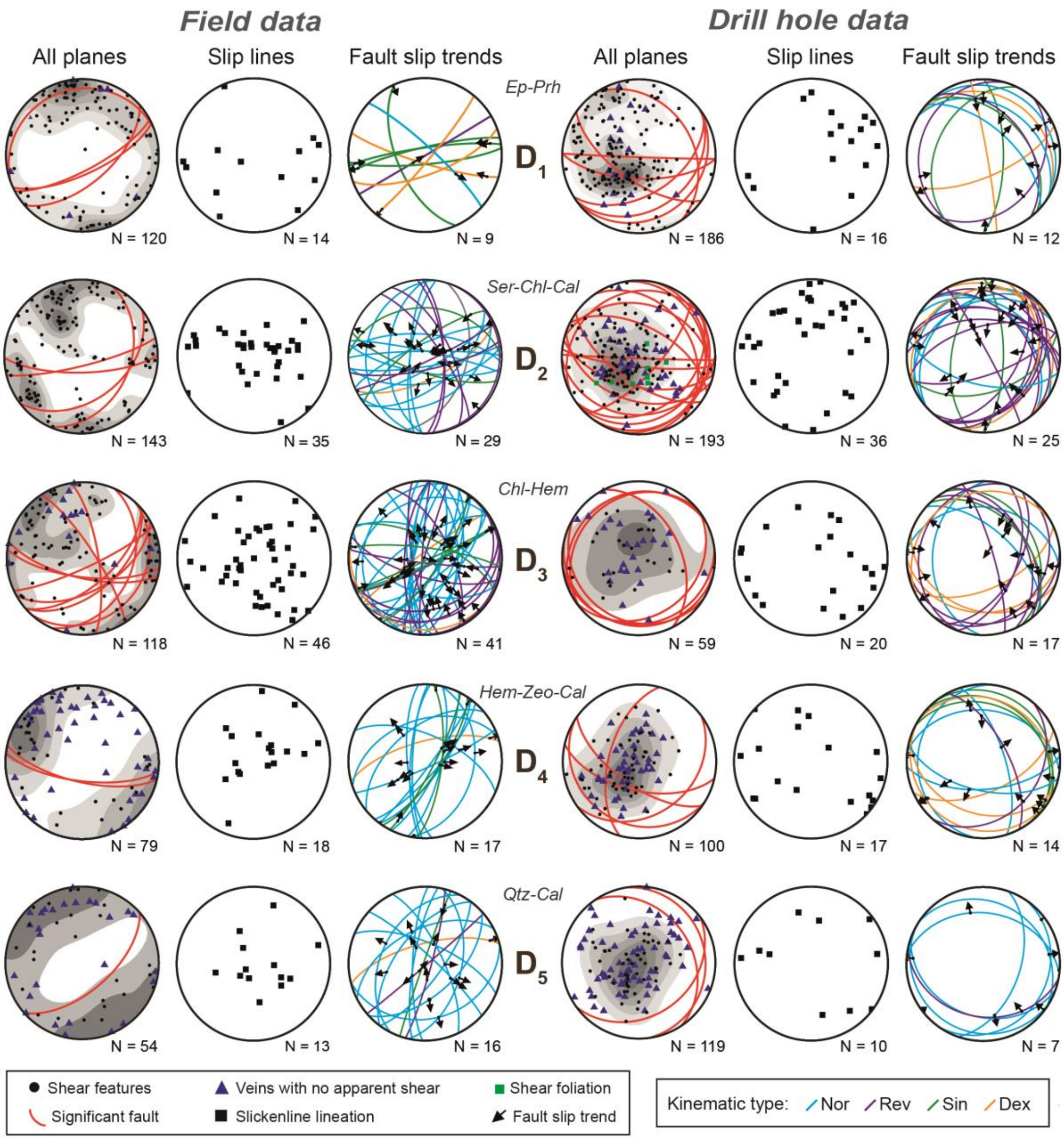

Figure 5.3. Equal area, lower hemisphere stereonet plots of deformation features in outcrop or drill core, sorted by deformation episode D_1 to D5, and coeval mineral assemblages. All plane plots Kamb contoured at 2σ interval, with drill hole stereonets not Terzaghi corrected. Mineral types: "Ep"=epidote, "Prh"=prehnite, "Ser"=sericite, "Chl"=chlorite, "Cal"=calcite, "Hem"=hematite, "Zeo"=zeolite, "Qtz"=quartz. Kinematic types: "Nor"=normal, "Rev"=reverse, "Sin"=sinistral, and "Dex"=dextral.

The epidote mineralisation consists of early pale/light green-yellow (Ep 1 and 2) or a later grass-green type (Ep 3). Early epidote typically infills tensile or shear veins, with well-developed slickenside surfaces on the vein-host rock interfaces or internally on crack-seal surfaces (Figure 5.5a). In contrast, later grass-green epidote occurs as infill of irregular, bifurcating to anatomising veins (Figure 5.5b), which in places crosscuts and reworks the early epidote. All three types cross-cut host rock lithological features, such as aplitic veins.

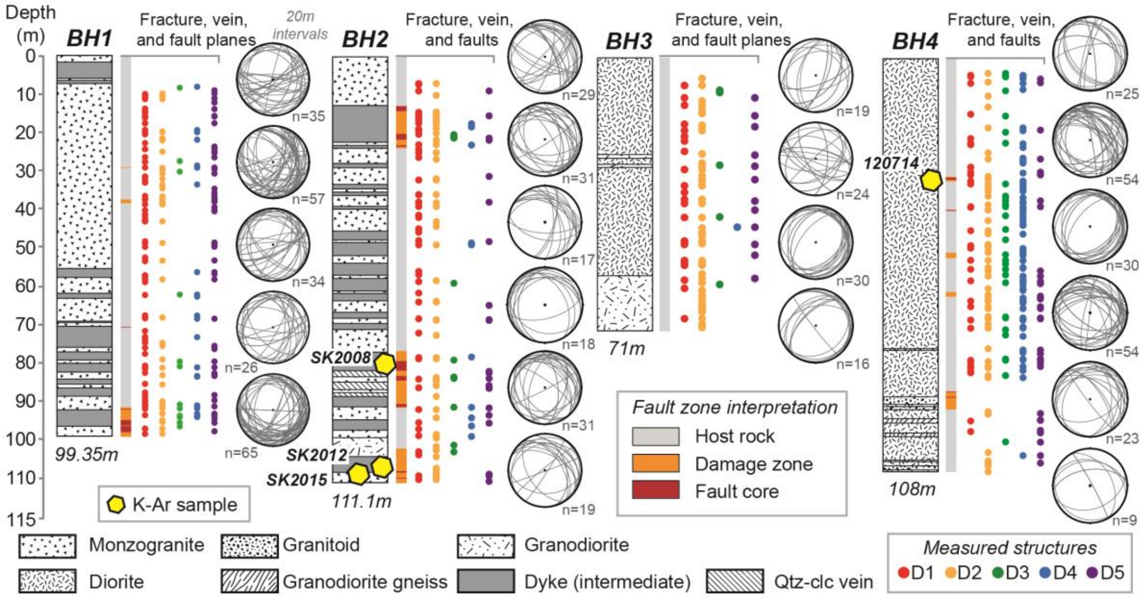

Figure 5.4. Graphic logs showing both downhole lithology and fault zone interpretations for each of the four Smøla diamond drill holes. Measured structural data are shown distributed downhole, grouped by mineral assemblage (and deformation episode), with D_1 = epidote-prehnite, D_2 = sericite-chlorite-calcite, D_3 = chlorite-hematite (+/- calcite), D_4 = hematite-zeolite-calcite, and D5 = quartz-calcite. Measured structures are also represented plotted as planes on the adjacent stereonets. Each stereonet represents at least 20m of drill core and correspond to the downhole depths of the drill holes.

Prehnite veins, significantly less common than epidote veins, occur in drill holes BH1 and BH2 together with epidote. Prehnite typically pale grey-green, infills veins, and can form dense networks grading to dilatant hydraulic breccias (Figure 5.5a, drill core). In the case of the hydraulic breccias, included fragments are either host rock fragments of polycrystalline aggregates of quartz-feldspar or reworked epidote cataclasites/veins (in places with host rock fragments with included veins; Figure 5.6c).

The earlier epidote locally forms the matrix mineral of at least two generations of cataclasite to ultracataclasite, which are associated with the major structures on Figure 5.3. The earliest epidote cataclasite to ultracataclasite (Ep 1) is typically preserved as isolated fragments (1-5 mm in size), which possibly originated as thin discrete pockets with a weak to distinct foliated to banded matrix dominated by very fine-grained epidote and clay (forming up to 75 %-90 % of the pockets). The included clasts are fine-grained (average size <60 µm), poorly sorted and subangular, and are typically mono- to polycrystalline aggregates of quartz-feldspar host rock (Figure 5.6a & b). The later epidote cataclasite (Ep 2) occurs as localised zones (typically <10 cm in width), with a massive matrix (making up 60 %-70 % of the zones) formed by fine-grained epidote and clay (Figure 5.6b). The included fragments are very fine- to coarse-grained (10 µm-6 mm), poorly sorted, angular- to sub-angular, and polycrystalline fragments of host rock (quartz-feldspar) or reworked fragments of the earlier epidote ultracataclasite. The included Ep 1 and host rock fragments within the Ep 2 cataclasite exhibit minor offset and rotation from each other, suggesting that there was limited to no rigid-body rotation and mechanical comminution of the fragments.

Rarely, prehnite ultra-cataclasites occur as discrete zones 3-5 cm in width, striking NNW-SSE and NW-SE, with shallow to moderate dips (30°-65°) (Figure 5.3, drill data). Prehnite comprising >90 % of the matrix of these zones, is very fine-grained, with interspersed clay. The included clasts are fine-grained (<50 µm-1 mm), moderately sorted, subrounded to angular, and made up of mono to polycrystalline fragments of host rock and epidote cataclasite. The prehnite ultracataclasites are associated with the epidote cataclasites, with both the cataclasites mutually reworking one another.

5.5.2.2 D_2: repeated sericite-chlorite-calcite faulting

D_2 sericite-chlorite-calcite shear features (Figure 5.5e) invariably rework D_1 structures. These structures occur as single shear fractures or dense networks and local brittle-ductile shear zones.

Field data reveal three main trends of the shear fracture orientations (Figure 5.3): E-W to ENE-WSW striking, steeply to moderately S dipping; NE-SW striking, moderately SE dipping; and NNW-SSE striking, steeply E dipping. Slip lineations mostly plunge steeply, indicating dip-slip kinematics, with shallower trends toward W or SE. Kinematically, most shear features exhibit normal or oblique-normal shear-sense, striking E-W or NE-SW. Some N-S striking, steeply E-dipping reverse faults are also observed. Sinistral and dextral strike- to oblique-slip features strike E-W, dipping moderately N or S. Overall, these features indicate an extensional regime with a mean NW-SE extension direction. Drill data show predominantly NW-SE striking, shallowly NE dipping fractures and veins. Major structures mostly dip shallowly SE, with steeper dipping features striking E-W. Kinematically, shear features are mostly reverse, dipping SE or NE, with some normal and strike-slip features.

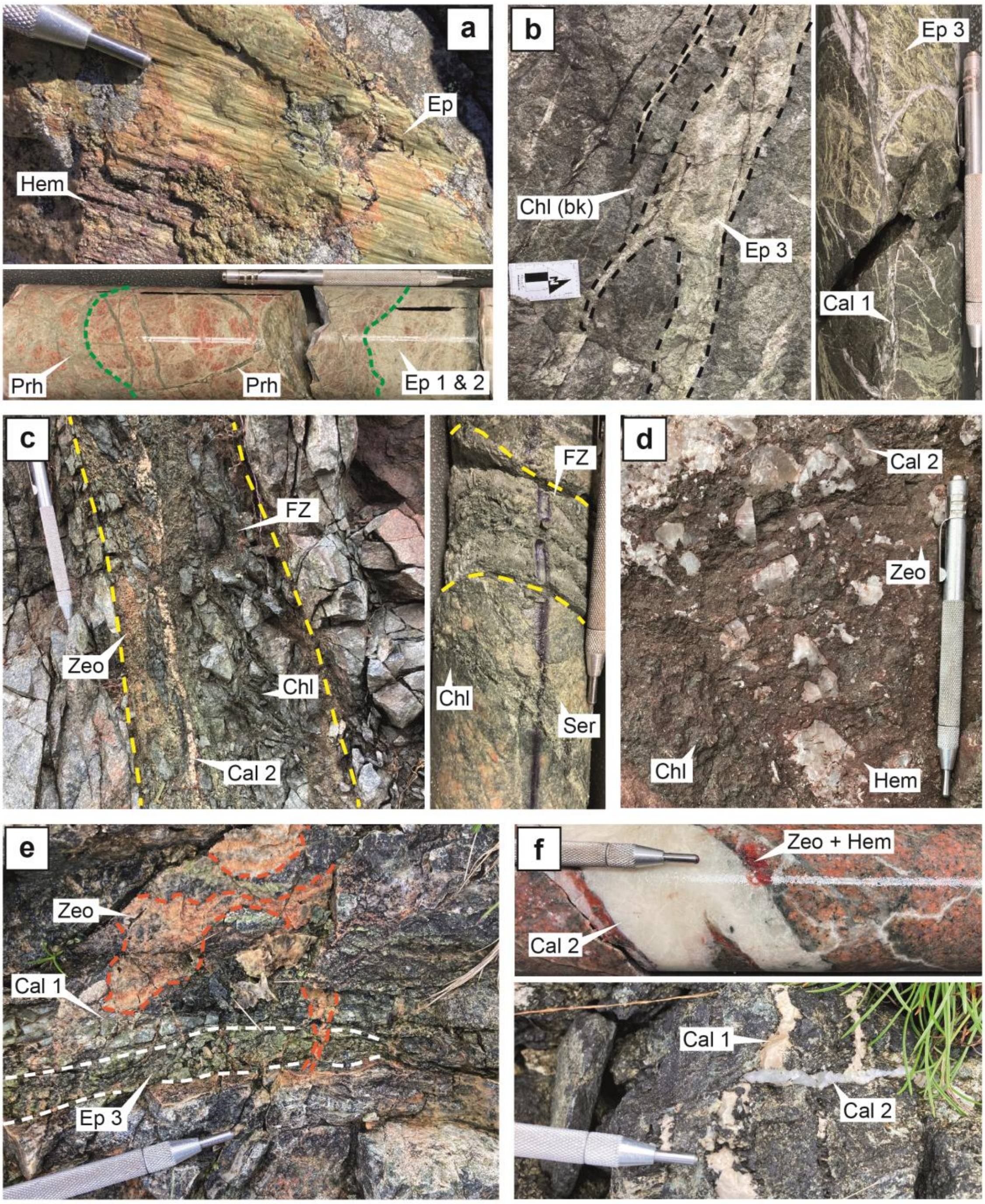

Figure 5.5. Representative examples of mesoscale deformation features on Smøla. (a) Epidote slickenside surface (combination of light green and grass-green epidote) and light green epidote (Ep 1 and 2) veins and cataclasite being cross-cut by prehnite (Prh) vein breccia in BH1. (b) Bifurcating diffuse veins of grass-green epidote (Ep 3) with black chlorite (Chl (bk)); core-hosted abundant grass-green epidote veins are cross-cut by early calcite veins (Cal 1). (c) Chloritic (Chl) fault zone (+/- sericitic) with later zeolite (Zeo) and calcite vein (Cal 2). The zone is highly fractured, the friable gouge (left side of the zone) represents a fault core; a similar narrow fault zone in BH2, with strong foliation and abundant sericite (Ser) infill. (d) Chlorite (Chl)-hematite (hem) cataclasite veneer on a fault surface with a later zeolite overprint and late quartz (Qtz)-

calcite (Cal 2) infill. (e) Zeolite (Zeo) veins cross-cutting early calcite (Cal 1) and epidote (Ep 3) veins. (f) Deformed early calcite veins (pale brown coloured) (Cal 1) being cross-cut by translucent white late quartz-calcite vein (Cal 2). (a-f) Scratch pen for scale = 13 cm, (b) Scale bar arrow = 10 cm.

The well-developed deformation zones, with locally foliated gouge with highly fractured and disaggregating host rock clasts and early deformed calcite veins (Figure 5.5c) are typically oriented the same as the first two shear fracture outcrop trends (Figure 5.3). D_2 structures, especially the well-developed deformation zones, are almost phyllitic at the microscale (Figure 5.6d & E), locally involving fine to medium-grained sericite/muscovite (30-40 %), chlorite (30 %), and clay (>5 %), with elongate domains of fine-grained recrystallised quartz (>20 %; the matrix forms ~80 % of the total volume). The host-rock clasts within this groundmass are 20 μm-1 cm monocrystalline quartz fragments or polycrystalline aggregates of subrounded quartz and altered feldspar.

Microstructural relationships indicate at least two distinct deformation events: an early event with localised shearing along axial planar cleavages in an early folded sericite groundmass with calcite veins (Figure 5.6d); and a subsequent event, reworking and rotating the earlier axial planar cleavage shear planes (S-surfaces) by later C'-planes. This resulted in the development of an extensional crenulation cleavage (ECC)-type fabric (Figure 5.6e) (e.g. Passchier and Trouw, 2005). These ECC zones also rework D_1 epidote cataclasite and fragmented host rock. The host rock fragments locally form σ porphyroclasts with very fine-grained quartz in the strain shadows, and the sericite-chlorite groundmass (and very fine-grained clay) deflected around them.

5.5.2.3 D_3: chlorite-hematite-decorated fault rocks and shear fractures

The D_3 chlorite-hematite structures (Figure 5.5d), involve brown-red staining or 'dusting' of hematite and chlorite decorating and infilling these structures. D_3 structures occur as individual anastomosing shear fractures, which locally have hematite slickensides, grading to networks, and breccias and gouges (and possible cataclasites).

Field data show four trends of these shear fractures: NE-SW striking, steeply SE dipping; N-S striking, subvertical to steeply W dipping; NE-SW striking, shallowly SE dipping; and WNW-ESE striking, steeply SSW dipping. Tensile veins mostly strike ENE-WSW and dip moderately to steeply SSE. Major D_3 structures (with breccia and gouge) are sub-parallel to these trends. Slip lineations vary, with steep dip-slip predominating and shallower strike-slip orientations trending NE, W, and SW. Kinematically, shear features are mainly normal to oblique-normal, striking NNE-SSW, with shallow S-dipping thrusts and vertical N-S striking reverse faults. Sinistral strike-slip features strike ~ENE-WSW, with occasional dextral features striking NE-SW. These features suggest associated WNW-ESE to NW-SE extension. Shear fractures and veins from drill data, primarily strike ENE-WSW and dip shallowly SE. Major drill core structures have shallow dipping geometries, either S or NW. Shear features are predominantly dip-slip and reverse, dipping either ~E or NW, with some dextral features striking E-W to NE-SW. Overall, these structures suggest a mean NW-SE contraction.

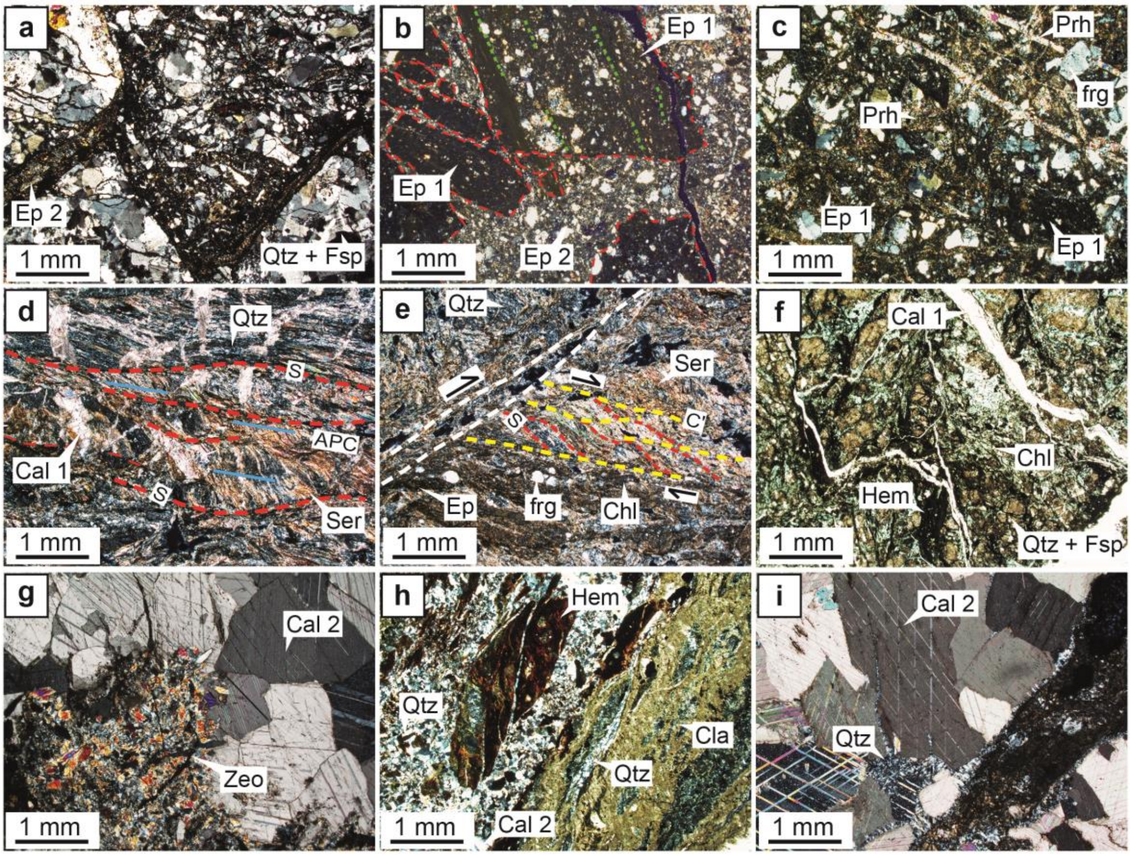

Figure 5.6. Photomicrographs outlining the progressive deformation episodes affecting Smøla over time. (a) An Ep 2 vein and cataclasite reworking host rock monzogranite; (b) Two generations of light green epidote cataclasites, an earlier ultracataclasite (Ep 1) fragments, almost isotropic, banded to foliated (green dashed lines highlighting the foliation), set within a later cataclasite (Ep 2). (c) Prehnite (Prh) hydraulic breccia and veins reworking Ep 1 cataclasite/veins and host rock fragments (frg). (d) Asymmetric folds in a sericitic fabric, and early calcite veins. Associated with the folds, a rootless axial planar cleavage has formed (blue lines), along which a later foliation (red lines). (e) Possible extensional crenulation cleavage ECC fabric reworking the fabric since in D, forming in a sericite-chlorite shear zone. C'-planes (yellow lines), associated with chlorite, have formed inclined to a main shear surface (white line), and are reworking and back-rotating the cleavage-related foliation (from D), forming S-surfaces. Reworked host rock fragments are also present associated with the C'-planes, and chlorite. (f) Chlorite-hematite breccia to gouge with deformed early calcite veins (Cal 1), and highly altered host rock minerals (feldspars). (g) Zeolite-calcite (+/- interstitial hematite in the zeolite) relatively undeformed vein, with the zeolite crystals

subhedral to euhedral crystal faces within the calcite. (h) Hematite indurated gouge reworked by a later quartz-calcite vein. Abundant clays are adjacent to the vein. (i) Late quartz-calcite vein (Cal 2), exhibiting calcite twinning (low deformation overall). All photomicrographs are 2.5x, XPL, except for F, which PPL.

The chlorite-hematite breccias to gouges, typically diffuse zones (up to ~3 m thick), exhibit abundant D_3 fractures forming damage zones around them. The gouges are indurated and are moderately to well consolidated features in hand specimen (Figure 5.5d). These features at the microscale are cemented by chlorite (40 %), hematite (30-50 %), and clay (10-20 %), with the matrix forming 5-20% of the overall zones (rarely up to 60 %; Figure 5.6f). The chlorite grains, either overprinting or as growths between the fragmented host rock (and host rock clasts), form elongate grains in places. The hematite cement is dark red-brown to opaque in PPL, with the staining/ 'dusting' occurring as very fine-grained particles within fractures/matrix and overprinting the host rock. The host rock clasts themselves are typically medium- to coarse-grained in size (2 mm-1 cm), moderately to poorly sorted, clast-supported, and comprised by altered quartz-feldspar (feldspar is partially altered to sericite) polycrystalline fragments. Elsewhere, the D_3 structures are associated with thin pockets of hematite-rich foliated to banded cataclasite/indurated gouge (<2 cm in thickness; Figure 5.6h), with a very fine-grained matrix (up to 80% of the zone) comprised of hematite (80%), clay (15%), and chlorite (5%), with incorporated fine-grained (20-600 µm), poorly sorted and sub-rounded host rock clasts.

5.5.2.4 D_4: hematite-zeolite-calcite veining

The D_4 hematite-zeolite-calcite structures, mostly tensile veins (0.1-6 mm in thickness) (Figure 5.5e & f), crosscut the earlier epidote, sericite-chlorite-calcite (Cal 1), and chlorite-hematite structures. D_4 veins are pervasive across Smøla (Figure 5.5e & f, drill core), along with rare examples of hydraulic breccias and shear fractures with slickenside surfaces.

Field data indicate the tensile veins strike ~ENE-WSW, dipping steeply SE or NW. Shear fractures primarily strike NNE-SSW to NE-SW with moderate to steep ESE dips. The D_4 major structures (breccias and gouges) strike WNW-ESE, steeply dipping SSW. Slip lineations typically plunge steeply, showing dominant dip-slip, with subordinate shallower strike-slip lineation orientations ~NE/SW. Kinematically, features are mainly normal shear-sense, striking NE-SW, with minor sinistral strike-slip (NNE-SSW strike) and rare dextral strike-slip (ENE-WSW strike) features, possibly representing conjugate features. This suggests NW-SE extension with NE-SW contraction. The drill data indicate shallow NE-dipping fractures and veins, with major structures striking NW-SE or NE-SW (steeper dipping). Kinematically, these features are mostly moderately dipping oblique- to strike-slip, with sinistral features dipping NE and dextral features dipping SW. Subordinate normal features dip moderately to steeply SSW or ENE. Overall, this indicates a mean ~NNE-SSW extension direction.

Along with zeolite, hematite typically occurs as a bright-red type (different from the D_3-related hematite), along with a later less deformed type of calcite (Cal 2) (Figure 5.7). In outcrop and in drill core, D_4 structures are associated with coarse-grained 'sugary' masses of zeolite-calcite, locally mineralising over pre-existing veins of epidote or chlorite-hematite (Figure 5.5e). At the microscale, the D_4 veins consist of zeolite (laumontite) occurring as fine to medium-grained, decussate, subhedral prismatic crystals, in places with interstitial Fe staining. Locally, where zeolite crystals have intergrown with late calcite, they form bounding comb-type textures with euhedral crystal morphologies (Figure 5.6g). Additionally, radial masses of zeolite occur as grain boundary growths within the calcite portions of the veins, indicating the coeval mineralisation of both minerals. The zeolite, hematite, and late calcite (Cal 2) components in these veins show little to no significant post-crystallisation deformation, implying the D_4 veins are indeed relatively late.

5.5.2.5 D_5: quartz-calcite veining

The D_5 quartz-calcite veins, involving the late calcite variety (Cal 2) and mineralised quartz, rework and offset all other deformation features (D_1 to D_4) (Figure 5.7).

The shear fractures and veins in outcrop strike NE-SW, dipping steeply SE or moderately NW. Major structures strike the same but dip more moderately SE. Slip lineations are mainly dip-slip, plunging steeply, with shallow strike-slip lineation orientations toward NNE and ENE. Kinematically, the features have predominantly normal shear-sense, and NE-SW striking. The sinistral and dextral strike-slip planes, possibly conjugates, are oriented similarly to the normal features. Overall, the geometries and kinematics indicate a mean ~E-W extension orientation. In drill core, fractures and veins show a dominant NW-SE strike, shallowly dipping NE. Tensile veins strike similarly NW-SE but with shallow to steep NE or SW dips. Major structures are subparallel to the fracture trends. Kinematically, most features are shallowly NNE/SSW-dipping, WNW-ESE to NW-SE striking normal dip-slip features, indicating a mean NNW-SSE/N-S extensional direction.

The D_5 quartz-calcite veins, in outcrop or drill core, are translucent to opaque white, exhibit crack-seal layering parallel to the vein-host boundary and are planar to bifurcating features (Figure 5.5f). The veins occur as singular narrow to wide veins (0.1 mm-22 cm) or complex vein networks, and in places, hydraulic breccias with included angular fragments of the host rock. Commonly, these late veins are within and subparallel to existing deformation features, such as sericite-chlorite deformation zones, and may represent a later tensile reactivation of these features (exploiting mechanically weak planes) (Figure 5.5d). The late quartz-calcite veins crosscut the earlier calcite veins (Cal 1; Figure 5.5f), which are less quartz-rich, relatively massive, more opaque white, and possess deformed non-planar morphologies to disaggregated irregular domains (for example in D_2).

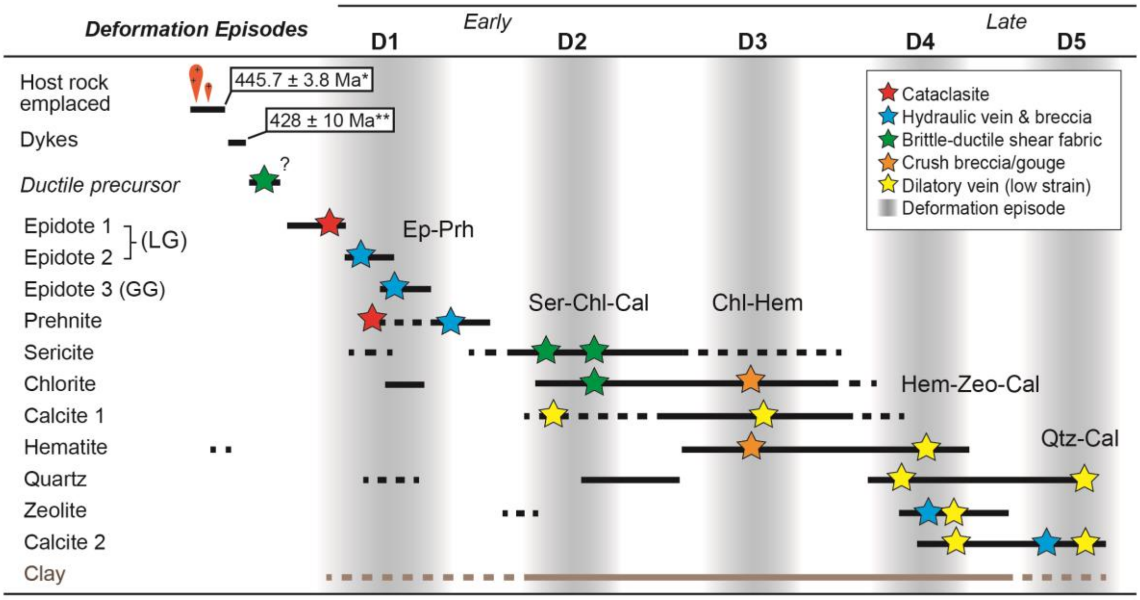

*Figure 5.7. Chronological table showing the relative mineralisation times of different mineral types, key deformation features associated with each mineral type is shown in relative chronology, with clustering of mineralisation and deformation features grouped into five main deformation episodes. These episodes are associated with specific mineral assemblages. Mineral types: Ep=epidote, Prh=prehnite, Ser=sericite, Chl=chlorite, Cal=calcite, Hem=hematite, Zeo=zeolite, Qtz=quartz. *Host rock age provided by (Tucker et al., 2004); **Age of dyke emplacement by Gautneb (1988).*

At the micro-scale, D_5 veins exhibit medium to coarse-grained calcite crystals, typically anhedral, with distinct cleavage, or show fine-grained rims on the quartz grains and between adjacent calcite grains (Figure 5.6i). In places, coarser-grained quartz form comb-type textures with euhedral crystal terminations into the larger calcite crystals. Commonly, quartz and calcite also mineralise as vein border-parallel alternating bands, indicating multiple crack-seal mineralisations. Finally, while these veins exhibit minimal post-mineralisation deformation (like D_4), the calcite in the veins is twinned, suggesting some later strain.

5.6 Basement deformation in 3D

The four oriented drill holes (Figure 5.4, with locations on Figure 5.1b) provide a 3D view of Smøla's geology. Using Leapfrog Works (Seequent, 2022) 3D modelling software, we could delineate the hangingwall and footwall boundaries of deformation zones using logged downhole intersections and orientation data. Implicit volumes were then generated to reproduce the actual thickness, orientation, and extent of zones through 3D space. The modelling of different zones in one volume provides insights into the continuity and extent of deformation zones, as well as potential fracture connectivity. Furthermore, by incorporating both relative (Figure 5.7) and absolute deformation ages, the modelling also includes a temporal dimension.

In this study, we have specifically used drill holes BH1 and BH2 for the modelling. These drill holes are close enough together to allow confident correlations between the drill holes. These drill holes intersected deformation zones, veined intervals, and shear zones/fault cores (Figure 5.4). Considering the geological and deformation characteristics of each of these zones, particularly the fault core intersections (assumed to have the greatest strike continuity) and the associated damage zones, we have correlated at least four zones between the drill holes. The correlations and modelling also used the orientations of bounding deformation features to resolve the geometries of these zones. Examples of modelled zones which are correlated between BH1 and BH2 (labelled I-IV in Figure 5.8a) are the following:

I) BH1 (37.46 m-37.81 m) and BH2 (12.94 m-23.59 m) intersect a S-dipping E-W striking zone characterised by early D_1 epidote veins and hydraulic breccia (Ep 2) crosscut by D_2 chloritic/sericitic fractures and breccia, and late D_5 quartz-calcite veins (Cal 1 and Cal 2).

II) Both BH1 (70.6 m-70.77 m) and BH2 (79.39 m-81.78 m) intersect a NE-SW striking NW-dipping zone, which widens in BH2, involving early D_1 epidote veins and later chlorite-hematite (D_3) breccia, with stronger hematite mineralisation in BH2. The zone also features deformed early calcite veins (Cal 1).

III) A NE-SW striking shallowly S-dipping zone in both BH1 (92.03 m-96.33 m) and BH2 (83.33 m-84.51 m), characterised by a D_1 epidote cataclasite reworked by chlorite and zeolite deformation features (host rock fragments are overprinted by zeolite). These cataclasites are also cross-cut by D_4 zeolite-calcite and late D_5 quartz-calcite veins (dense vein network).

IV) More clearly intersected in BH2 (108.08 m-111.1 m), a moderately to shallowly SW-dipping zone characterised by intensely sheared D_2 sericite-chlorite gouge and phyllitic bands, with a broader damage zone of sericite and chlorite fractures, is also intersected at the base of BH1 (96.57 m-99.24 m).

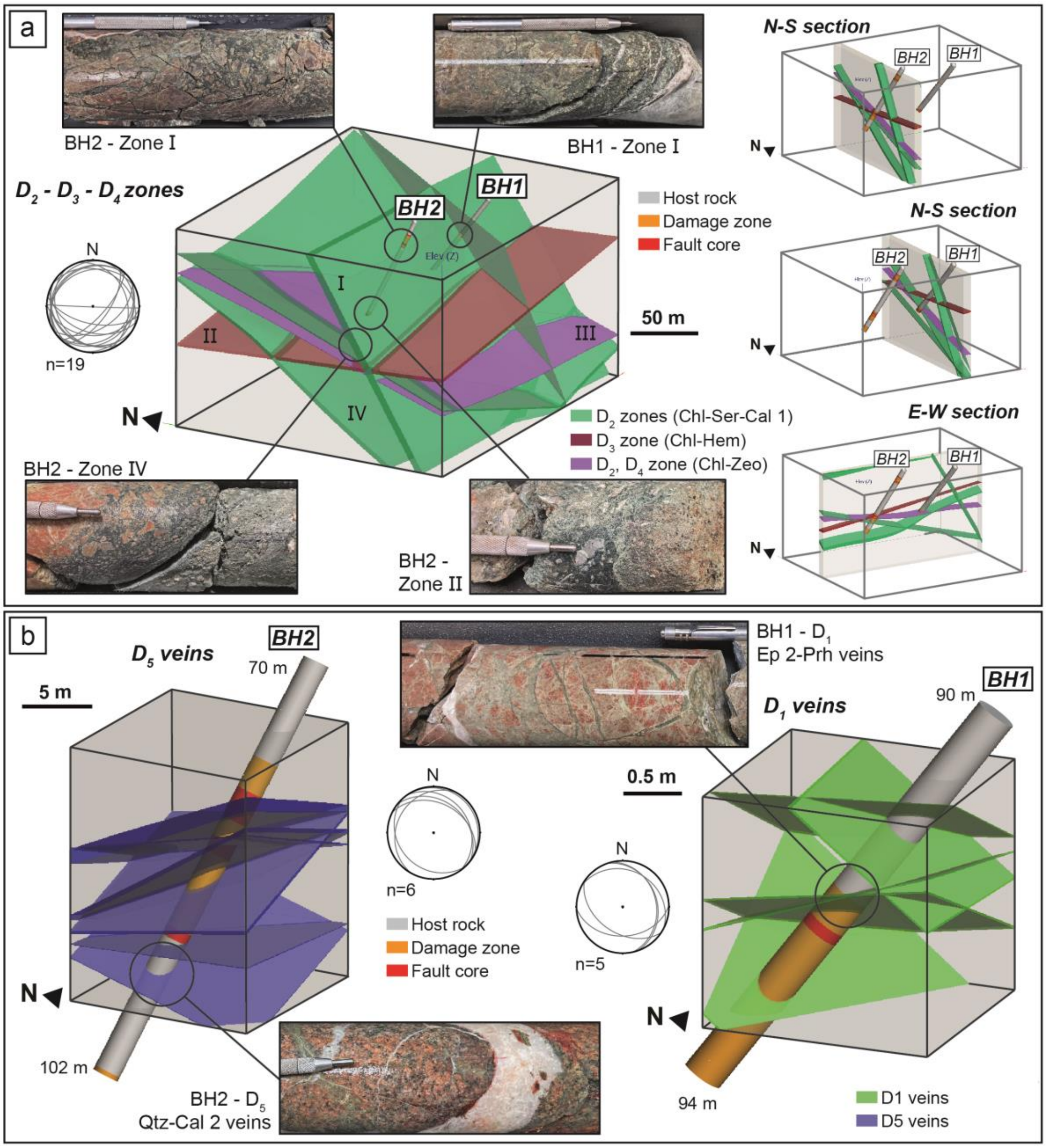

Figure 5.8. A) 3D model of major intersected brittle structures (green, red, and purple planar volumes) in drill holes BH1 and BH2. Modelling completed in Leapfrog using bounding deformation features, such as shear fractures (plotted in included stereonet). Zones I to IV are representative of the deformation zones present in one or both the drill holes, descriptions include in the text. N-S and E-W cross sections included on the right of the figure, with the N-S sections taken through each drill hole. B) 3D models at different scales to (a), with both quartz-calcite (D5) and epidote-prehnite (D_1) modelled from drill core structures (included in associated stereonet plots).

The modelled zones crosscut each other, assumed here with no offsets or lateral terminations. Their true thicknesses range from 1 m to 6 m and exhibit some dip and thickness variation (as shown in N-S and E-W sections in Figure 5.8a). The zones display different orientation trends: with the D_2-related zones moderately S to SE-dipping, and D_3-related zones shallowly W-dipping.

To explore Smøla's deformation features across scales, 3D models were created for selected intervals, such as: D_5 quartz-calcite veins in BH2 (~10 m scale) or epidote-prehnite (D_1) veins in BH1 (~1 m scale) (Figure 5.8b). These models, along with Figure 5.8a (~100 m scale), demonstrate the systematic to semi-systematic fracture arrays at various scales. Additionally, they illustrate differences in aperture widths and potential strike extents among structures associated with different deformation episodes: D_2 structures, for example, typically have the widest apertures and longest strike extents, while D_1 features exhibit the smallest apertures and the least lateral continuity on average but have the highest number of fractures per modelled volume.

5.7 K-Ar geochronology and X-ray diffraction

Seven fault gouge samples (Table 5.2, Figure 5.9) were collected from drill holes BH2 (SK2008, SK2012, SK2015), BH4 (120714) (Figure 5.4), and outcrops on Smøla island (SK1024_1, SK1029_1, SK1033_1) for dating of potential authigenic and synkinematic potassium (K)-bearing clays. The dated samples compositions by X-ray diffraction (XRD) is shown in Figure 5.10, with the K-Ar dating results in Table 5.3 & Figure 5.11a are sub-divided by grain size fraction for each sample (<0.1 to 6-10 µm). The orientations of the sampled structures (Figure 5.11b) is provided in the text as dip inclination (0-90°) and dip direction (0-360°). None of the samples have associated kinematics, apart from sample SK1033_1. The samples descriptions are ordered by interpreted deformation episode, with the full sample characterisations available in Appendix A.

5.7.1 4.3.1 Field relationships and XRD results

Sample SK2012 is from a 25 cm-wide foliated gouge/phyllite to cataclasite interval (Figure 5.9a), oriented 15/320, in monzogranite. The zone has strong chlorite and sericite (D_2) mineralisation and host rock fragments. XRD results indicate the K-Ar ages are provided by K-bearing illite/muscovite and smectite. Both illite/muscovite and smectite content increases with decreasing grain size fraction, with highest abundance in the <0.1 µm fraction. Quartz is present in the coarser size fractions (0.4-2 to 6-10 µm), deriving from groundmass or host rock fragments.

Sample SK2015 is from a 20 cm-wide well-milled, foliated, clay-rich gouge zone (Figure 5.9b), oriented 37/183. The interval is within a well-defined damage zone of highly fractured monzogranite. The gouge has abundant host rock and quartz-calcite vein fragments. XRD results show the K-Ar ages derived from illite/muscovite, smectite, and potassium feldspar. The illite/muscovite content increases in the finer fractions. The coarser fractions (2-6 to 6-10 µm) are quartz-dominated, with minor calcite and potassium feldspar.

Table 5.2. Summary of K-Ar samples collected from either drill holes BH2 and BH4, or field stations on Smøla island.

Sample	Site/BH	Host rock	Orientation (dip/dip direction)	Deformation episode	Description
SK2012	BH2	Monzogranite, fault rock	15/320	D_2	From 108.3 m in BH2, involving a sheared and foliated gouge band, possibly phyllitic.
SK2015	BH2	Monzogranite, fault gouge	37/183	D_2	From 109.74 m in BH2, from a well-milled gouge, some residual veins, and lithic fragments present (possibly from the host monzogranite).
SK1029_1	1029	Monzodiorite, fault gouge	80/166	D_2, D_3	Gouge sample, green, chloritic, structure sub-parallel/inclined to major E-W structure.
SK2008	BH2	Monzogranite, fault rock	10/285	D_3	From 79.7 m in BH2, involving a hydraulic breccia to crackle breccia with hematite-bearing veins.
SK1033_1	1033	Gabbro	80/155?	D_3	Possible fault gouge within a saprolite zone.
120714	BH4	Diorite, clays	54/059	D_3, D_4	Collected at 31.3 m in BH4, involving friable gouge in shear band, clay rich, with zeolite veins.
SK1024_1	1024	Diorite, fault gouge	73/179	D_2, D_3	Sample from upper portion of exposed sub-vertical structure; well-developed gouge.

Field sample SK1029_1 is from a ~5 cm-wide chlorite-clay-rich gouge zone, within monzodiorite (Figure 5.9f), oriented 80/166 and extending >10 m. The zone is proximal and inclined to a major E-W structure, mapped as a second-order L3 lineament (Figure 5.2). XRD results indicate the K-Ar ages are from smectite, illite/muscovite, and zeolite. The size fractions are dominated by chlorite-smectite mixed clay (tosudite). Illite/muscovite is absent in finest fraction, but present in the 0.1-0.4 to 6-10 µm fractions. Zeolite is abundant in the coarser fractions (2-6 to 6-10 µm).

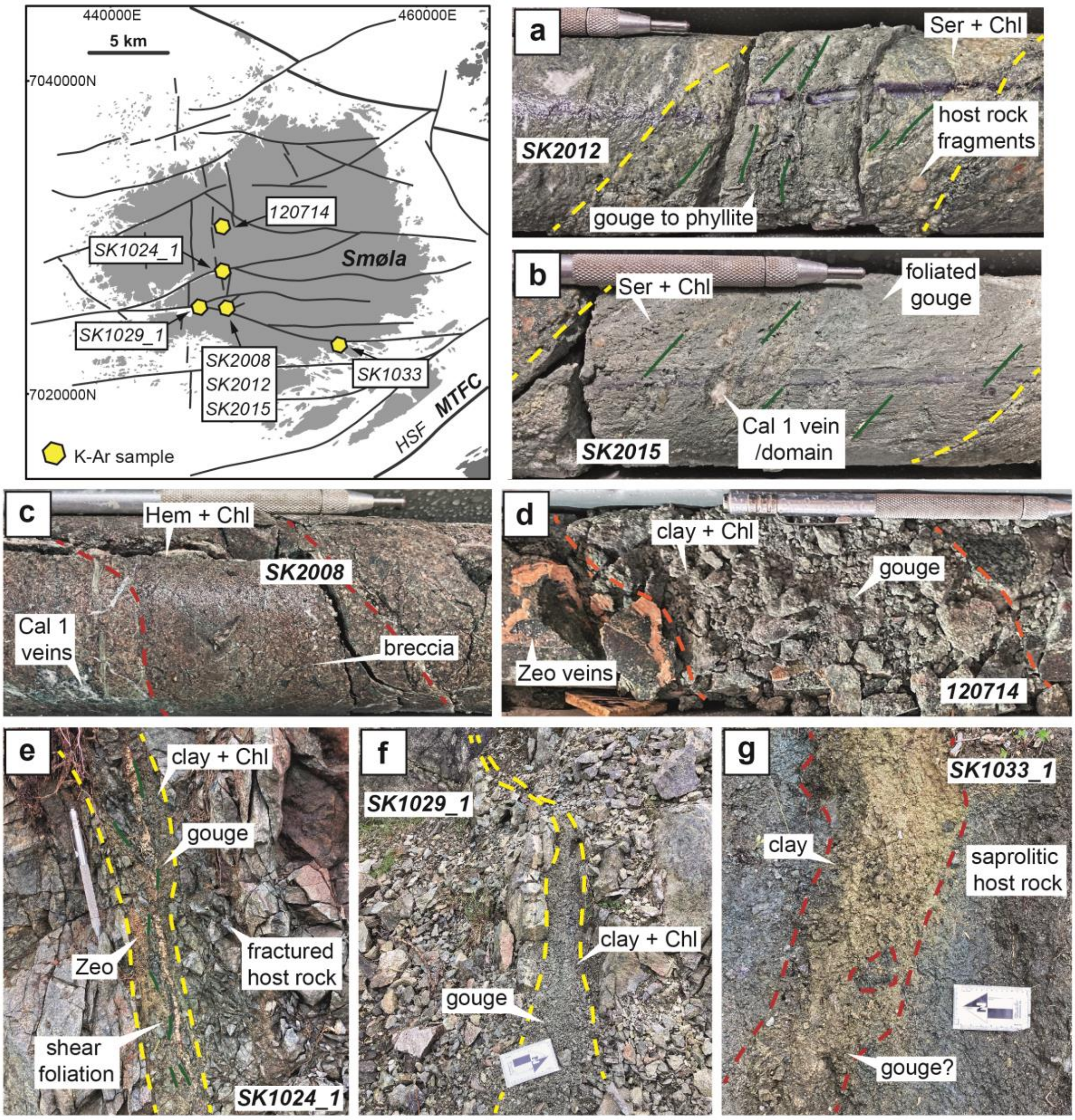

Figure 5.9. The locations of the collected K-Ar samples on Smøla, relative to mapped lineaments. A-G) K-Ar sample sites, with samples SK2008, SK2012, and SK2015, 120714 collected from diamond drill core, and samples SK2024_1, SK1029_1, and SK1033_1 collected from field locations. Map adapted from DTM data courtesy of the NGU. Scratch pen for scale = 13 cm, or scale bar arrow = 10 cm.

Sample SK2008 is from an 8 cm-wide indurated gouge to micro-vein breccia (Figure 5.9c), oriented 10/285. The interval is within a ~5 m wide damage zone of chlorite-hematite (D_3) mineralised and altered monzogranite. XRD results show the K-Ar ages derived from illite/muscovite, smectite, and potassium feldspar. Hematite is present in all size fractions except the <0.1 µm fraction. Illite/muscovite is present in all fractions but a minor component in the <0.1 µm fraction. Smectite increases towards the finer fractions. The coarser fractions (2-6 to 6-10 µm) contain potassium feldspar, calcite, and quartz.

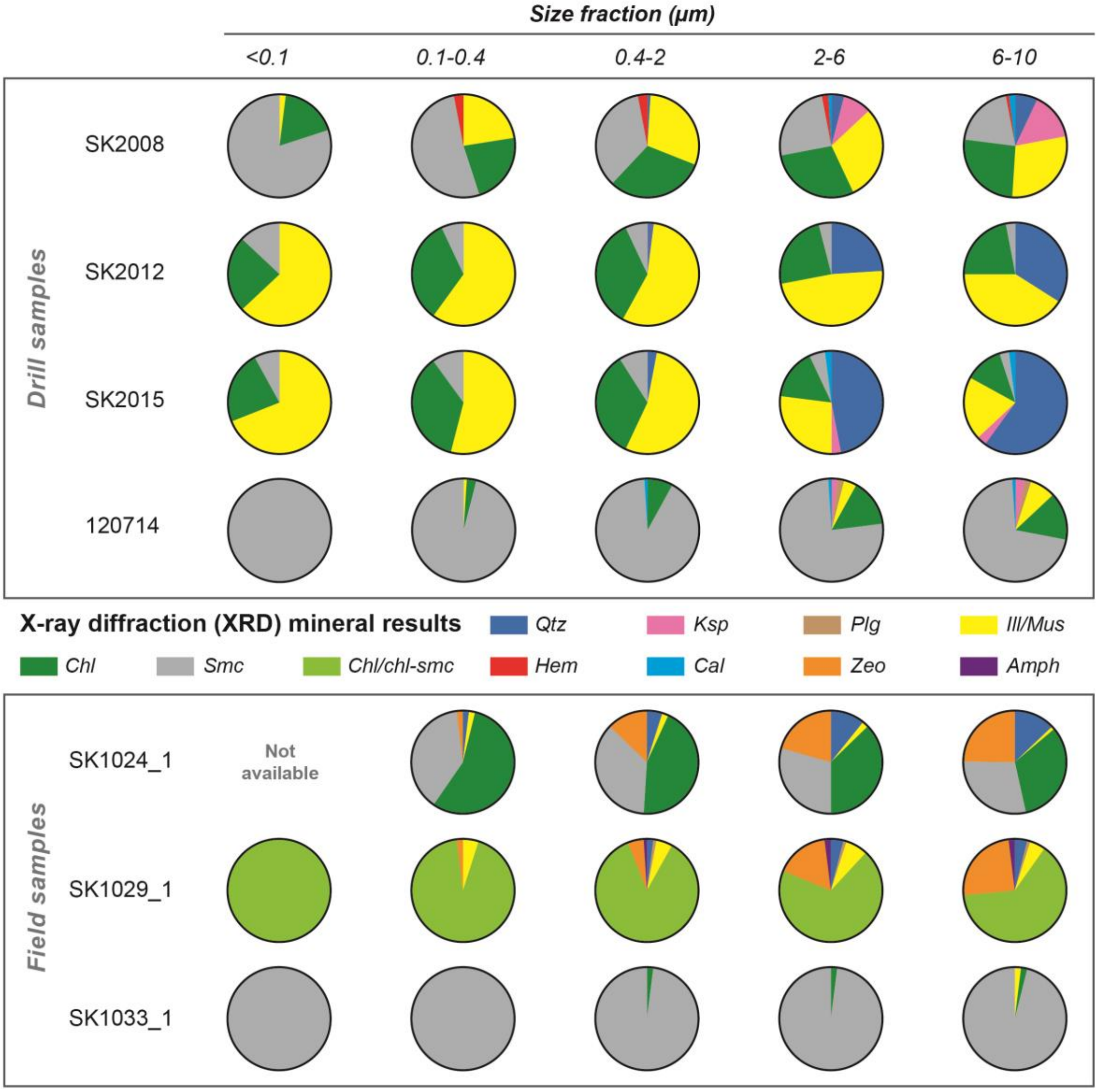

Figure 5.10. Pie charts with mineral compositions by weight percent (wt%) from X-ray diffraction results of the K-Ar samples. Mineral abbreviations: Qtz = quartz, Ksp = Potassic feldspar, Plg = plagioclase, Ill/mus = illite/muscovite, Chl = chlorite, Smc = smectite, Hem = hematite, Cal = calcite, Zeo = zeolite, Amp=amphibole. Note that due to poor crystallinity and/or the lack of structural data for mixed-layer clay minerals, only semi-quantitative assessments could be made.

Field sample SK1033_1 is from a ~25 cm-wide possible weathered gouge zone within a saprolite horizon (Figure 5.9g), bound by adjacent chloritic-hematite slickensides, oriented 80/155 with low confidence (due to poor preservation), possibly dip-slip (slickenlines too subtle to orient accurately). XRD results indicate the K-Ar ages come from smectite and illite/muscovite. The size fractions are dominated by smectite, with minor chlorite, and illite/muscovite only present in coarsest fraction (6-10 µm).

Sample 120714 is from a 40 cm-wide friable clay-rich gouge within a shear band, oriented 54/059, in diorite, with cross-cutting zeolite veins (Figure 5.9d). XRD results show the K-Ar ages derived from smectite, illite/muscovite, and potassium feldspar. Smectite is dominant in all size fractions, comprising the <0.1 µm fraction entirely. Illite/muscovite is present in coarser fractions, and the 0.1-0.4 µm fraction. Potassium feldspar, plagioclase, and calcite are present in the coarser fractions (2-6 to 6-10 µm).

Field sample SK1024_1 is from a ~8 cm-wide foliated chloritic gouge zone (Figure 5.9g), oriented 73/179, within an 8 m wide damage zone with hematite fractures. The gouge zone, a D_2 to D_3 feature, is crosscut by zeolite veins. The XRD analysis for the finest fraction was not possible due to insufficient material. XRD results however indicate the K-Ar ages come from smectite, illite/muscovite, and zeolite. Minor illite/muscovite is present in all size fractions, with major amounts of smectite and chlorite. Zeolite and quartz are particularly abundant in the 0.4-2 to 6-10 µm size fractions.

4.3.2 K-Ar geochronology results

The K-Ar geochronology results (Figure 5.11 & Table 5.3) indicate that the samples can be grouped into four groups associated with mineral assemblages and deformation episodes (D_2 to D_4):

Associated with D_2, samples SK2012, SK2015, and SK1029_1 returned K-Ar ages for the finest fractions (<0.1 µm) of 196.1 ± 2.8 Ma, 201.4 ± 2.9 Ma, and 204.1 ± 3.7 Ma respectively. These ages likely correspond to authigenic illite-muscovite-smectite. Samples SK2012, SK2015 yielded coarsest fraction (6-10 µm) K-Ar ages of 290.7 ± 4.4 Ma and 287.0 ± 4.7 Ma respectively. Both samples SK2012, SK2015 have similar inclined age spectra curves with a plateau at ~300 Ma. The plateau implies an inherited component (potentially inherited illite/muscovite) from an earlier tectonic episode. Sample SK1029_1 returned a much younger coarsest fraction K-Ar age of 218.2 ± 3.8 Ma. The younger ages are attributed to zeolite, with potentially radiogenic ^{40}Ar loss from the crystal structure, leading to lower age results (e.g. Levy and Woldegabriel, 1995).

Associated with D_3, samples SK2008, SK1033_1 yielded <0.1 µm fraction K-Ar ages of 99.6 ± 1.8 Ma and 128.1 ± 11.8 Ma respectively, associated with likely authigenic illite-muscovite-smectite. The coarsest fractions provided ages of 195.2 ± 3.1 Ma and 263.3 ± 5.4 Ma respectively. The SK2008 fractions 0.4-2 to 6-10 µm have ages clustering at ~200 Ma, coinciding with the finest fraction ages for samples SK2012, SK2015, and SK1029_1, implying D_2 inheritance. The SK1033_1 ages may reflect authigenic clay growth during saprolite formation or hydrothermal activity, suggesting this sample's results should be treated with caution.

Table 5.3. K-Ar analysis age results of the Smøla samples by size fraction.

Sample		40Ar*				K			Age Data	
	Fraction (µm)	Mass (mg)	mol/g	σ (%)	40Ar* %	Mass (mg)	wt %	σ (%)	Age (Ma)	σ (Ma)
SK2008	<0.1	2.088	2.894E-10	0.57	40.4	50.6	1.63	1.76	99.6	1.8
	0.1-0.4	2.036	3.821E-10	0.54	53.9	51.6	1.46	1.78	144.9	2.6
	0.4-2	2.096	6.728E-10	0.50	77.2	52.8	1.79	1.74	204.7	3.5
	2-6	3.604	1.161E-09	0.46	89.6	52.2	3.06	1.64	206.5	3.3
	6-10	2.672	1.376E-09	0.47	94.7	51.0	3.85	1.58	195.2	3.1
SK2012	<0.1	2.016	2.065E-09	0.49	90.3	51.0	5.75	1.43	196.1	2.8
	0.1-0.4	3.654	2.221E-09	0.46	92.4	52.0	5.46	1.44	220.5	3.1
	0.4-2	2.938	2.716E-09	0.46	95.6	52.8	5.40	1.44	268.9	3.8
	2-6	2.524	2.536E-09	0.47	98.3	50.9	4.50	1.53	298.8	4.4
	6-10	2.452	2.106E-09	0.47	98.6	50.9	3.85	1.58	290.7	4.4
SK2015	<0.1	2.596	2.036E-09	0.47	90.4	51.5	5.51	1.44	201.4	2.9
	0.1-0.4	3.048	2.202E-09	0.46	93.1	51.3	5.33	1.46	223.7	3.2
	0.4-2	3.122	2.522E-09	0.46	95.5	51.6	5.16	1.47	261.8	3.8
	2-6	3.612	1.832E-09	0.46	97.0	51.1	3.37	1.62	289.1	4.5
	6-10	2.466	1.370E-09	0.47	98.4	50.9	2.54	1.69	287.0	4.7
120714	<0.1	2.750	5.869E-11	1.24	8.2	50.7	0.44	1.91	74.7	1.7
	0.1-0.4	1.368	1.122E-10	1.26	14.5	50.7	0.58	1.90	109.0	2.4
	0.4-2	3.600	1.844E-10	0.47	28.8	50.8	0.77	1.88	132.6	2.5
	2-6	2.710	2.786E-10	0.45	51.6	50.1	1.11	1.85	138.8	2.5
	6-10	2.554	3.933E-10	0.42	51.0	52.6	1.41	1.82	153.6	2.7
SK1024_1	0.1-0.4	2.220	1.982E-10	0.58	42.3	50.5	0.67	1.92	162.1	3.1
	0.4-2	1.600	3.118E-10	0.59	31.1	50.4	0.95	1.89	180.5	3.4
	2-6	2.568	3.196E-10	0.45	42.9	52.6	1.00	1.88	176.1	3.2
	6-10	3.186	2.926E-10	0.42	53.2	54.6	0.99	1.88	163.5	3.0
SK1029_1	<0.1	2.618	5.023E-10	0.41	50.4	51.3	1.34	1.85	204.1	3.7
	0.1-0.4	3.728	5.895E-10	0.38	57.3	57.2	1.18	1.85	267.3	4.7
	0.4-2	3.136	9.189E-10	0.38	77.4	56.0	1.54	1.82	314.9	5.4
	2-6	2.582	8.275E-10	0.39	84.9	62.8	1.92	1.76	232.8	3.9
	6-10	1.636	8.246E-10	0.45	88.3	52.5	2.05	1.78	218.2	3.8
SK1033_1	<0.1	2.224	1.814E-11	9.36	0.8	51.7	0.08	1.97	128.1	11.8
	0.1-0.4	2.236	2.085E-11	7.31	0.9	51.4	0.09	1.97	126.0	9.2
	0.4-2	2.854	9.294E-11	1.33	5.0	53.2	0.21	1.96	234.5	5.2
	2-6	3.042	1.020E-10	0.91	9.0	60.3	0.22	1.95	247.2	5.0
	6-10	2.354	1.219E-10	0.98	8.6	54.5	0.25	1.95	263.3	5.4

Sample 120714, associated with D_3 and D_4, yielded a <0.1 µm fraction K-Ar age of 74.7 ± 1.7 Ma, and a 6-10 µm fraction age of 153.6 ± 2.7 Ma. The finest fraction age is likely authigenic, but the coarsest fraction age, owing to the presence of potassic feldspar and illite/muscovite may represent an inherited/protolithic age. The zeolite veins (not in the XRD results), crosscutting the sampled gouge, would have mineralised after the ~75 Ma age, indicating a possible upper limit on the timing of D_4.

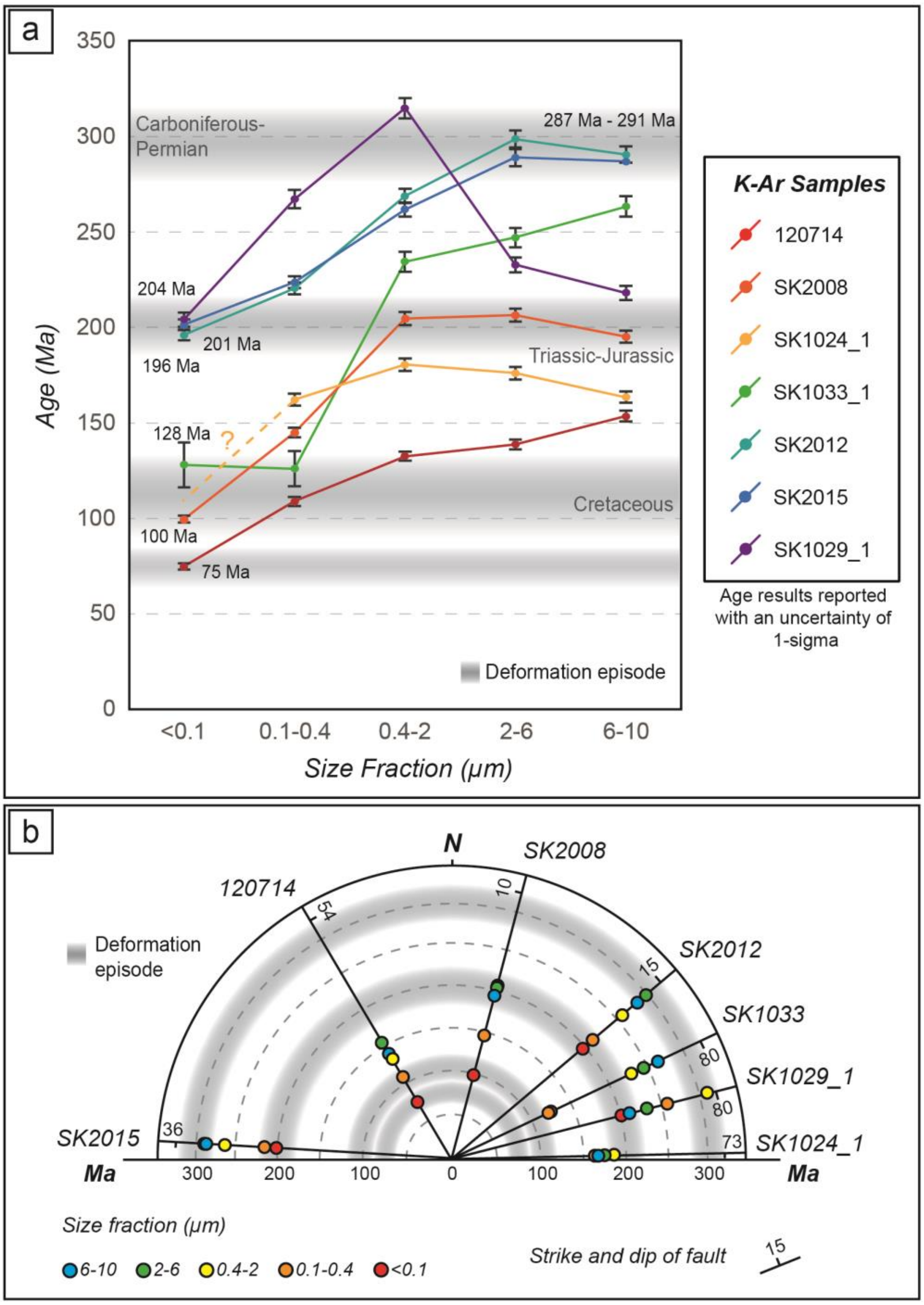

Figure 5.11. A) K-Ar age spectra results for the seven samples. Data are expressed by size fraction of the sampled medium against determined age, with age clustering indicating possible authigenic (and deformation) episodes; B) Radial plot showing dated samples with K-Ar ages and size fraction (coloured circles) plotted on lines indicating the strike orientations of sampled structures

Sample SK1024_1 lacked enough material for the <0.1 µm fraction and is for demonstrative purposes only. The K-Ar ages range from 162.1 ± 3.1 Ma (0.1-0.4 µm fraction) to 163.5 ± 3.0 Ma (6-10 µm fraction), with the oldest age (180.5 ± 3.4 Ma) associated with the 0.4-2 µm fraction. The age spectra curve on Figure 5.11a, a convex-upward shape, indicates the zeolite presence in the coarser fractions is also lowering ages, like sample SK1029_1.

Overall, the K-Ar age results by structure orientation (Figure 5.11b) indicate that the D_2-associated structures striking NE-SW, E-W, ENE-WSW yielded authigenic Triassic-Jurassic (~196 – 204 Ma) ages, with possible inherited Carboniferous-Permian (~287 – 291 Ma) ages. The D_3-associated structures striking NNE-SSW, ENE-WSW yielded authigenic Cretaceous (100 – 128(?) Ma) ages, with inherited Triassic-Jurassic (~200 Ma) material. Lastly, structures striking NW-SE, crosscut by later D_4 zeolite veins, yielded Cretaceous (75 Ma) ages.

5.8 Discussion

5.8.1 5.1 Polyphase evolution of Smøla and the passive margin

Based on our new multiscalar and multi-technique results, we propose an evolutionary tectonic history for Smøla (Figure 5.12) and discuss its implications for the evolution of the passive margin:

The D_1 epidote-prehnite mineralisation, although not directly dated in this study, has been shown in other areas of the Norwegian margin to have formed from syn- to post Devonian times until ~290 Ma (Indrevær et al., 2014; Seranne, 1992; Sherlock et al., 2004; Watts et al., 2023). The D_1 brittle structures (Figure 5.5a, b, & Figure 5.8b) rework primary host rock features, and are systematically offset by the D_2 to D_5 structures, indicating that epidote and prehnite mineralised prior to all other deformation episodes (Figure 5.7). The D_1 tensile veins or sinistral strike-slip features, striking ENE-WSW (subvertical to steep SSE dips, shallow-plunging slip lineations) (Figure 5.3), likely formed during post-Caledonian brittle sinistral transtension on the MTFC (Seranne, 1992; Watts et al., 2023) and WNW-ESE extension (represented on Figure 5.12).

Later, the NW-SE striking features (moderately to shallowly NE dipping), as well as the ~NNW-SSE to NNE-SSW striking features (steeply ~E dipping), being either normal dip-slip features or both dextral and sinistral (conjugate) features, may have formed because of local N-S to NNE-SSW shortening. This shortening direction is also implied by the Mid-Late Devonian development of E-W trending folds in the Edøyfjorden Basin Devonian rocks (Bøe et al., 1989 and Fossen, 2010) (Figure 5.12). From relative timing and structural data correlations, the lineaments L1, L3, and L4, may have formed during D_1, with later reactivations. Overall, despite being the least strike-continuous features (as shown in the 3D model in Figure 5.8b), D_1 is pervasive across Smøla, the Devonian-aged Edøyfjorden Basin, and the WGR to the SE of the MTFC (Figure 5.2a & b.I, II).

The D_2 sericite-chlorite-calcite structures (Figure 5.5c, & Figure 5.6d & e) are dated to ~204-196 Ma (finest fractions for samples SK2012, SK2015, and SK1029_1 on Figure 5.11). However, microstructural and field evidence (Figure 5.6d & e) and the plateau in the age-spectra graph for the two coarsest fractions for SK2012 and SK2015 (Figure 5.11a), suggest a possibility of an earlier inherited deformation episode at ~300 Ma. Early faulting-related sericitisation of host rock feldspar (e.g. Wibberley, 1999) could explain the coarsest fraction illite/muscovite content and this inherited age. As such, two deformation (sub-)episodes may be associated with the sericite-chlorite-calcite mineral assemblage, and thus tentatively to D_2. Considering these two possible deformation phases, we can sort the complex array of D_2 structures (Figure 5.3) into two structural frameworks: 1) The sinistral strike-slip ~E-W, and NE-SW striking features (moderately to steeply dipping ~N, SSW, NW), the normal faults striking ~N-S (moderately to steeply dipping W), and the ENE-WSW striking (steeply SSE dipping) reverse dip-slip features; and 2) the ENE-WSW striking (steeply SSE dipping) dextral strike-slip features, the ~N-S striking (steeply E dipping) reverse faults, and the ~E-W to NE-SW striking (moderately to steeply dipping ~N/S to SE) normal dip-slip features.

The first set of structures indicate sinistral strike-slip or transtension conditions along the MTFC, with ~WNW-ESE crustal extension and ~NNE-SSW shortening. This is largely consistent with the Late Carboniferous-Early Permian MTFC evolution as proposed by Seranne (1992) and Watts et al. (2023) (Figure 5.12). Furthermore, the ~N-S striking normal dip-slip features on Smøla have a similar geometry to the ~N-S extensional faults (Raudtinddalen Fault) off the VF, which have been associated with a similar age and kinematics (Watts et al., 2023). The moderately to shallowly south-dipping D_2 features in drill holes BH1 and BH2, as shown in 3D modelling (Figure 5.8a), likely coincide with the damage zone of the nearby major E-W structure. Adjacent to the drill holes, the major ~E-W structure also locally changes strike to a NW-SE trend (Figure 5.2b.I). The shallow dipping D_2 features, although possibly the result of local stress perturbations (e.g. Kim et al., 2004), may have formed from local shortening associated with the strike rotation of the major E-W structure (forming a restraining bend) (e.g. Cunningham and Mann, 2007) further supporting sinistral faulting.

Based on the above interpretation, the ~E-W, ENE-WSW, and NE-SW sinistral and reverse features may correspond to L2 and L3 (Figure 5.2b.I & II) second to third-order lineaments, and the ~N-S striking normal dip-slip features correlate with the L1 lineaments. Within this setting, the L3 lineaments could represent sinistral R and R' Riedel shears off the L2 lineaments (Figure 5.2b.I), with the L1 lineaments predominantly involving extensional features accommodating ~E-W/WNW-ESE extension. Additionally, during this phase, the L2 second-order lineaments which correlate with the major E-W structures and steep sinistral features (with sub-horizontal slip lineations) could also have formed as synthetic P-shears off the main MTFC trend (Figure 5.12). This earlier episode may therefore correspond to an overall NE-SW crustal stretching and rifting during the Late Carboniferous-Early Permian (timeline on Figure 5.12), resulting in the Late Palaeozoic basins such as the Froan Basin and Høybakken fault-related basin (Faleide et al., 2008; Kendrick et al., 2004; Peron-Pinvidic and Osmundsen, 2018).

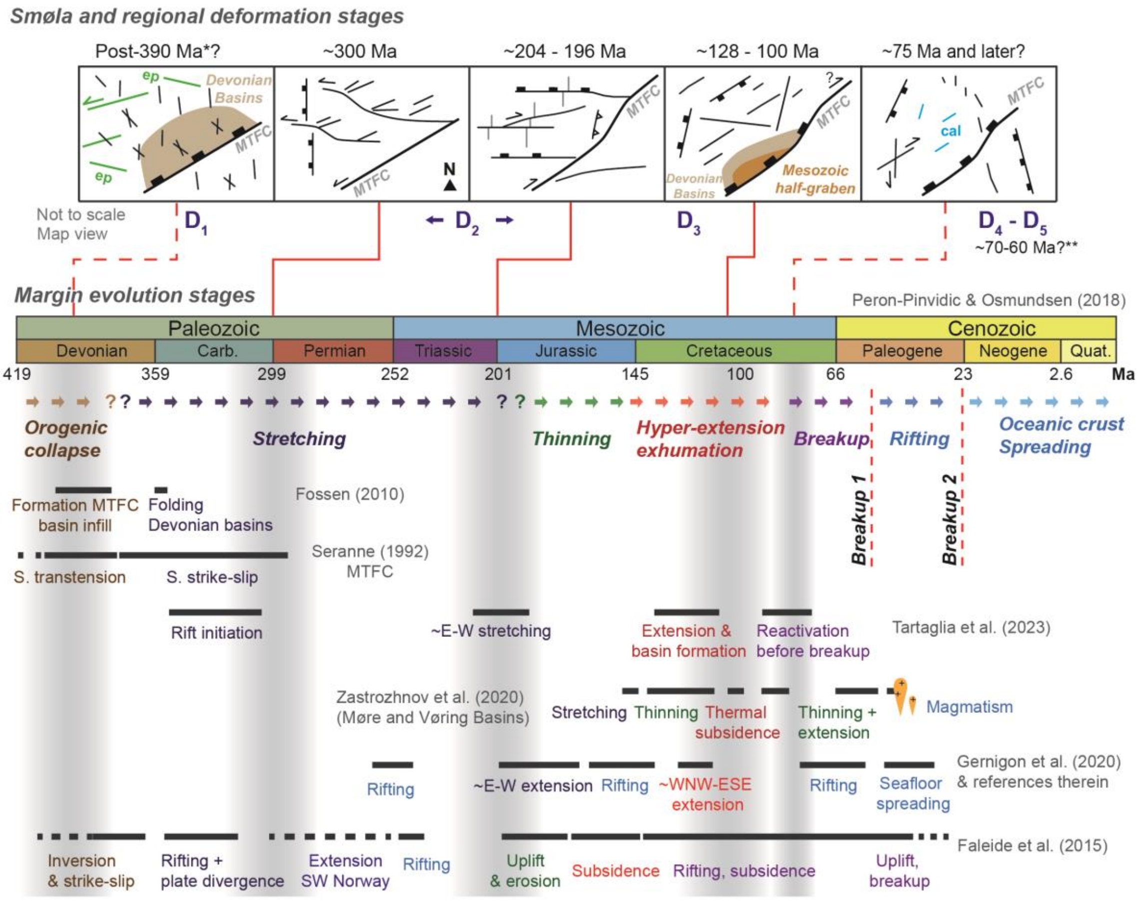

*Figure 5.12. Summary figure integrating this study's results, represented at the top, relative to other Mid-Norwegian passive margin evolution studies. The main margin evolution stages are adapted from Peron-Pinvidic and Osmundsen (2018). Ages provided by *Fossen et al. (2017), ** Hestnes et al. (2023).*

The second set of structures may be associated with the ~200 Ma ages constrained by the finest grain size fractions of the D_2 associated samples. These structures suggest dextral strike-slip along the MTFC, with an overall extension direction ~NNE-SSW. Moreover, the steeply-dipping ENE-WSW striking dextral strike-slip features (with a horizontal slip lineation), being sub-parallel to the HSF (MTFC) trend, also correspond to the L3 lineaments. These L3 lineaments do show rare dextral offsets of both the L1 and L4 lineaments, further suggesting some dextral kinematics is subtlety preserved (Figure 5.2b.I).

Therefore, reflecting the above, both the steep ~N-S striking reverse faults associated with D_2, and the major E-W structures (L2 lineaments) converging on the NE side of the Edøyfjorden Basin (Figure 5.2a) where there is a ENE-WSW to NE-SW strike rotation of the MTFC, may indicate a possible restraining band (associated with dextral strike-slip; represented on Figure 5.12). As such, the E-W structures could represent a positive flower structure forming off the MTFC due to local transpression (e.g. Cunningham and Mann, 2007). The ~E-W to NE-SW moderately dipping normal features (with steeply plunging slip lineations) however indicate that extensional conditions mostly prevailed over Smøla, and many of the ~E-W structures formed during earlier D_2 times, were reactivated as steep normal faults, or involve oblique dextral-normal kinematics. Additionally, the shallow D_2 structures 3D modelled in Figure 5.8a, dipping south towards the major E-W structures, might represent shallow-dipping antithetic or conjugate features formed during an extensional setting (related to late MTFC dextral faulting and extension). The shallow dipping D_2 structures in BH3 and BH4, in contrast, are within diorite and gneiss units (Figure 5.1b) and may involve the reactivation of foliation planes commonly associated with more micaceous intervals during either early or late D_2 times.

Dextral kinematics on the MTFC during the Jurassic was proposed by Grønlie and Roberts (1989), with Watts et al. (2023) suggesting it instead occurred later along the VF, during the Late Jurassic/Early Cretaceous. Dextral strike-slip faulting could have resulted from poorly constrained Triassic-Jurassic far-field compressive forces acting on a mechanically weak MTFC and associated structures. However, at that time, the region was experiencing the start of an extensional phase with regional subsidence (Peron-Pinvidic and Osmundsen, 2018; Tsikalas et al., 2012), in response to ~E-W crustal extension (Gernigon et al., 2020; Tartaglia et al., 2023) (shown on the timeline on Figure 5.12), which does not fit well with dextral kinematics, suggesting this tectonic phase remains uncertain.

Associated with D_3, the hematite-bearing structures (Table 5.2, Figure 5.9c, g) yielded finest size fraction K-Ar ages of between ~128 and ~100 Ma (Figure 5.11). Importantly, however, the ~128 Ma age from sample SK1033_1 may reflect local saprolitisation or hydrothermalism instead of deformation linked to D_3, even though most Norwegian margin saprolite ages fall within the Triassic/Jurassic time interval (e.g. Fredin et al., 2017; Knies et al., 2022; Olesen et al., 2023). The age spectra plateau for sample SK2008, corresponding to ~200 Ma (fractions 0.4-2 to 6-10 µm), and the finest fraction K-Ar ages for samples SK2012, SK2015, and SK1029_1, also suggest a D_2 inheritance within the coarser fractions of this sample. Thus, the D_3 outcrop structures (Figure 5.3) can be sub-divided into two groups: 1) the majority of the normal to oblique-normal features striking NNE-SSW (dipping steeply W) and NE-SW (dipping moderately to steeply SE), the ~ENE-WSW sinistral strike to oblique-slip features (moderately to steeply NNE, SE dipping, with inclined to sub-horizontal slip lineations), and the ~NW-SE striking reverse dip-slip features (moderately ENE, and steeply SSW dipping); and 2) ~N-S striking (steeply W dipping) reverse faults, and dextral features striking ENE-WSW (steeply NW dipping, inclined slip lineation, suggesting oblique-normal kinematics).

The first group of structures (dominated by dip-slip features, with steeply plunging slip lineations), being subparallel to the trace of the MTFC and the axis of the Edøyfjorden Basin, probably relate to a WNW-ESE to NW-SE extension, half-graben development, and Mesozoic sediment deposition within the Edøyfjorden Basin (Bøe and Bjerkli, 1989). A subset of pervasive L1 and L3 lineaments (mostly third-order), also correspond to the moderately SE or steeply W-dipping normal dip- to oblique-slip faults, either formed or reactivated during D_3 (suggested by their lack of offset across the earlier lineaments). The mostly sinistral strike-slip features, however, could involve the coeval reactivation of steeply dipping D_2 sinistral features within an extensional setting. Associated with these features, some lineaments also have limited horizontal offsets of the magnetic fabric over the D_3 lineaments (Figure 5.2b.II). Regionally, this relates to Jurassic-Cretaceous extension and exhumation, with regional rifting and basin development (Figure 5.12), leading to numerous Cretaceous basins (including the Møre and Vøring basins) (Faleide et al., 2008; Peron-Pinvidic and Osmundsen, 2018).

The second group of structures, particularly the steeply W-dipping ~N-S striking reverse faults, indicate ~E-W shortening. This corresponds to gentle folds (N-S oriented fold axes) in the Mesozoic basin rocks in the Edøyfjorden Basin (Bøe and Bjerkli, 1989). The steep NNW-SSE, N-S significant structures (red great circles on the D_3 'all planes' stereonets Figure 5.3) and the shallowly SE/W dipping thrusts, which is 3D modelled on Figure 5.8a, are also associated with this setting. Geometrically, these folds indicate Late Mesozoic dextral transpressional conditions after dip-slip faulting on the HSF/MTFC, with ~E-W shortening of the basin sediments (Bøe and Bjerkli, 1989). Watts et al. (2023)

however, associated the late dextral strike-slip kinematics with zeolite-calcite mineralisations on the VF (less distinct on the HSF; D_4 in this study).

The D_4 zeolite and calcite structures were not dated in this study (Table 5.2, Figure 5.9d, & Figure 5.11). However, these veins would have formed after ~75 Ma owing to cross-cutting relationships (Figure 5.9d). Tartaglia et al. (2023) and Watts et al. (2023) noted similar zeolite-calcite mineralisation in other parts of the margin (Hitra and Runde islands) and on the Fosen Peninsula associated with the VF (only locally along the HSF). This mineralisation has been attributed to: I) earlier Mesozoic dextral strike-slip to transpressional faulting related to the N-S folds in the Edøyfjorden Basin (D_3 structures, this study); and II) later extensional dip-slip faulting on the HSF post-dating the zeolite-calcite features (Watts et al., 2023); or III) Late Cretaceous extension in the distal part of the rift margin (Gernigon et al., 2020; Tartaglia et al., 2023). The D_4 NNE-SSW and ENE-WSW sinistral/dextral faults, and associated L1 and L3 lineaments may therefore preserve evidence of the earlier D_3 Mesozoic (Jurassic) dextral strike-slip movement on the MTFC, and the NNE-SSW to NE-SW normal features (dipping ESE/W), with corresponding L1 and L4 lineaments, attributed to a later D_4 Cretaceous to Late Cretaceous (NW-SE) extension.

Representing the last Cretaceous-Palaeocene deformation episode, the D_5 quartz-calcite veins (Figure 5.5f, & Figure 5.6h & i) are similar to calcite veins U-Pb dated in W Norway and the WGR (Hestnes et al., 2023). Different veins oriented NE-SW yielded ages between ~90 Ma and ~80 Ma, associated with Cretaceous reactivation of the MTFC; ~NW-SE (and NE-SW) veins formed between ~70 Ma to 60 Ma, associated with regional uplift possibly related to the doming of the proto-Icelandic plume; and NE-SW veins forming <50 Ma, associated with different Cenozoic extensional processes (lithospheric flexure, uplift from far-field tectonic stresses) (Hestnes et al., 2023).

The D_5 structures, mostly normal dip-slip features or tensile veins, strike NE-SW (dipping steeply to moderately NW/SE), and NW-SE (steeply NE dipping) (Figure 5.3), and correspond to the L3, L4, and late L1 lineaments. These structures and lineaments are mostly late reactivations of older features and are present in all parts of Smøla and SE of the MTFC (HSF) in the WGR (Figure 5.12). Overall, they suggest ~E-W to NE-SW crustal extension. Similar to these D_5 structures, and likewise indicating a late timing for D_5, Bøe and Bjerkli (1989) also documented NW-SE striking normal faults (SW/NE-dipping) offsetting Mesozoic sediments within the Edøyfjorden Basin. Based on geometry and timing, the D_4 and D_5 structures potentially relate to both a Cretaceous reactivation of the MTFC and the Cretaceous-Palaeocene rifting preceding the break-up of Greenland and Norway (Faleide et al., 2008). Importantly, the D_4 and D_5 features are subparallel to extensional structures offshore, particularly to the Klakk Fault Complex on the western side of the Frøya High, and the Halten Terrace, as well as the HD to the NW of Hitra and Frøya, suggesting a temporal and genetic association.

5.8.2 Smøla as an analogue for similar offshore basement volumes

Smøla island represents an ideal onshore analogue for offshore basement highs in the area. The Frøya High, offshore Norway, as an example (owing to it having similar basement rocks as Smøla), is likewise bound by major structures, such as the Klakk Fault Complex (Figure 3.4), a major west-dipping extensional fault zone (Muñoz-Barrera et al., 2020). The Frøya High experienced a comparable polyphase deformation related to crustal stretching and thinning from the mid-Carboniferous to the Late Cretaceous-Palaeocene rifting (Faleide et al., 2008, 2015; Peron-Pinvidic and Osmundsen, 2018). To unravel its complex tectonic history, this structural high would therefore require a similar approach as our Smøla study. Although numerous drill holes have been completed along the mid-Norwegian margin, with at least three drill holes on Frøya (e.g. Slagstad et al., 2008; Bunkholt et al., 2022), the quality of the drill hole material is poor (only rock cuttings or rock plugs) (Muñoz-Barrera et al., 2020). Similarly, margin-wide geophysical (magnetic, gravity, and 2D, 3D seismic reflection surveys) datasets are also available (Muñoz-Barrera et al., 2020; Skilbrei et al., 2002), but most will only afford the ability to interpret at or above the seismic resolution-scale. The advantage, therefore, of using an onshore analogue such as Smøla is the access and the availability of numerous datasets, without these limitations.

Moreover, investigating fractured and weathered basement is crucial for understanding basement-hosted oil and gas reservoirs or fluid pathways (Trice, 2014; Trice et al., 2022). The petrophysical attributes of various deformation features associated with the D_1 to D_5 episodes could significantly impact fluid migration or storage. As these features exhibit cross-cutting relationships and different orientation trends, structural permeability anisotropy is clearly present in the Smøla basement volume. Therefore, using an onshore analogue to produce high-resolution structural characterisations aided by the absolute time dimension, may be crucial in the future understanding of basement-hosted plays offshore.

5.9 Conclusions

The integration of various methodologies and data types including multiscalar geophysical, drill core, outcrop, 3D modelling, microstructural data, and geochronological results, give the following key conclusions:

1) From regional to microscale evidence, we have identified five distinct tectonic episodes since the Devonian affecting Smøla associated with specific mineral assemblages and structural trends (Figure 5.12):
    I. The earliest D_1 episode is associated with epidote-prehnite syn- to post-Devonian ENE-WSW striking (subvertical to steep SSE dips) tensile veins and sinistral strike-slip features, from brittle sinistral transtension along the MTFC. A later ~N-S contraction resulted in NW-SE (moderate to shallow NE dips) normal features, and ~NNW-SSE to NNE-SSW (steep ~E dips) strike-slip features.
    II. The D_2 sericite-chlorite-calcite structures document two brittle-ductile phases, the first during the Carboniferous (~300 Ma), and a later during the Late Triassic-Early Jurassic (~204-196 Ma). The first phase accommodated sinistral strike-slip/transtension along the MTFC, associated with ~E-W and NE-SW sinistral strike-slip features (moderate to steep ~N, SSW, NW dips), ~N-S normal faults (moderate to steep W dips), and ENE-WSW reverse faults (steep SSE dips). The second phase involved possible dextral strike slip along the MTFC (with local transpression related to a restraining bend east of the Edøyfjorden Basin), associated with ENE-WSW dextral strike-slip features (steep SSE dips), ~N-S reverse faults (steep E dips), and ~E-W to NE-SW normal features (moderate to steep ~N/S to SE dips).
    III. The D_3 chloritic-hematite breccias and gouges are due to Cretaceous (~128-100 Ma) WNW-ESE to NW-SE extension and half-graben development and are coeval with Edøyfjorden Basin sediment infill. This episode is characterised by mostly dip-slip normal to oblique-normal features striking NNE-SSW (steep W dips), NE-SW (moderate to steep SE dips), the ~ENE-WSW oriented sinistral features (moderate to steep NNE, SE dips), and the ~NW-SE reverse faults (moderate to steep ENE, SSW dips). A possible later ~E-W shortening during dextral transpression on the MTFC also caused ~N-S trending folds within Mesozoic sediments (Edøyfjorden Basin) and ~N-S striking D_3 reverse faults (steep W dips).
    IV. The D_4 hematite-zeolite-calcite structures form after ~75 Ma and are associated with NNE-SSW to NE-SW striking normal dip-slip faults and tensile veins (moderate to steep ESE/SE, W dips). These structures developed during Cretaceous to Late Cretaceous ~E-W crustal extension. Additionally, D_4 may have accommodated late Mesozoic dextral strike-slip movement on the MTFC, which is related to NNE-SSW and ENE-WSW striking sinistral/dextral features (moderate to steep ESE/NNW dips).

   V. D_5, a possible Cretaceous to Paleogene episode, is associated with NE-SW (moderate to steep NW/SE dips), and NW-SE (steep NE dips) quartz-calcite shear (normal dip-slip) and tensile veins. These veins crosscut all previous deformation features. The D_5 features are likely to have formed during continued ~E-W/ NE-SW crustal extension related to reactivation of the MTFC and rifting preceding the Greenland-Norway break-up.

2) Using the drill logging results and the temporal constraints of this study, 3D modelling has revealed the complex geometric characteristics of basement deformation. The modelling allowed several deformation zones to be modelled, with four zones correlated between the BH1 and BH2, characterised by epidote veins (D_1), chlorite-sericite foliated gouge (D_2), chlorite-hematite breccia (D_3), and zeolite-calcite veins (D_4). For comparison, models were produced at scales of 100 m, 10 m, and 1 m based on D_2-D_4, D_5, and D_1 features. These models highlight how the D_2 structures possess the greatest size/strike extents, and the D_1 features the most localised. Additionally, the modelling provides indications that some of the zones (D_2, D_4) can be linked to adjacent major structures, such as inclined splays from the nearby major E-W structures.

This study presents a method for understanding the tectonic evolution and structural characterisation of basement volumes with complex geological histories. The approach used could be valuable for studying offshore structures, such as the Frøya High, and other fracture-hosted unconventional hydrocarbon reservoirs associated with basement highs.

Chapter 6: Interlude: transitioning from deterministic descriptions to stochastic modelling

As this thesis involves two main parts, I will briefly describe the shift from the observational (and deterministic) aspects of the study (Chapter 5) to the stochastic and theoretical components (Chapters 7 & 8).

The findings from Chapter 5 build on published work by Hodge et al. (2024b), who used multiscalar geological observations to characterise fault and fracture (including vein) arrays on Smøla island. Those observations were combined with K-Ar dating and additional literature-sourced temporal information to establish a comprehensive and internally consistent tectonic framework to explain the sequential formation of Smøla's deformation features. That systematic work generated a fracture database, populated by hundreds of fracture measurements (orientation, aperture, and length) and fracture geological descriptions (including deformation style, type of fracture (tensile or shear), cross-cutting relationships, and mineral infill types), which is sorted by deformation episode (D_1 to D_5) with associated relative and absolute timing. That database is utilised in the following chapter (Chapter 7) and serves as the basis for deriving key input parameters for the stochastic modelling.

It is important to note, however, that some of the geological and observation-derived parameters had to be adapted and slightly modified to conceptualise and simplify the modelling process. This included the reallocation of the N-S lineament set (L_1) from D_1 (with later reactivations) to D_3, which is based on field evidence, such as the fact that the highest number of N-S striking structures had already been attributed to D_3 (Figure 5.3), many L_1 lineaments (linear topographical depressions) were spatially and geometrically associated with N-S striking hematite mineralised fractures, and the associated D_3 K-Ar sample (SK2008) derives from a NNE-SSE striking structure (similar enough to the N-S orientation). An additional implemented change for the stochastic modelling is that the D_4 and D_5 fractures (and related veins) were combined as geologically 'late' features and assigned a mean orientation NW-SE (planar dip/dip direction of 82/062).

The proceeding chapter is currently an accepted and 'in press' manuscript (Hodge et al., 2024a) in Communications Earth & Environment (Nature Portfolio). Owing to the journal's stringent word count limits, specific results relating to geological data processing and deterministic inputs were not included in the manuscript (and therefore not in the chapter) but, for the sake of completeness, are provided in Appendix B at the end of the thesis. Additionally, as Nature Portfolio journals do not commonly require a methodology section for brevity (unless essential), Chapter 7 also lacks a methodology section. Instead, the methods used in the paper have been adapted from the relevant online supplementary material from the manuscript and are included in the Methodology chapter (Chapter 4).

Chapter 7: Discrete fracture network modelling reconstructs fracture array and petrophysical property evolution through geological time

Matthew S. Hodge[1*], Mark Cottrell[2], Jochen Knies[3], & Giulio Viola[1*]

1: Department of Biological, Geological and Environmental Sciences, University of Bologna, Italy
2: WSP UK Ltd., United Kingdom
3: Geological Survey of Norway (NGU), Trondheim, Norway

This chapter is currently accepted and *in press* with Communications Earth & Environment (Nature Portfolio journal), with a preprint available with the reference: Hodge, M. S., Cottrell, M., Knies, J., and Viola, G.: Capturing secondary permeability and fracture connectivity through geological time by fracture back-stripping, Research Square [PREPRINT] (Version 1), https://doi.org/10.21203/rs.3.rs-4844693/v1, 2024. The manuscript text has been amended in places to align with the general format of the thesis.

7.1 Abstract

Fractured rock petrophysical studies rarely use temporal constraints, thus hindering fracture-related permeability and connectivity estimation during past geofluid migration. Here we present a conceptual approach, using a stochastic method incorporating absolute ages to reconstruct fracture arrays back in geological time. Generating 'grown' discrete fracture network models, we simulate the hydraulic behaviour of fractured rock volumes from the late-Cretaceous/Palaeocene to the Devonian, via progressive fracture back-stripping. We reveal that for the examined rock mass, maximum principal permeability increased through time from 9.47e-14 m^2 to 4.44e-13 m^2 (~3 orders of magnitude) along with the maximum horizontal permeability orientation shifting from NE-SW to NW-SE. Similarly, the connectivity metric increased with fracture saturation, peaking in the mid-Cretaceous. For comparison, dated offshore hydrocarbon secondary migration potentially coincides with our results. Back-stripping of time-constrained fracture sets is therefore a powerful method to investigate and quantify the dynamic evolution of petrophysical properties through geological time.

7.2 Introduction

Time constraints, such as the age of fracturing or veining, are seldom utilised in fractured media petrophysical studies (e.g. Engelder and Geiser, 1980; Laubach and Kira, 2009;

Olson et al., 2007, 2009) due to the general difficulty in deriving such constraints. In turn, the lack of absolute temporal information makes it challenging to constrain the chronological evolution of fracture-related petrophysical characteristics and to establish, for example, what role permeability and fracture connectivity played during past reservoir charging events. Applying time constraints to a well-studied fracture network may resolve which fracture sets, or combination thereof, afforded preferential fluid pathways at specific times. Furthermore, as geofluids may form and migrate episodically (Drake et al., 2009; Viola et al., 2009), the transient increase of fracture-related permeability (particularly in rocks with low matrix permeabilities) may be a key control on when and how fluid flow occurs. In addition to contributing to pure petrophysical studies, appreciating when higher secondary ('paleo'-) permeability formed in a rock volume, and when meaningful fracture connectivity was established, can, in turn, provide crucial insights into the dynamics of reservoir charging and geofluid flow histories, thus crucially aiding geofluid exploration efforts and informing strategies for fluid storage project developments.

Old crystalline basement rocks become progressively saturated with fractures over time when experiencing extended polyphase deformation (Figure 7.1), with new fractures forming, or inherited fractures accommodating different deformational episodes (Mattila and Viola, 2014; Munier and Talbot, 1993; Viola et al., 2012). The addition of each new fracture set to a pre-existing fracture network may change how geofluids flow through a host rock (Cox, 2005). Accordingly, a fractured rock volume today represents the sum of past configurations of fractures, chemical processes, petrophysical characteristics, and fluid flow states through geological time (Figure 7.1). Unfortunately, the study of selected portions of this typically long history generally requires unravelling a seemingly chaotic array of cross-cutting fractures by relative timing, which is difficult to do (Scheiber and Viola, 2018). Absolute dating techniques (e.g. Torgersen et al., 2015; Viola et al., 2016), however, can assist in establishing the formation ages of individual fracture sets, thus permitting us to separate out a specific fracture event in absolute time. Assessing the secondary structural permeability associated with these fractures at the time of their formation remains, however, always challenging. Indeed, secondary permeability is both transient and dynamic, being first created by fracturing and then rapidly destroyed by the precipitation of different vein-infilling minerals within relatively brief spans of geological time (Becker et al., 2010; Cox, 2005, 2010; Sibson, 1994). Even so, the opening and sealing of fractures can involve highly variable time-scales between 10^3 and 10^6 years or more depending on a variety of factors such as fracture aperture, fluid chemistry and flow (Becker et al., 2010; Fisher and Brantley, 1992; Lee and Morse, 1999; Williams and

Fagereng, 2022). Accordingly, evidence of paleo-permeability in fractured media today can be represented by sealed to vuggy, propped, and open fractures depending on the scale and age of the features (Becker et al., 2010; Forstner and Laubach, 2022; Hosono et al., 2022).

To address these challenges, we present a case study using a stochastic approach to reconstruct complex fracture networks in absolute time, replicating the transient permeability and fracture connectivity evolution of a selected rock volume. Fracture networks are routinely modelled using the discrete fracture network (DFN) approach (e.g. Dershowitz, 1984; Dershowitz and Einstein, 1988; Long et al., 1985; Welch et al., 2020), which relies on inputs such as fracture size, intensity, shape, orientation, and aperture (Davy et al., 2018) to generate statistically sound three-dimensional (3D) geometric fracture representations. These ‘static’ DFN models (representing the geometric description of one single geological moment) are then used to simulate a range of bulk rock petrophysical properties, such as permeability and fracture connectivity (Welch et al., 2020). To make our stochastic approach time-integrated, we implemented the 'grown' FracMan (WSP UK Limited, 2024) DFN modelling method (Bonneau et al., 2013; Libby et al., 2019, 2024), whereby modelled fractures ‘grow’ in sequential time steps, with dynamic interactions between fractures (Libby et al., 2019). Crucially, this approach can replicate complex fracture networks involving multiple fracture sets of different relative ages, with younger fractures being affected by older pre-existing fractures (Libby et al., 2019).

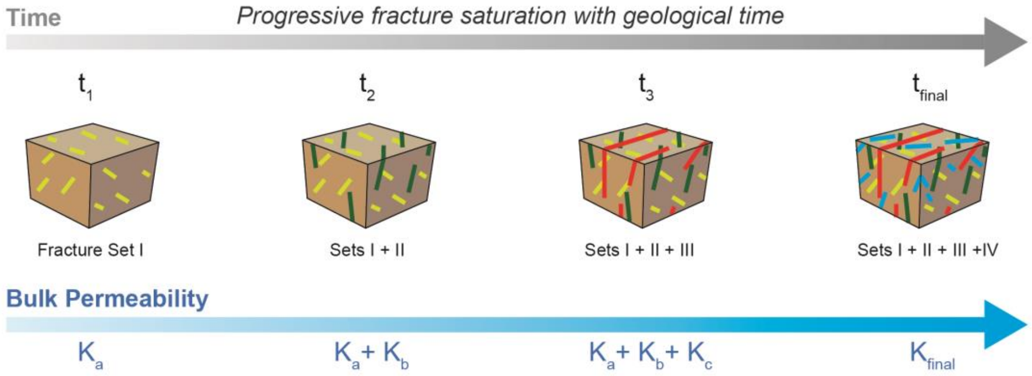

Figure 7.1. Conceptual framework of this study, highlighting the progressive saturation of the rock volume with fractures through time. Polyphase deformation leads to a progressive increase in fractures (coloured by set) through time (t). Corresponding to the sequential facture formation events, bulk rock petrophysical properties, such as secondary permeability (K) cumulatively evolve with time. The final time stage (t_{final}) representing the sum of previous fracture events, and current fractured rock volume, also coincides with the present secondary permeability quality.

As DFN modelling inputs we used a combination of multiscalar deterministic datasets and temporal constraints provided in Chapter 5 from Smøla island, mid-Norwegian passive margin (Figure 7.2a). Smøla is an ideal setting for this study, it being a crystalline basement exposure that has experienced at least five deformation episodes from the Devonian to Early Palaeogene, which formed complex fracture and fault arrays that have been comprehensively structurally characterised and dated (Hodge et al., 2024; Chapter 5). Using these inputs, we could therefore generate multiple DFN models representing distinct yet interacting fracture networks from the present-day back to the Palaeozoic, quantifying the associated and progressive evolution of key petrophysical and network properties through geological time.

Our modelling shows that bulk permeability and fracture connectivity generally increased through geological time with progressive fracture saturation. To test the approach and validate our results, we used known events of hydrocarbon secondary migration and their timing offshore Norway. Our modelled events of enhanced permeability and connectivity values do coincide with the onset of most secondary migration activity in the Mid-Cretaceous, thus showing how past reservoir charging can be related to progressive secondary permeability enhancement in response to connectivity development. Furthermore, our determined maximum permeability orientations (as part of the permeability tensor anisotropy) highlight which fracture sets may have represented important fluid pathways at that time.

7.3 Results

Smøla island (Figure 7.2a) is comprised of crystalline basement rocks (including monzogranite, diorite, gabbro; Chapters 3 & 5), which typically have low matrix permeability (between 10^{-18} – 10^{-19} m^2) (Selvadurai et al., 2005). To generate our DFN models, we used numerous input parameters, which are described below, and in more detail in the Chapter 4 and in Appendix B. Crucial to enabling us to undertake this study, we have made use of multiscalar spatial datasets (lineament trace mapping), high-resolution drill hole and field mapping datasets, and absolute dating of brittle deformation.

7.3.1 Deterministic inputs

Surface lineament traces on Smøla (Figure 7.2a) were mapped at four scales (deterministic trace maps: 1:500, 1:7 500, 1:25 000, and 1:100 000) on orthophoto imagery, digital terrain models (DTM), and aeromagnetic survey data. A total of 9554 fracture traces were picked and the distribution of their trace lengths over four orders of magnitude is best accounted for by a power-law relationship (Figure 7.3). The power-law distributions, indicating that the number of fractures of relative lengths are consistent across multiple scales (exhibiting a fractal fracture pattern), let us model the fracture networks at our chosen volume dimensions. Lineament trace mapping provided the fracture size distributions and scaling exponents for each of the four identified lineament sets, which are oriented ~N-S (to NNE-SSW), NE-SW, E-W, and NW-SE (to WNW-ESE). The details of these parameters are available in Chapter 4 and Appendix B.

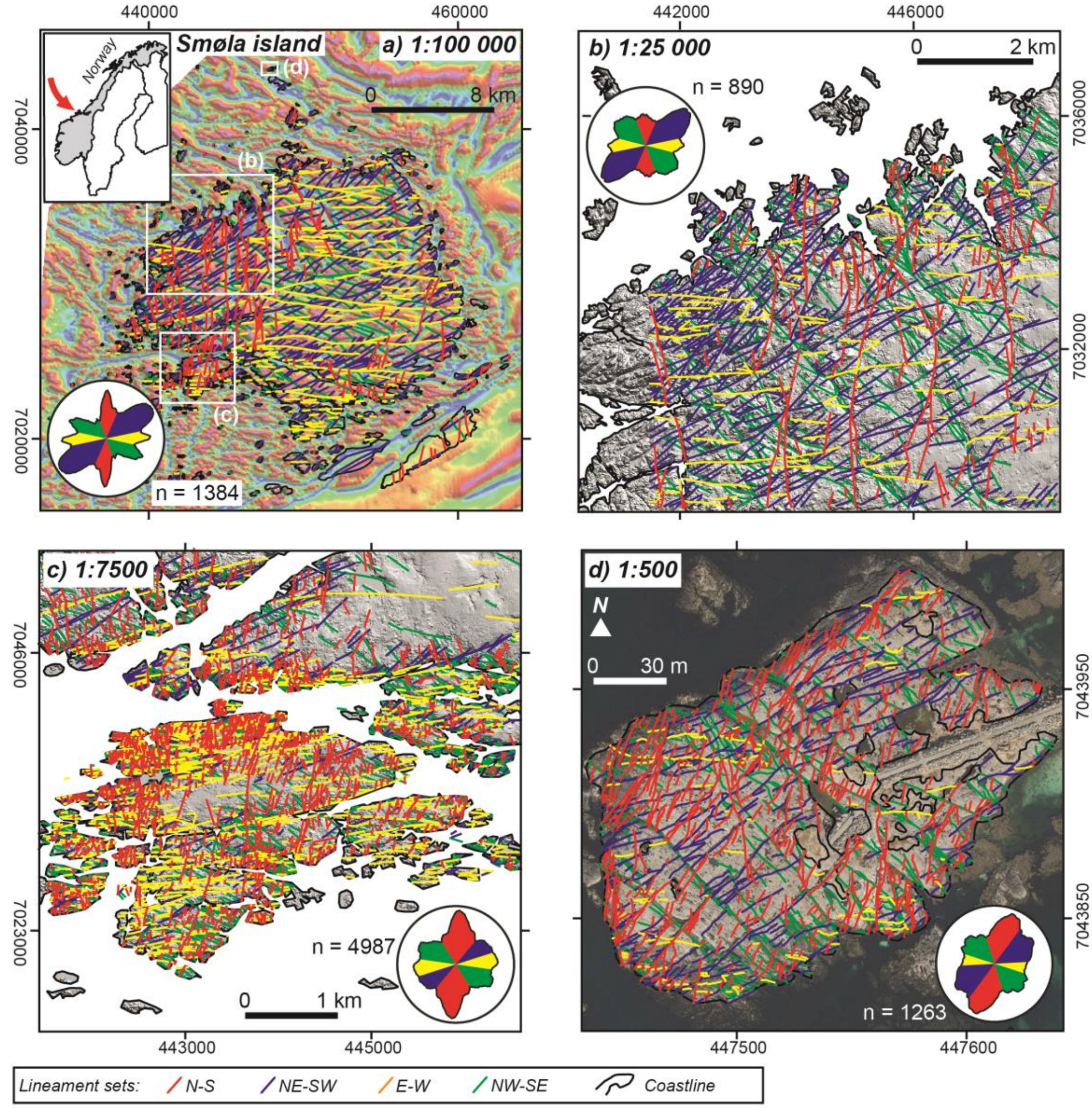

Figure 7.2. Trace maps over different portions of Smøla at different scales. Mapped lineament traces are coloured by azimuth trend (N-S coloured red, NE-SW coloured blue, E-W coloured yellow, and NW-SE coloured green), with associated rose plots showing the azimuth frequency trends. Panel (a) shows the 1:100 000 trace map, panel (b) the 1:25 000 trace map, panel (c) the 1:7500 trace map, and panel (d) the 1:500 trace map. Location of Smøla island study area within the mid-Norwegian passive margin is shown in panel (a). Locations of the (b) to (d) panels are shown with white boxes over Smøla island in panel (a). All the base maps, including geophysical imagery, digital elevation data, and orthophoto imagery is courtesy of the NGU.

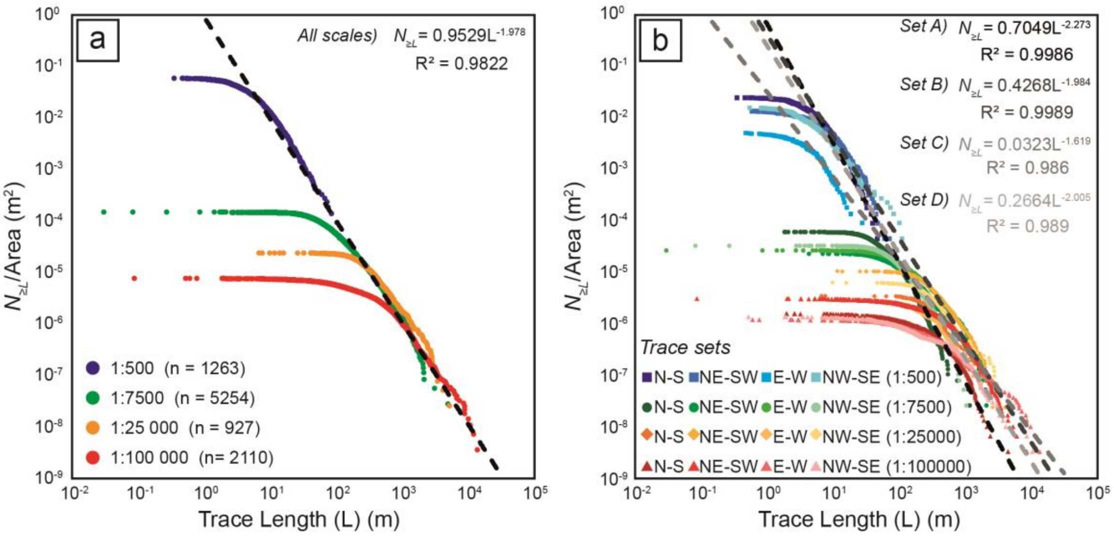

Figure 7.3. Cumulative fracture number vs. trace length log-log plots. (a) All the mapped lineament traces coloured by map scale; (b) mapped lineament traces sub-divided and coloured by azimuth trend and mapped scale. For panels (a) and (b) the associated linear regression lines are shown relative to each trace length distribution, with the regression equation and R² value.

In addition to the two-dimensional (2D) multiscalar datasets, downhole televiewer data from four oriented diamond drill holes (by the Geological Survey of Norway-NGU) afforded crucial *in-situ* geometric information on drill-intersected structures (Figure 7.4a). These data were sorted by pole to plane clusters, with twelve fracture sets identified over the four drill holes (Figure 7.4a). As already outlined in Chapter 5, Hodge et al. (2024) interpreted five deformation episodes (labelled D_1 to D_5) with associated systematic fracture sets on Smøla from field mapping and high-resolution logging of the same four oriented diamond drill holes. Each set is associated with distinct regional geometric trends, synkinematic mineralisations (Figure 7.4b & c), different deformation episodes, deformation ages derived from K-Ar geochronology of fault gouges (Chapter 5; Hodge et al., 2024) and U-Pb dating from other studies (Hestnes et al., 2023). Comparing both the downhole televiewer data to the field studies by Hodge et al. (2024), the following five fracture sets from the televiewer data were thus selected for the DFN modelling (Table 7.1 & Table 7.2) and associated with drill hole linear fracture intensities (P_{10}, refer to Chapter 4), fracture characteristics (from field work and drill logging), and ages:

i) The earliest D_1 fractures (mean pole plunge and trend orientation: 01/123) are mostly tensile veins (locally associated with cataclasite bands), infilled by epidote-prehnite mineralisations (Figure 7.4c) and have been associated with a post-Caledonian deformation episode >395 Ma based on a study from the Bergen area further to the SW of Smøla (Western Norway) (Fossen et al., 2017);

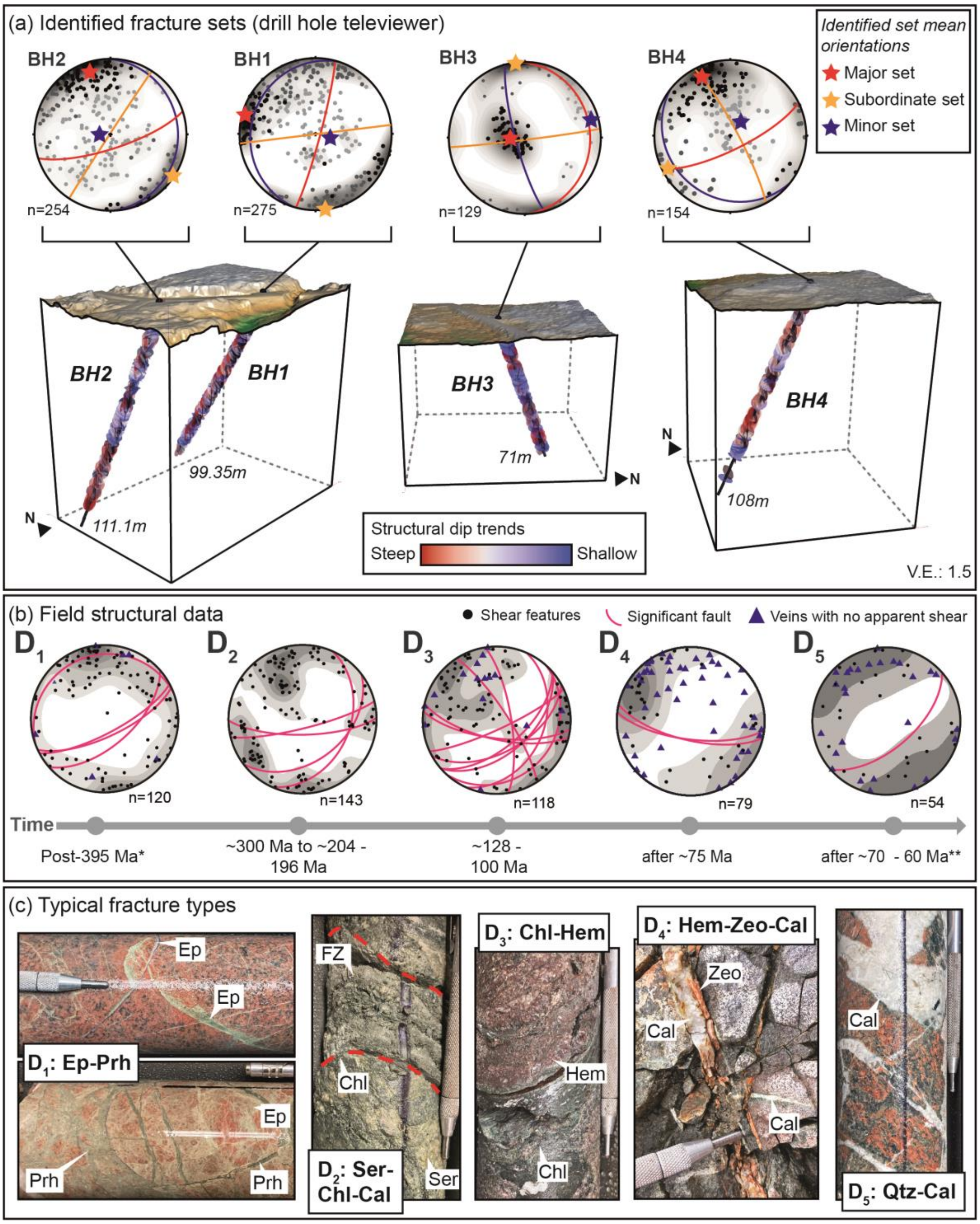

*Figure 7.4. Drill hole structural data and field data utilised in the study. (a) 3D blocks of the four drill holes with downhole televiewer structural data coloured by dip to demonstrate geometric trends. The televiewer data shown in the stereonets are sorted by fracture sets. All the stereonets are Equal Area, lower hemisphere projected, Kamb contoured at the 2σ interval, and Terzaghi corrected based on the azimuth and inclination of the drill hole surveys (maximum correlation factor of 7; Table 4.2), V.E = vertical exaggeration. (b) Field data sorted by deformation episode based on mineral assemblage and relative or absolute age or timing and modified from Chapter 5. Absolute ages provided by *Hestnes et al. (2023), and **Fossen et al. (2017). c) Typical fracture*

types in drill core and field outcrops. Mineral types are Ep = epidote, Prh = prehnite, Chl = chlorite, Ser = sericite, Hem = hematite, Cal = calcite, Zeo = zeolite, Qtz = quartz; "FZ" = fault zone.

ii) The two D_2 fracture sets (mean pole plunge and trend orientation: 00/173 and 74.5/107) are shear features associated with sericite-chlorite-carbonate mineralisations (Figure 7.4c), and were dated to ~300 Ma and ~204 – 196 Ma (Hodge et al., 2024b);

iii) D_3 fractures (mean pole plunge and trend orientation: 10/075) are shear fractures (with local breccias) decorated by chlorite-hematite mineral coatings (Figure 7.4c) and were dated to ~128 – 100 Ma (Hodge et al., 2024b);

iv) The D_4 and D_5 fracture sets were grouped together for simplicity, owing to similar geometries (mean pole plunge and trend orientation: 08/242), and are both mostly tensile features, formed post ~75 Ma (70 – 60 Ma) (Hestnes et al., 2023; Hodge et al., 2024b) with quartz-calcite-zeolite vein infill (Figure 7.4c).

7.3.2 DFN modelling

Using the deterministic input values above, we applied the stochastic 'grown' DFN modelling approach described by Libby et al. (2019, 2024) to generate five fracture sets within a 500 m^3 modelling volume. These fracture sets, representing the natural fracture trends accumulated in the Smøla basement during progressive deformation episodes, were used to model the D_1, D_2, D_3, and D_4 and D_5 (labelled as D_{4+5}) fracture sets.

From the drill hole televiewer data, each of the selected fracture sets has a statistical orientation distribution (Table 7.1), and an associated target volumetric fracture intensity (P_{32}) converted from the relevant downhole linear fracture intensity (P_{10}) as shown in Table 7.2. Lower-limit P_{32} values were also calculated for comparison from the areal intensity (P_{21}) values from the 1:500 trace map lineaments (Figure 7.2d; see Chapter 4 and Appendix B).

Each fracture set is attributed a related fracture size (minimum and cut-off size), and a power-law size exponent (α; Figure 7.3) from the lineament trace maps. Internal fracture properties are also provided for each set, such as aperture values (appraised from extensive drill core vein and fracture measurements, Figure B1) and fracture permeability. All the modelled fractures are assumed not to be sealed for this exercise. Termination relationships (Table 7.3) between the different lineament traces, which have been correlated to the fracture sets, were also included in the modelling. Further information is provided in Chapter 4 and Appendix B regarding all the input parameters.

Table 7.1. Mean orientations of selected fracture sets from the downhole televiewer data. Fracture sets are classified by general strike orientation, except for the 'Shallow' set, which represents the shallowly dipping D_2 fracture set.

Drill Hole	Fracture Set	Fracture Count	Mean Pole Trend (°)	Mean Pole Plunge (°)	Def. Episode
BH2	NE-SW	53	122.9	0.66	D_1
BH1	E-W	122	173.2	0.19	D_2
BH1	Shallow	133	106.7	74.53	D_2
BH3	N-S	31	74.65	10.04	D_3
BH4	NW-SE	31	242.04	8.02	D_{4+5}

Four 'grown' DFN models were stochastically generated as single realisations (Figure 7.5), starting with the D_{4+5} model representing the current fractured rock volume on Smøla (post ~75 Ma). For each temporal iteration, fracture sets of younger sequential ages were progressively removed (back-stripped). The first model (D_{4+5}) thus contains five fractures sets (8 244 732 individual fractures), with a mean P_{32} value of 1.56 m^{-1}, and contains fractures formed during all the deformation episodes (D_1 to D_5). The second model, with four fracture sets (5 206 985 individual fractures) and an average P_{32} value of 1.3 m^{-1}, represents the rock volume post-D_3 deformation (~128 – 100 Ma). The third model, with three fracture sets (5 193 773 individual fractures), and an average P_{32} value of 1.24 m^{-1}, represents the volume after D_2 (~300 Ma and ~204 – 196 Ma). The fourth model, with one fracture set (10 107 858 individual fractures) and an average 0.67 m^{-1} P_{32} value, represents the volume post-D_1 deformation (>395 Ma).

*Table 7.2. Key model input parameters by fracture sets and ordered by deformation episode. The fracture intensity P_{32} values are estimated from P_{10} using the *Wang et al. (2005) conversion method. Refer to the Chapter 4 and Appendix B for further information on the target P_{32} values used. Truncation sizes (min=minimum, max=maximum) relates to equivalent radius of modelled fractures. K stands for permeability value of the fracture infill.*

Frac. Set Name	P_{10} (1 m^{-1})	P_{32}* (m^2.m^{-3})	Target P_{32} used				Size (min) (m)	Size (max) (m)	Scaling exp. (α)	Apert. (mm)	K (m^2)
			D_1	D_2	D_3	D_{4+5}					
NE-SW	0.48	0.76	0.6	0.3	0.3	0.3	1	20	1.984	0.03	5.1e-12
E-W	1.07	1.68		0.5	0.3	0.3	10	80	1.619	0.04	5.1e-12
Shallow	1.17	1.84		0.4	0.2	0.2	5	60	1.619	0.04	5.1e-12
N-S	0.44	0.66			0.6	0.3	10	80	2.273	0.09	5.1e-12
NW-SE	0.29	0.47				0.5	5	45	2.005	0.1	5.1e-12

Within the 500 m^3 modelling volumes, we nested a second 200 m^3 grid volume with 1000 grid cells (Figure 7.5). The 200 m^3 grid was then used to estimate P_{32} volumetric intensities and, using the 'Oda crack tensor' from Oda (1985), the equivalent permeability tensor for each grid cell (Oda, 1985). From the permeability tensor output (orientation shown in Figure 7.5, and magnitude in Figure 7.6), the principal permeability axes (K_i), subdivided into maximum (K_1), intermediate (K_2), and minimum (K_3) eigenvectors, could be estimated. For each deformation episode, the three eigenvectors for each of the 1000 grid cells are plotted as poles on stereoplots (Figure 7.5). An overall mean eigenvector for each of the K_1, K_2, and K_3 poles was then plotted, providing the average 3D orientation of the principal permeability tensor components (Figure 7.5).

Table 7.3. Probability of termination (%) of a younger mapped lineament trace set against an older 'passive' set. Based on geometric similarity to the fracture sets (Table 7.1), the NE-SW traces are associated with D_1, the E-W traces with D_2, the N-S traces with D_3, and the NW-SE traces with D_{4+5} for the modelling. The 'Shallow' fracture set has no corresponding lineament set, as there is no clear 2D map view trace. The adjusted termination probability values used (including for the 'Shallow' set), are detailed in the Appendix B, Table B3

		Younger (lineament trace sets)			
		NE-SW	E-W	N-S	NW-SE
Older	NE-SW	19%	21%	15%	27%
	E-W	39%	36%	67%	31%
	N-S	16%	27%	6%	30%
	NW-SE	26%	16%	12%	12%

The principal permeability tensor for the D_{4+5} DFN model represents the current permeability anisotropy of the fractured Smøla rock volume; the components exhibit a sub-vertical K_1, a sub-horizontal K_2 oriented NNW, and a K_3 oriented WSW. The average permeability values (Figure 7.6) are 4.44e-13 m^2 for K_1, 4.01e-13 m^2 for K_2, and 1.77e-14 m^2 for K_3 ($K_1 > K_2 > K_3$). The D_3 tensor components show a K_1 oriented sub-vertically, K_2 oriented ~S, and K_3 oriented ~W to WNW. The permeability values are ~1.6 orders of magnitude lower than those for D_{4+5}, with K_1 at 3.25e-13 m^2, K_2 at 2.84e-13 m^2, and K_3 at 1.31e-13 m^2. The D_2 tensor has a sub-horizontal K_1 oriented ENE-WSW, a sub-vertical intermediate K_2, and a K_3 oriented NNW-SSE. The average permeability values are ~1.7 orders of magnitude lower than D_3, with 2.06e-13 m^2 for K_1, 1.55e-13 m^2 for K_2, and 1.10e-13 m^2 for K_3. For D_1, the earliest permeability tensor, K_1 is sub-vertical to steeply inclined, K_2 is shallowly plunging to sub-horizontal and oriented NNE to NE, and K_3 is oriented NW. The average permeability values are ~2.2 orders of magnitude lower than

D_2, with K_1 at 9.47e-14 m^2, K_2 at 9.36e-14 m^2, and K_3 at 1.55e-14 m^2 ($K_1 \approx K_2 > K_3$). Overall, there is a consistent increase in the principal permeability tensor magnitude through time periods from D_1 to D_{4+5} (increase of ~2.6 (for K_1), ~2.5 (for K_2), and ~3 orders of magnitude (for K_3)).

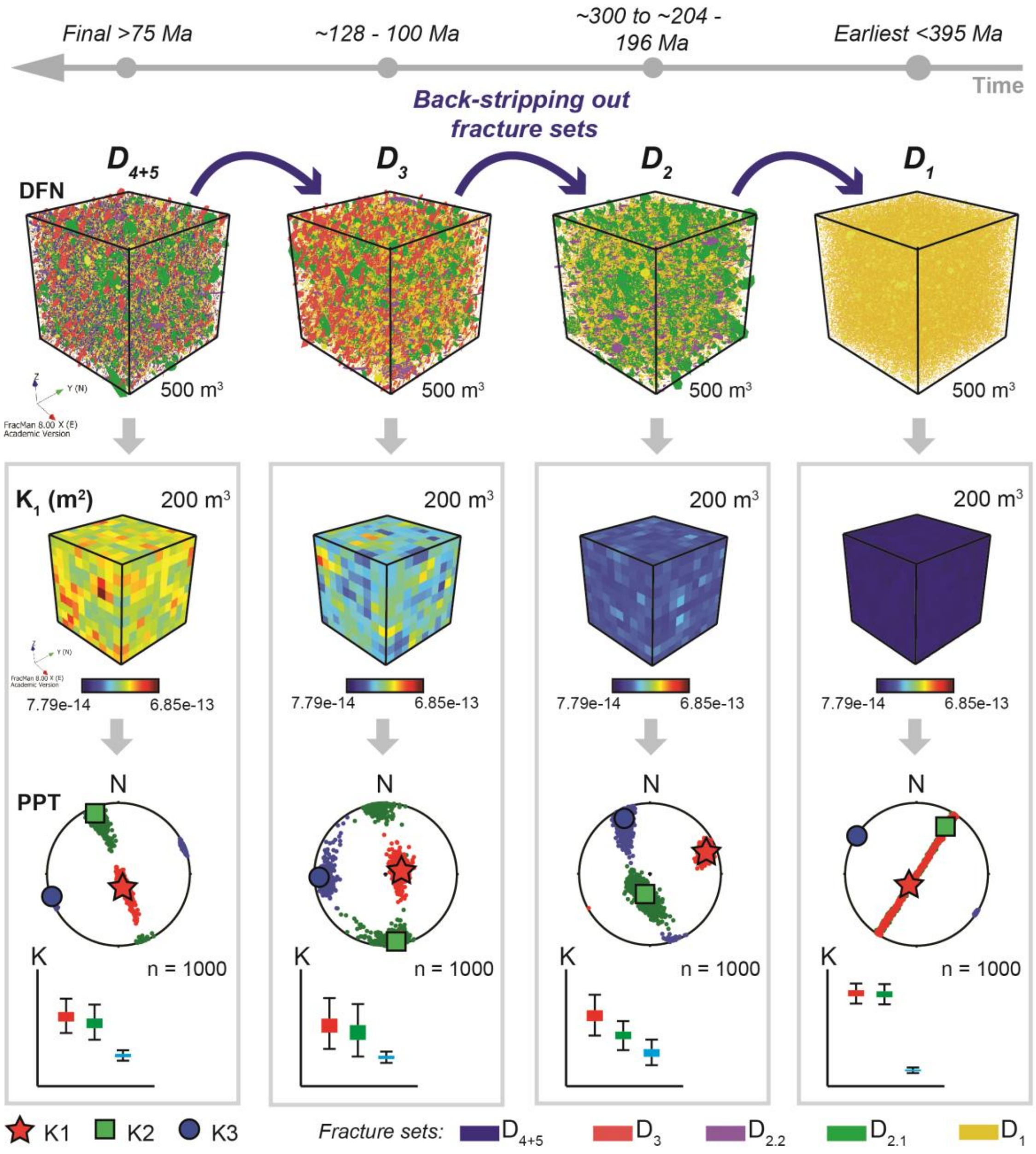

Figure 7.5. DFN model outputs with fractures back-stripped out of each deformation episode (D4+5 to D1) through geological time. For each 500 m³ DFN model, the fracture upscaling grid outputs (200 m³) are shown below with the 1000 grid cells coloured by maximum permeability eigenvector (K1) value (m2); the principal permeability tensor (PPT) axes K_1 (red star), K_2 (green box), K_3 (blue circle) are indicated in terms of orientation (on stereonet plots) and relative magnitude (m^2) (box plots) for each deformation episode. Illustrative box plots display the interquartile region (boxes; 50 % of permeability magnitudes), and whiskers which extend to the first and third quartiles, respectively. Mean permeability magnitude values are not shown.

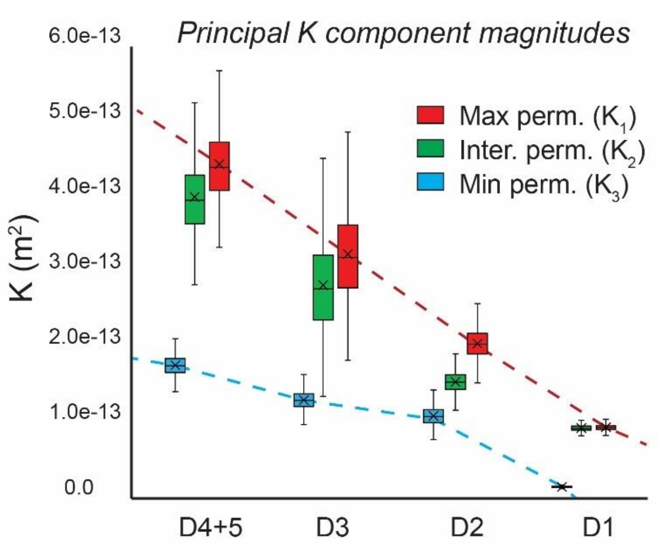

Figure 7.6. Box and whisker plot of permeability (K) values for each of the principal permeability axes (K_1, K_2, K_1) through geological time. Preceeding backwards through time, the deformation episodes start at D_{4+5}, being the most recent episode, and extend to the oldest time at D_1.

The principal permeability tensor component orientations and magnitudes are strongly influenced by the youngest fracture set(s) in each DFN model (most evident in the D_1 model). In the D_3 and D_{4+5} models the sub-vertical intersections between the different steeply dipping fracture sets result in K_1 orientations typically sub-vertical and parallel to these intersections. The D_2 model, however, is a combination of these two situations, with the sub-horizontal intersections of the two D_2 fracture sets and the earlier D_1 fracture set causing K_1 to be sub-horizontal. In general, the principal permeability eigenvector orientations rotate between the models, with K_2 (or K_1 for D_2) changing from towards the NE, to S, then NNW, and K_3 shifting from NW, NNW to W, WSW from D_2 to D_3 (Figure 7.5).

7.3.3 Topology and fracture connectivity analysis

Both the 3D modelled fractures (Figure 7.7a) and the 2D mapped (deterministic) lineament traces (Figure 7.7b) have been quantitatively characterised, following the methodology of Sanderson and Nixon (2015), for network topology and spatial connectivity (Figure 7.7c). To make comparisons with the final DFN (D_{4+5}) model (representing the same time interval as the deterministic trace maps), and to confirm scale-independent self-similarity between the different deterministic trace maps (mapped at various scales from different parts of Smøla; Figure 7.2 & Figure 4.2), all the trace maps were analysed using a branch and node counting method (Nyberg et al., 2018). The proportional counts of branches and nodes were then used to confirm whether the maps form part of the same fracture system, and to obtain network topology and connectivity characteristics.

Four modelled trace maps were produced with the 3D fractures represented as 2D lines on horizontal slices through each of the four DFN models (traces being intersection lineations on the planar surface). Three circular representative scan areas (20 m diameters) were selected within each model trace map for network topology analysis (selected scan areas shown on Figure 7.7a). The branch types include II (isolated), C-I (semi-isolated), and C-C (connected)-type branches. The nodes counted included I (isolated), Y (terminating), and X (cross-cutting), and E (edge)-type nodes(Sanderson and Nixon, 2015). In total, 2001 nodes and 2530 branches were counted across the maps. Subsequently, each of the four deterministic lineament trace maps were similarly analysed following the same procedure. For each trace map at the different scales, we selected three circular representative scan areas from 4 km (1:100 000) to 40 m (1:500) in diameter. Within each scan area, all the network branches and nodes were similarly counted (selected scan areas shown on Figure 7.7b). Overall, 2685 branches and 2154 nodes were counted for all the different scales. Further information is available in Chapter 4 and Appendix B, specifically in Figure B2, Tables B4 & B5.

The topology ternary diagrams of Figure 7.7c plot the proportions of nodes and branches from the modelled and deterministic trace maps. Out of the modelled trace maps, the D_1 trace map yielded the highest proportion of I-nodes (~76 %), with D_2 and D_3 having the highest number of X-nodes (~ 41% and ~45 % respectively), and D_{4+5} the highest proportion of Y-nodes (~32 %). In contrast, the deterministic trace maps show on the node ternary plot that the 1:500 trace map has the highest proportion of Y-nodes (~64 %), while the 1:7500 and the 1:100 000 trace maps exhibit the highest proportion of I-nodes (~41 % and 38 %, respectively). Overall, X-nodes become more abundant with the increasing scale (~9 % to 24 %), suggesting that the resolution of lineament mapping may affect the detection of node type. For all the maps, however, X-nodes are less common than other node types. The final modelled D_{4+5} trace map has fewer Y-nodes, but a similar abundance of C-C branches as the mapped lineament trace maps across the scales. Overall, the modelled trace maps back through time show a trend of increasing number of isolated branches and nodes. Finally, the similar branch and node proportions in the deterministic trace maps suggest they belong to the same fracture system, supporting the use of lineament trace-derived fracture length distributions (Figure 7.3) in our DFN modelling.

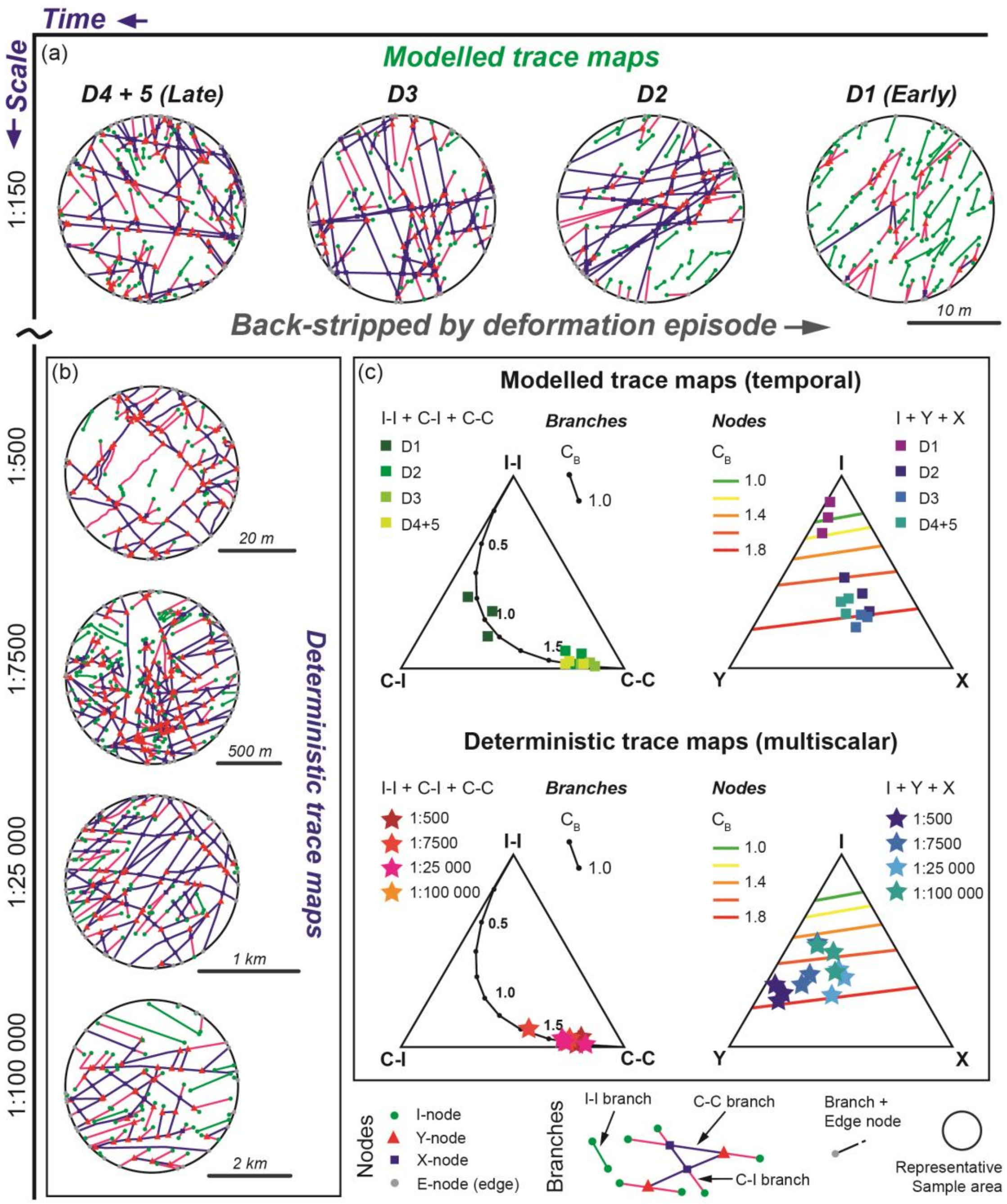

Figure 7.7. Network topology analysis results. (a) representative 2D trace maps, extracted from the 500 m^3 DFN models, shown back-stripped through time, and (b) multiscalar deterministic trace maps for comparison (all representing the same deformation episode as the D$_{4+5}$ model trace map, with all deterministic trace maps shown on Figure B2, Appendix B. (c) Ternary plots illustrating the proportions of both nodes and branches for both modelled (single realisation) trace maps, with data points (small blocks) coloured by deformation episode; and deterministic trace maps (representative scan areas), with the data points (stars) coloured by scan area scale.

To assess fracture connectivity for the modelled and deterministic maps (Figure 7.7c), we used the 'connections per branch' (C_B) average value (combined for each scale's scan areas). The C_B parameter is defined as $C_B = (3N_Y + 4N_X) / N_B$, where N_y is the number of Y-nodes, N_x is the number of X-nodes, and N_B is the total number of branches expressed as $0.0<C_B<2.0$ (Sanderson and Nixon, 2015). In this example, rather than using the 'effective' connectivity, which would have to take fracture sealing into account, we use the 'apparent' connectivity that accounts for all present fractures (and related branches and nodes) irrespective of the openness (e.g. Lei and Wang, 2016). For the modelled trace maps, the calculated C_B values are 1.01 for D_1, 1.74 for D_2, 1.82 for D_3, and 1.79 for D_{4+5}. In time, the networks become therefore well-connected from D_2 onwards, indicating an evolution in the inter-connectivity of the fracture system through time following a general trend towards higher connectivity with progressive fracture saturation. For comparison, the deterministic lineament traces have calculated C_B values of 1.5 for the 1:100 000 map, 1.75 for 1:25 000, 1.65 for 1:7 500, and 1.8 for the 1:500 map. In general, all the maps have C_B values >1.5, suggesting a good degree of interconnectivity on average. Importantly, the C_B values, and the proportions of branches and nodes for the D_{4+5} modelled trace maps, overlap well and show similarity to the lower-resolution deterministic trace maps (1:100 000 and 1:25 000).

7.4 Discussion

The variety of our deterministic inputs and our stochastic approach allowed us to estimate the evolution of secondary permeability and fracture connectivity within a fractured basement rock volume over geological time. The petrophysical conditions allocated to the recognised, characterised, and dated deformation episodes are assumed to have existed at distinct times corresponding to our D_1 to D_{4+5} models and have evolved with time.

Fractures forming by brittle failure may result from transient fault-valve behaviour, controlled by critical combinations of pore-fluid pressure and differential stress conditions (Cox, 2010; Sibson, 1994). Assuming this, fractures can form and progressively evolve during each deformation episode, as also shown by crack-and-seal vein textures in some of the veins on Smøla (Hodge et al., 2024b). During the episodes, dynamic conditions existed where paleo-apertures, represented by transiently open fractures, repeatedly formed allowing fluid ingress and flow (Cox, 2010). These open fractures were also repeatedly sealed in brief geological time spans by the precipitation of vein minerals (Sibson, 1996). Maximum caution is thus necessary when discussing bulk petrophysical characteristics, as they represent not only the effects of transient conditions but may also be the result of multiple events during a single deformation episode that we are now grouping together. Furthermore, as fracture sealing will decrease connectivity through time (Olson et al., 2009), our modelling only considers the apparent connectivity related to assumed open fractures, and not necessarily connectivity related to active fluid flow pathways.

7.4.1 The evolution of fracture-related petrophysical properties (secondary permeability and fracture connectivity) through time

Remarkably our modelling results make it possible to assess how permeability anisotropy and fracture connectivity have varied through time during the evolution of a tract of the mid-Norwegian passive margin. Insights into how the actual geology of Smøla impacted the results are discussed below. For ease of comparison between the different DFN models, we project our computed maximum and intermediate permeability eigenvectors (K_1 and K_2) of the 3D permeability tensor components onto the 2D horizontal plane as the estimated maximum permeability direction (K_{Hmax}; Figure 7.8).

Model D_{4+5} (Figure 7.5) represents the current fractured rock volume, which is the sum of the accumulated fractures from the Devonian to at least the Late-Cretaceous-Palaeogene (<75-60 Ma). The model predicts a bulk NNW-SSE oriented K_{Hmax} (Figure 7.8), which reflects all the earlier and newly formed fractures. Compared to the earlier models (D_1 to D_3), this model has the highest principal permeability tensor (PPT) component magnitudes (4.44e-13 m² for K_1 to 1.77e-14 m² for K_3), implying that PPT magnitude increases with fracture saturation related to increasing numbers of (interconnected) fracture sets. During late-Cretaceous to Tertiary times, fluid migration would have therefore focussed along structures oriented ~NNW-SSE (sub-parallel to our K_{Hmax}) with steep dips (K_1 sub-vertical), before later mineral precipitation (calcite-quartz-zeolite in our case; see Chapter 5 (Hodge et al., 2024b)) and infill (e.g. Sibson, 1994). Despite the relative high permeability, the D_{4+5} model has lower connectivity (C_B = 1.79) compared to the earlier D_3 model (C_B = 1.82) (Figure 7.8). Influencing the C_B modelled connectivity, the D_{4+5} veins are commonly isolated features, rarely cross-cutting older features (contributing few X-nodes), and commonly utilise pre-existing fractures (reactivating older fractures as tensile veins; see Chapter 5 (Hodge et al., 2024b)), which would indeed result in lower fracture connectivity. But, as fracture sealing is not incorporated in our modelling, the effective connectivity should not decrease (as isolated branches will only affect the apparent connectivity measure, not effective connectivity), it can only increase or remain constant during the addition of new fracture sets.

Back-stripping out the D_{4+5} fractures, model D_3 represents the rock volume during the mid-Cretaceous (~128 – 100 Ma). It constrains a N-S to NNW-SSE K_{Hmax} (Figure 7.8), and lower PPT magnitudes (3.25e-13 m² for K_1 to 1.31e-13 m² for K_3). Potential fluid-flow during the mid-Cretaceous would thus have occurred along fractures oriented sub-parallel to this K_{Hmax} orientation. In terms of connectivity, the fracture termination relationships (Table 7.3) promoted abundant cross-cutting traces for the D_3 model, which, in turn, resulted in the highest obtained fracture connectivity (C_B = 1.82; Figure 7.8). The fracture orientation trends used here shift dramatically from D_2 to D_3 (~E-W to N-S; Figure 7.5), which correlates with a regional stress-field shift in mid-Norway in the mid-Cretaceous (Tartaglia et al., 2023). Whether this is the cause for new cross-cutting fractures rather than reactivating earlier D_2 or D_1 fractures is not however clear. Notably though, the D_3 fractures are indurated and infilled with cataclasite (to gouge; chlorite-hematite mineralised) (Hodge et al., 2024b). Possible fluid ingress into these fractures may have been thus aided by host rock clasts potential 'propping' the features open during fluid flow events (Holdsworth et al., 2019). Overall, the D_3 model supports major fluid flow during the mid-Cretaceous, with relatively high permeability magnitudes (aided by 'propped' fractures), and the highest fracture connectivity.

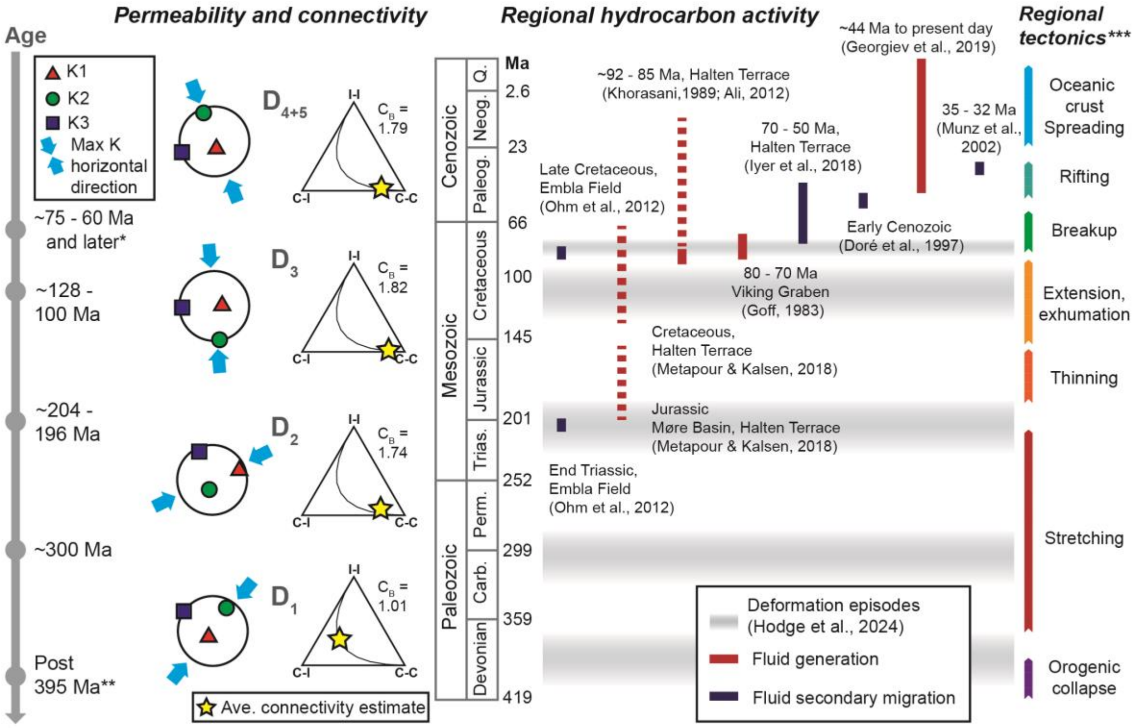

*Figure 7.8. Comparison of the DFN modelling results relative to regional hydrocarbon and tectonic activity in geological time. The absolute time-constrained permeability anisotropy (simplified stereonets, with blue arrows indicating K_{Hmax} orientation) and fracture connectivity (ternary plots with yellow stars showing the proportion of branch types) are shown relative to dated regional hydrocarbon generation (red bars), secondary migration (blue bars), and tectonic activity (coloured by tectonic stage). Ages provided by *Hestnes et al. (2023), and **Fossen et al. (2017), and tectonic stages modified ***from Peron-Pinvidic and Osmundsen (2018).*

After stripping out the D_3 fracture set, the D_2 model reproduces the rock volume during the Late Carboniferous to Permian and the late Triassic to early Jurassic (~300 Ma to ~204 – 196 Ma). For that time, modelling yielded a permeability anisotropy K_{Hmax} oriented NE-SW to ENE-WSW, with a sub-horizontal K_1 orientation (K_1 is sub-vertical in the other models), with the second-lowest PPT magnitudes (2.06e-13 m^2 for K_1 to 1.10e-13 m^2 for K_3). The D_2 model represents a prolonged episode, which we modelled by means of three fracture sets (two for D_2 and one for D_1). Both D_2 sets contain phyllosilicate-rich (chlorite-sericite) phyllite shears to shear fractures, with fault gouge (Hodge et al., 2024b). In fact, the D_2 fractures type and the orientation of the permeability anisotropy indicate complex fluid-flow regimes along either the sub-vertical ~E-W structures or laterally along shallowly dipping structures (as suggested by the K_1 orientation). Further complicating this picture, authigenic phyllosilicates may have impeded potential fluid-flow (which our modelling ignores), with the D_2 fractures later acting as impermeable barriers (Faulkner et al., 2010). Irrespectively, the fracture connectivity of this model, being nearly equal to the D_3 and D_{4+5} models, does demonstrate how a high degree of connectivity (C_B >1.5) was achieved by the late Triassic. The sudden increase in C_B indicates that, at this resolution, fracture networks rapidly become interconnected during deformation (e.g. Cox, 2005).

Finally, back-stripping out the D_2 fracture set, only the earliest initial fractures remain, recreating the basement volume during the Devonian (>395 Ma). The D_1 model, with early tensile epidote-prehnite veins (Hodge et al., 2024b) infilling those fractures, provides a NE-SW oriented K_{Hmax} and the lowest PPT magnitudes (9.47e-14 m^2 for K_1 to 1.55e-14 m^2 for K_3) (Figure 7.8), ~3 orders of magnitude lower than the D_{4+5} model (Figure 7.6). Overall, the D_1 model reflects the mostly isolated modelled fractures, and is the least connected of all DFN models, with a C_B value of 1.01. The low C_B value notwithstanding, owing to the low permeability of the host-rock, these initial fractures may still have imparted an important bulk permeability anisotropy, with fluid flow during the Devonian focused along hydraulically connected fractures sub-parallel to the K_{Hmax} where available.

7.4.2 Reactivation

As the host rock matrix permeability is intrinsically very low, the fracture sets modelled are the basement's most permeable features. However, without clear control on the reactivation of pre-existing features, it is challenging to fully constrain the 3D principal permeability tensor. Our modelling addresses this by incorporating pre-existing features with lower volumetric intensity, P_{32} values (typically decreased by ~50 % from their initial intensity value) to try and simulate selective reactivation. A noteworthy limitation in our modelling, however, concerns fracture reactivation between different DFN model generations.

Assuming adequate pore fluid pressures, and necessary cohesion and shear strength values (Nortje et al., 2011; Sibson, 1985), fractures optimally oriented 30° to the maximum principal stress (σ_1) and containing the intermediate principal stress (σ_2) should reactivate as shear fractures, while those oriented ~0° to σ_1 (and containing σ_2) should reactivate as tensile fractures (with fractures between these two endmember situations reactivating as hybrid fractures) (Blenkinsop, 2008; Sibson, 1985).

For Smøla, the stress fields during the Triassic-Jurassic (D_2) and Early to Late Cretaceous (D_3 and potentially D_{4+5}) indicate a least compressive stress (σ_3) oriented E-W and NW-SE to WNW-ESE, respectively (Tartaglia et al., 2023). The stress field orientations suggest that, assuming a sub-vertical σ_1 (maximum horizontal stress $\approx \sigma_2$), a portion of favourably oriented fractures from D_1 to D_3 would have been progressively reactivated. Examples of this are late D_{4+5} quartz-calcite tensile veins in both D_2 and D_3 fractures (Hodge et al., 2024b). Considering mid-Norway's more recent glacial history, isostatic uplift from ice unloading may have also reactivated many low-angle fractures (sub-vertical σ_3) (Stephens et al., 2015).

Quantifying the proportion of reactivating fractures in each DFN model remains unresolved. Dilation and shear tendency studies using assumed paleostress fields may define statistical probabilities of reactivation, providing a basis for intensity estimates, and confirming bulk permeability trends, but this remains presently unanswered in this study.

7.4.3 Novelty of this approach and wider implications

Unique insights are offered by our approach, using selective back-stripping of components, formed at specific geological times, to study the evolution of selected petrophysical characteristics in crystalline basement blocks. A similar approach has previously been proposed only in a 3D tomography study of paleo-porosity evolution (e.g. Macente et al., 2022), and, in an opposite sense, in stepwise forward modelling (restoration) to understand progressive deformation and evolution of permeability (e.g. Roberts et al., 2022). However, those studies lack absolute time constraints, making it difficult to place any results within geologically meaningful time frames. Other fracture network studies have demonstrated the evolution of fracture pattern development within absolute time frames (e.g. Becker et al., 2010; Engelder and Geiser, 1980; Laubach and Kira, 2009)). Those studies, however, typically have attributed fractures (and associated petrophysical properties) to formation ages through indirect means (for example, via thermal and burial ages, quartz accumulation rates, and dated paleostress-field trajectories). In contrast, our modelling benefits remarkably from an absolute time-dimension and an unprecedented well-resolved structural characterisation of the fracture sets on Smøla. These constraints enabled us to precisely control the structure and timing of fracture formation in our DFN reconstructions. Additionally, the 'grown' DFN modelling approach includes temporal aspects related to fracture propagation and interaction (Davy et al., 2013; Libby et al., 2019; Maillot et al., 2016), simulating pre-existing fractures, during each generation of DFN. Also, considering that sub-seismic-resolution faults and fractures (<10-30 m in size) in impermeable reservoirs may considerably affect fluid flow (Walsh et al., 1998), using the presented stochastic approach our modelling can model fractures at that resolution. The flexibility in modelling resolution is an advantage when comparing to 3D tomography (fine resolution on the mm to cm-scale) and forward modelling techniques (large resolutions on the km-scale).

To further test and validate our approach, we use hydrocarbon dynamics from offshore Norway as a useful example owing to available absolute time-constraints. Hydrocarbons are generally dated using geochronology and biostratigraphic techniques such as Re-Os radiometric dating and biomarkers (Bhullar et al., 1999; Selby and Creaser, 2005). Our DFN models with the associated ages can, therefore, be compared against known reservoir migration events (assuming our 500 m^3 modelling volume and the 200 m^3 fracture upscaling volume represent a typical reservoir, see Appendix B for further details), and broader tectonic events through geological time.

The D_2 DFN model, for example, temporally coincides with the earliest known episode of hydrocarbon generation and secondary migration (Triassic-Jurassic) in the Embla field (Late Triassic fluid migration) and the Halten Terrace (Jurassic oil generation) (Matapour and Karlsen, 2018; Ohm et al., 2012) (Figure 7.8). Even though hydrocarbon generation is linked to the burial and thermal history (maturation) of source rocks (Palumbo et al., 1999), subsequent tectonic activity may have led to enhanced fracturing and increased secondary permeability in adjacent rock volumes, potentially facilitating the secondary migration activity. The Triassic and Jurassic witnessed crustal stretching and thinning due to the drifting of Norway and Greenland (Peron-Pinvidic and Osmundsen, 2018) and strike-slip faulting along the Møre-Trøndelag Fault Complex (MTFC), a major NE-SW feature extending from Central Norway into the northern North Sea (Hodge et al., 2024b; Watts et al., 2023). Transtensional kinematics on the MTFC, splay development, and related extension influenced the orientation of the fracture sets that we have used for our modelling, with many being oblique to the strike of the MTFC. Despite hydrocarbon generation in the Halten Terrace during the Late Triassic to

Jurassic, major reservoir-scale secondary migration may have been limited owing to the lack of permeable or communicable E-W faults and reactivated NE-SW fractures.

During the Cretaceous to Paleogene (D_{4+5} and D_3 models), most hydrocarbon generation and secondary migration events initiated, extending into the Neogene and later (Ali, 2012; Georgiev et al., 2019; Goff, 1983; Khorasani, 1989; Ohm et al., 2012) (Figure 7.8). Remarkably, our D_3 and D_{4+5} models temporally correspond to secondary migration events in the Halten Terrace (mid-Norwegian margin) and Viking Graben (SW Norway), such that we can tentatively suggest a link between secondary migration, reservoir charging, and fracturing as per our DFN modelling also at that time. However, assuming this migration activity is recorded by our modelling results, from the Cretaceous onwards, crustal extension of the newly forming passive margin led to major rift basins, basement structural highs (representing 'buried hill-type' hydrocarbon traps (Holdsworth et al., 2019)) and NE-SW to NW-SE striking extensional faults, such as the Klakk fault complex oriented ~NNW-SSE (similar geometries as our D_3 and D_{4+5} fracture sets). Therefore, structures oriented ~N-S to NW-SE forming during the Norway-Greenland rifting and break-up, being parallel to our K_{Hmax} orientations at these times, may well have been important fluid pathways during the Mid-Cretaceous (D_3) onwards. These conduits would enable communication between basin source rocks and potential trap sites, facilitating fluid percolation and reservoir charging of, for example, fractured basement plays with similar lithologies as Smøla.

As demonstrated by this example, our approach can be adapted to quantify similar geofluid migration histories and is applicable in various contexts where understanding the evolution of bulk rock permeability or fracture interconnectivity is crucial, such as in fracture-hosted groundwater systems, nuclear waste repositories, and CO_2 storage studies.

7.5 Conclusions

Our study offers a conceptual approach to constrain fracture-related petrophysical properties through time. Using temporally constrained basement-hosted fractures from Smøla, mid-Norwegian passive margin, stochastic modelling reconstructs the evolution of fractured rock volumes as 'grown' DFN models, from the present back to the Devonian. To improve realism, we integrated various deterministic remote sensing, geophysical, drill core, and field studies datasets, combined with absolute dating results, to generate stochastic DFN models with petrophysical estimates.

Our well-constrained orientation trends and sorting criteria of different fracture sets, along with absolute ages, allowed us to recreate the fractured rock volume during each deformation episode. By applying a back-stripping methodology to the fracture sets, we deconvoluted a complex present-day fracture network into four time-specific models representing the Late Cretaceous-Palaeocene (and later), the mid-Cretaceous, Late Triassic-Jurassic to Carboniferous-Permian, and finally the Devonian (spanning over ~300 Ma). Each of these models are stochastic representations of fracture networks back through time and provide estimates of the bulk principal permeability tensor (component orientations and magnitudes), and fracture connectivity at specific episodes in geological time.

Comparison of our results with an example of absolute-dated geofluid activity, namely petroleum secondary migration offshore Norway, shows that our modelled time-specific petrophysical characteristics fit well with known episodes of hydrocarbon activity and reservoir charging. The ability to estimate permeability and connectivity properties during past fluid migration events represents an important advancement in understanding fluid flow histories. Understanding how the orientation of permeability anisotropy has changed through geological time can indicate which structures were subparallel to the maximum permeability anisotropy and thus served as preferential fluid pathways during specific episodes. Additionally, identifying when peak fracture connectivity occurred, which in our example of offshore hydrocarbons activity was during the mid-Cretaceous, provides a basis for understanding why geofluid activity may have commenced at that time (notwithstanding the burial history and source rock maturation in our example).

While incorporating more geological characteristics that affect permeability (such as fracture infill types) and structural reactivation into our models remains beyond the scope of this study, those inputs could further refine similar approaches in the future. Nonetheless, the framework highlighted in this study remains statistically sound and can be adapted and applied broadly to other geological terranes where absolute time constraints on fractures are available, providing a novel perspective on the history of fluid flow in fractured media.

Chapter 8: Validation and refinement of discrete fracture network (DFN) models by comparative analysis and fracture conditioning

8.1 Introduction

Progressing from the initial focus on defining a relative and absolute chronology of deformation and mineralisation of different fractures, veins, and fault arrays (Chapter 5), this work then defined deterministic inputs, which were subsequently used to generate a series of time-constrained discrete fracture network models (DFN). DFN's were used to conceptually explore the transient evolution of permeability (K) and fracture connectivity (C_B) within a 500 m^3 modelling volume (Chapter 7). That modelling volume is considered representative of the fracture-saturated rock on Smøla, which, as a correlative, is relevant to any fractured crystalline basement volume elsewhere.

However, as the modelling remains conceptual and significantly affected by inputs and boundary conditions (such as the selectively decreased P_{32} values), the DFNs need to be refined to better correspond to the observed fracture networks on Smøla island. This refinement aimed to identify the modelling scale that best facilitates a computationally efficient replication of the observed natural fracture network, while also providing improved inputs for future simulations of fractured crystalline basement volumes. Initially, however, a validation exercise was undertaken on the DFNs to evaluate and demonstrate how successful the 'grown' DFN modelling approach was at realistically replicating time-constrained fracture arrays. It is important to note, however, that this thesis is not primarily intending to use the DFN modelling approach for predicting petrophysical properties in unknown rock volumes. Instead, it is focused on developing a conceptual approach for reconstructing past fracture systems, in absolute time, within an analogue rock volume. The validation and refinement process are therefore focussed on improving the realism of the DFNs, and the reliability of the petrophysical estimates.

For the validation exercise, I have selected to run the assessments at the outcrop and drill core-scales on the 500 m^3 DFN models (Chapter 7, Figure 7.5) compared against the observed geology on Smøla (Figure 7.4a). Replication of fractures at this scale may provide insight into fluid flow along sub-seismic resolution structures (<30 m), which are key in understanding bulk fluid flow within larger reservoir volumes (Walsh et al., 1998). As validation metrics, I have opted to use the 1D fracture intensity (P_{10}) and in some places, the fracture orientations. I chose the deterministic and stochastic P_{10} values as a validation metric, as it derives from the drill hole traces and is therefore readily available (either as acoustic televiewer data or modelled drill hole intersections). The main advantage of utilising the drill holes as ‘sampling objects’ (e.g. Bym et al., 2022), is that the drill traces can transect through the inner portion of the DFNs, such that edge-effects related to the stochastic fractures extending outside of the modelling volume (resulting in local lower fracture intensities) have a minimum effect on the validation. The fracture orientations from the televiewer data, sorted by fracture set (based on geometric trends of the D_1 to D_5 field data and mean televiewer fracture set orientations; Figure 7.4a & b), offer an additional measure to assess how well the models have replicated the deterministic data.

To further refine modelling, I made use of ‘Fracture Conditioning’, which is a modelling approach whereby stochastically generated fractures are adjusted, fine-tuned and calibrated to match as closely as possible observed deterministic geological data, such as downhole acoustic televiewer data (Golder Associates Ltd., 2001). Stochastic DFN models, where fractures are randomly ‘seeded’ based on a variety of attributes and statistical distributions (e.g., fracture size and orientation), often generate fractures that differ in actual location, intersection, and intensity compared to natural fractures observed in drill holes (Kim et al., 2024). If the unconditioned DFN models are sufficiently realistic, however, the conditioning of the stochastic fractures will provide a good match between simulated and observed fractures. The process of conditioning stochastically generated fracture sets to trace maps, geophysical data (such as ground-penetrating radar), or drill hole data is a common procedure (e.g. Bym et al., 2022; Dorn et al., 2013), and typically uses either geometric or genetic characteristics of the fracture sets to regenerate the conditioned fractures.

This Chapter, in addition, also presents several extra DFN models (utilising the same input parameters where possible as the conceptual 500 m^3 DFN models) generated at the drill hole scale. These new DFN models, together with the conditioned stochastic fractures, were used to validate the replication of the Smøla natural fractures in drill core at a finer modelling volume. This assessment considered all four of the diamond drill holes across Smøla, which was pivotal to highlight local variations in, for example, volumetric intensity and fracture orientation trends, which can potentially indicate heterogeneity in the Smøla crystalline basement fractured reservoir. Additionally, as this project is also interested in exploring the sub-seismic resolution scale, providing an application of the modelling into fracture characterisation of an actual basement volume is useful for future studies requiring discrete fracture network modelling at that scale. The determination of the size, orientation, intensity, and spacing parameters of both the unconditioned and conditioned fractures provide key modelling parameters that can be used to realistically simulate the Smøla fracture network at the scale of the drill holes BH1 to BH4.

8.2 Results of the 500 m^3 DFN modelling analysis and validation

8.2.1 Assessment approach

The DFN modelling in Chapter 7 was primarily designed for conceptual purposes, using a single 500 m^3 modelling volume without any specific spatial relationship to the four available drill holes. Translating the X, Y, and Z boundary coordinates of the 500 m^3 modelling volume in order to have them coincide with the positions of the four drill holes (four different locations centred on each of the four drill hole axes), enabled us to make a direct comparison between the stochastic fractures intersecting the drill holes and the relevant actual observed downhole televiewer data.

Applying the same DFN modelling input parameters and fracture back-stripping approach as in Chapter 7 (adapted from Table B3), DFN models were generated within the different 500 m^3 modelling volumes centred on each drill hole. To assess local variations between the drill holes, the televiewer data for each hole were compared sequentially. For each drill hole, the different televiewer datasets, representing observed in-situ fractures intersected by the drill holes, were sub-divided by geometry based on the D_1 to D_{4+5} orientation trends (Figure 5.3 & Figure 7.4). To compare with the observed data, drill hole-intersected stochastic fractures from the corresponding deformation episodes (extracted by spatial intersection with the drill hole length) were then plotted on cumulative fracture intensity (CFI) plots versus the televiewer data attributed to the same deformation episode (Figure 8.1).

The CFI plots are a graphic indication of the total percentage (%) of fractures at any given downhole depth of the drill hole. While typically used to identify local variations of fracture intensity (P_{10}), potentially related to lithological or stratigraphic anisotropies or possible damage zones associated with major structures, these kinds of plots also provide a useful tool in assessing the similarity of two different fracture sets or models in terms of P_{10} variation by drill hole depth, and absolute number of fractures intersected by the drill holes. In this study, the CFI plots are used, therefore, as a comparison tool between stochastic models and observed fractures.

8.2.2 Match between stochastic and observed fractures

The comparison between stochastic and televiewer fractures is discussed below with the aid of relevant CFI plots for the whole drill holes:

The CFI plots for drill hole BH1 (Figure 8.1a) show a relatively constant fracture intensity downhole for the observed televiewer data, except for D_1, where local breaks are associated with the isolated nature of D_1 fractures. The intersected stochastic fractures from the 500 m^3 modelling exhibit less constant downhole fracture intensities, and generally fewer fractures than the televiewer data, typically ~80 to 50 % fewer. Locally, the intensity curves for D_1, D_2, and D_3 coincide with the observed data, inferring similar rates of fracture percentage increase with depth.

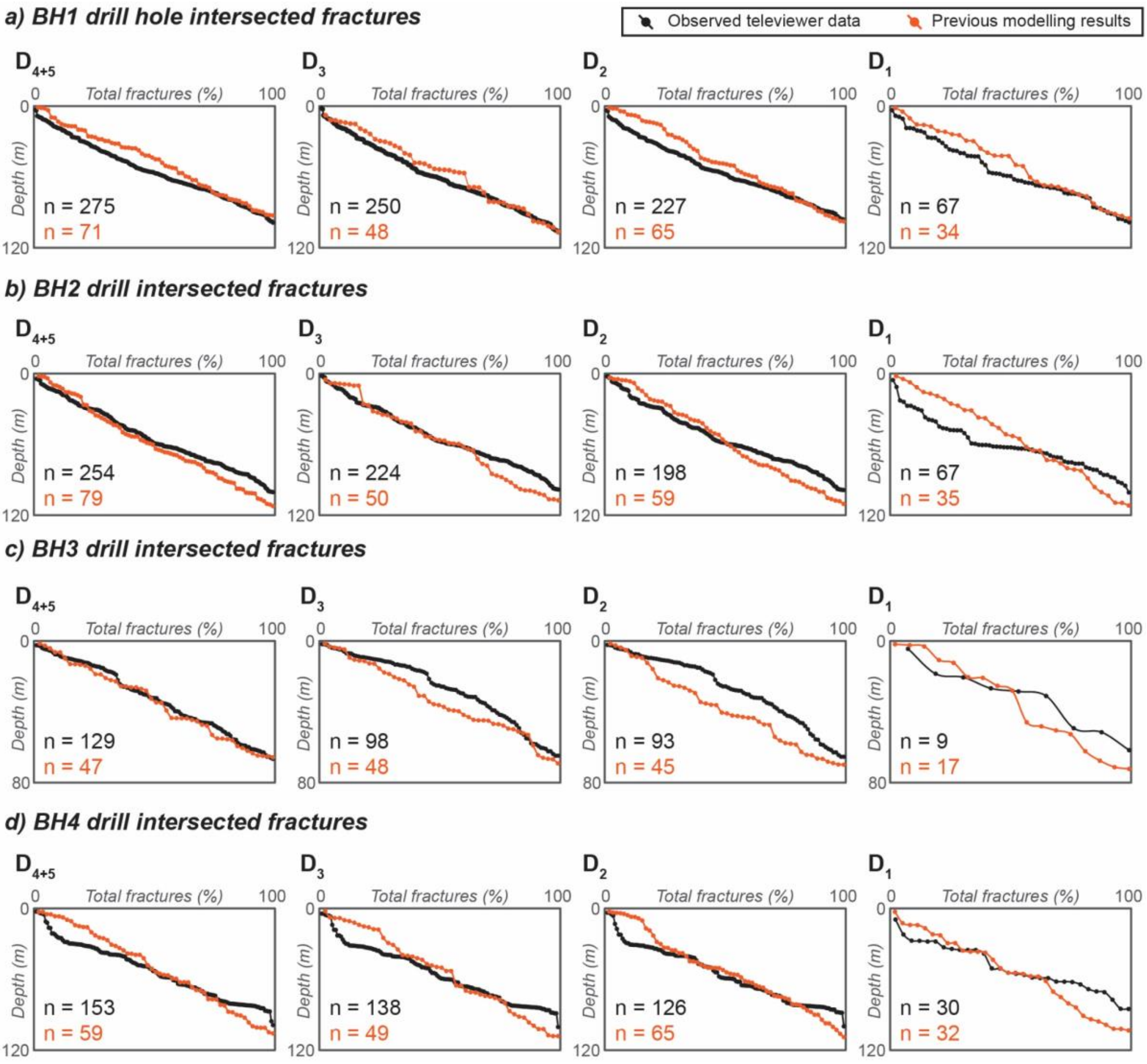

Figure 8.1. Cumulative fracture intensity (CFI) plots of the 500 m^3 cube models from Chapter 7 vs. sub-divided downhole televiewer data by deformation episode.

The BH2 CFI plots (Figure 8.1b) also exhibits constant fracture intensities in the televiewer data, apart from D_1, where there is a local variation (higher intensity in the centre of the drill hole). The consistent match occurs in D_{4+5}, whereas D_1 stochastic fractures exhibit a significantly different fracture intensity distribution when compared to the televiewer data, indicating a poor match between the models and the relevant televiewer data. Again, stochastic fractures are fewer in number (~70 to 50 % fewer) than the televiewer data.

In the BH3 CFI plots (Figure 8.1c), the televiewer data show constant intensity in D_{4+5}, with more variable intensities in D_3, D_2, and especially D_1, which has distinct concave down-shaped CFI curves. The D_{4+5} and D_1 stochastic fractures show similar rates of increase in fracture intensity with drill hole depth, while D_3 and D_2 show significant differences from the observed data. As with BH1 and BH2, the number of stochastic fractures is lower than the observed, with 65 to 50 % fewer stochastic fractures.

Finally, the CFI plots for BH4 (Figure 8.1d), exhibit a variable televiewer intensity curve down hole (present in all the deformation episodes), with distinct low intensity zones both at the beginning and the end of the hole traces. Between these zones, the fracture intensity increases. The stochastic fracture curves, as with the previous drill holes, do not accurately replicate the intensity variation, although the D_1 plot shows a good match between observed and simulated fracture counts (30 observed versus 32 simulated fractures). For the D_{4+5}, D_3, and D_2 plots, the simulated fracture counts are less than the observed fractures (65 to 50 % fewer stochastic fractures).

8.2.3 Model limitations and required adjustments

Overall, the CFI plots in Figure 8.1 indicate that the 500 m^3 DFN modelling in Chapter 7 did not fully replicate the observed natural fracture intensity or spatial patterns at the drill core-scale and the fracture counts are generally lower (only the D_1 episode models for BH3 and BH4 have greater fracture counts of stochastic fractures). Importantly, even though DFNs should not simulate observed geology exactly, the statistical descriptions of both the stochastic and the observed data should approximately match. Consequently, using the intensity and spatial pattern metrics it can be inferred that this is not the case here. This discrepancy is evidently due to the lower target P_{32} values that were used in the initial modelling (lowered due to computational demands for a 500 m^3 DFN) and simplified termination relationships among the fracture sets (refer to Chapter 4).

Although the modelling approach and resolution of Chapter 7 did not recreate the fracture networks at the resolution of the televiewer data and, therefore, the drill core-scale, it was sufficient to model the evolution of petrophysical (permeability and connectivity) properties over extended geological time spans. However, to refine the models and overcome these limitations, the modelling approach was adapted and fine-tuned to generate fractures within a smaller volume, with both target fracture intensity (P_{32}) and termination relationships calibrated to more closely reflect the deterministic data and observed fracture intersection relationships.

8.3 Results of the drill core-scale DFN modelling, their analysis and validation

8.3.1 The 50 m^3 DFN modelling approach

To refine the replication ability of the DFN modelling at the drill core-scale, iterative modelling at progressively decreasing modelling volumes (from 500 m^3) led to a reduced

50 m^3 modelling volume centred on the middle depths of each drill hole (Figure 8.2). The new modelling volume was able to balance the deterministic input parameters and an optimal processing time. Some adjustments to the modelling inputs were made to account for the new modelling scale, including the fracture size (minimum and maximum truncations) to force the generated fractures to have equivalent radius sizes <50 % of the modelling volume to mitigate edge-effects. To improve the 'grown' DFN aspect, the termination relationships were set to correspond to the observed relationships. Finally, the target P_{32} values were fixed to match the P_{10} Wang et al. (2005) conversions of the televiewer data (Table 7.2), proportioned by the number of televiewer fractures attributed to each deformation episode. These values were calculated for each drill hole as well as for each deformation episode (Table 8.1). The remaining input parameters, such as orientation distributions (Figure 7.4a), and scaling exponent (Figure 7.3), were the same as the 500 m^3 modelling. The input parameters for the DFN modelling are available in the Table C1, Appendix C.

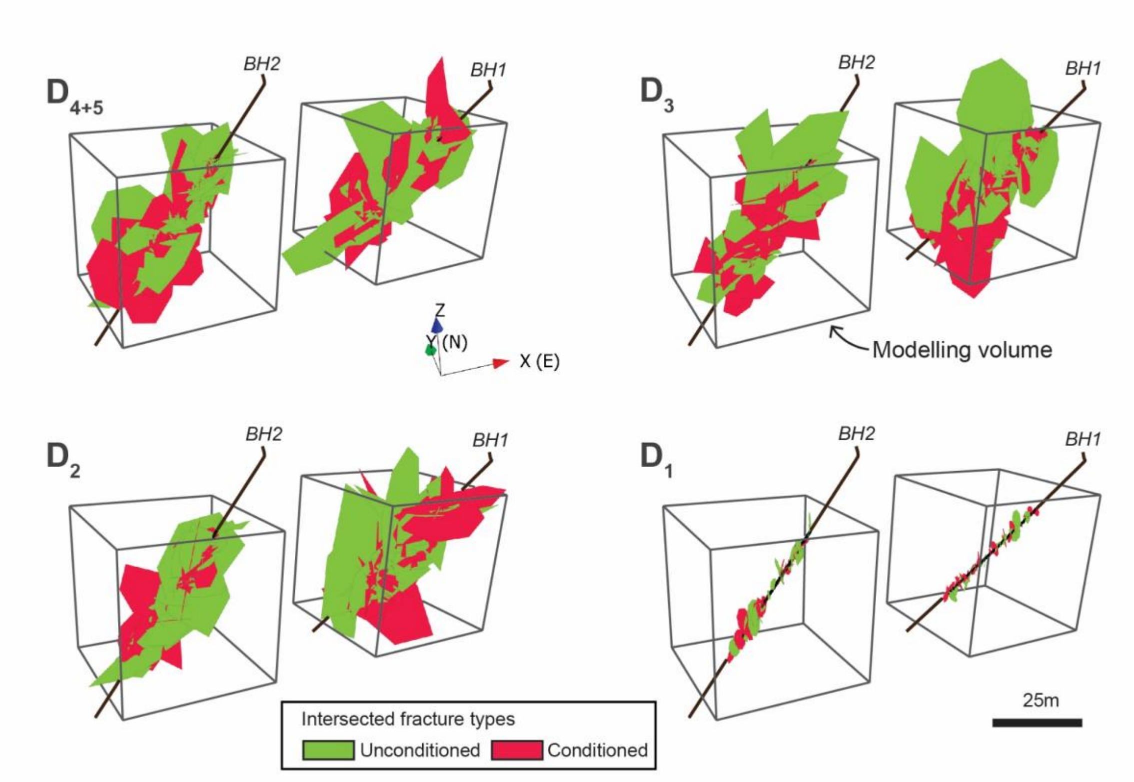

Figure 8.2. Drill hole intersected modelled fractures (only BH1 and BH2 shown here), which are either unconditioned (green) to the downhole televiewer data, representing the raw stochastic modelling output, or conditioned (red) to fit the televiewer data. Fractures are sorted by deformation episode (D_{4+5} to D_1).

Table 8.1. Overview of volumetric intensities (P_{32}) from drill hole intersections used in the modelling. Observed P_{32} values (derived from P_{10} using the Wang et al. (2005) method) are seperated by either total drill hole length (0 m to end of hole depth), or 50 m length (used in the 50 m^3 modelling). The modelling target P_{32} values for each drill hole are provided, with the P_{32} results of the modelling (converted from drill hole intersection P_{10} values using Wang et al. (2005) method). The modelled fractures' P_{32} values are seperated by unconditioned and conditioned processing, with the conditioned values matched to the observed televiewer data over the 50 m of drill lengths.

D_{4+5} P_{32} modelled ($m^2.m^{-3}$)

Drill hole	Observed entire BH	Observed over 50 m	Target	Unconditioned	Conditioned
BH1	4.35	5.36	4.40	2.52	5.36
BH2	3.65	4.43	3.65	2.68	4.43
BH3	2.74	2.82	2.74	2.52	2.88
BH4	2.31	3.48	2.31	3.30	3.90

D_3 P_{32} modelled ($m^2.m^{-3}$)

Drill hole	Observed entire BH	Observed over 50 m	Target	Unconditioned	Conditioned
BH1	3.95	4.56	3.90	2.70	4.56
BH2	3.21	4.28	3.46	2.88	4.28
BH3	2.08	2.33	2.28	3.23	2.37
BH4	2.09	2.96	2.01	2.66	3.03

D_2 P_{32} modelled ($m^2.m^{-3}$)

Drill hole	Observed entire BH	Observed over 50 m	Target	Unconditioned	Conditioned
BH1	3.59	4.11	3.50	3.37	4.11
BH2	2.84	3.94	3.07	2.59	3.94
BH3	1.97	2.06	2.05	2.80	2.09
BH4	1.91	2.68	1.81	2.31	2.74

D_1 P_{32} modelled ($m^2.m^{-3}$)

Drill hole	Observed entire BH	Observed over 50 m	Target	Unconditioned	Conditioned
BH1	1.06	1.59	1.20	0.98	1.59
BH2	0.96	2.38	1.47	1.99	2.38
BH3	0.19	0.28	0.22	0.46	0.46
BH4	0.45	0.84	0.51	0.87	0.94

Sixteen DFN models (one for each of the four deformation episodes per each of the four drill holes) were generated using the procedure outlined in Chapters 4 and 7, and following the same fracture back-stripping methodology: with the D_{4+5} DFN model reflecting the most recent fracture network on Smøla, produced first, and the D_1 DFN model, corresponding to the earliest fracture network, generated last (Figure 8.2). These new stochastic fractures are labelled as 'unconditioned' for the remaining part of this chapter.

The new 50 m^3 DFN modelling inputs, which are more similar to the deterministic parameters than what had been shown to poorly replicate the televiewer data at the drill core-scale, allowed us to expect that the models would be a better replication of the observed televiewer data. Therefore, it allowed us to apply the fracture conditioning approach to stochastically recreate the fracture networks as accurately as possible. To accomplish this, we subsequently ran the fracture conditioning tool in FracMan (WSP UK Limited, 2024) for each of the deformation episode fracture sets, D_{4+5} (five sets), D_3 (four sets), D_2 (three sets), D_1 (one set), for each of the drill holes (Figure 8.2). This conditioning was undertaken using the observed televiewer data for the 50 m drill hole length as the fractures to be matched to. The fracture conditioning procedure is outlined in greater detail in the Chapter 4.

To assess the effectiveness of the fracture conditioning on the DFN modelling, I have utilised three geometric properties to contrast between the stochastic and observed fractures, these being the orientation, spatial pattern, and the volumetric fracture intensity (P_{32}). As the fracture conditioning procedure uses the drill hole televiewer data to adjust the stochastic fractures, the drill holes are used to sample both the unconditioned and conditioned fractures as 'intersected structures' along a 50 m drill hole length within each of the 50 m^3 modelling volumes (Figure 8.2). Each of these extracted drill hole intersected stochastic fractures provide the linear fracture intensity values, P_{10}, which are subsequently converted to P_{32} (see Chapter 4), with the results shown in Table 8.1. Additionally, the orientations of the drill intersected stochastic fractures are plotted against the relevant televiewer datasets (Figure 8.5) to compare the orientations of the unconditioned simulated fractures relative to the observed televiewer data, and then the adjusted 'matched' conditioned fractures relative to both these datasets.

8.3.2 Analysis of 50 m^3 DFN modelling and fracture conditioning

The assessment of the similarity or difference of the observed televiewer data to the modelled fractures (both the unconditioned and the conditioned fracture sets) is split into two parts, firstly looking at P_{32} values and spatial patterns, and then at orientation.

8.3.2.1 Volumetric fracture intensity (P_{32}) and spatial pattern differences

As shown in Table 8.1, the P_{32} values derived from the original televiewer data used in this exercise involved two different drill hole length intervals. These are either the entire drill hole length (utilised to derive the P_{32} values for each deformation episode involving one or more fracture sets), or a drill hole length interval of 50 m set within the centre of the entire drill hole length.

Before comparing P_{32} differences between unconditioned, conditioned, and observed fractures, the P_{32} variation between the televiewer intervals must be addressed. The two drill hole length intervals (entire hole and 50 m length) show different P_{32} values for the same deformation episode televiewer data for each of the same drill holes. Also, the P_{32} values appear to be influenced by the total drill hole length, which varies by drill hole (ranging from 111.1 to 71 m for the entire drill hole length intervals) compared to the consistent 50 m length for the 50 m interval. Overall, the entire drill hole P_{32} values are lower than the 50 m interval by approximately 20 % for BH1, 33 % for BH2, 13 % for BH3, and 34 % for BH4.

The P_{32} values also vary between the drill holes by deformation episodes for the same drill length interval. In the entire hole interval, BH1 has the highest values for $D_{4+5,}$ and the lowest value for BH4 (~47 % lower than BH1); while for the shorter 50 m interval, BH1 is also the highest with BH3 the lowest (also ~47 % lower than BH1). For D_3, BH1 has the highest P_{32}, while BH3 shows the lowest (~47% and ~49% lower for the entire hole and 50 m length intervals, respectively). In D_2, BH1 has the highest values in both length intervals, with BH4 (~47% lower) in the entire drill hole length, and BH3 (~50% lower) showing the lowest in the 50 m drill hole length interval. In D_1, BH1 has the highest P_{32} for the entire hole interval, with BH2 for the 50 m interval, while BH3 has the lowest for both intervals (~82% lower for the entire hole, and ~88% lower than BH2 for the 50

The target P_{32} values (Table 8.1) consequently mirror the variation in P_{32} values by drill hole, and deformation episode. For this modelling though, I chose that the target P_{32} values would more closely resemble the observed P_{32} values derived from the entire drill hole length (as utilised in Chapter 7; Figure 7.5). In several cases, however, they have values which are between the lower entire drill hole and the higher 50 m drill length interval P_{32} values. Overall, BH1 commonly has the highest target P_{32} values, and BH3 the lowest, with BH4 in a few cases having the lowest depending on the deformation episode being modelled.

As the 50 m drill hole length intervals were subsequently set within the 50 m^3 DFN modelling, I will now compare the P_{32} values as derived from the drill intersection sampling of the new DFN stochastic fractures (unconditioned fractures) against the 50 m drill length televiewer P_{32} values (Table 8.1), and plot the downhole CFI of both these datasets for each drill hole and deformation episode on Figure 8.3 & Figure 8.4.

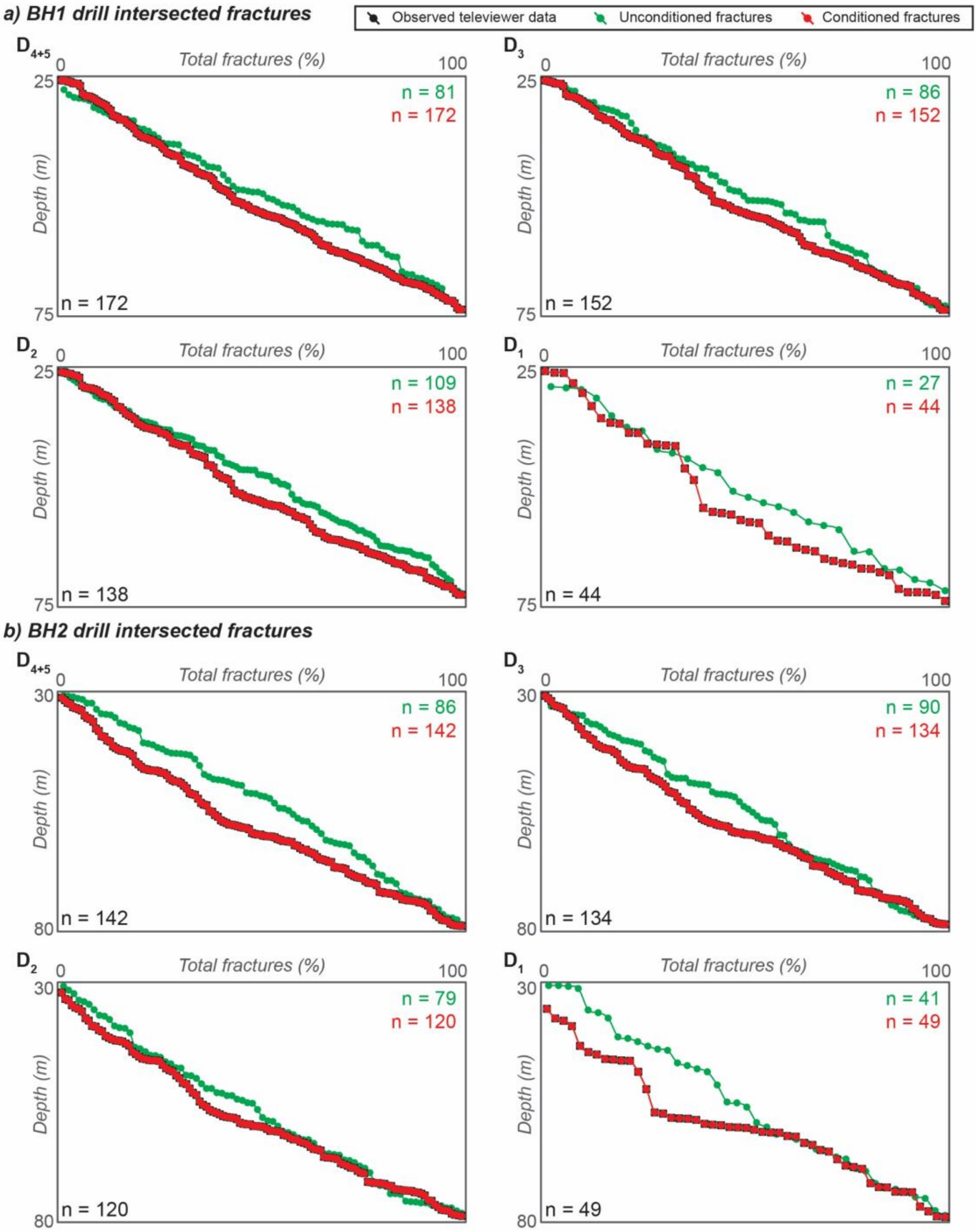

Figure 8.3. Cumulative fracture intensity (CFI) plots for BH1 and BH2 showing the observed downhole televiewer data for the two drill holes (black) against the modelled fractures, seperated into unconditioned fractures (green), and conditioned fractures (red).

For each drill hole, the unconditioned fractures sorted by deformation episode returned P_{32} values that did not match the target P_{32} values. For drill holes BH1 and BH2, the unconditioned fractures had associated P_{32} values that were consistently lower than the target P_{32} values (except for BH2 for the D_1 episode), ranging from ~ 4 to 42 % lower than the target P_{32} values. BH3 and BH4 on the other hand typically returned P_{32} values which were all greater than the target P_{32} values, except for BH3 for the D_{4+5} episode, with differences ranging from ~27 to >100 % higher. This over-estimation of volumetric fracture intensity is particularly evident in the D_1 episode modelled fractures for BH3 and BH4. Interestingly, in places (such as the D_2 and D_1 episodes for BH4) the higher P_{32} values are more similar to the 50 m observed televiewer P_{32} values than the values which were selected for the target P_{32}.

When plotted on the CFI plots (green curves on Figure 8.3 & Figure 8.4), the unconditioned fractures exhibit relatively uniform downhole fracture intensities for all the deformation episodes. In BH1 and BH2 (Figure 8.3a and b), the fracture counts are lower, as is expected with the associated lower P_{32} values (as discussed above, Table 8.1) and the relevant linear fracture intensities (P_{10}). Compared to the CFI curve for the televiewer data (black curve, covered by the red curve of the conditioned fractures in Figure 8.3), the change in downhole fracture intensities, and spatial pattern of the fracture occurrences are not particularly well replicated by the unconditioned fractures. The BH3 and BH4 CFI plots (Figure 8.4a and b) however, the fracture counts are more similar to the televiewer data. For BH3, the modelled unconditioned fractures for both D_{4+5} and D_1 replicate the observed data relatively well in terms of rate of increase in total percentage of fractures and spatial patterns in fracture intensity. Likewise, the unconditioned fractures for the deformation episodes D_3 and D_1 in BH4 also exhibit relatively similar CFI curves to the observed televiewer fractures.

The conditioned modelled fractures, as shown on Table 8.1, returned P_{32} values which are typically all higher than the unconditioned fractures (average increase in volumetric fracture intensity of between 16 to 30 %). The P_{32} values do, however, match the observed televiewer data for the 50 m drill length interval for the majority of the models, with BH1 and BH2 replicating the P_{32} with 0 % difference in the values, while BH3 replicates most of the P_{32} values with only a ~2 % difference (except for D_1 where the conditioned fracture P_{32} is ~39 % higher than the observed televiewer data), and BH4 conditioned fractures being the least similar with a ~2 % difference for D_3 and D_2, while D_{4+5} and D_1 returned a P_{32} value ~11 % greater than the observed televiewer data. Overall, the conditioned fractures returned less similar P_{32} values when the fracture counts of the observed data were lower, such as for the D_1 deformation episode.

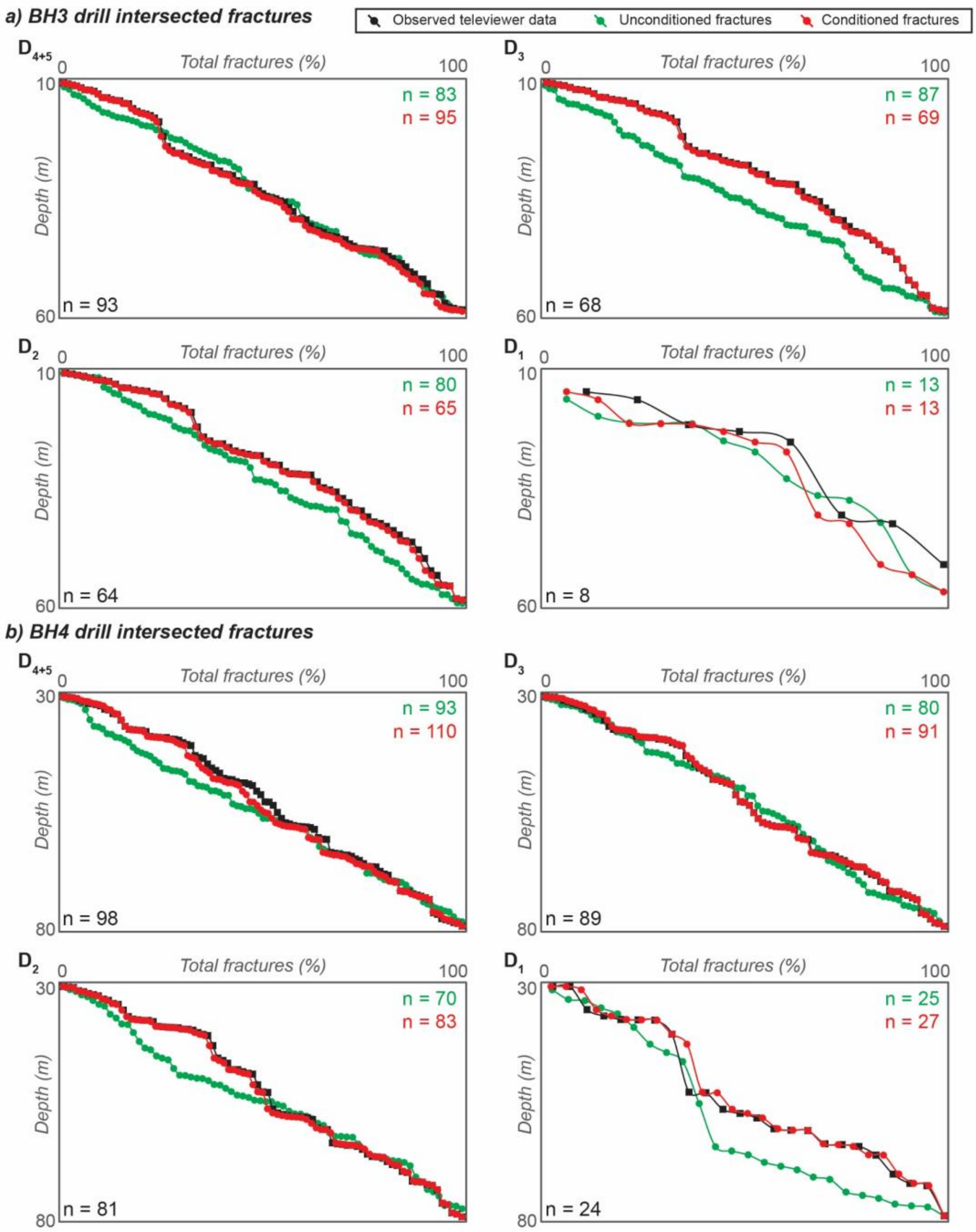

Figure 8.4. Cumulative fracture intensity (CFI) plots for BH3 and BH4 showing the observed downhole televiewer data for the two drill holes (black) against the modelled fractures, seperated into unconditioned fractures (green), and conditioned fractures (red).

The conditioned fracture sets on the CFI plots (red curves on Figure 8.3 & Figure 8.4) demonstrate how conditioned fractures have also been able to effectively reproduce the observed televiewer fractures downhole for each of the drill holes. The replication of the downhole rate of increase of fracture intensity and the spatial distribution of fractures (spatial pattern) is particularly good for BH1 and BH2, where the red conditioned fracture curve on Figure 8.3a and b overlaps the observed televiewer data black curve. The CFI plot for BH3 drill hole in Figure 8.4c has the next best fit between the conditioned fractures and the observed televiewer, with the DFN models for D_{4+5} and D_1 showing local poor replication (red curve deviating off the black curve) compared to the cumulative fracture count being different. The CFI plots for BH4, for the D_{4+5} and D_2 deformation episode models locally deviate as well. However, the shape of the conditioned fracture curves is similar to the observed data, suggesting that the spatial pattern of fracture occurrence downhole is well replicated (except for D_1 for BH3, where the curves only locally coincide).

However, aside from the local deviations between the conditioned modelled fractures and the observed televiewer data, fracture conditioning can be considered to have significantly improved the match between the stochastic fractures and the observed data, which provided the original deterministic inputs. To further compare and test the fracture conditioning, the geometric matching between the stochastic fractures (both unconditioned and conditioned) and the observed televiewer data is now analysed.

8.3.2.2 Simulated and observed fracture orientation comparison

Plotting the orientations of the observed televiewer, unconditioned, and conditioned fractures as poles to planes on the stereonet plots on Figure 8.5, by drill hole and by deformation episode, I can make a direct comparison of how well the data types match.

The unconditioned fractures (green triangles on Figure 8.5) exhibit orientation distributions related to the modelling input parameters used for the DFN modelling. As the deterministic input parameters for the modelling were simplified representations of actual geological data, in places the modelling has failed to fully reproduce the observed data. This is most evident in the low angle fractures (associated to the D_2 deformation episode) in BH1, BH2, and BH4 drill holes have more numerous poles to planes than expected from the observed data (black squares on Figure 8.5). Additionally, the moderately SE-dipping NE-SW to E-W striking fractures (D_2 deformation episode-related) are also poorly modelled for in BH1, BH2, and BH4 (unconditioned fracture poles to planes rarely plot in this part of the stereonet). Furthermore, in BH3, the D_2-related low angle fractures have a cluster orientation that does not coincide with the distinct cluster of observed televiewer fractures (representing shallow NE-dipping, ~NW-SE striking fractures).

The conditioned fractures (solid red dots on Figure 8.5) do however have an overall good match to the observed televiewer data. The good fit of the conditioned fractures is clearest in the BH1 stereonets (Figure 8.5a), where there is an almost perfect orientation match through the different models related to the various deformation episodes. Aside from the overall good match, in places the conditioned fracture data do not fit the observed data and typically remain in the same orientation as the unconditioned data. In BH2 (Figure 8.5b), a low number of low angle fractures (D_2-related) did not adjust their orientation with the fracture conditioning and remain in the same orientation as the unconditioned equivalent fractures.

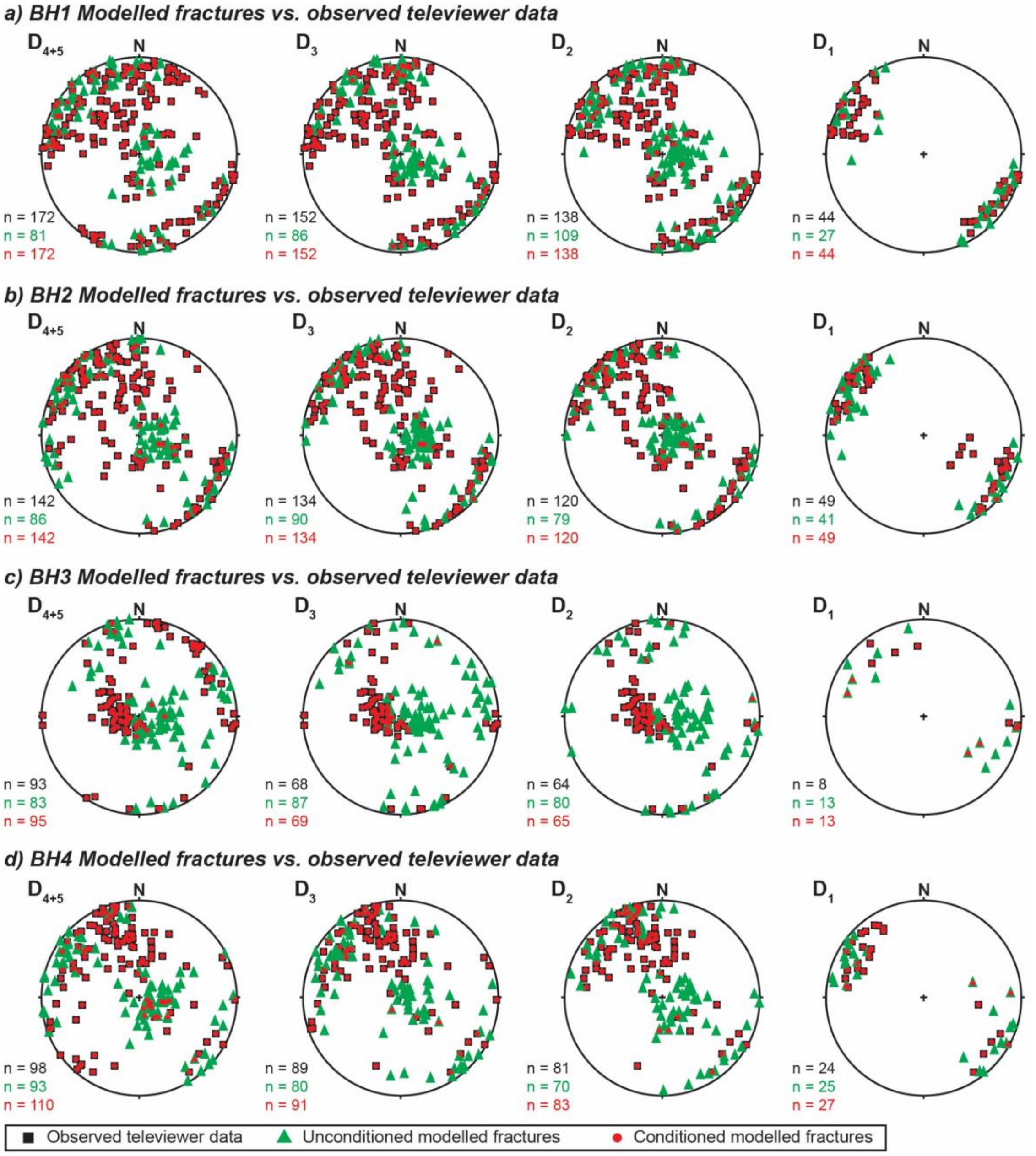

Figure 8.5. Stereonet plots showing both the modelled fractures and the observed downhole televiewer data used in the modelling by drill hole and deformation episode. The modelled fractures are shown as both conditioned (to match the televiewer data), and unconditioned (does not match the televiewer data).

Similarly, in BH3 and BH4, the low angle D_2 fractures only experienced limited fracture conditioning (several fractures remained not adjusted). Other conditioned fractures in BH3 (Figure 8.5c), for the steeply dipping N-S (D_3-related) and the NE-SE striking (D_1-related) fractures also remined in the same orientation as the unconditioned fractures. BH4 also shows the same lack of adjustment for a few of the D_1 NE-SW fractures (Figure

8.5d). In general, for all the drill holes and deformation episode models, all the pole to planes of the observed televiewer fractures are matched with associated adjusted conditioned fractures (all the black square symbols on Figure 8.5 are overlapped with the red solid dots). The unadjusted conditioned fractures appear to relate to when there are too many fractures available for the conditioning (FracMan does not allow two stochastic fractures to be conditioned to the same orientation of an observed datum).

8.3.3 Key modelling-derived fracture characteristics and parameters

The fracture conditioning process applied to the DFN models has been shown to replicate the natural fracture pattern on Smøla, as observed in the four different downhole televiewer surveys. Consequently, the different fracture characteristics and parameters related to these stochastic fractures (unconditioned and conditioned) can be considered representative of the fracture arrays which formed in a response to the four different deformation episodes. These characteristics are summarised in Table 8.2.

The parameters for the four drillholes are separated by deformation episode and include information on fracture size (equivalent radius), mean fracture spacing, and fracture counts. Along with the P_{32} values in Table 8.1, these parameters should allow for the representative modelling of the fracture networks on Smøla island at the drill hole-scale.

8.4 Discussion

I have validated and semi-quantitatively assessed both the 500 m^3 and new 50 m^3 DFN models to evaluate their ability to reproduce natural fracture networks. Using the same methodology as Chapter 7, I refined the modelling parameters to better replicate the observed fracture, vein, and fault arrays by deformation episode on Smøla. This section discusses the approach's intricacies, limitations, and potential directions for further research.

8.4.1 The 500 m^3 modelling validation

The resolution selected for DFN modelling significantly affects the fracture size range (equivalent radius) incorporated. Coarser scales tend to include more large fractures, while finer resolutions have smaller fractures dominating. This sample bias in fracture sizes affects P_{32} (or P_{10}) and therefore the number of fractures potentially intersected by drill holes. In the CFI plots comparing the conceptual 500 m^3 models to the observed televiewer data for the entire drill hole intervals (Figure 8.1), the key discrepancy is the fracture count difference. As described in Chapter 7, the P_{32} values were selectively reduced by 30 to 80 % (of the associated deterministic P_{32} value) to improve computational efficiencies related to modelling within a 500 m^3 volume.

Table 8.2. Summary of key model output parameters for both the unconditioned and the conditioned fractures (representing refined potential input parameters). Parameters are seperated by drill hole and by deformation episode. Size of the fractures is provided in equivalent radius size, where equiv. = equivalent.

D_{4+5}	**Unconditioned fractures**					**Conditioned fractures**				
Drill hole	Fracture count	Max. equiv. radius (m)	Min. equiv. radius (m)	Mean equiv. radius (m)	Mean spacing (m)	Fracture count	Max. equiv. radius (m)	Min. equiv. radius (m)	Mean equiv. radius (m)	Mean spacing (m)
BH1	81	17.44	1.01	4.57	0.59	172	17.44	1.00	3.29	0.29
BH2	86	17.05	1.04	4.15	0.58	142	17.05	1.01	3.44	0.35
BH3	83	11.99	1.10	4.40	0.59	95	11.99	1.10	4.55	0.53
BH4	93	13.89	1.04	3.38	0.53	110	13.89	1.02	3.43	0.46

D_3	**Unconditioned fractures**					**Conditioned fractures**				
Drill hole	Fracture count	Max. equiv. radius (m)	Min. equiv. radius (m)	Mean equiv. radius (m)	Mean spacing (m)	Fracture count	Max. equiv. radius (m)	Min. equiv. radius (m)	Mean equiv. radius (m)	Mean spacing (m)
BH1	86	19.44	1.18	5.24	0.57	152	19.44	1.00	4.31	0.33
BH2	90	12.82	1.01	4.21	0.55	134	12.82	1.01	4.04	0.37
BH3	87	19.57	1.18	4.47	0.57	69	19.57	1.32	4.74	0.72
BH4	80	11.08	1.00	3.46	0.62	91	11.08	1.00	3.53	0.55

D_2	**Unconditioned fractures**					**Conditioned fractures**				
Drill hole	Fracture count	Max. equiv. radius (m)	Min. equiv. radius (m)	Mean equiv. radius (m)	Mean spacing (m)	Fracture count	Max. equiv. radius (m)	Min. equiv. radius (m)	Mean equiv. radius (m)	Mean spacing (m)
BH1	109	19.32	1.01	4.57	0.46	138	19.58	1.01	4.63	0.36
BH2	79	15.86	1.05	4.05	0.63	120	15.86	1.01	3.51	0.41
BH3	80	19.31	1.02	4.31	0.63	65	19.31	1.03	4.50	0.76
BH4	70	11.42	1.04	4.28	0.70	83	11.42	1.04	4.16	0.61

D_1	**Unconditioned fractures**					**Conditioned fractures**				
Drill hole	Fracture count	Max. equiv. radius (m)	Min. equiv. radius (m)	Mean equiv. radius (m)	Mean spacing (m)	Fracture count	Max. equiv. radius (m)	Min. equiv. radius (m)	Mean equiv. radius (m)	Mean spacing (m)
BH1	27	4.17	1.06	1.79	1.68	44	4.17	1.04	1.74	1.15
BH2	41	4.54	1.03	1.97	1.23	49	4.54	1.02	1.90	0.93
BH3	13	4.91	1.08	1.98	3.42	13	4.91	1.08	1.98	3.56
BH4	25	3.93	1.03	1.62	2.01	27	3.93	1.03	1.60	1.88

Despite the lower fracture intensities, the 500 m^3 DFNs still involved between ~5 to 10×10^6 individual fractures, generally on the metre-scale on average. Nevertheless, the overall lower fracture counts, as demonstrated here, are a direct consequence of user-related reduction in P_{32} values. If these models were generated with intensity values as defined by the original deterministic inputs, fracture counts would be significantly higher and likely match the observed data. This analysis demonstrates that reducing the P_{32} values necessitates refining and adjusting the modelling to better replicate the observed geology in such a way to mitigate computational efficiency issues, which is discussed further on in this section. Thus, the P_{32} values used in the 500 m^3 modelling, may only be applicable at coarser resolutions (where larger fractures dominate) such as similar to the trace maps in Figure 7.2 (as shown in the "Observed entire BH" column in Table 8.1).

However, the D_1 modelled fractures' CFI plots (Figure 8.1), show fracture counts comparable to the observed fractures, particularly in BH4, where 32 D_1 modelled fractures nearly match the 30 D_1 observed fractures. This suggests that the reduced P_{32} values are not the only reason for the underestimated fracture counts. For deformation episodes with lower fracture intensities such as the epidote-prehnite veins in D_1, the 500 m^3 modelling may adequately represent the fracture system at the drill core or outcrop scale.

Another possible reason for the underestimation is the modelling input parameters, especially fracture size and scaling. These characteristics were derived from observed data, such as the 2D lineament trace maps (Figure 7.2). While the finest scale used in the trace mapping exercise is comparable to the 500 m^3 modelling, it is coarser than the drill hole data used to derive the downhole P_{10} values (subsequently used to estimate P_{32}). When determining the fracture size distribution and the scaling exponent (such as in Figure 7.3), resolution effects such as censoring smaller fractures may also result in the incomplete documentation of fractures (Dichiarante et al., 2020). Along with potentially misallocating the statistical spread of fracture sizes to a power law distribution, the ratio between small to large fractures may not be scale-independent through all scales (only fractal at larger scales) (Berkowitz et al., 2000; Davy et al., 2010; Dichiarante et al., 2020). Therefore, fractures characterised at coarser scales may struggle to accurately describe networks at the outcrop scale, as seen with the Smøla drill holes (Davy et al., 2018). This all suggests that the 500 m^3 DFN are more suitable for larger-scale networks at resolutions greater than the drill core-scale.

8.4.2 The 50m^3 modelling and fracture conditioning

The extra 50 m^3 DFN modelling in this Chapter shows a significantly improved replication of drill core-scale televiewer observed fractures compared to the 500 m^3 conceptual models. This improvement is most evident in the fracture conditioning, whereby the unconditioned DFN models provided sufficiently realistic simulations of the observed features to be, in most of the cases, easily adjusted to match the observed data in terms of orientation, intensity, and spatial distribution of fractures.

However, an important issue associated with the refining and validation of the DFN models relates to the use of the same drillhole data for both model calibration and validation (even considering the variety of deterministic data sources). Particularly, in the case of the fracture conditioning, these models lack validation by an independent dataset which has not been previously used as a model input parameter. Consequently, these DFN models are not suitable to be used for predictive purposes in rock volumes which are not already geologically constrained. The conditioned DFNs therefore offer generalised fracture parameters which can be utilised to model outcrop to drill-core-scale fracture networks in the Smøla crystalline basement or analogue. These DFN modelling parameters may also be applied to other crystalline basement volumes in terms of a conceptual ‘starting point’ which would require additional calibration and validation with other datasets such as dynamic fluid flow modelling. However, several details regarding the general characteristics warrant further discussion, as outlined below.

The variation in P_{32} and orientation trends for the different televiewer datasets is especially remarkable. Focusing on the 50 m drill hole length intervals for the four drill holes (Table 8.1), clear differences in fracture intensity are present between the drill holes, especially between the BH1/BH2 and the BH3/BH4 group, across different deformation episodes. The orientation trends, both in geometry and data frequency (Figure 8.5) are also distinct. By replotting the field data (Figure 5.3) for selected field mapping sites across Smøla, and the televiewer data (Figure 7.4) relative to the major lithologies on the island (Figure 8.6), the variation in orientation trends becomes clear. Similar studies in crystalline basement indicate fracture orientation, intensity, and clustering vary according to lithology and proximity to major structures (Beacom et al., 2001; McCaffrey et al., 2020; Seeburger and Zoback, 1982). As the Smøla rock volume is lithologically heterogeneous, it is possible that the intensity of fractures potentially forming during a given deformation episode are similarly influenced by the local geology.

The 50 m^3 DFN modelling used input parameters based on a composite of televiewer data from the four drill holes ('global' parameters). However, since the televiewer data is locally variable, the ‘global' parameters may therefore be a poor fit. For example, in BH4, the higher P_{32} values for D_{4+5} deformation episode fractures suggest an inclusion of more fractures than necessary to match the stochastic fractures with the observed televiewer data. These fractures, which correspond to the global parameters, are less prevalent in BH4. The fracture conditioning process uses the observed dataset (to be matched against) to select best fit fractures from the unconditioned dataset, and then, if mis-oriented from the target orientation, readjust them (Golder Associates (UK) Ltd., 2001). However, if these stochastic fractures have orientations greater than the 'maximum adjustment angle' (>45° in our study), the orientation will not be changed (Golder Associates (UK) Ltd., 2001). These unconditioned fractures however will still appear in the conditioned fracture dataset as the algorithm will ensure that the spatial distribution of the stochastic fractures will match the observed data (as seen in the CFI plots in Figure 8.3 & Figure 8.4) even if the orientations are incorrect. Alternatively, if the unconditioned fracture dataset has a low P_{32}, and the orientations of the fractures are outside of the maximum adjustment angle, additional fractures will not be generated to match with the observed fracture intensity. This is because the fracture conditioning process also prioritises compliance to the 'global' fracture set parameters, even if a lower match with observed fracture intensities will occur (Golder Associates (UK) Ltd., 2001). Consequently, the fracture conditioning process returns sub-optimal results when fracture orientation input parameters are not properly represented in the local observed fracture orientations.

Consequently, although our DFN modelling at the 50 m^3 drill hole-scale typically replicates the observed televiewer very well overall, the local discrepancies, mentioned above, suggest that spatially domaining the data over the island by lithology or proximity to major structures may further improve the modelling results. Domaining of low permeability reservoir volumes, by mechanical or stratigraphic units/facies, is commonly done when deriving fracture-related parameters (e.g. Ceccato et al., 2021b; Giuffrida et al., 2020) which can be potentially used for DFN modelling, and is applicable to fracture characterisation in crystalline basement volumes. Geocellular DFN modelling includes local variabilities in fracture and fault orientation, intensity, and spacing which could be defined by a domaining approach (Golder Associates (UK) Ltd., 2001). However, geocellular modelling lacks the temporal component present in our 'grown' DFN method. An integrated approach, combining multiple locally derived 'grown' DFN models (to constrain the grid-based inputs) with a larger geocellular model, could better characterise a larger basement volume sub-divided by domains. This approach is however outside of the scope of this project and is a suggested way forward for future research.

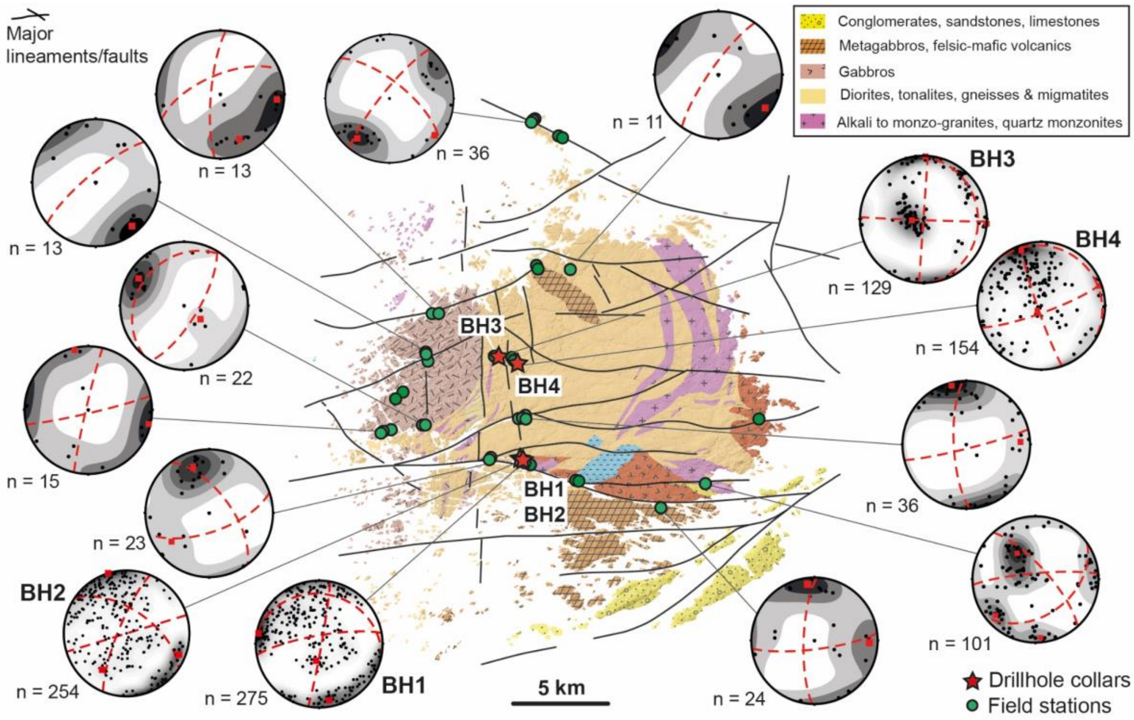

Figure 8.6. Adapted representative field data for selected outcrop sites across Smøla island, and the televiewer data by drill hole, highlights the variation in structural trends over the study area. The pole to plane clusters are indicated by red squares on the cluster maxima (assumed to represent a fracture orientation trend), with red dashed planes showing the associated fracture orientations for the different maxima. All stereonet plots are Kamb contoured at the 2σ interval.

Lastly, the generalised DFN parameters provided in Table 8.2 propose suitable inputs for modelling the polyphase fracture networks on Smøla. However, the fracture size (equivalent radius) and scaling exponent (Table 7.2) parameters were not adjusted during the conditioning process, and remain related to the input parameters influenced by the deterministic inputs in Chapter 7, which assume a fractal Power Law scaling. Our fracture conditioning approach did not validate fracture size distributions, which require outcrop-scale 2D fracture trace maps, such as derived by drone-based (UAV) photogrammetry surveys (e.g. Ceccato et al., 2021a). For future work, finer-scale trace map conditioning is also recommended to further validate and refine our DFN models.

8.5 Conclusion and summary

This chapter has offered a critical analysis of the DFN modelling undertaken. I have assessed how well the stochastic and conditioned fracture modelling results match with the observed fracture data (downhole acoustic televiewer datasets) and produced a set of generalised fracture output characteristics which could be used for input parameters to realistically model polyphase deformation on Smøla island at the sub-seismic scale (drill core-scale).

The assessment initially looked at the conceptual 500 m³ DFN models against the observed data using CFI plots to visually identify differences in the spatial patterns of the stochastic fractures relative to the natural observed fractures in the four drill holes (by deformation episode). This comparison highlighted the effect of resolution had on the modelling, showing that the 500 m³ DFN models had lower fracture counts (and P_{32} values) relative to the observed data, and suggesting the models were suitable for conceptual modelling at coarser scales than the drill core scale.

To improve and refine the representativeness of the DFN modelling at the drill core-scale, I remodelled the different deformation episodes' fractures using a smaller modelling volume of 50 m³. This modelling incorporating P_{32} values and termination relationships more in line with the deterministic inputs derived earlier in the study. The 50 m³ DFN modelling generated stochastic fractures (unconditioned) which should an improved replication of the observed televiewer data. This was further refined by undertaking a process of fracture conditioning which was able to largely match the modelled fractures to the observed fractures. However, some minor mis-match between the modelled fractures and the observed fractures were present in certain deformation episode models for BH3 and BH4.

These mis-matches between modelled and observed data were due to local variation in the fracture intensity and orientations present between the different drill holes. The 'global' modelling input parameters, derived from composite fracture characteristics from all the drill holes and the 2D trace maps across Smøla, resulted in the 50 m³ DFN models not always accommodating local differences. This was particularly clear in the difference in abundance of fractures of certain orientations between the drill holes. However, overall, the conditioned modelled fractures did typically match the P_{32} values, spatial patterns, and orientations of the observed fractures (making the models more deterministic in a sense), making them representative of the Smøla fracture networks.

Chapter 9: Synthesis and discussion

9.1 Project synopsis

This study has focussed on two main themes: 1) The geological and structural 3D characterisation of an onshore crystalline basement fractured reservoir analogue (Smøla island), which involved documenting and arranging exposed faults and fractures within a relative and absolute temporal, mineralisation, kinematic, and geometric framework. This framework enabled the sequential deformation of Smøla to be unravelled and allowed the prolonged tectonic history of this part of the passive margin to be constrained. From this characterisation, key deterministic parameters were compiled and used for the second part of the project. 2) The application of the observed geology and structural characterisation (deterministic parameters) from Smøla to conceptually reproduce the progressive deformation of the basement block using a stochastic modelling approach. A summary of these two study components is provided here.

For the first part of the study, an integrated workflow incorporating remote sensing and geophysical data for lineament analysis, field mapping of 65 outcrops across the island, high resolution logging of ~389 m of oriented diamond drill core (available for the first time for an onshore basement analogue in a mid-Norwegian passive margin setting), and the detailed petrographic and microstructural analysis of 42 thin sections taken from strategic outcrop and drill core locations, produced a relative chronology of fracture and fault formation (Figure 5.7). Seven K-Ar samples collected from both geometrically and kinematically constrained outcrop and drill core fault gouge intervals provided absolute ages, which then could be used via mineral assemblage and geometric comparison to absolute age-sort the various documented deformation stages (Figure 5.11). Integrating all the multiscalar datasets and the absolute time components together, five deformation episodes (referred to as D_1 to D_5) were unravelled spanning from the Devonian (< 390 Ma) late Caledonian-related extension and transtension on the MTFC, through to the Cretaceous-Paleogene (~70-60 Ma) prior to the break-up of Norway-Greenland (Figure 5.12).

For the second part, reconstructing the progressive fracture-saturation of a rock volume through geological time, and simulating the petrophysical properties through the process involved significant conceptual and technical challenges. To offer a possible solution to these hurdles, this study employed and demonstrated an integrated deterministic-stochastic workflow. To effectively recreate these fracture sets in absolute time, a ‘grown’ DFN modelling approach was selected owing to its ability to replicate multiscalar complexity, statistical variability, and to include a temporal component. Utilising a rich array of high-resolution datatypes, structural characterisations, and tectonic interpretations from the first part of the study, I defined a series of deterministic input parameters for stochastic DFN modelling, enabling the reconstruction of Smøla's progressive deformation history via fracture-back-stripping in four different time-constrained DFN models. These DFNs enabled the estimation of petrophysical properties at specific geological episodes, from the Devonian to the Early Paleogene. Further refinement of the DFN models improved the replication of fracture networks, providing validated input parameters for future DFN modelling of similar fractured crystalline rocks.

For the very first time, it has been possible to estimate certain fracture-related petrophysical properties back in geological time from simulated 'fossil' fracture networks, which reflect the evolution of an actual fractured rock volume through time. Essentially, it is now possible to determine which fractures (with associated geometries and paleo-apertures) or combination of thereof may have facilitated reservoir charging back in time, and how progressive fracture saturation of the crust affected the evolution of bulk petrophysical characteristics of a crystalline basement like Smøla.

Therefore, making this study approach particularly robust is the inclusion of the detailed deterministic characterisations of the fractures and related networks on Smøla. In fact, this study has only been possible because of the deterministic foundation and the absolute time frames of the study. These inputs allowed me to comprehensively constrain the evolution of fracture-related characteristics on Smøla, as reported above, and in the scientific papers compiled herein.

9.2 Progressive fracture saturation and petrophysical evolution

Integrating the two parts of the study, I will now discuss the temporal evolution of Smøla's deformation features and the wider tectonic history within the context of the DFN modelling results and combine the different components to understand the variation of petrophysical properties (secondary permeability and fracture connectivity) I estimated, through geological time. I will also address a selection of limitations and insights derived from the study, along with how this work may apply to the offshore domain off Norway and offer suggestions for future research opportunities based on the study findings. This section therefore provides a high-level synthesis of the study, highlighting its novelty, contributions, and key lessons learnt from this approach.

9.2.1 The Smøla DFN models through geological time

Even though this study's DFN modelling approach has been to progressively back-strip out the youngest fractures from each overall fracture network, from the current fracture network on Smøla back to the earliest in the Devonian, the subsequent youngest fracture set in each DFN generally exhibits the largest aperture and highest fracture intensity (Figure B1, Appendix B). Each of the DFNs, therefore, virtually simulates the youngest fracture set (by specific deformation episode and timing) and a ’selection‘ of the pre-existing, inherited fracture sets. The DFN models consequently realise specific fracture set configurations with a combination of different fracture types, apertures, fracture intensity, and ages based on the deterministic inputs (e.g. Libby et al., 2019, 2024). It is these fracture-set configurations that provide the input for the petrophysical characteristics estimation. Therefore, comparing the model results with age determination methods, tectonic settings, and stress orientations yields useful insights into the evolution of crustal fracture saturation, and fluid flow histories.

The D_1 fracture network, involving epidote-prehnite veins formed during post-Caledonian (< ~390 Ma) brittle sinistral transtension along the MTFC (Figure 5.12), is recreated and modelled in the D_1 DFN model (Figure 7.5). The D_1 DFN model therefore captures the earliest permeability anisotropy in the Smøla rock volume. The timing of these fractures falls within the age range attributed to other epidote veins dated in Norway such as: epidote veins with ages of ~396 Ma (using Sphene U/Pb dating) in SW Norway (Larsen et al., 2003), a ~404 Ma (U/Pb) low confidence age of allanite (epidote) mineralisation in Late Caledonian pegmatites in the Tysfjord region in northern-central Norway (Hetherington et al., 2021), and a epidote U/Pb age of ~386 Ma from Finnmark in northern Norway (Piraquive, A., Pers. Comm. 2024). Refining the D_1 age in the structural characterisation and DFN modelling by directly dating the Smøla epidotes would, therefore, surely represent a clear future research opportunity to further improve this study.

From characterisation work done on the D_1 veins, these features appear to commonly include reworked banded or foliated cataclasites (Figure 5.6), which, along with the closure (or crystallisation) temperature of hydrothermal epidote (~200-350 °C; Bird and Spieler, 2004), suggest possible cataclastic flow from brittle fluidisation events occurring close to the brittle-ductile transition (which, for quartzo-feldspathic rocks, is between ~300-400 °C; Fossen, 2010b) with later cementation of epidote (Marchesini et al., 2019; Sibson, 1977; Wehrens et al., 2016). Our stochastic modelling may therefore have recreated the early ‘self-generating’ permeability structure that formed during post-Caledonian times, potentially through fluid overpressure and hydrofracturing owing to migrating fluids in a tectonically active orogenic domain (Cox, 2010; Sibson, 1996). The exact origin of this D_1-related fluid and the mechanism driving the overpressure are currently unknown, but from field evidence and documentation of similar features along the passive margin (e.g. Indrevær et al., 2014), a possible regional-scale fluid migration and circulation can be inferred.

The stochastic D_1 modelling results show abundant isolated fractures (Low C_B value, with mostly I-I-type branches; Figure 7.7), and are also associated with a highly anisotropic permeability tensor ($K_1 \approx K_2 > K_3$). The low matrix permeability of the Smøla host rocks, as well as the lack of significant percolation owing to low connectivity, may have enhanced hydraulic fracturing and focussed fluid flow along the NE-SW oriented D_1 structures (corresponding to the K_{Hmax} orientation). This orientation, along with the SW Norway post-Caledonian (Late Devonian-Early Carboniferous) stress field (assumed to be applicable here) and characterised by a NE-SW SH_{max} and a NW-SE SH_{min} (transtension) orientation (Scheiber and Viola 2018), seems to have had a strong control on the D_1 fracture orientations and therefore the fluid pathway at the time.

Unlike D_1, the absolute dated D_2 sericite-chlorite-calcite mineralised shear fractures on Smøla (including phyllitic shear bands and gouge zones) that formed during two phases of strike-slip faulting during the Carboniferous-Permian and Triassic-Jurassic (~291-287 Ma and ~204-196 Ma; Figure 5.12) provided absolute age constraints on the D_2 DFN model. The DFN modelling of the D_2 fracture and fault network was particularly challenging owing to the evidence of multiple deformation stages, as suggested by microstructural analysis and confirmed by the possibly inherited (older authigenic?) ~300 Ma and a younger authigenic ~200 Ma K-Ar age results (possible multiple reactivations or different events; Figure 5.11). To account for the polyphase deformation recorded by the K-Ar results, the stochastic modelling thus incorporated both the multiphase D_2 fractures and selectively reactivated D_1 fractures into the D_2 model realisation (generating a configuration of three fracture sets).

However, the connectivity assessment (C_B value) for D_2 indicated it was nearly equivalent to that of the later D_3 and D_{4+5} episodes. This suggests that D_2 should be subdivided into two sub-episodes to better assess the intermediate evolution of connectivity and permeability between D_1 and D_3. This highlights the importance of calibrating the number of static DFN models to appropriately recreate the step-wise fracture network development, even if they may form part of the same overall deformation episode (as documented by similar K-Ar ages and similar mineral-assemblage infill). Further work is therefore needed to distinguish the relative ages of the two D_2 structural orientation trends, and remodelling these two fracture sets separately should potentially avoid abrupt changes in petrophysical property measurements and indicate a more distinct variation through time.

This example also suggests that the discrete deformation episodes I have used in this study may potentially be overly simplistic. As suggested by, for example, Fossen et al. (2019), natural deformation processes may not always be episodic, with deformation features, such as fracture sets, forming instead progressively during a long-lived event. Additionally, the development of later deformation features during a progressive deformation process may be influenced by pre-existing (older) structures, resulting in changes in geometry, with the changes independent from any wider regional tectonic processes (Fossen et al., 2019). However, to simulate complex fracture networks like those on Smøla, it is likely essential to use a 'reductionist approach' with discrete deformation episodes, which in this study has been based on coeval mineralisation assemblages, geometries, and K-Ar ages (along with indirect ages, such as for D_1). This approach provides a simplified series of inputs that can effectively represent the complexity of natural systems.

The D_3 fracture network, characterised by the chlorite-hematite fractures (including breccia intervals) related to ~128-100 Ma aged dip-slip and possible transpression faulting (including the MTFC) (Figure 5.12), afforded the associated D_3 DFN the ability to recreate the active fracture network during the Cretaceous. This DFN model possessed the highest connectivity (C_B values), and the second highest permeability (K) out of all the DFNs produced (less than the final DFN model; Figure 7.8). Despite not having the highest associated bulk permeability overall, the pervasive hematite mineralisation associated with the D_3 fractures (Figure 5.5), potentially linked to hydrothermal or metamorphic fluid circulation (with hematite precipitation likely from fluid-rock alteration and metamorphic reactions; Indrevær et al., 2014; Putnis and Austrheim, 2010), may indicate significant geofluid circulation along the D_3 structures, tapping into deep crustal fluid sources (Putnis et al., 2007). The integrated use of both field work (deterministic observations) and the DFN modelling approach demonstrates how it is possible to infer that the D_3 fractures on Smøla may represent a considerable 'fossil' geofluid plumbing system, potentially the largest and most connected permeable structures within the nascently forming passive margin. The D_3 fractures combined with reactivated D_2 and D_1 fractures, being favourably oriented to the prevailing Cretaceous SH_{min} NW-SE to WNW-ESE orientations (Tartaglia et al., 2023), could have enhanced fracture connectivity all the way to the percolation threshold necessary for major crustal fluid circulation from the basins into the basement highs (Cox, 2005; Manzocchi, 2002).

Also, during D_3, the MTFC dip-slip faulting, half-graben development, and deepening of the Edøyfjorden basin (Figure 5.12) is a good example proximal to Smøla of similar coeval fault-related basin formation processes occurring offshore, with extension along the ~N-S striking Klakk Fault Complex (KFC on Figure 3.4) and the deepening of the

Rås Basin (Møre basin), and the formation of potential fluid pathways related to the KFC within and along the Frøya High (Bøe and Bjerkli, 1989; Faleide et al., 2015; Muñoz-Barrera et al., 2020). The D_3 fractures may well be associated with this activity. As discussed earlier in this thesis (and illustrated in Figure 7.8), the formation of the D_3 features also corresponds to the initiation of major generation and secondary migration of hydrocarbon offshore Norway (Ali, 2012; Georgiev et al., 2019; Goff, 1983; Khorasani, 1989; Ohm et al., 2012), although this timing may be more related to the burial and maturation history of the hydrocarbon-bearing units (Palumbo et al., 1999). The regional SH_{max} orientations (~NNE-SSW to NE-SW) would have further driven fluids along the most permeable N-S oriented (horizontal D_3 permeability anisotropy orientation or K_{Hmax}) fractures, implying that lateral geofluid (including petroleum) migration and percolation may have utilised basement high bounding structures (such as the KFC) and fracture networks which are equivalent to the D_3 fracture configuration and sub-parallel to the D_3 permeability anisotropy as is observed on Smøla.

The D_4 hematite-zeolite-calcite veins and the D_5 quartz-calcite veins, unlike the D_2 and D_3 deformation features, do not have direct absolute ages attributed to them. The D_4 veins have an ascribed age from cross-cutting relationships (suggesting a <75 Ma age), and the D_5 veins are assumed to have formed after ~70 to 60 Ma from direct dating by Hestnes et al. (2023) on calcite veins further south along the passive margin (Western Gneiss Region (WGR) and the Nordfjord-Sogn Detachment). From these ages (and geometric and kinematic characteristics) they have been interpreted to have both formed because of regional crustal extension and dip-slip (and possible strike-slip) faulting on the MTFC and other pervasive faults just prior to the opening of the North Atlantic (Figure 5.12). However, further U-Pb dating work on the calcite-bearing D_4 and D_5 veins on Smøla, like previously suggested for the D_1 epidote-bearing veins, represents an obvious next step to confirm and refine the absolute time sequence of the Smøla deformation features up to the final most recent episode.

However, the D_4 and D_5 veins combined with selectively reactivated D_1, D_2, and D_3 fractures in the D_{4+5} network (all recreated together in the D_{4+5} DFN model), represent the final fracture saturated rock volume on Smøla from the Late Cretaceous to Paleogene onwards. The corresponding DFN output permeability tensor, has the highest K values of all the DFN models (Figure 7.5 & Figure 7.6), and exhibits a K_{Hmax} anisotropy oriented ~NW-SE (Figure 7.8), which is subparallel to the bounding faults of the late Jurassic-Cretaceous rifting basins in North Atlantic (associated with rifting and crustal extension prior to the break-up of Greenland and Norway). The DFN also provided a connectivity value (C_B) of 1.79, which is only slightly lower than D_3 (1.82). The permeability anisotropy K_{Hmax} orientation and the high connectivity measure suggest that the D_{4+5} is like D_3, with the D_{4+5} fracture network also forming of a major geofluid circulation system, assuming Smøla is representative of offshore fracture networks.

However, at least on the onshore portion of the passive margin, $\delta^{18}O$ and $\delta^{13}C$ stable isotope analyses by Hestnes et al. (2023) on calcite veins in western Norway relatively proximal to Smøla, indicate that calcite precipitated from percolating ground water. Additionally, found with the calcite in the D_4 veins, is zeolite, a relatively low temperature mineral forming at shallow crustal depths of 3-5 km depths (Frey, 1987; Watts et al., 2023). The presence of zeolite and the stable isotope evidence implies that the D_4 and D_5 fracture network configuration may have very effectively (owing to high fracture connectivity) facilitated geofluid circulation at relatively shallow crustal levels rather than basin wide or deep fluid circulation systems, such as possibly the case of D_3. Whether the D_{4+5} fracture network exists in crystalline basement units offshore and facilitated hydrocarbon or other geofluids offshore remains an open question at this stage, although the D_{4+5} timing does correspond to the majority of hydrocarbon activity offshore Norway (Ali, 2012; Georgiev et al., 2019; Goff, 1983; Khorasani, 1989; Ohm et al., 2012; Figure 7.8).

9.2.2 Connectivity comparison with other measures

As previously outlined in Chapter 2, the C_B value is related to the abundance of connected nodes (Y and X nodes) relative to all present fractures (or network branches), even those unrelated to fluid flow (essentially the isolated fractures or I-I branches). The back-stripping out of predominantly more connected branches (C-I and C-C types) with each DFN led to an increasing proportion of more isolated branches dominating the network. This resulted in the C_B value progressively decreasing through the deformation episodes back through time. Even so, a fluid-flow ‘backbone’ pathway (Cox, 2005) of connected branches may be present through multiple iterations of the DFNs and would be unaffected by the relative change in proportion of isolated fractures. The enduring presence of these flow ‘backbone’ fractures (which essentially would facilitate fluid flow), implies that the actual connectivity of the network remains constant or increases as time progresses. To illustrate this, the C_B value for D_{4+5} is lower than D_3, with C_B only reflecting the additional I-nodes in D_{4+5} relative to D_3, rather than a real increase in the actual connectivity related to the flow-facilitating fractures (only involving the C-C or perhaps C-I-type branches), which should remain constant or increase (assuming no active fracture sealing). I will therefore briefly compare the C_B results against two other network topology-related measurements (branch clusters and enclosed regions) to assess the reliability of the C_B measure for tracking connectivity:

As demonstrated in Chapter 7, the C_B values change through time from 1.01 for D_1, 1.74 for D_2, 1.82 for D_3, and 1.79 for D_{4+5}. These values largely reflect the proportion of connected nodes (Y and X nodes) with a proportion of 24 %, 65 %, 74 %, and 68 % respectively from D_1 to D_{4+5}. Comparing these values against the number of branch clusters (Table B6, Appendix B) averaged over the scan areas for each deformation episode, there are ~54 clusters for D_1 with a largest cluster possessing combined branch trace lengths of ~50 m, ~16 clusters for D_2 with the largest cluster involving ~331 m of combined branch trace length, ~7 clusters for D_3 with a largest cluster branch trace length of ~424 m, and ~14 clusters for D_{4+5} with a largest cluster trace length of ~370 m. Overall, the trend in cluster count and combined trace length amount for the largest cluster indicates that the number of clusters decreases and the combined trace lengths increase (the networks become more connected on average) (Figure B4a, Appendix B). Although the D_{4+5} largest cluster does have ~13 % less average combined trace length compared to the average values for the largest cluster for D_3, overall, the D_3 and D_{4+5} modelled trace maps have almost all trace lines incorporated in either the largest or the second-largest branch cluster (Figure B3, Appendix B). The progressive amalgamation of the traces into extensive clusters highlights how these trace maps become more connected through time in an absolute sense (not considering the smaller isolated branch clusters or single branches).

Furthermore, for each of the deformation episodes the enclosed regions (Figure B3, Appendix B) vary in a similar manner as the C_B values. The count of enclosed regions changes from D_1 with very few blocks, with an average count of 3 (averaged over all the scan areas), to an average number of ~48 for D_2, an average number of ~85 for D_3 (maximum count), and a slightly lower average count of ~69 for D_{4+5} (Table B6, Appendix B). For the same deformation episodes, the average size in m^2 (averaged over the scan areas) shows a progressively increasing size in enclosed regions through time (from D_1 with 0.14 m^2, to 1.84 m^2, to 2.05 m^2, and finally to 2.09 m^2 for D_{4+5}). The block intensity (R_{22}) values for the deformation episode show a moderately intact rock volume for D_1 (R_{22}= 0.46 averaged for the scan areas), with a significant shift in value to D_2 (R_{22}=0.02), with both the R_{22} values for D_3 and D_{4+5} indicating strongly disaggregated rock masses (0.01 on average for the scan areas) (Appendix B, Figure B4b). Overall, D_3 has the lowest R_{22} average value (0.012) compared to the other deformation episodes (Table B6, Appendix B), which also coincides with the highest spatial coverage of the scan areas by enclosed regions (Figure B4c, Appendix B). Generally, as seen in the C_B values from D_2 onwards, block analysis (enclosed region count, size, and block intensity values) shows that the modelling simulated highly disintegrated Smøla rock volumes, with a peak in D3.

Generally, as demonstrated here, the C_B values does provide a relatively acceptable estimate for connectivity based on topology components when fracture networks are represented by 2D trace maps. The cluster analysis (particularly the combined total trace length measure of the largest branch cluster), enclosed region counts and size, and the R_{22} measures do not consider all branch-types present (effectively these measures ignore the isolated I-I branches). Even so, the C_B metric by deformation episode approximately mirrors the other two connectivity proxies, with all three connectivity proxies indicating D_3 fracture network was the most connected, and that there is a general increase in connectivity through time from D_1.

Importantly, every analysed trace map was extracted from different stochastic (single realisation) output for each deformation episode. The branches (either isolated or connected) are thus not identical for more than one trace map, which consequently implies for my modelling, that the actual connectivity (or flow backbone pathways) cannot be the same between different model iterations. Ultimately, the C_B values (and other connectivity proxy values) can only be associated with a specific DFN, and as is the case for D_{4+5}, do not therefore represent the sum of all the geologically ‘older’ trace maps (the connectivity measure for $D_{4+5} \neq D_3 + D_2 + D_1$).

9.2.3 The time dimension in recreating fracture and fault networks

A significant aspect of this study, making it both unique and novel, is the use of both direct absolute dating of the fractures and faults, and indirect relative age associations, to reconstruct configurations of fracture sets back through time. Relative genetic relationships between fractures (such as cross-cutting or termination relationships) generally cannot reveal absolute timing, and, as such, specific fracture sets cannot be exactly attributed to any specific deformation episode in a region, particularly if a given region possesses a complex polyphase deformation history (Lacombe et al., 2022).

Typically, previous studies that have attributed fracture sets to absolute ages or placed their formation within an absolute time frame, have used indirect methods (e.g. Engelder and Geiser, 1980; Laubach and Kira, 2009). These indirect methods may include using known thermal and burial histories of a region or dated paleostress-field trajectories, as well as cross-cutting relationships, to place fracture sets within a chronology of formation (Laubach and Kira, 2009). More recently, direct methods have been also used such as U-Pb dating of calcite (e.g. Hestnes et al., 2023; Roberts et al., 2020), K-Ar geochronology of illite clays in fault gouges (such as this study), or Argon-Argon ($^{40}Ar/^{39}Ar$) dating of micas and potassium-feldspar (e.g. Drake et al., 2009).

Neither the directly nor indirectly dated studies, however, have used the age attributes to progressively deconvolute and stochastically recreate fracture networks at scales representative of basement rock volumes. They have also not used any form of back-stripped (time-specific) fracture network configurations to estimate fracture-related petrophysical properties. The absolute ages for this study's fracture sets, enable the individual facture sets to be directly 'placed' into the tectonic history of the region (mid-Norwegian passive margin in this case), and using the stochastic toolset, quantify the petrophysical properties and image the fracture networks connectivity for each deformation episode in time.

9.3 Insights gained from the structural characterisation of Smøla

Challenges encountered in the first part of the study are worth briefly discussing here as they offer important insights for future work. Many of the issues faced here are not unique to a study such as this one, but may nonetheless have influenced the results and, consequently, the interpretations applied in the later stages of the study.

The remote sensing and geophysical survey-based lineament analysis undertaken in the first part of this study (Chapter 5; Figure 5.2) used airborne magnetic data (250-1000 m line spacings), high-altitude orthophoto imagery, and sun-shaded DTMs from LiDAR surveys (1 m/pixel resolution). The lineament trace picking was, at times, affected by resolution limitations of certain imagery types (particularly relevant to the geophysical data). As already highlighted by Peacock et al. (2019), trace mapping with lower-resolution imagery often resulted in lineament traces appearing to abut or intersect other lineaments more frequently than reality (commonly with > four intersections at a single point). This may have influenced the network topology analyses, affecting the assignment of node and branch types to the lineament traces. However, in this study, care was taken to avoid mapping ambiguous or low confidence lineament intersections. Therefore, the lineament trace mapping approach should be integrated, using more than one imagery type (for example, DTM data overlain by geophysical survey imagery), sun-shaded in a variety of orientations, for mapping at a selected scale.

Characterising and sorting the various fractures and faults by geometric, kinematic, and mineral infill types during the field mapping component of the study was at times difficult. It is clear from field evidence that many fractures exposed in outcrop had experienced multiple reactivations (mineral infill overprinting relationships). This complex mineral infill (composite veins) also obscured slickenside surfaces required for measuring kinematic information from the fractures. In many examples, kinematic information from earlier deformation episodes had been covered by a later mineralisation type. Additionally, many outcrops studied were weathered with exposed fractures having lost their infill mineralisation, reducing the usefulness of these the fractures (these fractures could not be assigned to any specific deformation episode and were later discarded from the study fracture database). Consequently, the subsequent tectonic reconstructions in the first part of this study (Figure 5.12), were therefore interpretations based on as many different geological field data types and individual observations. To develop a statistically robust structural characterisation, this study therefore recommends mapping as many different outcrops as possible within a basement exposure, such as on Smøla.

The four diamond drill cores utilised in this study, in contrast, provided relatively pristine exposures of the geology. The drill cores were essential in resolving the cross-cutting relations between the different mineral-assemblages (Figure 5.7) and the fracture and fault types, which could then be assigned to deformation episodes. However, the downhole core exposures of the deformation features (for example, an intersected 10 cm quartz-calcite vein in the drill core) possess relatively small area extents (typically on the centimetre- to metre-scale). These limited drill core exposures are not always representative and often lack kinematic indicators, such as slickenside surfaces, requiring many drill hole measurements and descriptions to constrain the overall geological ‘picture’. This study overcame this challenge, this study compiled a standardised drill hole facture database (~550 fractures) of fracture measurements and descriptions from all four drill holes, enabling the identification of overall trends in mineralisation, geometry, and kinematics.

Owing to both the poor preservation of slickensides on outcrop fault or fracture surfaces and the limited core exposure area of intersected structures, none of the K-Ar samples (Figure 5.9) could be assigned a high confidence kinematic property (fault slip orientation). However, structural planar orientations were determined from bounding fault surfaces (Figure 5.11b). Overcoming this challenge is indeed problematic, and aside from recommending more field work, with additional sampling at different fault exposures that may preserve slickenside features, this problem may be inherent to the field area (owing to weathering and glacially impacted landscapes).

9.4 Insights gained through the stochastic modelling approach

9.4.1 Temporal validity of DFN models

A key concern for the stochastic models is that, conceptually, they represent a transient geological moment immediately following fracture formation or reactivation of pre-existing fractures and faults (if well-oriented to a prevailing stress field). The fracture and fault formation or reactivation process may stem from a ‘fault-valve behaviour’ (Figure 2.2), with cyclic transient creation and destruction of permeability (Sibson, 1992a). As transient fracture permeability is destroyed, with fractures changing from open features to sealed (Figure 2.9) through crack-healing and sealing (Cox, 2005), network branches within a fracture network fracture may progressively be eliminated, thus decreasing connectivity over time. Consequently, the duration for which temporally constrained DFNs remain applicable in geological terms is a critical question.

Once a fracture forms and a geofluid flows through it (Figure 2.2b), various minerals may begin to precipitate based on, among other factors, fluid composition, mineral saturation state, flow rate, temperature, dissolution rate, and fracture dimensions (Cox, 2005; Fisher and Brantley, 1992; Lee and Morse, 1999). To estimate this process's timeframe, the D_4 and D_5 veins are considered here first, where calcite and quartz infill (ignoring the zeolite content in this example) constitute the sealing minerals. Precipitation of calcite in thin short veins (set in Iceland spar calcite host substrate) has been estimated by Lee and Morse (1999) to occur in a 10^3 to 10^6 year timescale, while estimates by Fisher and Brantley (1992) indicate euhedral quartz precipitation may take between 10^5 and 10^6 years to infill a 1 cm wide fracture (at 250 °C and 280 MPa or ~10 km depth in the crust assuming a 25 °C/km geothermal gradient). Moreover, 8 μm increments of quartz infill in crack-seal veins may take from 10^3 to 10^6 years with crack-seal episodes recurring approximately every 10^2 to 10^4 years (Fisher and Brantley, 1992). As a comparison, quartz cementation along nm to μm wide fractures within low permeability material (such as cataclasite) has been proposed to potentially occur within days to years given the right precipitation conditions (Williams and Fagereng, 2022). On the other hand, illite growth within the D_2 and D_3 fractures can be inferred from illite growth within reservoir sandstones and is estimated to occur on the 10^6 year timescale (Small, 1993). If this growth estimate applies to clay infill in some Smøla fractures, it does provide an approximate timeframe for clay growth.

From the above mineral precipitation rates, I can deduce an estimated timeframe for how long the DFN models generated in this study would represent open fracture networks, with ideal permeability characteristics before crack-sealing would have occurred. The DFN models in this study used aperture values ranging from 0.03 to 0.1 mm (based on paleo-aperture, see Figure B1, Appendix B). Taking these modelled fracture widths into consideration, and assuming favourable precipitation conditions, it can be suggested that the DFN models would represent permeable fractures for at least 10^3 years after the initial formation or reactivation of the fractures. Consequently, estimated petrophysical properties for these stochastic fracture networks would only relate to a time period within this 10^3 year time span, and most reasonably immediately after the fracture formation or reactivation.

9.4.2 Modelling spatial resolution and fracture intensity

As highlighted in Chapter 8, the 500 m³ DFN models did not properly replicate drill core-scale fracture patterns and intensity, indicating they are best suited for coarser-resolution modelling. This resolution limitation is a key insight from the modelling part of this study, and it suggests that more fine-resolution trace mapping (for example drone-base photogrammetry) is required to refine the scaling and termination relationships inputs when aiming at outcrop-scale fracture simulations are required within similarly sized modelling volumes. More generally, however, this resolution limitation suggests that DFN models must be calibrated for a specific spatial resolution and conceptualised for a set purpose. Despite assuming self-similarity across all orders of magnitude for the input parameters (if the fracture sizes follow a power law distribution), the DFN modelling remains constrained within a limited range of fracture size dimensions and scaling (for example, from the 10 m to 100 m scale).

Furthermore, the challenge in proper replication of observed fractures may derive from the use of a Poisson point process for random 'seeding' fractures in a modelling volume (Libby et al., 2024), as natural fractures do not generally initiate and propagate randomly within rock volumes (Davy et al., 2018). This results in less fracture localisation and clustering of fractures, as commonly seen at the outcrops (associated with fault damage zones, for example). Also, the use of a 'grown' DFN approach, where termination relationships and fracture intersections control fracture set interactions, may also limit fracture growth. The probabilities of termination given to each fracture set may prevent the model from reaching the target P_{32} value due to fracture sizes being limited by fracture intersections and terminations (Libby et al., 2019), representing a limitation to the approach. This is a crucial theme, as alternatively, fracture intensity also controls the amount of fracture intersection, which in turn determines fracture connectivity (Libby et al., 2024).

In contrast, the validation and conditioning exercise using the 50 m³ DFN models did succeed in accurately replicating the observed drill core-scale fracture patterns, intensities (P_{10} and P_{32}), and the orientations of the fractures in most situations. This validation process did however use metrics that were not independent from the generation and calibration of the 50 m³ DFNs. These refined models conditioned to observed data, therefore remain only applicable to replicating past 'fossil' fracture networks within the Smøla rock volume. Nevertheless, where mismatches arose between the modelled and observed fractures, they could be attributed to local variations in fracture intensity and orientations between drill holes, deviating from the global input parameters initially used for the modelling. The previous suggestion of domaining Smøla into smaller regions of similar fracture intensity, spacing, and orientations, does conform well with how actual reservoir volumes are typically compartmentalised and domained as ‘reservoir facies’, based typically on fracture intensity or another mechanical property (Belaidi et al., 2018). Different lithologies also possess different characteristics and fracture intensities (Peacock et al., 2019), which given that Smøla is lithologically heterogeneous (Figure 3.5) should also be included in the domaining strategy. It is therefore suggested that future research using DFNs on Smøla should adopt a domaining approach, with relevant DFNs to each domain, to fully capture the local variation and to comprehensively characterise the island. Needless to say, a similar approach is also recommended for the DFN modelling of any heterogeneous fractured basement block.

9.5 Basement analogues and wider applicability

A key outcome of this study is the benefit of using a well-exposed onshore analogue, such as Smøla island, to infer structural characteristics and temporal evolution of petrophysical properties to other crystalline basement volumes. The utility of fractured reservoir analogues has already been shown and stressed by other studies (e.g. Ceccato et al., 2021b; Dichiarante et al., 2020; McCaffrey et al., 2020; Peacock et al., 2022). Specifically in an onshore-offshore fractured reservoir context, onshore analogues may be the only accessible source of rock fracture data. Offshore basement structural highs, such as the Frøya or Utsira highs (Figure 3.4), are generally inaccessible below younger sedimentary covers, such as successions of Mesozoic sandstone, shale, and chalk in the case of the Utsira High (Riber et al., 2016; Trice et al., 2022). Onshore highs, on the other hand, have greater site access and outcrop exposure, and, as in the example of Smøla, extensive coverage by datasets at regional to micro-scale resolutions, including, at times, the availability of oriented diamond drill cores.

By utilising an onshore analogue of crystalline basement fractured reservoirs, this study has been able to unravel over 300 Ma of polyphase deformation within both relative and absolute timeframes. Detailed geological analysis on Smøla provided deterministic inputs that enabled the reconstruction and simulation of complex fault and fracture networks over time. These reconstructions gave the framework to derive evolutionary descriptions of both secondary permeability and fracture connectivity which could then be applied offshore. The integrated deterministic and stochastic approach adopted here is only possible due to the availability of observable representative geology in an analogue rock volume. This study therefore emphasises the importance of analogue volumes in fractured reservoir studies, including those offshore Norway.

The novel approach conceptualised, developed, and demonstrated in this thesis has significant implications for characterising various types of reservoirs, including groundwater and petroleum systems. For example, it is now possible to, for the first time, estimate the permeability in absolute time, during known reservoir charging events, and it is possible to understand which fracture or structures may have played a role in past (and absolute dated) geofluid migration events. This conceptual approach and outcomes can therefore be potentially adapted and applied to predictive exploration strategies, whereby fluid pathways relevant to either reservoir charging, or mineral deposits emplacement can now be identified both spatially and temporally. Additionally, this method is relevant for injection reservoirs, including those used for greenhouse gas storage, where reservoir characterisation is essential for understanding petrophysical properties of the target reservoir. Finally, this study's approach is also applicable to nuclear storage projects, whereby any nuclear waste (radionuclides) needs to be isolated from fluid flow along fractures and/or faults (Drake et al., 2009; Mattila and Viola, 2014), requiring a full control on what or how petrophysical properties for any fractures within the rock volume may have varied through time, as well as forecasting into the future.

Chapter 10: Conclusion

10.1 Impact and conclusions

The novelty of this study is its multidisciplinary and multiscalar scientific and methodological approach, in which a complex fault and fracture network formed through a prolonged and polyphase deformation history, can be effectively resolved into distinct fracture formation events over geological time. This process is the only possible to provide the essential inputs required to stochastically recreate these events, permitting the estimation of fracture-related petrophysical characteristics back through geological time. The inclusion of multiscalar geological observations as deterministic inputs along with absolute time constraints addresses the inherent challenges that arise when unravelling the progressive development of any intricate fracture network and replicating them stochastically in the framework of a modelling scheme that is firmly attached to a temporal dimension. Such time-constraints also allow, for example, the identification of which fault or fracture set (or combination of sets) may have represented the most permeable structural trend through geological time or acted as a transient ‘fossil’ fluid pathway at specific times during past geofluid migration events. The evolution of other fracture-related characteristics, such as connectivity, can also be traced through the geological time span of interest.

With fracture arrays characteristic of fracture- and fault-saturated basement rock volumes, it is especially difficult to sort the various fractures into sequential fracture sets through relative cross-cutting relationships alone. The lack of absolute time constraints in this situation makes reconstructing an absolute time-based polyphase deformation history extremely challenging. Without time constraints, it is, in fact, impossible to establish when a specific deformation feature formed in a rock volume's deformation history. To address these challenges, this study has, therefore, utilised a two-pronged methodological and conceptual framework, with each stage incorporating a temporal component: 1) a deterministic approach, involving multiscalar geological observations, 3D structural characterisation of deformation features, and fault-related K-Ar geochronology on Smøla island within the mid-Norwegian passive margin and 2) a stochastic approach, using the results of the first approach to replicate and simulate the observed deformation features on Smøla through geological time.

Briefly, this approach involved the following: Using synkinetic mineral assemblages, geometry and kinematic trends, and K-Ar dating, at least five deformation episodes (D_1 to D_5) affecting Smøla island were established, spanning from the Devonian (after 390 Ma) through to the Cretaceous-Paleogene (~70-60 Ma). Time-integrated DFN modelling then demonstrated how the fracture networks progressively developed along with increasing connectivity (based on transient hydraulically-conductive fracture formation) and variations in the orientation of the associated 3D permeability anisotropy (simplified to the horizontal components K_{Hmax}-K_{Hmin}) over the same geological timeframe. The DFN modelling results of this study were only possible because of the robust foundation offered by the well-resolved deterministic inputs. Selected as the ideal 'tool' for recreating complex multiscalar fracture networks that have statistical variability, the stochastic modelling approach has proven to be well-suited for this type of research. Additionally, the flexibility and reliability of the DFN modelling method was refined through validation, to accurately replicate observed fractures on Smøla at the at the sub-seismic (drill core)-resolution.

The key implication of this study is, therefore, how other fracture network-related studies (including fluid flow 'dynamic' studies) can integrate this new methodology using well-resolved temporally-constrained deterministic inputs to model and understand fracture and fault network evolution in absolute time. On the other hand, this has major implications also on identifying ancient plumbing systems or 'fossil' fluid flow pathways back in absolute time. The concept of fracture 'back-stripping' in stochastic modelling is especially powerful: by sequentially removing the youngest defined fracture set when moving backwards in geological time, the progressively older fracture sets configuration for each deformation episode remains intact and is unveiled. These back-stripped fracture networks can subsequently be used for estimating petrophysical properties for each deformation episode. Importantly, as these stochastic fracture networks are also associated with absolute age constraints, for the first time it has been possible to recreate transient fault and fracture-related permeability conditions during known and dated reservoir charging events.

The other major impact of this study is the confirmation of the conceptual and practical value of onshore analogues of inaccessible offshore basement structural highs. Smøla island, well constrained by numerous multiscalar datasets including newly available oriented diamond drill core, is indeed an ideal analogous crystalline basement rock volume for this type of study. The island can therefore be considered a natural 'open air laboratory', which is easily accessible for future research activities. Owing to the similarity of Smøla to many offshore crystalline basement highs, this study's findings can be directly applied to characterising and modelling the progressive development of fractured basement reservoirs offshore. And because fracture-related petrophysical properties and tectonic history affect fluid flow and reservoir characteristics, past basement high-related hydrocarbon secondary migration and reservoir charging events can potentially be reconstructed. Additionally, due to the low matrix permeability of Smøla's host rocks, these findings are relevant to other studies involving secondary permeability associated fluid flow, including those focused on basement hosted groundwater, greenhouse gas storage, and nuclear waste repositories.

10.2 Critical review and recommendations

Overall, this study has achieved most of its original research aims. However, the following assessment and review of the study highlights areas of the workflow worth critically examining. And to conclude the thesis, I have also included recommendations for future research relevant to the work done.

The first research aim I composed, involving the characterisation of Smøla's deformation features within an absolute timeframe and inferred tectonic framework, was indeed successful. Furthermore, this work generated an extensive fracture database (including information on ~1000 fractures documented from both outcrop exposures and drill core), which includes quantitative and qualitative data that remain relatively unused in this study. These data include fracture morphology descriptions, and fracture mineralisation sealing assessments (including void width measurements), and much of the kinematic fault slip data (from both the drill core and field outcrops). The fault slip data, specifically, was intended for use in reconstructing paleostress conditions for Smøla. As these reconstructions remains never fully realised in this study, these data still represent a future research opportunity, particularly if any slip- or dilatant-tendency studies were applied to the DFNs to simulate possible reactivations of specific fracture orientations in later deformation episodes. Other drill hole logging data, including rock alteration and hydrological data have also not been incorporated into the structural characterisation. 3D modelling of mineralised alteration halos around drill hole intersected structures would represent an interesting comparison to the 3D permeability tensor outputs from the stochastic models, in terms of validating the modelling against actual fluid migration trajectories. Additionally, hydrological datasets (packer testing done previously on the Smøla drill holes) also represent a further research avenue to explore possible communicative structures between drill holes (most relevant to drill hole BH1 and BH2).

The second aim that I set out to accomplish, regarding the temporally-constrained DFN modelling and fracture network reconstructions, was both theoretically and practically achieved. 'Grown' DFN modelling with modelling volumes on the hundreds of metre-scale with individual fractures down to the metre-scale (1-10 m on average) as used in the 500 m^3 DFNs proved to be computationally heavy. The extensive time of model processing reduced fracture intensity inputs and simplified fracture interactions (termination relationships) in places. However, the 'grown' DFN approach was able to effectively integrate a time component into the modelling, in both the growth and interaction of new or later fractures against older pre-existing stochastic fractures, and in the later models (the D_3 and D_{4+5} DFNs) including up to five fracture sets of different timing with complex termination relationships. Even considering the decreased fracture intensities, at modelling scales relative to the overall crustal volume of Smøla, the models were indeed able to produce representative fracture networks for each of the deformation episodes (including the combined D_{4+5} episode). The 3D permeability tensors and the fracture connectivity estimates (from network topology analyses on the stochastic fractures) both showed how the petrophysical properties evolved with fracture saturation through geological time. However, the reduced fracture intensities and fracture interaction probabilities (for certain fracture sets) resulted in less fracture terminations and fewer Y-nodes from forming, decreasing the realism of the stochastic fracture networks. Nevertheless, for conceptual purposes, the 500 m^3 DFNs are deemed to be reliable and sound.

The final aim of the study was to validate the stochastic modelling, and to assess how well the stochastic networks could replicate the observed fracture and fault intersections in drill core (specifically in downhole televiewer data). Even though mis-matches between the modelled and observed fractures were detected (particularly for the 500 m^3 DFNs), after fracture conditioning, the 50 m^3 DFN modelling nevertheless did demonstrate that 'grown' DFN models at this scale better replicated observed fractures compared to the 500 m^3 models, providing a more accurate representation of deterministic fracture datasets from drill core. Local variations in fracture intensity and orientation trends, which led to some replication issues with the modelling, should be addressed by using a geocellular DFN modelling approach in future research efforts. This approach should incorporate structural and lithological domaining of the Smøla rock volume to enhance the DFNs local replication of local fracture intensity and structural orientation trends. A final potential improvement on this aim could incorporate Monte Carlo simulations in the DFN validation process, which during the current study was not undertaken owing to computational efficiency issues. Further simplified ‘grown’ DFNs (potentially customised to specific lithology domains for example) could be generated hundreds of times to produce enough model realisations to define statistical distributions of the validation parameters. A clear idea on the variation of the models would allow for a better evaluation of the performance of the models in replicating the Smøla natural fracture networks back through time and allow for predictive use in ‘unknown’ rock volumes potentially offshore.

References

Adler, P. M. and Thovert, J.-F.: Fractures and Fracture Networks, 1st ed., Springer Dordrecht, XII–431 pp., https://doi.org/10.1007/978-94-017-1599-7, 1999.

Ali, A.: Basin Modelling: HC Generation Modelling of the Åre, Melke and Spekk Formations, Haltenbanken Area, Master Thesis, University of Oslo, 2012.

Anderson, E. M.: The dynamics of faulting, Transactions of the Edinburgh Geological Society, 8, 387–402, https://doi.org/10.1144/transed.8.3.387, 1905.

Anderson, E. M.: The Dynamics of Faulting and Dyke Formation with Application to Britain, Second Edition., Oliver & Boyd, Edinburgh, 1951.

Barton, C. C.: Fractal Analysis of Scaling and Spatial Clustering of Fractures, in: Fractals in the Earth Sciences, edited by: Barton, C. C. and La Pointe, P. R., Springer US, Boston, MA, 141–178, https://doi.org/10.1007/978-1-4899-1397-5_8, 1995.

Beacom, L. E., Holdsworth, R. E., McCaffrey, K. J. W., and Anderson, T. B.: A quantitative study of the influence of pre-existing compositional and fabric heterogeneities upon fracture-zone development during basement reactivation, Geological Society, London, Special Publications, 186, 195–211, https://doi.org/10.1144/GSL.SP.2001.186.01.12, 2001.

Becker, S. P., Eichhubl, P., Laubach, S. E., Reed, R. M., Lander, R. H., and Bodnar, R. J.: A 48 m.y. history of fracture opening, temperature, and fluid pressure: Cretaceous Travis Peak Formation, East Texas basin, GSA Bulletin, 122, 1081–1093, https://doi.org/10.1130/B30067.1, 2010.

Belaidi, A., Bonter, D. A., Slightam, C., and Trice, R. C.: The Lancaster Field: Progress in opening the UK's fractured basement play, Petroleum Geology Conference Proceedings, 8, 385–398, https://doi.org/10.1144/PGC8.20, 2018.

Berkowitz, B., Bour, O., Davy, P., and Odling, N.: Scaling of fracture connectivity in geological formations, Geophys Res Lett, 27, 2061–2064, https://doi.org/10.1029/1999GL011241, 2000.

Bhullar, A. G., Karlsen, D. A., Backer-Owe, K., Seland, R. T., and Le Tran, K.: Dating reservoir filling — a case history from the North Sea, Mar Pet Geol, 16, 581–603, https://doi.org/10.1016/S0264-8172(99)00028-8, 1999.

Biddle, K. T. and Wielchowsky, C. C.: Hydrocarbon Traps: Chapter 13: Part III. Processes, in: The Petroleum System-From Source to Trap, AAPG Special Volumes, 219–235, https://doi.org/10.1306/M60585, 1994.

Bird, D. K. and Spieler, A. R.: Epidote in Geothermal Systems, Rev Mineral Geochem, 56, 235–300, https://doi.org/10.2138/gsrmg.56.1.235, 2004.

Blenkinsop, T., Doyle, M., and Nugus, M.: A unified approach to measuring structures in orientated drill core, in: Geological Society Special Publication, vol. 421, Geological Society of London, 99–108, https://doi.org/10.1144/SP421.1, 2015.

Blenkinsop, T. G.: Relationships between faults, extension fractures and veins, and stress, J Struct Geol, 30, 622–632, https://doi.org/10.1016/j.jsg.2008.01.008, 2008.

Bøe, R. and Bjerkli, K.: Mesozoic sedimentary rocks in Edøyfjorden and Beitstadfjorden, Central Norway: Implications for the structural history of the Møre-Trøndelag Fault Zone, Mar Geol, 87, 287–299, https://doi.org/10.1016/0025-3227(89)90066-2, 1989.

Bøe, R., Atakan, K., and Sturt, B. A.: The style of deformation in on Hitra and Smøla. Central, Norges Geologiske Undersøkelse Bulletin, 414, 1–19, 1989.

Bonneau, F., Henrion, V., Caumon, G., Renard, P., and Sausse, J.: A methodology for pseudo-genetic stochastic modeling of discrete fracture networks, Comput Geosci, 56, 12–22, https://doi.org/10.1016/J.CAGEO.2013.02.004, 2013.

Bonnet, E., Bour, O., Odling, N. E., Davy, P., Main, I., Cowie, P., and Berkowitz, B.: Scaling of fracture systems in geological media, Reviews of Geophysics, 39, 347–383, https://doi.org/10.1029/1999RG000074, 2001.

Bons, P. D., Elburg, M. A., and Gomez-Rivas, E.: A review of the formation of tectonic veins and their microstructures, https://doi.org/10.1016/j.jsg.2012.07.005, October 2012.

Bons, P. D., Cao, D., de Riese, T., González-Esvertit, E., Koehn, D., Naaman, I., Sachau, T., Tian, H., and Gomez-Rivas, E.: A review of natural hydrofractures in rocks, Geol Mag, 159, 1952–1977, https://doi.org/DOI: 10.1017/S0016756822001042, 2022.

Bonter, D. A. and Trice, R.: An integrated approach for fractured basement characterization: The lancaster field, a case study in the UK, Petroleum Geoscience, 25, 400–414, https://doi.org/10.1144/petgeo2018-152, 2019.

Bowen, R.: Potassium-Argon and Argon-40/Argon-39 Dating, in: Isotopes in the Earth Sciences, edited by: Bowen, R., Springer Netherlands, Dordrecht, 201–246, https://doi.org/10.1007/978-94-009-2611-0_5, 1994.

Brace, W. F.: An Extension of the Griffith Theory of Fracture to Rocks, J Geophys Res, 65, 3477–3480, https://doi.org/10.1029/JZ065i010p03477, 1960.

Brace, W. F.: Permeability of crystalline and argillaceous rocks, International Journal of Rock Mechanics and Mining Sciences & Geomechanics Abstracts, 17, 241–251, https://doi.org/10.1016/0148-9062(80)90807-4, 1980.

Bruton, D. L. and Bockelie, J. F.: The Ordovician Sedimentary Sequence on Smøla, West Central Norway, Norges Geologiske Undersøkelse Bulletin, 348, 21–31, 1979.

Bunkholt, H. S. S., Oftedal, B. T., Hansen, J. A., Løseth, H., and Kløvjan, O. S.: Trøndelag Platform and Halten–Dønna Terraces Composite Tectono-Sedimentary Element, Norwegian Rifted Margin, Norwegian Sea, Geological Society, London, Memoirs, 57, https://doi.org/10.1144/m57-2017-13, 2022.

Byerlee, J.: Friction of Rocks, Birkhauser Verlag, B I, 1978.

Bym, T., Turnbull, R., and L. Hartley: Conditioning of DFN Models To Fracture Trace Maps and Borehole Intersections, in: 3rd International Discrete Fracture Network Engineering Conference, https://doi.org/10.56952/ARMA-DFNE-22-0742, 2022.

Caine, J. S., Evans, J. P., and Forster, C. B.: Fault zone architecture and permeability structure, Geology, 24, 1025–1028, https://doi.org/10.1130/0091-7613(1996)024<1025:FZAAPS>2.3.CO;2, 1996.

Ceccato, A., Viola, G., Antonellini, M., Tartaglia, G., and Ryan, E. J.: Constraints upon fault zone properties by combined structural analysis of virtual outcrop models and discrete fracture network modelling, J Struct Geol, 152, 104444, https://doi.org/10.1016/J.JSG.2021.104444, 2021a.

Ceccato, A., Viola, G., Tartaglia, G., and Antonellini, M.: In–situ quantification of mechanical and permeability properties on outcrop analogues of offshore fractured and weathered crystalline basement: Examples from the Rolvsnes granodiorite, Bømlo, Norway, Mar Pet Geol, 124, https://doi.org/10.1016/j.marpetgeo.2020.104859, 2021b.

Ceccato, A., Tartaglia, G., Antonellini, M., and Viola, G.: Multiscale lineament analysis and permeability heterogeneity of fractured crystalline basement blocks, Solid Earth, 13, 1431–1453, https://doi.org/10.5194/se-13-1431-2022, 2022.

Cladouhos, T. T. and Marrett, R.: Are fault growth and linkage models consistent with power-law distributions of fault lengths?, J Struct Geol, 18, 281–293, https://doi.org/10.1016/S0191-8141(96)80050-2, 1996.

Clauer, N.: The K-Ar and 40Ar/39Ar methods revisited for dating fine-grained K-bearing clay minerals, Chem Geol, 354, 163–185, https://doi.org/10.1016/J.CHEMGEO.2013.05.030, 2013.

Corfu, F., Andersen, T. B., and Gasser, D.: The Scandinavian Caledonides: Main features, conceptual advances and critical questions, Geol Soc Spec Publ, 390, 9–43, https://doi.org/10.1144/SP390.25, 2014.

Cox, S. F.: Coupling between Deformation, Fluid Pressures, and Fluid Flow in Ore-Producing Hydrothermal Systems at Depth in the Crust, in: One Hundredth Anniversary Volume, Society of Economic Geologists, 39, https://doi.org/10.5382/AV100.04, 2005.

Cox, S. F.: The application of failure mode diagrams for exploring the roles of fluid pressure and stress states in controlling styles of fracture-controlled permeability enhancement in faults and shear zones, Geofluids, 10, 217–233, https://doi.org/10.1111/j.1468-8123.2010.00281.x, 2010.

Crider, J. G.: The initiation of brittle faults in crystalline rock, J Struct Geol, 77, 159–174, https://doi.org/10.1016/J.JSG.2015.05.001, 2015.

Cunningham, W. D. and Mann, P.: Tectonics of strike-slip restraining and releasing bends, Geological Society, London, Special Publications, 290, 1–12, https://doi.org/10.1144/SP290.1, 2007.

Darcy, H.: Les fontaines publiques de la ville Dijon, Dalmont, Paris, 674, 1856.

Davids, C., Wemmer, K., Zwingmann, H., Kohlmann, F., Jacobs, J., and Bergh, S. G.: K-Ar illite and apatite fission track constraints on brittle faulting and the evolution of the northern Norwegian passive margin, Tectonophysics, 608, 196–211, https://doi.org/10.1016/j.tecto.2013.09.035, 2013.

Davy, P., Le Goc, R., Darcel, C., Bour, O., de Dreuzy, J. R., and Munier, R.: A likely universal model of fracture scaling and its consequence for crustal hydromechanics, J Geophys Res Solid Earth, 115, https://doi.org/10.1029/2009JB007043, 2010.

Davy, P., Le Goc, R., and Darcel, C.: A model of fracture nucleation, growth and arrest, and consequences for fracture density and scaling, J Geophys Res Solid Earth, 118, 1393–1407, https://doi.org/10.1002/jgrb.50120, 2013.

Davy, P., Darcel, C., Le Goc, R., Munier, R., Selroos, J.-O., and Mas Ivars, D.: DFN, why, how and what for, concepts, theories and issues, in: ARMA International Discrete Fracture Network Engineering Conference, D013S000R001, 2018.

Dershowitz, W., Hosseinpour, H., and Cottrell, M.: A Geomechanical Approach for Evaluating Hydraulic Stimulation in Complex Stratigraphies, in: SPE/AAPG/SEG Unconventional Resources Technology Conference, D033S071R002, 2019.

Dershowitz, W. S.: Rock joint systems , Doctoral dissertation, Massachusetts Institute of Technology, 1984.

Dershowitz, W. S. and Einstein, H. H.: Characterizing rock joint geometry with joint system models, Rock Mech Rock Eng, 21, 21–51, https://doi.org/10.1007/BF01019674, 1988.

Dershowitz, W. S. and Herda, H. H.: Interpretation of fracture spacing and intensity, in: The 33rd U.S. Symposium on Rock Mechanics (USRMS), 757–766, 1992.

Dichiarante, A. M., McCaffrey, K. J. W., Holdsworth, R. E., Bjørnarå, T. I., and Dempsey, E. D.: Fracture attribute scaling and connectivity in the Devonian Orcadian Basin with implications for geologically equivalent sub-surface fractured reservoirs, Solid Earth, 11, 2221–2244, https://doi.org/10.5194/se-11-2221-2020, 2020.

Dorn, C., Linde, N., Borgne, T. Le, Bour, O., and de Dreuzy, J. R.: Conditioning of stochastic 3-D fracture networks to hydrological and geophysical data, Adv Water Resour, 62, 79–89, https://doi.org/10.1016/J.ADVWATRES.2013.10.005, 2013.

Drake, H., Tullborg, E. L., and Page, L.: Distinguished multiple events of fracture mineralisation related to far-field orogenic effects in Paleoproterozoic crystalline rocks, Simpevarp area, SE Sweden, Lithos, 110, 37–49, https://doi.org/10.1016/J.LITHOS.2008.12.003, 2009.

Engelder, T.: Joints and shear fractures in rock, Fracture mechanics of rock, 2, 27–69, 1987.

Engelder, T.: Transitional–tensile fracture propagation: a status report, J Struct Geol, 21, 1049–1055, https://doi.org/10.1016/S0191-8141(99)00023-1, 1999.

Engelder, T. and Geiser, P.: On the use of regional joint sets as trajectories of paleostress fields during the development of the Appalachian Plateau, New York, J Geophys Res Solid Earth, 85, 6319–6341, https://doi.org/10.1029/JB085iB11p06319, 1980.

Etheridge, M. A.: On the reactivation of extensional fault systems., Philosophical Transactions - Royal Society of London, Series A, 317, 179–194, https://doi.org/10.1098/rsta.1986.0031, 1986.

Faleide, J. I., Tsikalas, F., Breivik, A. J., Mjelde, R., Ritzmann, O., Engen, Ø., Wilson, J., and Eldholm, O.: Structure and evolution of the continental margin off Norway and the Barents Sea, International Union of Geological Sciences, 31, 82–91, https://doi.org/10.18814/epiiugs/2008/v31i1/012, 2008.

Faleide, J. I., Bjørlykke, K., and Gabrielsen, R. H.: Geology of the Norwegian Continental Shelf, in: Petroleum Geoscience: From Sedimentary Environments to Rock Physics, edited by: Bjørlykke, K., Springer Berlin Heidelberg, Berlin, Heidelberg, 603–637, https://doi.org/10.1007/978-3-642-34132-8_25, 2015.

Faulkner, D. R., Jackson, C. A. L., Lunn, R. J., Schlische, R. W., Shipton, Z. K., Wibberley, C. A. J., and Withjack, M. O.: A review of recent developments concerning the structure, mechanics and fluid flow properties of fault zones, J Struct Geol, 32, 1557–1575, https://doi.org/10.1016/j.jsg.2010.06.009, 2010.

Fediuk, F. and Siedlecki, S.: Smøla. Description of the geological map (AMS-M 711) 1321 I - 1:50 000, Universitetsforlaget, 1–26 pp., 1977.

Ferrill, D. A., Smart, K. J., and Morris, A. P.: Fault failure modes, deformation mechanisms, dilation tendency, slip tendency, and conduits v. seals, Geological Society, London, Special Publications, 496, 75–98, https://doi.org/10.1144/SP496-2019-7, 2020.

Filomena, C. M., Hornung, J., and Stollhofen, H.: Assessing accuracy of gas-driven permeability measurements: a comparative study of diverse Hassler-cell and probe permeameter devices, Solid Earth, 5, 1–11, https://doi.org/10.5194/se-5-1-2014, 2014.

Fisher, D. M. and Brantley, S. L.: Models of quartz overgrowth and vein formation: Deformation and episodic fluid flow in an ancient subduction zone, J Geophys Res Solid Earth, 97, 20043–20061, https://doi.org/10.1029/92JB01582, 1992.

Forstner, S. R. and Laubach, S. E.: Scale-dependent fracture networks, J Struct Geol, 165, 104748, https://doi.org/10.1016/J.JSG.2022.104748, 2022.

Fossen, H.: The role of extensional tectonics in the Caledonides of South Norway, J Struct Geol, 14, 1033–1046, 1992.

Fossen, H.: Extensional tectonics in the North Atlantic Caledonides: A regional view, Geol Soc Spec Publ, 335, https://doi.org/10.1144/SP335.31, 2010a.

Fossen, H.: Structural geology, First Edition., Cambridge University Press, 2010b.

Fossen, H., Khani, H. F., Faleide, J. I., Ksienzyk, A. K., and Dunlap, W. J.: Post-Caledonian extension in the West Norway-northern North Sea region: The role of structural inheritance, in: Geological Society Special Publication, vol. 439, Geological Society of London, 465–486, https://doi.org/10.1144/SP439.6, 2017.

Fossen, H., Cavalcante, G. C. G., Pinheiro, R. V. L., and Archanjo, C. J.: Deformation – Progressive or multiphase?, J Struct Geol, 125, 82–99, https://doi.org/10.1016/J.JSG.2018.05.006, 2019.

Fossen, H., Ksienzyk, A. K., Rotevatn, A., Bauck, M. S., and Wemmer, K.: From widespread faulting to localised rifting: Evidence from K-Ar fault gouge dates from the Norwegian North Sea rift shoulder, Basin Research, 33, 1934–1953, https://doi.org/10.1111/bre.12541, 2021.

Fredin, O., Viola, G., Zwingmann, H., Sørlie, R., Brönner, M., Lie, J. E., Grandal, E. M., Müller, A., Margreth, A., Vogt, C., and Knies, J.: The inheritance of a mesozoic landscape in western Scandinavia, Nat Commun, 8, https://doi.org/10.1038/ncomms14879, 2017.

Frey, M.: Low Temperature Metamorphism, Blackie, Glasgow and London, 1987.

Gale, J.: Assessing the Permeability Characteristics of Fractured Rock, in: Recent Trends in Hydrogeology, vol. 189, edited by: Narasimhan, T. N., Geological Society of America, 0, https://doi.org/10.1130/SPE189-p163, 1982.

Gautneb, H.: Structure, age and formation of dykes on the island of Smøla, Central Norway, Norsk geologisk tidsskrift, 68, 275–288, 1988.

Gautneb, Ha. and Roberts, D.: Geology and petrochemistry of the Smøla-Hitra batholith, Central Norway, Norges Geologiske Undersøkelse Bulletin, 416, 1–24, 1989.

Gee, D. G., Fossen, H., Henriksen, N., and Higgins, A. K.: From the Early Paleozoic Platforms of Baltica and Laurentia to the Caledonide Orogen of Scandinavia and Greenland, International Union of Geological Sciences, 31, 44–51, https://doi.org/10.18814/epiiugs/2008/v31i1/007, 2008.

Geological Survey of Norway: Bedrock map of Norway 1:1 350 000, 2021.

Georgiev, S. V., Stein, H. J., Hannah, J. L., Yang, G., Markey, R. J., Dons, C. E., Pedersen, J. H., and di Primio, R.: Comprehensive evolution of a petroleum system in absolute time: The example of Brynhild, Norwegian North Sea, Chem Geol, 522, 260–282, https://doi.org/10.1016/j.chemgeo.2019.05.025, 2019.

Gernigon, L., Franke, D., Geoffroy, L., Schiffer, C., Foulger, G. R., and Stoker, M.: Crustal fragmentation, magmatism, and the diachronous opening of the Norwegian-Greenland Sea, https://doi.org/10.1016/j.earscirev.2019.04.011, 1 July 2020.

Gillespie, P. A., Howard, C. B., Walsh, J. J., and Watterson, J.: Measurement and characterisation of spatial distributions of fractures, Tectonophysics, 226, 113–141, https://doi.org/10.1016/0040-1951(93)90114-Y, 1993.

Gillespie, P. A., Holdsworth, R. E., Long, D., Williams, A., and Gutmanis, J. C.: Introduction: geology of fractured reservoirs, J Geol Soc London, 178, jgs2020-197, https://doi.org/10.1144/jgs2020-197, 2020.

Giuffrida, A., Agosta, F., Rustichelli, A., Panza, E., La Bruna, V., Eriksson, M., Torrieri, S., and Giorgioni, M.: Fracture stratigraphy and DFN modelling of tight carbonates, the case study of the Lower Cretaceous carbonates exposed at the Monte Alpi (Basilicata, Italy), Mar Pet Geol, 112, 104045, https://doi.org/10.1016/J.MARPETGEO.2019.104045, 2020.

Goff, J. C.: Hydrocarbon generation and migration from Jurassic source rocks in the E Shetland Basin and Viking Graben of the northern North Sea, J Geol Soc London, 140, 445–474, https://doi.org/10.1144/gsjgs.140.3.0445, 1983.

Golder Associates (UK) Ltd.: FracMan 8.0 Manual, Golder Associates: Bourne End, UK, 2001.

Grønlie, A. and Roberts, D.: Resurgent strike-slip duplex development along the Hitra-Snåsa and Verran Faults, Møre-trøndelag fault zone, Central Norway, J Struct Geol, 11, 295–305, https://doi.org/10.1016/0191-8141(89)90069-2, 1989.

Grønlie, A., Naeser, C. W., Naeser, N. D., Mitchell, J. G., Sturt, B. A., and Ineson, P. R.: Fission-track and K-Ar dating of tectonic activity in a transect across the Møre-Trøndelag Fault Zone, central Norway., Norsk Geologisk Tidsskrift, 74, 24–34, 1994.

Haldorsen, H. H. and Damsleth, E.: Stochastic Modeling (includes associated papers 21255 and 21299), Journal of Petroleum Technology, 42, 404–412, https://doi.org/10.2118/20321-PA, 1990.

Hancock, P. L.: Determining contemporary stress directions from neotectonic joint systems, Trans. R. Soc. Lond. A, 29–40 pp., 1991.

Hartz, E. H., B. Martinsen, B., Øverli, P. E., Lie, H., Ditcha, E. M., Schmid, D. W., and Medvedev, S.: Newly Discovered Giant Oil Fields of North Sea - The Role of Fractured Basement Highs, cp-365-00017, https://doi.org/10.3997/2214-4609.20131805, 2013.

Hestnes, Å., Gasser, D., Scheiber, T., Jacobs, J., van der Lelij, R., Schönenberger, J., and Ksienzyk, A. K.: The brittle evolution of Western Norway – A space-time model based on fault mineralizations, K–Ar fault gouge dating and paleostress analysis, J Struct Geol, 160, 104621, https://doi.org/10.1016/J.JSG.2022.104621, 2022.

Hestnes, Å., Drost, K., Sømme, T. O., Gasser, D., Scheiber, T., Linge, H., Chew, D., and Jacobs, J.: Constraining the tectonic evolution of rifted continental margins by U-Pb calcite dating, https://doi.org/10.1038/s41598-023-34649-z, 2023.

Hetherington, C. J., Mailloux, G. A., and Miller, B. V.: A multi-mineral U-(Th)-Pb dating study of the Stetind pegmatite of the Tysfjord region, Norway, and implications for production of NYF-rare element pegmatites during orogenic collapse, Lithos, 398–399, 106257, https://doi.org/10.1016/J.LITHOS.2021.106257, 2021.

Hodge, M. S., Cottrell, M., Knies, J., and Viola, G.: Capturing secondary permeability and fracture connectivity through geological time by fracture back-stripping, Research Square PREPRINT (Version 1) , https://doi.org/10.21203/rs.3.rs-4844693/v1, 2024a.

Hodge, M. S., Venvik, G., Knies, J., van der Lelij, R., Schönenberger, J., Nordgulen, Ø., Brönner, M., Nasuti, A., and Viola, G.: Multiscalar 3D temporal structural characterisation of Smøla island, mid-Norwegian passive margin: an analogue for unravelling the tectonic history of offshore basement highs, Solid Earth, 15, 589–615, https://doi.org/10.5194/se-15-589-2024, 2024b.

Holcombe, R.: Oriented Drillcore: Measurement, Conversion and QA/QC Procedures for Structural and Exploration Geologists, http://www.holcombe coughlinoliver.com/downloads/, 2013.

Holcombe, R.: Geocalculator [Online], http://www.holcombe.net.au/software/rodh_software_purchase.htm, 2014.

Holdsworth, R. E.: Weak Faults--Rotten Cores, Science (1979), 303, 181–182, https://doi.org/10.1126/science.1092491, 2004.

Holdsworth, R. E., McCaffrey, K. J. W., Dempsey, E., Roberts, N. M. W., Hardman, K., Morton, A., Feely, M., Hunt, J., Conway, A., and Robertson, A.: Natural fracture propping and earthquake-induced oil migration in fractured basement reservoirs, Geology, 47, 700–704, https://doi.org/10.1130/G46280.1, 2019.

Hosono, H., Takemura, T., Asahina, D., and Otsubo, M.: Estimation of paleo-permeability around a seismogenic fault based on permeability tensor from observable geometric information of quartz veins, Earth, Planets and Space, 74, 141, https://doi.org/10.1186/s40623-022-01694-3, 2022.

Hueck, M., Wemmer, K., Basei, M. A. S., Philipp, R. P., Oriolo, S., Heidelbach, F., Oyhantçabal, P., and Siegesmund, S.: Dating recurrent shear zone activity and the transition from ductile to brittle deformation: White mica geochronology applied to the Neoproterozoic Dom Feliciano Belt in South Brazil, J Struct Geol, 141, 104199, https://doi.org/10.1016/J.JSG.2020.104199, 2020.

Hueck, M., Wemmer, K., Ksienzyk, A. K., Kuehn, R., and Vogel, N.: Potential, premises, and pitfalls of interpreting illite argon dates - A case study from the German Variscides, Earth Sci Rev, 232, 104133, https://doi.org/10.1016/J.EARSCIREV.2022.104133, 2022.

Imdex Limited: ioGAS, https://reflexnow.com/product/iogas/, 2022.

Indrevær, K., Stunitz, H., and Bergh, S. G.: On Palaeozoic–Mesozoic brittle normal faults along the SW Barents Sea margin: Fault processes and implications for basement permeability and margin evolution, J Geol Soc London, 171, 831–846, https://doi.org/10.1144/jgs2014-018, 2014.

Ioannou, S. E. and Spooner, E. T. C.: Fracture Analysis of a Volcanogenic Massive Sulfide-Related Hydrothermal Cracking Zone, Upper Bell River Complex, Matagami, Quebec: Application of Permeability Tensor Theory, Economic Geology, 102, 667–690, https://doi.org/10.2113/gsecongeo.102.4.667, 2007.

Jaeger, J. C., Cook, N. G. W., and Zimmerman, R. W.: Fundamentals of Rock Mechanics, Fourth Edition., Blackwell Publishing, 2007.

Jakob, J., Andersen, T. B., Mohn, G., Kjøll, H. J., and Beyssac, O.: Revised tectono-stratigraphic scheme for the Scandinavian Caledonides and its implications for our understanding of the Scandian orogeny, in: New Developments in the Appalachian-Caledonian-Variscan Orogen, Geological Society of America, 335–374, https://doi.org/10.1130/2022.2554(14), 2022.

Jing, L. and Stephansson, O.: Discrete fracture network (DFN) method, in: Developments in geotechnical engineering, vol. 85, Elsevier, 365–398, 2007.

Kelley, S.: K-Ar and Ar-Ar Dating, Rev Mineral Geochem, 47, 785–818, https://doi.org/10.2138/rmg.2002.47.17, 2002.

Kendrick, M. A., Eide, A., Roberts, D., and Osmundsen, P. T.: The Middle to Late Devonian Høybakken detachment, central Norway: 40Ar–39Ar evidence for prolonged late/post-Scandian extension and uplift, Geol Mag, 141, 329–344, https://doi.org/10.1017/S0016756803008811, 2004.

Khorasani, G. K.: Factors Controlling Source Rock Potential of the Mesozoic Coal-bearing Strata from Offshore Central Norway: Application to Petroleum Exploration, Bulletin of Canadian Petroleum Geology, 37, 417–427, https://doi.org/10.35767/gscpgbull.37.4.417, 1989.

Kim, J., Choi, J., Leem, J., and Song, J.-J.: Growth Parameter Conditioning of Genetic Discrete Fracture Networks to Trace Length Distribution Data, in: 58th U.S. Rock Mechanics/Geomechanics Symposium, https://doi.org/10.56952/ARMA-2024-0846, 2024.

Kim, Y. S., Peacock, D. C. P., and Sanderson, D. J.: Fault damage zones, J Struct Geol, 26, 503–517, https://doi.org/10.1016/J.JSG.2003.08.002, 2004.

Knies, J., Schönenberger, J., Zwingmann, H., van der Lelij, R., Smelror, M., Vullum, P. E., Brönner, M., Vogt, C., Fredin, O., Müller, A., Grasby, S. E., Beauchamp, B., and Viola, G.: Continental weathering and recovery from ocean nutrient stress during the Early Triassic Biotic Crisis, Commun Earth Environ, 3, 161, https://doi.org/10.1038/s43247-022-00480-z, 2022.

Ksienzyk, A. K., Wemmer, K., Jacobs, J., Fossen, H., Schomberg, A. C., Süssenberger, A., Lünsdorf, N. K., and Bastesen, E.: Post-Caledonian brittle deformation in the Bergen area,West Norway: results from K–Ar illite fault gouge dating, Norwegian Journal of Geology, 96, 275–299, https://doi.org/10.17850/njg96-3-06, 2016.

Lacombe, O., Tavani, S., Lamarche, J., Balsamo, F., and Agosta, F.: Introduction: Faults and fractures in rocks: mechanics, occurrence, dating, stress history and fluid flow, Geol Mag, 159, 1847–1854, https://doi.org/DOI: 10.1017/S0016756823000031, 2022.

Larsen, Ø., Fossen, H., Langeland, K., and Pedersen, R.-B.: Kinematics and timing of polyphase post-Caledonian deformation in the Bergen area, SW Norway., Norwegian Journal of Geology/Norsk Geologisk Forening, 83, 2003.

Laubach, S. E. and Kira, D.-T.: Laurentian palaeostress trajectories and ephemeral fracture permeability, Cambrian Eriboll Formation sandstones west of the Moine Thrust Zone, NW Scotland, J Geol Soc London, 166, 349–362, https://doi.org/10.1144/0016-76492008-061, 2009.

Lavoine, E., Davy, P., Darcel, C., and Munier, R.: A Discrete Fracture Network Model With Stress-Driven Nucleation: Impact on Clustering, Connectivity, and Topology, Front Phys, 8, 2020.

Leckenby, R. J., Sanderson, D. J., and Lonergan, L.: Estimating flow heterogeneity in natural fracture systems, Journal of Volcanology and Geothermal Research, 148, 116–129, https://doi.org/10.1016/J.JVOLGEORES.2005.03.017, 2005.

Lee, Y. J. and Morse, J. W.: Calcite precipitation in synthetic veins: implications for the time and fluid volume necessary for vein filling, Chem Geol, 156, 151–170, https://doi.org/10.1016/S0009-2541(98)00183-1, 1999.

Lei, Q. and Wang, X.: Tectonic interpretation of the connectivity of a multiscale fracture system in limestone, Geophys Res Lett, 43, 1551–1558, https://doi.org/10.1002/2015GL067277, 2016.

Levy, S. and Woldegabriel, G.: Ion Exchange and Dehydration Effects on Potassium and Argon Contents of Clinoptilolite, MRS Proceedings, 412, 791, https://doi.org/DOI: 10.1557/PROC-412-791, 1995.

Li, Y. and Elmo, D.: A Critical Discussion on the Use of Discrete Fracture Network Models in Rock Engineering Practice: Why Rock Mass Characterisation Methods can Benefit from Considering Fracture Connectivity, Rock Mech Rock Eng, https://doi.org/10.1007/s00603-024-04049-4, 2024.

Libby, S., Hartley, L., Turnbull, R., Cottrell, M., Bym, T., Josephson, N., Munier, R., Selroos, J. O., and Mas Ivars, D.: Grown Discrete Fracture Networks: a new method for generating fractures according to their deformation history, in: Proceedings of the 53rd US Rock Mechanics/Geomechanics Symposium, 23–26, 2019.

Libby, S., Hartley, L., Turnbull, R., Cottrell, M., Bym, T., Josephson, N., Munier, R., Selroos, J.-O., and Mas Ivars, D.: Exploring the impact of fracture interaction on connectivity and flow channelling using grown fracture networks, Quarterly Journal of Engineering Geology and Hydrogeology, 57, qjegh2023-010, https://doi.org/10.1144/qjegh2023-010, 2024.

Long, J. C. S., Gilmour, P., and Witherspoon, P. A.: A Model for Steady Fluid Flow in Random Three-Dimensional Networks of Disc-Shaped Fractures, Water Resour Res, 21, 1105–1115, https://doi.org/10.1029/WR021i008p01105, 1985.

Macente, A., Dobson, K. J., MacDonald, J., Wadsworth, F. B., and Vasseur, J.: The Evolution of Paleo-Porosity in Basalts: Reversing Pore-Filling Mechanisms Using X-Ray Computed Tomography, Transp Porous Media, 145, 697–717, https://doi.org/10.1007/s11242-022-01869-2, 2022.

Maillot, J., Davy, P., Le Goc, R., Darcel, C., and de Dreuzy, J. R.: Connectivity, permeability, and channeling in randomly distributed and kinematically defined discrete fracture network models, Water Resour Res, 52, 8526–8545, https://doi.org/10.1002/2016WR018973, 2016.

Manzocchi, T.: The connectivity of two-dimensional networks of spatially correlated fractures, Water Resour Res, 38, 1-1-1–20, https://doi.org/10.1029/2000WR000180, 2002.

Marchesini, B., Garofalo, P. S., Menegon, L., Mattila, J., and Viola, G.: Fluid-mediated, brittle–ductile deformation at seismogenic depth – Part 1: Fluid record and deformation history of fault veins in a nuclear waste repository (Olkiluoto Island, Finland), Solid Earth, 10, 809–838, https://doi.org/10.5194/se-10-809-2019, 2019.

Matapour, Z. and Karlsen, D. A.: Ages of Norwegian oils and bitumen based on age-specific biomarkers, Petroleum Geoscience, 24, 92–101, https://doi.org/10.1144/petgeo2016-119, 2018.

Mattila, J. and Viola, G.: New constraints on 1.7 Gyr of brittle tectonic evolution in southwestern Finland derived from a structural study at the site of a potential nuclear waste repository (Olkiluoto Island), J Struct Geol, 67, 50–74, https://doi.org/10.1016/j.jsg.2014.07.003, 2014.

McCaffrey, K. J. W., Holdsworth, R. E., Pless, J., Franklin, B. S. G., and Hardman, K.: Basement reservoir plumbing: fracture aperture, length and topology analysis of the Lewisian Complex, NW Scotland, J Geol Soc London, 177, 1281–1293, https://doi.org/10.1144/jgs2019-143, 2020.

Mosar, J., Eide, E. A., Osmundsen, P. T., Sommaruga, A., and Torsvik, T. H.: Greenland – Norway separation: A geodynamic model for the North Atlantic, Norwegian Journal of Geology, 82, 282–299, 2002.

Munier, R. and Talbot, C. J.: Segmentation, fragmentation and jostling of cratonic basement in and near Äspö, southeast Sweden, Tectonics, 12, 713–727, https://doi.org/10.1029/92TC02722, 1993.

Muñoz-Barrera, J. M., Rotevatn, A., Gawthorpe, R. L., Henstra, G. A., and Kristensen, T. B.: The role of structural inheritance in the development of high-displacement crustal faults in the necking domain of rifted margins: The Klakk Fault Complex, Frøya High, offshore mid-Norway, J Struct Geol, 140, https://doi.org/10.1016/j.jsg.2020.104163, 2020.

Munro, M. A. and Blenkinsop, T. G.: MARD-A moving average rose diagram application for the geosciences, Comput Geosci, 49, 112–120, https://doi.org/10.1016/j.cageo.2012.07.012, 2012.

Murphy, P. J., Briedis, J., and Peck, J. H.: Dating techniques in fault investigations, in: Geology in the Siting of Nuclear Power Plants, edited by: Hatheway, A. W. and Mcclure, C. R., Geological Society of America, https://doi.org/10.1130/REG4-p153, 1979.

Nasuti, A., Olesen, O., Baranwal, O., and Dumais, M.: Compilation of aeromagnetic data, in: Coop Phase 2 - Crustal Onshore-Offshore Project. NGU confidential Report , vol. 063, edited by: Olesen, O., Baranwal, O., Brönner, M., Dalsegg, E., Dumais, M. , A., Gellein, J., Gernigon, L., Heldal, T., Larsen, B. , E., Lauritsen, T., Lutro, O., Maystrenko, Y., Nasuti, A., Roberts, D., Rueslåtten, H., Rønning, J. S., Slagstad, T., Solli, A., and Stampolidis, A., Norges Geologiske Undersøkelse, 11–24, 2015.

Nelson, R.: Geologic Analysis of Naturally Fractured Reservoirs, Second Edition., Gulf Professional Publishing, Houston, TX, 2001.

Nolen-Hoeksema, R.: Defining and determining permeability, Oilfield Review, 26, 2014.

Nortje, G. S., Oliver, N. H. S., Blenkinsop, T. G., Keys, D. L., Mclellan, J. G., and Oxenburgh, S.: New faults v. Fault reactivation: Implications for fault cohesion, fluid flow and copper mineralization, Mount Gordon Fault Zone, Mount Isa District, Australia, Geol Soc Spec Publ, 359, 287–311, https://doi.org/10.1144/SP359.16, 2011.

Nyberg, B., Nixon, C. W., and Sanderson, D. J.: NetworkGT: A GIS tool for geometric and topological analysis of two-dimensional fracture networks, Geosphere, 14, 1618–1634, https://doi.org/10.1130/GES01595.1, 2018.

Oda, M.: Similarity rule of crack geometry in statistically homogeneous rock masses, Mechanics of Materials, 3, 119–129, https://doi.org/10.1016/0167-6636(84)90003-6, 1984.

Oda, M.: Permeability tensor for discontinuous rock masses, Géotechnique, 35, 483–495, https://doi.org/10.1680/geot.1985.35.4.483, 1985.

Oda, M.: A method for evaluating the representative elementary volume based on joint survey of rock masses, Canadian Geotechnical Journal, 25, 440–447, https://doi.org/10.1139/t88-049, 1988.

Oda, M., Takemura, T., and Aoki, T.: Damage growth and permeability change in triaxial compression tests of Inada granite, Mechanics of Materials, 34, 313–331, https://doi.org/10.1016/S0167-6636(02)00115-1, 2002.

Ohm, S. E., Karlsen, D. A., Phan, N. T., Strand, T., and Iversen, G.: Present Jurassic petroleum charge facing Paleozoic biodegraded oil: Geochemical challenges and potential upsides, Embla field, North Sea, Am Assoc Pet Geol Bull, 96, 1523–1552, https://doi.org/10.1306/01021211094, 2012.

Olesen, O., Rueslåtten, H. G., Schönenberger, J., Smelror, M., van der Lelij, R., Larsen, B. E., Olsen, L., Baranwal, V., Bjørlykke, A., and Brönner, M.: Jurassic heritance of the geomorphology in Mid Norway., Norwegian Journal of Geology, 103, 2023.

Oliver, N. H. S. and Bons, P. D.: Mechanisms of fluid flow and fluid–rock interaction in fossil metamorphic hydrothermal systems inferred from vein–wallrock patterns, geometry and microstructure, Geofluids, 1, 137–162, https://doi.org/10.1046/j.1468-8123.2001.00013.x, 2001.

Olsen, E., Gabrielsen, R. H., Braathen, A., and Redfield, T. F.: Fault systems marginal to the Møre-Trøndelag Fault Complex, Osen-Vikna area, Central Norway, Norwegian Journal of Geology, 87, 59–73, 2007.

Olson, J. E., Laubach, S. E., and Lander, R. H.: Combining diagenesis and mechanics to quantify fracture aperture distributions and fracture pattern permeability, Geological

Society, London, Special Publications, 270, 101–116, https://doi.org/10.1144/GSL.SP.2007.270.01.08, 2007.

Olson, J. E., Laubach, S. E., and Lander, R. H.: Natural fracture characterization in tight gas sandstones: Integrating mechanics and diagenesis, Am Assoc Pet Geol Bull, 93, 1535–1549, https://doi.org/10.1306/08110909100, 2009.

Osmundsen, P. T., Eide, E. A., Haabesland, N. E., Roberts, D., Andersen, T. B., Kendrick, M., Bingen, B., Braathen, A., and Redfield, T. F.: Kinematics of the Høybakken detachment zone and the Møre–Trøndelag Fault Complex, central Norway, J Geol Soc London, 163, 303–318, https://doi.org/10.1144/0016-764904-129, 2006.

Palumbo, F., Main, I. G., and Zito, G.: The thermal evolution of sedimentary basins and its effect on the maturation of hydrocarbons, Geophys J Int, 139, 248–260, https://doi.org/10.1046/j.1365-246X.1999.00877.x, 1999.

Paluszny, A., Thomas, R. N., Saceanu, M. C., and Zimmerman, R. W.: Hydro-mechanical interaction effects and channelling in three-dimensional fracture networks undergoing growth and nucleation, Journal of Rock Mechanics and Geotechnical Engineering, 12, 707–719, https://doi.org/10.1016/J.JRMGE.2020.04.004, 2020.

Passchier, C. W. and Trouw, R. A. J.: Microtectonics, 2nd Edition., Springer Science & Business Media, Berlin, 2005.

Peacock, D. C. P.: The temporal relationship between joints and faults, J Struct Geol, 23, 329–341, https://doi.org/10.1016/S0191-8141(00)00099-7, 2001.

Peacock, D. C. P. and Sanderson, D. J.: Structural analyses and fracture network characterisation: Seven pillars of wisdom, Earth Sci Rev, 184, 13–28, https://doi.org/10.1016/J.EARSCIREV.2018.06.006, 2018.

Peacock, D. C. P., Nixon, C. W., Rotevatn, A., Sanderson, D. J., and Zuluaga, L. F.: Glossary of fault and other fracture networks, J Struct Geol, 92, 12–29, https://doi.org/10.1016/J.JSG.2016.09.008, 2016.

Peacock, D. C. P., Sanderson, D. J., and Rotevatn, A.: Relationships between fractures, J Struct Geol, 106, 41–53, https://doi.org/10.1016/J.JSG.2017.11.010, 2018.

Peacock, D. C. P., Sanderson, D. J., Bastesen, E., Rotevatn, A., and Storstein, T. H.: Causes of bias and uncertainty in fracture network analysis, Norwegian Journal of Geology, 99, 113–128, 2019.

Peacock, D. C. P., Sanderson, D. J., and Leiss, B.: Use of analogue exposures of fractured rock for enhanced geothermal systems, Geosciences (Basel), 12, 318, https://doi.org/10.3390/geosciences12090318, 2022.

Peron-Pinvidic, G. and Osmundsen, P. T.: The Mid Norwegian - NE Greenland conjugate margins: Rifting evolution, margin segmentation, and breakup, https://doi.org/10.1016/j.marpetgeo.2018.08.011, 1 December 2018.

Peron-Pinvidic, G. and Osmundsen, P. T.: From orogeny to rifting: insights from the Norwegian ‘reactivation phase,’ Sci Rep, 10, https://doi.org/10.1038/s41598-020-71893-z, 2020.

Peron-Pinvidic, G., Manatschal, G., and Osmundsen, P. T.: Structural comparison of archetypal Atlantic rifted margins: A review of observations and concepts, Mar Pet Geol, 43, 21–47, https://doi.org/10.1016/J.MARPETGEO.2013.02.002, 2013.

Petrik, A., Vahle, C., Gianotten, I. P., Trøan, L. I., Rojo, L., and Galbraith, K.: Quantitative characterisation of fracture connectivity from high-resolution borehole image logs, Mar Pet Geol, 155, https://doi.org/10.1016/j.marpetgeo.2023.106405, 2023.

van der Pluijm, B. A., Hall, C. M., Vrolijk, P. J., Pevear, D. R., and Covey, M. C.: The dating of shallow faults in the Earth’s crust, Nature, 412, 172–175, https://doi.org/10.1038/35084053, 2001.

Price, N. J. and Cosgrove, J. W.: Analysis of geological structures, Cambridge University Press, 1990.

Putnis, A. and Austrheim, H.: Fluid-induced processes: metasomatism and metamorphism, Geofluids, 10, 254–269, https://doi.org/10.1111/j.1468-8123.2010.00285.x, 2010.

Putnis, A., Hinrichs, R., Putnis, C. V., Golla-Schindler, U., and Collins, L. G.: Hematite in porous red-clouded feldspars: Evidence of large-scale crustal fluid–rock interaction, Lithos, 95, 10–18, https://doi.org/10.1016/J.LITHOS.2006.07.004, 2007.

Ramsay, J. G.: The crack–seal mechanism of rock deformation, Nature, 284, 135–139, https://doi.org/10.1038/284135a0, 1980.

Ramsey, J. M. and Chester, F. M.: Hybrid fracture and the transition from extension fracture to shear fracture, Nature, 428, 63–66, https://doi.org/10.1038/nature02333, 2004.

Rasbury, E. T. and Cole, J. M.: Directly dating geologic events: U-Pb dating of carbonates, Reviews of Geophysics, 47, https://doi.org/10.1029/2007RG000246, 2009.

Redfield, T. F., Torsvik, T. H., Andriessen, P. A. M., and Gabrielsen, R. H.: Mesozoic and Cenozoic tectonics of the Møre Trøndelag Fault Complex, central Norway: constraints from new apatite fission track data, Physics and Chemistry of the Earth, Parts A/B/C, 29, 673–682, https://doi.org/10.1016/j.pce.2004.03.005, 2004.

Riber, L., Dypvik, H., and Sørlie, R.: Altered basement rocks on the Utsira High and its surroundings, Norwegian North Sea, Norwegian Journal of Geology, 95, 57–89, 2015.

Riber, L., Dypvik, H., Sørlie, R., and Ferrell Jr., R. E.: Clay minerals in deeply buried paleoregolith profiles, Norwegian North Sea, Clays Clay Miner, 64, 588–607, https://doi.org/10.1346/CCMN.2016.064036, 2016.

Roberts, D.: Petrochemistry and palaeogeographic setting of the Ordovician volcanic rocks of Smøla, central Norway, Norges Geologiske Undersøkelse Bulletin, 359, 43–60, 1980.

Roberts, D. and Gee, D. G.: An introduction to the structure of the Scandinavian Caledonides., in: The Caledonide orogen–Scandinavia and related areas, vol. Part 1, 55–68, 1985.

Roberts, D. and Myrvang, A.: Contemporary stress orientation features in bedrock, Trøndelag, central Norway, and some regional implications., Norges Geologiske Undersøkelse Bulletin, 442, 53–63, 2004.

Roberts, D., Luneburg, C., Jin, D., and Kato, J.: Utilizing a kinematic and mechanical modelling workflow to constrain fracture network characteristics: Application to the Teapot Dome, Wyoming, USA, J Struct Geol, 159, 104596, https://doi.org/10.1016/J.JSG.2022.104596, 2022.

Roberts, N. M. W., Drost, K., Horstwood, M. S. A., Condon, D. J., Chew, D., Drake, H., Milodowski, A. E., McLean, N. M., Smye, A. J., and Walker, R. J.: Laser ablation inductively coupled plasma mass spectrometry (LA-ICP-MS) U–Pb carbonate geochronology: strategies, progress, and limitations, Geochronology, 2, 33–61, https://doi.org/10.5194/gchron-2-33-2020, 2020.

Robinson, P., Roberts, D., Gee, D. G., and Solli, A.: A major synmetamorphic early devonian thrust and extensional fault system in the mid norway caledonides: Relevance to exhumation of HP and UHP rocks, Geol Soc Spec Publ, 390, 241–270, https://doi.org/10.1144/SP390.24, 2014.

Rønning, J. S. and Elvebakk, H.: Onshore-Offshore Resistivity studies. Basement resistivity at the Frøya High, 2005.

Rubey, W. W. and Hubbert, K. M.: Role of fluid pressure in mechanics of overthrust faulting: II. Overthrust belt in geosynclinal area of Western Wyoming in light of fluid-pressure hypothesis, GSA Bulletin, 70, 167–206, https://doi.org/10.1130/0016-7606(1959)70[167:ROFPIM]2.0.CO;2, 1959.

Sanderson, D. J. and Nixon, C. W.: The use of topology in fracture network characterization, J Struct Geol, 72, 55–66, https://doi.org/10.1016/J.JSG.2015.01.005, 2015.

Sanderson, D. J., Peacock, D. C. P., Nixon, C. W., and Rotevatn, A.: Graph theory and the analysis of fracture networks, J Struct Geol, 125, 155–165, https://doi.org/10.1016/J.JSG.2018.04.011, 2019.

Scheiber, T. and Viola, G.: Complex Bedrock Fracture Patterns: A Multipronged Approach to Resolve Their Evolution in Space and Time, Tectonics, 37, 1030–1062, https://doi.org/10.1002/2017TC004763, 2018.

Scheiber, T., Fredin, O., Viola, G., Jarna, A., Gasser, D., and Łapińska-Viola, R.: Manual extraction of bedrock lineaments from high-resolution LiDAR data: methodological bias and human perception, GFF, 137, 362–372, https://doi.org/10.1080/11035897.2015.1085434, 2015.

Scheiber, T., Viola, G., Wilkinson, C. M., Ganerød, M., Skår, Ø., and Gasser, D.: Direct 40Ar/39Ar dating of Late Ordovician and Silurian brittle faulting in the southwestern Norwegian Caledonides, Terra Nova, 28, 374–382, https://doi.org/10.1111/ter.12230, 2016.

Scheiber, T., Viola, G., van der Lelij, R., Margreth, A., and Schönenberger, J.: Microstructurally-constrained versus bulk fault gouge K-Ar dating, J Struct Geol, 127, https://doi.org/10.1016/j.jsg.2019.103868, 2019.

Scholz, C. H.: The mechanics of earthquakes and faulting, Third Edition., Cambridge University Press, https://doi.org/10.1017/9781316681473, 2019.

Schultz, R. A.: Introduction to Geologic Structural Discontinuities, in: Geologic Fracture Mechanics, Cambridge University Press, 1–26, https://doi.org/10.1017/9781316996737.001, 2019.

Schultz, R. A. and Fossen, H.: Terminology for structural discontinuities, https://doi.org/10.1306/02200807065, 2008.

Scibek, J.: Multidisciplinary database of permeability of fault zones and surrounding protolith rocks at world-wide sites, Sci Data, 7, 95, https://doi.org/10.1038/s41597-020-0435-5, 2020.

Seeburger, D. A. and Zoback, M. D.: The distribution of natural fractures and joints at depth in crystalline rock, J Geophys Res Solid Earth, 87, 5517–5534, https://doi.org/10.1029/JB087iB07p05517, 1982.

Seequent, T. B. S. C.: Leapfrog Works, 2022.

Selby, D. and Creaser, R. A.: Direct Radiometric Dating of Hydrocarbon Deposits Using Rhenium-Osmium Isotopes, Science (1979), 308, 1293–1295, 2005.

Selvadurai, A. P. S., Boulon, M. J., and Nguyen, T. S.: The Permeability of an Intact Granite, Pure Appl Geophys, 162, 373–407, https://doi.org/10.1007/s00024-004-2606-2, 2005.

Seranne, M.: Late Paleozoic kinematics of the Møre-Trøndelag Fault Zone and adjacent areas, central Norway, Norsk Geologisk Tidsskrift, 72, 141–158, 1992.

Sherlock, S. C., Watts, L. M., Holdsworth, R. E., and Roberts, D.: Dating fault reactivation by Ar/Ar laserprobe: an alternative view of apparently cogenetic mylonite–pseudotachylite assemblages, J Geol Soc London, 161, 335–338, https://doi.org/10.1144/0016-764903-160, 2004.

Sibson, R.: Crustal stress, faulting and fluid flow, Geological Society, London, Special Publications, 78, 69–84, https://doi.org/10.1144/GSL.SP.1994.078.01.07, 1994.

Sibson, R. H.: Fault rocks and fault mechanisms, J Geol Soc London, 133, 191–213, https://doi.org/10.1144/gsjgs.133.3.0191, 1977.

Sibson, R. H.: A note on fault reactivation, J Struct Geol, 7, 751–754, https://doi.org/10.1016/0191-8141(85)90150-6, 1985.

Sibson, R. H.: Implications of fault-valve behaviour for rupture nucleation and recurrence, Tectonophysics, 211, 283–293, https://doi.org/10.1016/0040-1951(92)90065-E, 1992.

Sibson, R. H.: Structural permeability of fluid-driven fault-fracture meshes, J Struct Geol, 18, 1031–1042, https://doi.org/10.1016/0191-8141(96)00032-6, 1996.

Sibson, R. H.: Brittle failure mode plots for compressional and extensional tectonic regimes, J Struct Geol, 20, 655–660, https://doi.org/10.1016/S0191-8141(98)00116-3, 1998.

Skilbrei, J. R., Olesen, O., Osmundsen, P. T., Kihle, O., Aaro, S., and Fjellanger, E.: A study of basement structures and onshore-offshore correlations in Central Norway., Norwegian Journal of Geology, 82, 263–279, 2002.

Slagstad, T. and Kirkland, C. L.: Timing of collision initiation and location of the Scandian orogenic suture in the Scandinavian Caledonides, Terra Nova, 30, 179–188, https://doi.org/10.1111/ter.12324, 2018.

Slagstad, T., Ramstad, R. K., Davidsen, B., and Barrére, C.: Petrophysical and thermal properties of pre-Devonian basement rocks on the Norwegian continental margin, 2008.

Slagstad, T., Davidsen, B., and Stephen Daly, J.: Age and composition of crystalline basement rocks on the norwegian continental margin: Offshore extension and continuity of the Caledonian-Appalachian orogenic belt, J Geol Soc London, 168, 1167–1185, https://doi.org/10.1144/0016-76492010-136, 2011.

Small, J. S.: Experimental Determination of the Rates of Precipitation of Authigenic Illite and Kaolinite in the Presence of Aqueous Oxalate and Comparison to the K/Ar Ages of Authigenic Illite in Reservoir Sandstones, Clays Clay Miner, 41, 191–208, https://doi.org/DOI: 10.1346/CCMN.1993.0410208, 1993.

Snow, D. T.: Anisotropie Permeability of Fractured Media, Water Resour Res, 5, 1273–1289, https://doi.org/10.1029/WR005i006p01273, 1969.

Stephens, M. B., Follin, S., Petersson, J., Isaksson, H., Juhlin, C., and Simeonov, A.: Review of the deterministic modelling of deformation zones and fracture domains at the site proposed for a spent nuclear fuel repository, Sweden, and consequences of structural anisotropy, Tectonophysics, 653, 68–94, https://doi.org/10.1016/j.tecto.2015.03.027, 2015.

Stober, I. and Bucher, K.: Hydraulic properties of the crystalline basement, Hydrogeol J, 15, 213–224, https://doi.org/10.1007/s10040-006-0094-4, 2007.

Tagami, T.: Thermochronological investigation of fault zones, Tectonophysics, 538–540, 67–85, https://doi.org/10.1016/J.TECTO.2012.01.032, 2012.

Tanner, D. C., Buness, H., Igel, J., Günther, T., Gabriel, G., Skiba, P., Plenefisch, T., Gestermann, N., and Walter, T. R.: Fault detection, Understanding Faults: Detecting, Dating, and Modeling, 81–146, https://doi.org/10.1016/B978-0-12-815985-9.00003-5, 2020.

Tartaglia, G., Viola, G., van der Lelij, R., Scheiber, T., Ceccato, A., and Schönenberger, J.: “Brittle structural facies” analysis: A diagnostic method to unravel and date multiple slip events of long-lived faults, Earth Planet Sci Lett, 545, https://doi.org/10.1016/j.epsl.2020.116420, 2020.

Tartaglia, G., Ceccato, A., Scheiber, T., van der Lelij, R., Schönenberger, J., and Viola, G.: Time-constrained multiphase brittle tectonic evolution of the onshore mid-Norwegian passive margin, GSA Bulletin, 135, 621–642, https://doi.org/10.1130/b36312.1, 2023.

Terzaghi, R. D.: Sources of Error in Joint Surveys, Géotechnique, 15, 287–304, https://doi.org/10.1680/geot.1965.15.3.287, 1965.

Thomas, R. N., Paluszny, A., and Zimmerman, R. W.: Permeability of Three-Dimensional Numerically Grown Geomechanical Discrete Fracture Networks With Evolving Geometry and Mechanical Apertures, J Geophys Res Solid Earth, 125, e2019JB018899, https://doi.org/10.1029/2019JB018899, 2020.

Torgersen, E., Viola, G., Zwingmann, H., and Harris, C.: Erratum to "Structural and temporal evolution of a reactivated brittle-ductile fault - Part II: Timing of fault initiation and reactivation by K-Ar dating of synkinematic illite/muscovite" [Earth Planet. Sci. Lett. 407 (2014) 221-233], https://doi.org/10.1016/j.epsl.2014.11.013, 5 January 2015.

Trice, R.: Basement exploration, West of Shetlands: Progress in opening a new play on the UKCS, Geol Soc Spec Publ, 397, 81–105, https://doi.org/10.1144/SP397.3, 2014.

Trice, R., Hiorth, C., and Holdsworth, R.: Fractured basement play development on the UK and Norwegian rifted margins, in: Cross-Border Themes in Petroleum Geology II: Atlantic Margin and Barents Sea, vol. 495, edited by: Chiarella, D., Archer, S. G., Howell, J. A., Jackson, C. A. L., Kombrink, H., and Patruno, S., The Geological Society of London, London, 73–97, https://doi.org/10.1144/SP495-2018-174, 2022.

Tsikalas, F., Faleide, J. I., Eldholm, O., and Blaich, O. A.: The NE Atlantic conjugate margins, Regional Geology and Tectonics: Phanerozoic Passive Margins, Cratonic Basins and Global Tectonic Maps, 140–201, https://doi.org/10.1016/B978-0-444-56357-6.00004-4, 2012.

Tucker, R. D., Robinson, P., Solli, A., Gee, D. G., Thorsnes, T., Krogh, T. E., Nordgulen, Ø., and Bickford, M. E.: Thrusting and Extension in the Scandian Hinterland, Norway: New U-Pb Ages and Tectonostratigraphic Evidence, Am J Sci, 304, 477–532, 2004.

Viola, G., Venvik Ganerød, G., and Wahlgren, C.-H.: Unraveling 1.5 Ga of brittle deformation history in the Laxemar-Simpevarp area, southeast Sweden: A contribution to the Swedish site investigation study for the disposal of highly radioactive nuclear waste, Tectonics, 28, https://doi.org/10.1029/2009TC002461, 2009.

Viola, G., Kounov, A., Andreoli, M. A. G., and Mattila, J.: Brittle tectonic evolution along the western margin of South Africa: More than 500Myr of continued reactivation, Tectonophysics, 514–517, 93–114, https://doi.org/10.1016/j.tecto.2011.10.009, 2012.

Viola, G., Scheiber, T., Fredin, O., Zwingmann, H., Margreth, A., and Knies, J.: Deconvoluting complex structural histories archived in brittle fault zones, Nat Commun, 7, https://doi.org/10.1038/ncomms13448, 2016.

Viola, G., Torgersen, E., Mazzarini, F., Musumeci, G., van der Lelij, R., Schönenberger, J., and Garofalo, P. S.: New Constraints on the Evolution of the Inner Northern Apennines by K-Ar Dating of Late Miocene-Early Pliocene Compression on the Island of Elba, Italy, Tectonics, 37, 3229–3243, https://doi.org/10.1029/2018TC005182, 2018.

Walsh, J. J., Watterson, J., Heath, A., Gillespie, P. A., and Childs, C.: Assessment of the effects of sub-seismic faults on bulk permeabilities of reservoir sequences, Geological Society, London, Special Publications, 127, 99–114, 1998.

Wang, X., Dove, C., Dunne, J. E., Gutierrez, W. M., and Westman, M. S.: Stereological Interpretation of Rock Fracture Traces on Borehole Walls and Other Cylindrical Surfaces, Doctoral dissertation, Virginia Polytechnic Institute and State University, 2005.

Watson, G. S.: The Statistics of Orientation Data, J Geol, 74, 786–797, https://doi.org/10.1086/627211, 1966.

Watts, L. M.: The walls boundary fault zone and the Møre Trøndelag fault complex: a case study of two reactivated fault zones., PhD thesis, Durham University, 0–550 pp., 2001.

Watts, L. M., Holdsworth, R. E., Roberts, D., Sleight, J. M., and Walker, R. J.: Structural evolution of the reactivated Møre-Trøndelag Fault Complex, Fosen Peninsula, Norway, J Geol Soc London, https://doi.org/10.1144/jgs2022-139, 2023.

Wehrens, P., Berger, A., Peters, M., Spillmann, T., and Herwegh, M.: Deformation at the frictional-viscous transition: Evidence for cycles of fluid-assisted embrittlement and ductile deformation in the granitoid crust, Tectonophysics, 693, 66–84, https://doi.org/10.1016/J.TECTO.2016.10.022, 2016.

Welch, M. J., Lüthje, M., and Oldfield, S. J.: Modelling the evolution of natural fracture networks, Springer, Cham, 973–978 pp., https://doi.org/10.1007/978-3-030-52414-2, 2020.

Whitaker, A. E. and Engelder, T.: Characterizing stress fields in the upper crust using joint orientation distributions, J Struct Geol, 27, 1778–1787, https://doi.org/10.1016/j.jsg.2005.05.016, 2005.

White, N. C.: Geological Interpretation of Aeromagnetic Data (David J. Isles and Leigh R. Rankin), Economic Geology, 109, 1495–1496, https://doi.org/10.2113/econgeo.109.5.1495, 2014.

Wibberley, C.: Are feldspar-to-mica reactions necessarily reaction-softening processes in fault zones?, J Struct Geol, 21, 1219–1227, https://doi.org/10.1016/S0191-8141(99)00019-X, 1999.

Williams, R. T. and Fagereng, Å.: The Role of Quartz Cementation in the Seismic Cycle: A Critical Review, Reviews of Geophysics, 60, e2021RG000768, https://doi.org/10.1029/2021RG000768, 2022.

WSP UK Limited: FracMan Energy Edition, Version 8.3, https://www.wsp.com/en-gb/services/fracman, 2024.

Yardley, B. W. D. and Bodnar, R. J.: Fluids in the Continental Crust, Geochem Perspect, 3, 1–2, 2014.

Zastrozhnov, D., Gernigon, L., Gogin, I., Planke, S., Abdelmalak, M. M., Polteau, S., Faleide, J. I., Manton, B., and Myklebust, R.: Regional structure and polyphased Cretaceous-Paleocene rift and basin development of the mid-Norwegian volcanic passive margin, Mar Pet Geol, 115, https://doi.org/10.1016/j.marpetgeo.2020.104269, 2020.

Zwingmann, H. and Mancktelow, N.: Timing of Alpine fault gouges, Earth Planet Sci Lett, 223, 415–425, https://doi.org/10.1016/J.EPSL.2004.04.041, 2004.

Zwingmann, H., Mancktelow, N., Antognini, M., and Lucchini, R.: Dating of shallow faults: New constraints from the AlpTransit tunnel site (Switzerland), Geology, 38, 487–490, https://doi.org/10.1130/G30785.1, 2010.

Appendix A

The material included in this appendix is from the published article Hodge et al. (2024b) supplementary material at the following location: https://doi.org/10.5194/se-15-589-2024-supplement

Locations of field, drill hole samples, and meso/microscale deformation images

Table A1. GPS locations for each of the images are provided below, either as sample site ID with UTM coordinates (Projected coordinate system UTM-WGS 1984, 32N)

Mesoscale deformation features						
Image ID	**Site ID**	**Sample ID**	**X**	**Y**	**Drill hole ID**	**Depth (m)**
A	1001	N/A	447053	7025827	BH1	97.95
B	1029	N/A	445432	7025769	BH2	15.5
C	1024	N/A	447264	7027955	BH2	108.3
D	1033	N/A	454471	7023250	N/A	N/A
E	1020	N/A	447104	7027930	N/A	N/A
F	1019	N/A	446969	7027950	BH2	93.4
Microscale deformation features						
A	N/A	125602	N/A	N/A	BH1	15.655
B	N/A	125612	N/A	N/A	BH1	92.74
C	N/A	125611	N/A	N/A	BH1	92.63
D	N/A	125644	N/A	N/A	BH2	108.27
E	N/A	125644	N/A	N/A	BH2	108.27
F	N/A	125622	N/A	N/A	BH2	79.735
G	1033	SP1033_1b	454471	7023250	N/A	N/A
H	N/A	125616	N/A	N/A	BH2	20.105
I	N/A	125628	N/A	N/A	BH2	91.65
K-Ar samples						
A	N/A	SK2012	N/A	N/A	BH2	108.3
B	N/A	SK2015	N/A	N/A	BH2	109.9
C	N/A	SK2008	N/A	N/A	BH2	79.7
D	N/A	120714	N/A	N/A	BH4	31.3
E	1024	SK1024_1	447264	7027955	N/A	N/A
F	1029	SK1029_1	445432	7025769	N/A	N/A
G	1033	SK1033_1	454471	7023250	N/A	N/A

Additional K-Ar sample descriptions incorporating X-ray diffraction results

In addition to the K-Ar sample geochronology and XRD results in Chapter 5, the following more detailed descriptions are provided for the seven fault gouge samples (Table 5.2) collected from drill holes BH2 (SK2008, SK2012, SK2015), BH4 (120714) (Figure 5.9), and fault core outcrop exposures on Smøla Island (SK1024_1, SK1029_1, SK1033_1). Please refer to the dated sample compositions by X-ray diffraction (XRD) results as shown in Figure 5.10 by weight percent (wt%), with the K-Ar dating results in Table 5.3 & Figure 5.11a, with the dating results relative to structure geometries in Figure 5.11b. The samples are characterised below, and are ordered by interpreted deformation episode (D_2 to D_4):

SK2012

Sample from BH2 at 108.3 m, from a 25 cm-wide foliated gouge/phyllite to cataclasite interval (Figure 5.9a), within monzogranite, with strong chlorite and sericite D_2 mineralisation and host rock fragments. The sampled interval strikes NE-SW with a shallow NW dip and exhibits no clear kinematics. XRD results (Figure 5.10) show that the K-Ar dates are provided by K-bearing illite/muscovite and smectite. In the sample, illite/muscovite (muscovite involves mostly sericite from the petrography work) increases with decreasing grain size fraction, with the highest abundance for the <0.1 µm size fraction (63 wt%). Smectite similarly increases in abundance within the smaller size fractions. The mineralogy of the sample is consistent through the size fractions, except for the quartz component within the coarser size fractions (0.4-2 to 6-10 µm), which derives from either the crystalline groundmass or host rock fragments. This sample yielded an age of 196.1 ± 2.8 Ma for the <0.1 µm size fraction, potentially authigenic, and 290.7 ± 4.4 Ma for the 6-10 µm (Table 5.3) fraction, potentially a protolithic/inherited component (e.g. Viola et al., 2016). The age results for the intermediate fractions, particularly 0.1-0.4 to 0.4-2 µm, are mixed authigenic-protolithic ages. Overall, the results for SK2012 indicate an inclined age spectra curve on Figure 5.11a.

SK2015

Sample from BH2, at 109.74 m, from a 20 cm-wide well-milled foliated clay-rich gouge zone, striking E-W, moderately S-dipping (Figure 5.9b), and is 3D modelled on Figure 5.8a as Zone IV. The sampled interval is set within highly fractured monzogranite, representing a well-defined damage zone. Within the gouge interval there are abundant host rock and quartz-calcite vein fragments. XRD results indicate the K-Ar ages derive from illite/muscovite, smectite, and potassium feldspar (Figure 5.10). Like SK2012, illite/muscovite (sericite) content increases in the finer grain size fractions. The coarser size fractions are quartz-dominated, with minor components of calcite, and potassium feldspar (limited to the size fractions 2-6 to 6-10 µm), potentially representing an inherited potassium source. Chlorite is present throughout the size fractions. The <0.1 µm size fraction yielded an age of 201.4 ± 2.9 Ma, and the 6-10 µm size fraction an age of 287.0 ± 4.7 Ma (Table 5.3), indicating a similar inclined age spectra curve as SK2012 (Figure 5.11a). Both the samples SK2012 and SK2015 returned similar ages for the 4-6 and 6-10 µm fractions, even though they from different structures with unique orientations (Figure 5.11a, b). This implies that there is an inherited component (potentially inherited illite/muscovite) present in both samples from an earlier tectonic episode.

SK1029_1

The field sample, collected from a ~5 cm-wide well-developed gouge, chlorite, and clay-rich zone, hosted in monzodiorite (Figure 5.9f). The sampled zone extends >10 m, striking ENE-WSW and dipping steeply SE, with no observable kinematics. The sampled zone is proximal and inclined to a major E-W structure, mapped as a 2nd order L3 lineament (Figure 5.2). XRD results show K-Ar ages derive from smectite, illite/muscovite, and zeolite. Overall, the sample is dominated by chlorite-smectite mixed clay (tosudite) and is the only mineral phase in the <0.1 µm size fraction. Illite/muscovite is present in the size fractions 0.1-0.4 to 6-10 µm and absent in the finest fraction. Zeolite is similarly present in the coarser size fraction, being particularly abundant in 2-6 µm, and 6-10 µm size fractions (Figure 5.10). In the coarser fractions, quartz, plagioclase, and amphibole are all present, representing host-rock fragments. The sample's finest fraction (<0.1 µm) yielded an age of 204.1 ± 3.7 Ma, which derives from authigenic smectite, with the largest fraction (6-10 µm) yielding and age of 218.2 ± 3.8 Ma (Table 5.3). The oldest age however come from the size fraction 0.4-2 µm (314. ± 5.4 Ma). The younger ages for the coarser fractions can be attributed to zeolite, which both mineralised at a later stage and while providing K to the system, potentially experienced radiogenic 40Ar loss from the crystal structure, leading to lower age results (e.g. Levy and Woldegabriel, 1995). The convex-upward age spectra curve on Figure 5.11a for SK1029_1, indicates that only the finest fraction provides a reliable age result.

SK2008

This sample, collected at 79.7 m in BH2, is from an 8 cm-wide indurated gouge to micro-vein breccia (Figure 5.9c), striking NNE-SSW, and dipping shallowly WNW, and exhibits no kinematic indicators. The sampled zone has typical D_3 chlorite-hematite mineralisation, in altered monzogranite, defining a ~5 m wide damage zone. XRD results indicate that illite/muscovite, potassium feldspar, and smectite (a significantly lower source of K compared to the other minerals) contribute towards the K-Ar ages. Hematite, which is the distinguishing feature of the sample, is present in all the size fractions (0.1-0.4 to 6-10 μm), except for the finest fraction. The illite/muscovite component is present in all size fractions but becomes a minor component in the <0.1 μm fraction (2 wt%). Smectite increases in abundance towards the finest fraction (80 wt% in the <0.1 μm fraction), while chlorite remains consistent through the size fractions. The coarser size fractions (2-6 to 6-10 μm) contain potassium feldspar, calcite, and quartz (with quartz also present in 0.4-2 μm fraction), representing host rock fragments. The <0.1 μm fraction returned a K-Ar age of 99.6 ± 1.8 Ma, with illite/muscovite and smectite potentially authigenic. The largest fraction provided a 195.2 ± 3.1 Ma age (Table 5.3), which with potassium feldspar present in the size fraction, could be a protolithic age. Overall, the age spectra curve for SK2008 on Figure 5.11a shows a plateau trend for the fractions 0.4-2 to 6-10 μm corresponding to ~200 Ma, which coincides with the finest fraction ages for samples SK2012, SK2015, and SK1029_1, also suggesting D_2 inheritance within the coarser fractions.

SK1033_1

A field sample from a ~25 cm-wide possible weathered gouge zone within a saprolite horizon (Figure 5.9g), bound by chloritic-hematite slickenside surfaces adjacent to the zone. The plane adjacent to the zone, oriented with low confidence owing to poor preservation, strikes ENE, dipping steeply SE, with dip-slip oriented slickenlines (too subtle to accurately measure). XRD results show a mineralogy dominated by smectite with minor illite/muscovite both contributing towards the K-Ar ages (Figure 5.10). Illite/muscovite is only present in the coarsest size fraction 6-10 μm, with minor abundance of chlorite also present within the fractions 0.4-2 to 6-10 μm. The finest fraction returned an age of 128.1 ± 11.8 Ma, with the large uncertainty associated to the low K wt % (Table 5.3) for the size fraction (<0.1). The coarsest fraction yielded an age of 263.3 ± 5.4 Ma (Table 5.3). The finest fraction K-Ar age, deriving entirely from smectite, may represent authigenic clay growth during saprolite formation or hydrothermal activity, or a mixture of the two processes. On Figure 5.11a, the age spectra curve for SK1033_1 is overall inclined from the finest to the coarsest fractions, however the youngest age is 126.0 ± 9.2 Ma corresponding to the 0.1-0.4 μm size fraction.

120714

Sample collected at 31.3 m in BH4, from a 40 cm-wide friable clay-rich gouge within a shear band, with cross-cutting zeolite veins, in diorite (Figure 5.9d). The sampled zone strikes NW-SE, with a moderate NE dip. XRD results show that the K-Ar dates derive from smectite, illite/muscovite, and potassium feldspar. The sample overall is smectite-dominated, and becomes more abundant in finer size fractions, with the finest fraction <0.1 µm composed entirely by smectite. Illite/muscovite is present in the two coarsest fractions, 2-6 to 6-10 µm, and the fraction 0.1-0.4 µm. The two coarsest fractions also have minor amounts of potassium feldspar, plagioclase, and calcite (which also occurs in the fraction 0.4-2 µm), representing potential host rock fragments. Chlorite is moderately abundant in all fractions except the finest fraction. The finest size fraction <0.1 µm yielded an age of 74.7 ± 1.7 Ma, the youngest age for all the samples collected from Smøla Island (Table 5.3). The coarsest fraction 6-10 µm returned an age of 153.6 ± 2.7 Ma, which may represent an inherited age owing to the presence of host rock potassium feldspar, and illite/muscovite. The zeolite veins, not present in the XRD results, crosscutting the sampled gouge, would have mineralised after these ages, indicating a possible upper limit on the timing of D4. Overall, the age spectra curve for 120714 is inclined from the finest to the coarsest size fraction (Figure 5.11a).

SK1024_1

This field sample, from a ~8 cm-wide foliated chloritic gouge zone (Figure 5.9g) within an 8 m wide damage zone. The sampled gouge zone, a D_2 to D_3 feature, strikes E-W, dips sub-vertically to steeply south, with crosscutting by zeolite veins, and is adjacent to hematite fractures. Due to insufficient material in the finest fraction (<0.1 µm), both XRD and K-Ar dating analysis could not be undertaken for this size fraction. This sample is therefore included for demonstrative purposes only. For the other size fractions, the XRD analysis indicates that smectite, illite/muscovite, and zeolite all contributed to the K-Ar ages. The size fractions 0.4-2 to 6-10 µm have similar mineral compositions, with major amounts of smectite, chlorite, and zeolite, and lower abundances of quartz and illite/muscovite. The 0.1-0.4 µm has much lower abundances of zeolite, quartz, and illite/muscovite. The K-Ar ages for the size fractions range from 162.1 ± 3.1 Ma to 163.5 ± 3.0 Ma for the coarsest fraction (Table 5.3), with the oldest age (180.5 ± 3.4 Ma) associated with the 0.4-2 µm fraction. The age spectra curve on Figure 5.11a is a convex-upward shape, with zeolite presence in the coarser fractions resulting in a lower age, similar to sample SK2029_1.

Appendix B

The material included in this appendix is from the manuscript under revision Hodge et al. (2024a), the supplementary material at the following location:

https://assets-eu.researchsquare.com/files/rs-4844693/v1/2b2a1135a9e03D$_2$936863c31.pdf

The location of the supplementary material is subject to change depending on the outcome of the review and publishing process.

Lineament traces mapped over different parts of Smøla island

Table B1. Trace length parameters for each trace set by mapping scale area.

Area	Trace set	Minimum length (m)	Maximum length (m)	Minimum cut-off length (m)	Total length (m)
1:500 (20807.66 m^2)	N-S	0.35	47.54	10.30	3541.6
	NE-SW	0.60	72.34	11.64	2783.2
	E-W	0.48	60.70	6.45	639.4
	NW-SE	0.55	113.74	7.54	2690.4
1:7500 (34241425.73 m^2)	N-S	1.86	1197.67	142.40	168794.0
	NE-SW	4.38	2146.51	203.06	150405.8
	E-W	0.03	4899.83	412.86	214663.1
	NW-SE	0.08	1064.82	124.08	148921.8
1:25 000 (37312970.23 m^2)	N-S	6.80	5177.12	232.83	66587.8
	NE-SW	11.70	4151.56	413.10	179317.4
	E-W	68.03	2674.26	420.23	42934.2
	NW-SE	9.93	3434.82	325.42	120565.9
1:100 000 (266043176 m^2)	N-S	1.98	4543.62	753.14	171599.5
	NE-SW	0.09	8791.90	1005.85	498734.0
	E-W	0.61	13641.66	774.66	259261.9
	NW-SE	0.53	10678.79	811.53	200668.8

Comparison of different volumetric intensity P_{32} values derived from areal intensity P_{21} and linear intensity P_{10}

In Table B2, the P_{32} estimates (both isotropic and oriented) derived from the 1:500 trace map, are significantly lower than the drill hole P_{32} estimates (derived for P_{10}). This is due to the lineament traces mapping at the 1:500 scale being at a lower resolution to the determined fracture occurrence in the downhole televiewer data.

Table B2. P_{32} *values derived using either the 1:500 trace map using the *Dershowitz (1984) and **Wang et al. (2005) methods. The drill hole televiewer data derived* P_{32} *are included for comparison.*

Fracture Set	**1:500 trace map P_{21} (m.m^{-2})**	**Trace map P_{32} isotropic* (m².m^{-3})**	**Trace map P_{32} (C_{23}) ** (m².m^{-3})**	**Drill hole P_{32} (C_{13}) ** (m².m^{-3})**
NE-SW (D_1)	0.13	0.17	0.14	0.76
E-W (D_2)	0.03	0.04	0.03	1.68
‘Shallow’ (D_2)	0.03	0.04	0.06	1.84
N-S (D_3)	0.17	0.22	0.17	0.66
NW-SE (D_{4+5})	0.13	0.16	0.13	0.47

Aperture input

Please note for the below plot, the vein true thicknesses range from 0.1 mm to 280 mm, with average values of 3.44 mm (D_1), 3.94 mm (D_2), 10.26 mm (D_3), 7.18 (D_4), and 14.74 mm (D_5). As I combined D_4 and D_5 related deformation features for this study (D_{4+5}), an average paleo-aperture value of 11 mm has been chosen for this fracture generation.

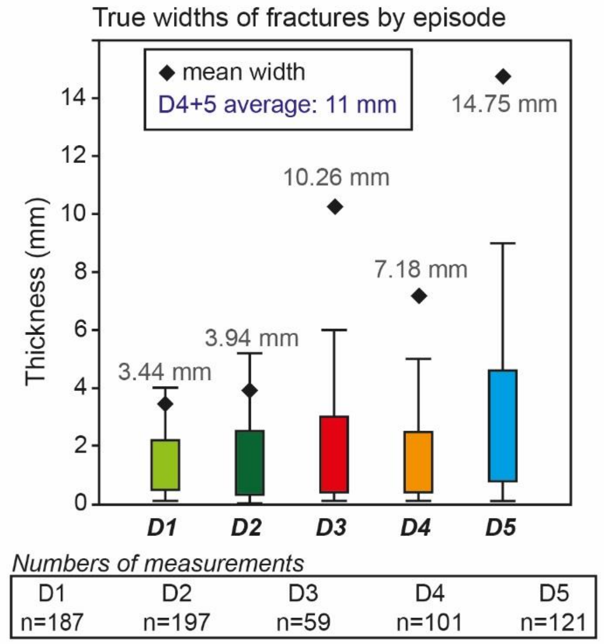

Numbers of measurements

D1	D2	D3	D4	D5
n=187	n=197	n=59	n=101	n=121

Figure B1. True width (taken as corresponding to fracture paleo-aperture) measurements of veins corresponding to D_1 to D_5 deformation episodes. The mean width values are illustrated on the graph with black diamonds. The average true width for D_4 and D_5 (grouped together in this study) is 11 mm. Number of measurements per deformation episode is also shown. Outliers are not shown in this graph for visual clarity reasons

Model parameters

Table B3. Input parameters for the 500 m^3 'grown' DFN models

Grown DFN input parameters

Model Generation:	**D4+5**					**D3**				**D2**			**D1**
Fracture sets	NE -SW D1	E-W D2.1	Shallow D2.2	N-S D3	NW -SE D4+5	NE -SW D1	E-W D2.1	Shallow D2.2	N-S D3	NE -SW D1	E-W D2.1	Shallow D2.2	NE -SW D1
P32 target intensity	0.3	0.3	0.2	0.3	0.5	0.3	0.3	0.2	0.6	0.3	0.5	0.4	0.6
Orientation pole trend	122.9	173.2	106.7	75	242.04	122.9	173.2	106.7	75	122.9	173.2	106.7	122.9
Orientation pole plunge	0.66	0.19	74.53	10	8.02	0.66	0.19	74.53	10	0.66	0.19	74.53	0.66
Orientation distribution	Fisher	Fisher	Fisher	Fisher	Fisher	Fisher	Fisher	Fisher	Fisher	Fisher	Fisher	Fisher	Fisher
Pole concentration	11.78	15	20	25	11.12	11.78	15	20	25	11.78	15	20	11.78
Size distribution	Power Law	Power Law	Power Law	Power Law	Power Law	Power Law	Power Law	Power Law	Power Law	Power Law	Power Law	Power Law	Power Law
Size min. length (m)	1	10	5	10	5	1	10	5	10	1	10	5	1
Size length slope (α)	1.984	1.619	1.619	2.273	2.005	1.984	1.619	1.619	2.273	1.984	1.619	1.619	1.984
Truncate min. (m)	1	9	5	10	5	1	9	5	10	1	9	5	1
Truncate max. (m)	20	80	60	80	45	20	80	60	80	20	80	60	20
Shadow factor	0.3	0.1	0.2	0.1	0.1	0.3	0.1	0.2	0.1	0.3	0.1	0.2	0.3
Generation timestep	10	30	30	30	30	10	30	30	30	10	30	30	10
Fracture growth timesteps	1	10	10	10	10	1	10	10	10	1	10	10	1
Termination NE -SW	0.19	0.2	0.2	0.1	0.2	0.19	0.2	0.2	0.1	0.19	0.2	0.2	0.19
Termination E -W		0.3	0	0.3	0.3		0.3	0	0.3		0.3	0	
Termination Shallow			0	0.3	0.3			0	0.3			0	
Termination N -S				0.06	0.3				0.06				
Termination NW -SE					0.1								
Aperture (mm)	0.03	0.04	0.04	0.09	0.1	0.03	0.04	0.04	0.09	0.03	0.04	0.04	0.03
Aperture distribution	Constant	Constant	Constant	Constant	Constant	Constant	Constant	Constant	Constant	Constant	Constant	Constant	Constant
Permeability (m2)	5.10E -12	5.10E -12	5.10E -12	5.10E -12	5.10E -12	5.10E -12	5.10E -12	5.10E -12	5.10E -12	5.10E -12	5.10E -12	5.10E -12	5.10E -12
Permeability distribution	Constant	Constant	Constant	Constant	Constant	Constant	Constant	Constant	Constant	Constant	Constant	Constant	Constant

Permeability tensor conversion for stereonet plot analysis

The procedure for converting the Oda permeability eigenvector components into a principal direction axis (linear data) which could be plotted on a stereonet plot using trend/plunge orientations (after Ceccato, A., Pers. Comm. 2023) is briefly outlined here:

For each time-constrained DFN, the nested 200 m^3 grid upscaling volume generated Oda permeability eigenvector components in the x, y, and z directions in the following format: 'Oda' V1 (x, y, z), V2 (x, y, z), V3 (x, y, z)). To subsequently derive the trend and plunge orientations, the eigenvector components for V1, V2, and V3 are processed systematically one by one using the following procedure:

Using V1 as an example, the x and y components provided the azimuth (trend) value (θ^{azi}) in degrees (converted from radians), as the resultant horizontal vector angle with following formula: $\theta=\arctan\left(\frac{V1_X}{V1_Y}\right)\times\frac{180}{\pi}$ which in Microsoft Excel involves the formula "=DEGREES(ATAN($V1_x$/$V1_y$))". The value is then converted into a 0-360° azimuth angle system depending on the cartesian quadrant that the X and Y components plotted in. These are when $V1_x>0$ and $V1_y>0$, $\theta^{azi} = \theta$; when $V1_x<0$ and $V1_y>0$, $\theta^{azi} = 360+\theta$; and when $V1_x<0$ and $V1_y<0$, or when $V1_x>0$ and $V1_y<0$, $\theta^{azi} = 180+\theta$. Effectively, the converted degree azimuth (trend) value (θ^{azi}) is either kept the same as θ, or added to 360 or added to 180.

Still using V1 as an example, the z component then is used to provide the inclination (plunge) value (θ^{p}) in degrees (converted from radians), as the resultant vertical vector angle with following formula: $\theta=\text{arcsine}(V1_Z)\times\frac{180}{\pi}$ which in Microsoft Excel involves the formula "=DEGREES(ASIN($V1_z$))". The value is then converted into a 0-90° plunge angle system depending on the whether θ is positive or negative ($\theta>0$ or $\theta<0$). Therefore, when $\theta<0$, $\theta^{p} = \theta\times-1$; when $\theta>0$, $\theta^{p} = \theta$.

Consequently, for each V1, V2, and V3 vector a trend and plunge orientation can be calculated which can be associated with a principal permeability axis (with V1 corresponding to the principal axis K_1, V2 being K_2, and V3 being K_3). These linear orientations can then subsequently be plotted as points (or poles) on a stereonet plot and assessed for clustering trends to derive the mean orientations of the corresponding principal axis.

Network topology analysis

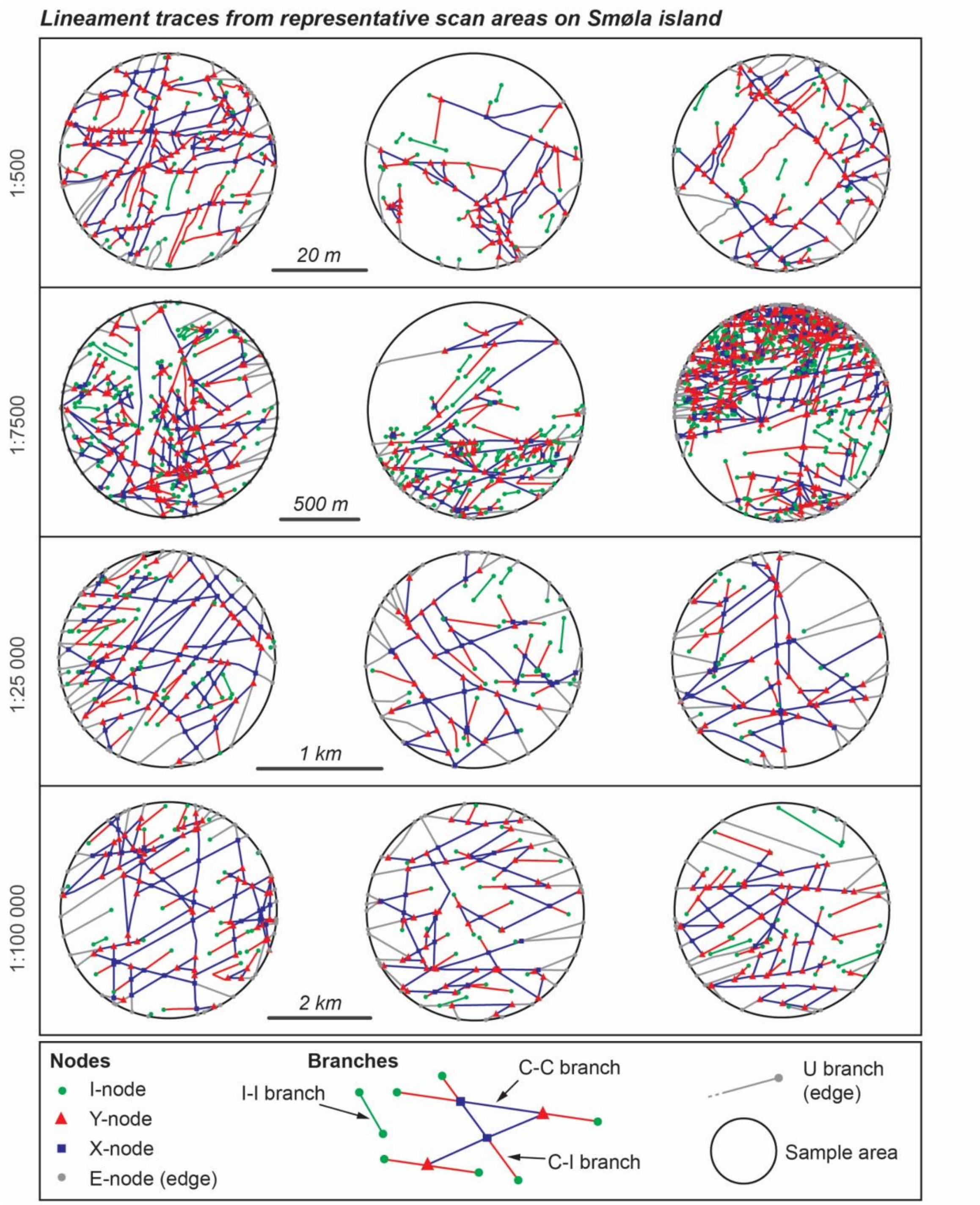

Figure B2. All representative scan areas used in the deterministic topology and termination relationship analyses.

Table B4. Counts of branches and nodes from the representative scan areas in Figure B2, with locations shown in Figure 4.2, used to calculate the connectivity measure C_B for the mapped (deterministic) lineaments.

Deterministic connections per branch (C_B) calculation

Scale	No. I-Node	No. Y-Node	No. X-Node	No. Branches	Calculated C_B	Average C_B
500	40	109	19	228	1.77	
500	33	70	12	139	1.86	1.80
500	25	54	4	101	1.76	
7500	110	138	54	373	1.69	
7500	124	72	28	217	1.51	1.65
7500	231	362	118	891	1.75	
25000	52	44	46	178	1.78	
25000	18	28	25	100	1.84	1.75
25000	33	24	22	98	1.63	
100000	40	43	35	165	1.63	
100000	33	35	10	98	1.48	1.50
100000	24	20	19	97	1.40	

Table B5. Counts of branches and nodes from the 500 m^3 DFN models (three representative scan areas per DFN), used to calculate the connectivity measure C_B *for the different deformation episodes.*

Modelled connections per branch (C_B) calculation

Deformation epidote	No. I-Node	No. Y-Node	No. X-Node	No. Branches	Calculated C_B	Average C_B
D_1	96	16	4	77	0.83	
D_1	99	24	9	101	1.07	1.01
D_1	110	37	11	136	1.14	
D_2	46	24	32	123	1.63	
D_2	45	27	57	172	1.80	1.74
D_2	47	35	78	232	1.80	
D_3	47	40	82	243	1.84	
D_3	57	61	89	306	1.76	1.82
D_3	46	68	92	306	1.87	
D_{4+5}	70	66	67	264	1.77	
D_{4+5}	64	82	91	329	1.85	1.79
D_{4+5}	64	53	65	241	1.74	

Table B6. Cluster and block analysis results for the scan areas by deformation episode.

Def. Episode	**Scan Area**	**P21 ($m.m^{-2}$)**	**No. Clusters**	**Largest Cluster: sum of trace lengths (m)**	**Enclosed Regions**	**Enclosed Regions Average Size (m2)**	**R_{22}**	**Enclosed Regions Average Size (m2)**
D_1	1	0.76	58	26.13	0	0	1.000	0
	2	1.05	47	58.68	4	0.11	0.200	0.11
	3	1.01	57	64.69	5	0.3	0.167	0.3
D_2	1	1.06	21	268.84	27	1.63	0.036	1.63
	2	1.36	4	414.4	63	2.43	0.016	2.43
	3	1.20	22	309.28	55	1.46	0.018	1.46
D_3	1	1.25	3	381.3	71	1.67	0.014	1.67
	2	1.51	6	458.66	94	2	0.011	2
	3	1.44	13	432.03	91	2.47	0.011	2.47
D_{4+5}	1	1.38	12	404.4	58	2.03	0.017	2.03
	2	1.16	14	328.85	57	2.99	0.017	2.99
	3	1.52	15	376.72	93	1.24	0.011	1.24

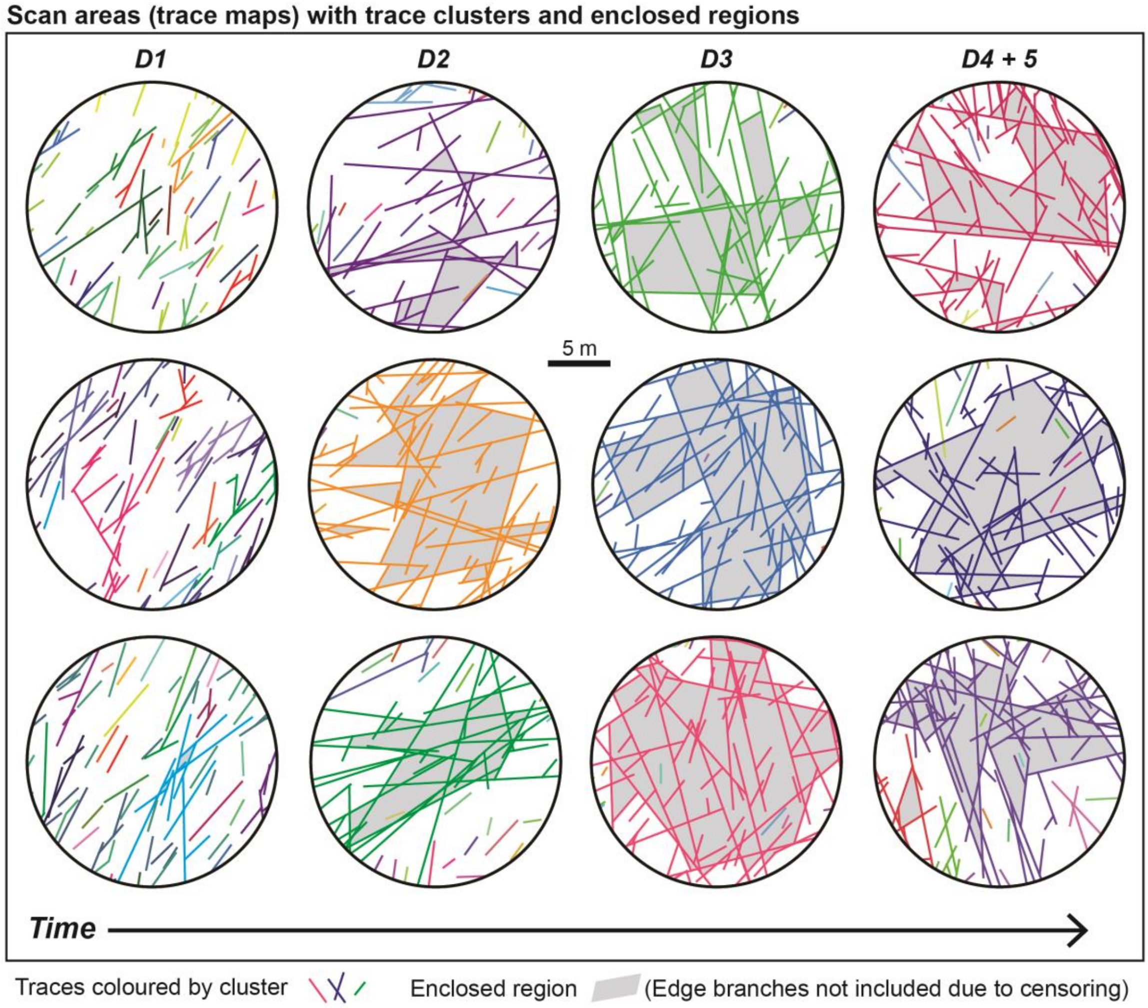

Figure B3. Scan areas with coloured modelled clusters (one or more connected trace lines) and enclosed areas (grey coloured polygons) by deformation episode.

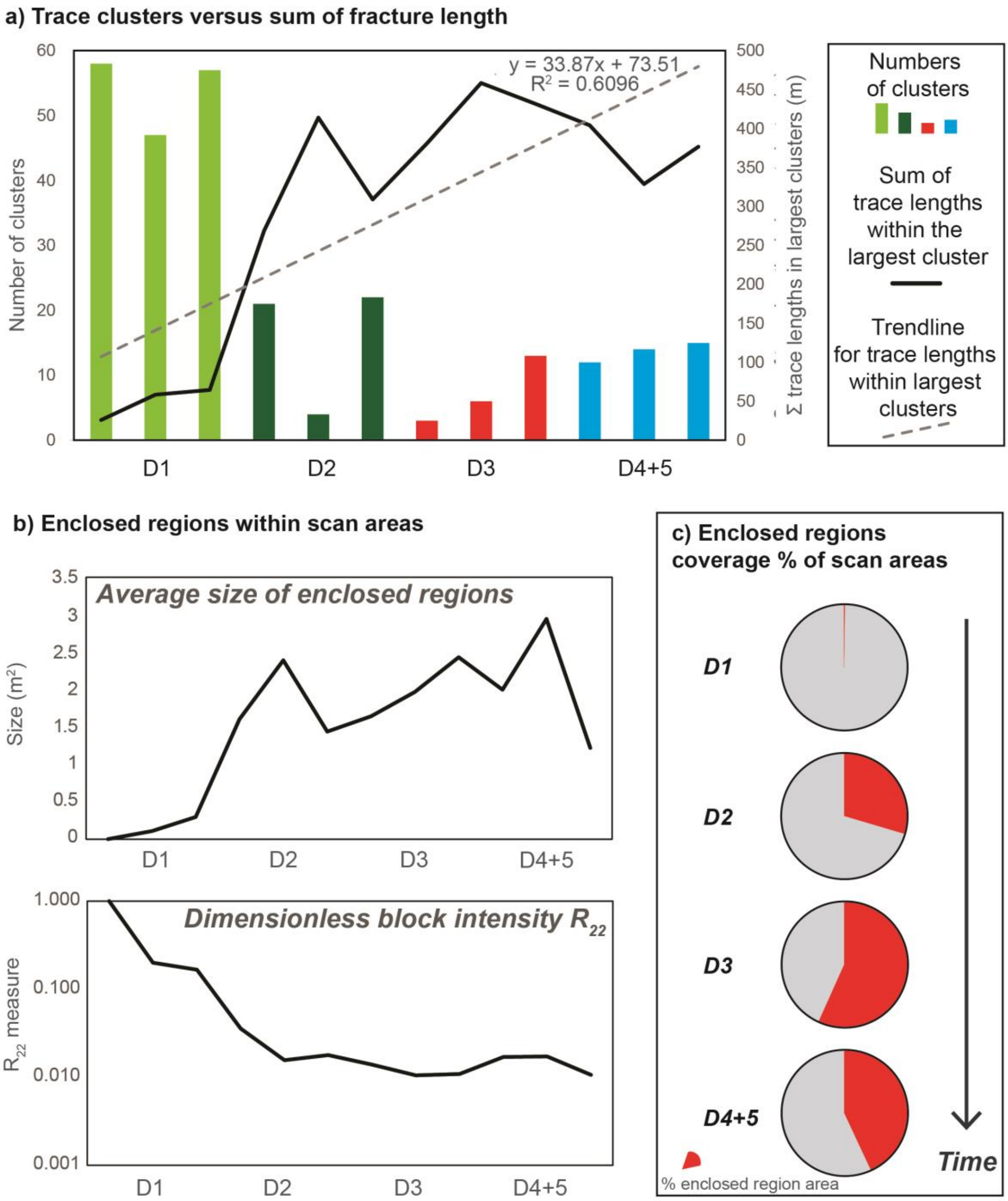

Figure B4. Graphical representation of the cluster and block analysis results by deformation episode. (a) Bar plot of numbers of clusters in each scan area by deformation episode, plotted against the combined length of included traces within the largest cluster in each scan area. A trend line has been included for visual purposes to indicatethe increasing trend of trace lengths against the decreasing number of clusters (through time there are generally fewer clusters with greater included trace lengths, or in other words, larger more connected clusters). (b) Line plots of both the average size of the enclosed regions and the dimensionless block intensity measure R_{22} by deformation episode. (c) As a complementary plot to the R_{22} measure, pie charts are included to show the change in proportion of the scan areas covered by enclosed regions (blocks), indicated by the red area of the plots, through time.

Assessment of model outputs

Additional model validation

Using the deterministic inputs, and adjusted P_{32} values, our models were able to replicate the target volumetric fracture intensities (Table B7). These P_{32} values, even though adjusted from the drill hole televiewer data-derived P_{10} values (and conversion to P_{32}), still allow for a realistic simulation of fractured rock volumes on Smøla, at the 1:500 scale given the fracture set size distribution parameters we have used. The DFN approach is therefore considered to be adequate for the purpose of this study.

In terms of validating the fracture connectivity (C_B) values derived from our 2D trace map slices, we rely on the final D_{4+5} model as we assume it to be replicating a similar pattern of fractures as is seen today on Smøla island. The D_{4+5} model did not return the highest fracture connectivity value of the modelled DFN outputs. However, the modelled 2D fracture pattern is visually similar to both the 1:25 000 and 1: 100 000 trace maps. In terms of proportions of nodes and connections per branch (C_B) the modelled output is similar to what is counted for the deterministic trace maps (Figure 7.7 and B2), suggests at least at those resolutions, the modelling can replicate the natural lineament pattern.

Table B7. Modelled P_{32} values vs Input P_{32} values

Model	Input P_{32}	Output P_{32}
D_{4+5}	1.60	1.56
D_3	1.40	1.30
D_2	1.20	1.24
D_1	0.60	0.67

Representativeness

Our modelling at 500 m³, and estimation of both bulk permeability tensors and fracture connectivity from nested 200 m^3 grids, aims for regional representativeness applicable to reservoir volumes. The datasets (2D trace maps and field data) were collected over ~25 km², with four drill holes in two parts of Smøla (~5 km apart) involving monzogranite and diorite rock volumes. High-resolution drill core data captured mesoscale to centimetre-scale fracture connectivity and volume permeability, translatable to km scales. Due to computational demands, target P_{32} values were reduced in the models compared to drill hole measurements (as already outlined above). The volumetric intensity values strike a balance between the drill hole derived P_{10} values, which derive from fracture counts at the centimetre to meter-scale, and the trace map derived P_{21} values (from traces mapped at the tens (1:500) of metres-scale). However, using the scaling exponents (α) derived from multiple trace map scales, up to the tens of kilometres-scale, permits us the ability to model selectively at the scale that we have chosen. We are therefore confident that the DFN models therefore strike a balance between computational efficiency and realistic mesoscale representation. Further work on ‘conditioning’ or calibrating the model fracture intensities better to the observed fracture intensities in drill hole or outcrops is included in Chapter 8.

Appendix C

DFN Model inputs

Table C1. Input parameters for 50 m^3 'grown' DFN models

Grown DFN input parameters

Model Generation:	**D4+5**					**D3**				**D2**			**D1**
Fracture sets	NE-SW D1	E-W D2.1	Shallow D2.2	N-S D3	NW-SE D4+5	NE-SW D1	E-W D2.1	Shallow D2.2	N-S D3	NE-SW D1	E-W D2.1	Shallow D2.2	NE-SW D1
P32 target intensity BH1	1.1	1.2	1.3	0.4	0.4	1.0	1.2	1.3	0.4	1.0	1.2	1.3	1.2
P32 target intensity BH2	1.0	0.9	0.9	0.4	0.4	1.0	1.0	1.0	0.4	1.0	1.0	1.0	1.5
P32 target intensity BH3	0.2	0.3	1.4	0.7	0.1	0.2	0.3	1.2	0.6	0.2	0.4	1.5	0.2
P32 target intensity BH4	0.5	0.3	1.1	0.2	0.2	0.4	0.3	1.1	0.2	0.4	0.3	1.1	0.5
Orientation pole trend	122.9	173.2	106.7	75	242.04	122.9	173.2	106.7	75	122.9	173.2	106.7	122.9
Orientation pole plunge	0.66	0.19	74.53	10	8.02	0.66	0.19	74.53	10	0.66	0.19	74.53	0.66
Orientation distribution	Fisher	Fisher	Fisher	Fisher	Fisher	Fisher	Fisher	Fisher	Fisher	Fisher	Fisher	Fisher	Fisher
Pole concentration	11.78	15	20	25	11.12	11.78	15	20	25	11.78	15	20	11.78
Size distribution	Power Law	Power Law	Power Law	Power Law	Power Law	Power Law	Power Law	Power Law	Power Law	Power Law	Power Law	Power Law	Power Law
Size min. length (m)	1	4	2.5	2	2	1	4	2.5	2	1	10	5	1
Size length slope (α)	1.984	1.619	1.619	2.273	2.005	1.984	1.619	1.619	2.273	1.984	1.619	1.619	1.984
Truncate min. (m)	1	2	1	1	1	1	2	1	1	1	2	1	1
Truncate max. (m)	5	20	12.5	10	10	5	20	12.5	10	5	20	12.5	5
Shadow factor	0.35	0.1	0.2	0.1	0.2	0.35	0.1	0.2	0.1	0.35	0.1	0.2	0.35
Generation timestep	10	20	25	20	20	10	20	25	20	10	20	25	10
Fracture growth timesteps	1	10	10	10	10	1	10	10	10	1	10	10	1
Termination NE -SW	0.19	0.2	0.2	0.1	0.2	0.19	0.2	0.2	0.1	0.19	0.2	0.2	0.19
Termination E -W		0.3	0	0.6	0.3		0.3	0	0.6		0.3	0	
Termination Shallow			0	0	0			0	0			0	
Termination N -S				0.06	0.3				0.06				
Termination NW -SE					0.1								
Aperture (mm)	0.03	0.04	0.04	0.09	0.1	0.03	0.04	0.04	0.09	0.03	0.04	0.04	0.03
Aperture distribution	Constant	Constant	Constant	Constant	Constant	Constant	Constant	Constant	Constant	Constant	Constant	Constant	Constant
Permeability (m2)	5.10E-12	5.10E-12	5.10E-12	5.10E-12	5.10E-12	5.10E-12	5.10E-12	5.10E-12	5.10E-12	5.10E-12	5.10E-12	5.10E-12	5.10E-12
Permeability distribution	Constant	Constant	Constant	Constant	Constant	Constant	Constant	Constant	Constant	Constant	Constant	Constant	Constant